Synthesis, Structural Characterisation and Physical Properties of Metal Oxychalcogenides

CHRISTOPHER MICHAEL AINSWORTH

Abstract

"Synthesis, Structural Characterisation and Physical Properties of Metal Oxychalcogenides"

PhD Thesis Chris M. Ainsworth January 2017

Chapter 1 is a literature review on oxychalcogenide materials, with emphasis on structures similar to those discussed in later chapters of this thesis. These materials display a whole host of interesting properties and have garnered particular interest in recent years.

Chapter 2 describes the synthetic methods and characterisation techniques used to study the materials discussed in this thesis. It includes the theory behind powder diffraction techniques, Rietveld refinement, and a range of physical property measurement techniques.

Chapter 3 discusses the synthesis, structural characterization, and physical properties of the new transition metal oxyselenide $Ce_2O_2ZnSe_2$. It adopts a ZrCuSiAs-related structure with Zn^{2+} cations in a new ordered arrangement within $[ZnSe_2]^{2-}$ layers. The cell volume of the sample, and consequently the physical properties, can be controlled by subtle modification of the synthetic conditions. $Ce_2O_2ZnSe_2$ is a semiconductor at all cell volumes with experimental optical band gaps of 2.2, 1.4, and 1.3 eV for high-, intermediate-, and low-cell volume samples, respectively. SQUID measurements show $Ce_2O_2ZnSe_2$ to remain paramagnetic down to low temperature.

Chapter 4 reports 60 new compositions across the $La_2O_2(Fe_{1-y}Zn_y)Se_2$, $La_2O_2(Zn_{1-y}Mn_y)Se_2$, $La_2O_2(Mn_{1-y}Cd_y)Se_2$, $Ce_2O_2(Fe_{1-y}Zn_y)Se_2$, $Ce_2O_2(Zn_{1-y}Mn_y)Se_2$, $Ce_2O_2(Mn_{1-y}Cd_y)Se_2$, $La_{2-z}Ce_zO_2FeSe_2$, $La_{2-z}Ce_zO_2ZnSe_2$, $La_{2-z}Ce_zO_2MnSe_2$, and $La_{2-z}Ce_zO_2CdSe_2$ solid solutions. These series reveal that the transition metal arrangement in the $Ln_2O_2MSe_2$ (*Ln* = La & Ce, *M* = Fe, Zn, Mn & Cd) compounds can be systematically controlled by either *Ln* or *M* substitution leading to an "infinitely adaptive" structural family.

Chapter 5 describes a new family of compounds containing both +1 and +2 transition metal ions in the $La_2O_2Cu_{2-2x}Cd_xSe_2$ family. It shows how Cu^{1+} and Cd^{2+} ions segregate into distinct fully occupied and half occupied checkerboard-like layers respectively, leading to complex long-range superstructures in the 3rd (stacking) dimension. To understand the structure and microstructure of these new materials a new methodology for studying low-probability stacking faults using a Rietveld-compatible supercell approach was developed and applied.

Chapter 6 investigates the solid solution $La_{2-z}Sr_zO_2Cu_{0.5}CdSe_2$. This takes the compound $La_2O_2Cu_{0.5}CdSe_2$ (x = 0.5 from Chapter 5, with a 1:1 ratio of Cu:Cd layers) and Sr^{2+} dopes on the La^{3+} site, where the solubility limit is shown to be ~15% (z = 0.3). At z = 0, ρ(300 K) = 1.5×10^{4} Ω cm. After Sr doping, ρ(300 K) decreased significantly to 8.2×10^{1} Ω cm at z = 0.05, reaching a minimum at ~6×10^{-1} Ω cm for z = 0.3. DFT calculations of $La_2O_2CuCd_{0.5}Se_2$ show that the valence band consists of Cu 3d and Se 4p states, hence electronic conduction should be confined to $[Cu_2Se_2]^{2-}$ layers.

Chapter 7 extends the work of Chapter 5 by discussing three more solid solutions analogous to $La_2O_2Cu_{2-2x}Cd_xSe_2$. These are $La_2O_2Cu_{2-2x}Fe_xSe_2$, $La_2O_2Cu_{2-2x}Zn_xSe_2$ and $La_2O_2Cu_{2-x}Mn_xSe_2$. It also investigates the effect of systematically varying the +2 transition

metal size in the solid solutions $La_2O_2Cu(M_{0.5-y}M'_y)Se_2$ and $La_2O_2Cu_{0.667}(M_{0.667-y}M'_y)Se_2$ (*M*/*M'* = Fe/Zn, Zn/Mn & Mn/Cd).

Chapter 8 will briefly summarise and link the work described in Chapters 3 to 7.

Synthesis, Structural Characterisation and Physical Properties of Metal Oxychalcogenides

Chris M Ainsworth M.Chem (Dunelm)

Durham University

Supervisor: Prof. John S. O. Evans

A thesis submitted in partial fulfilment of the requirements

for the degree of Doctor of Philosophy

Department of Chemistry

Durham University

2017

Table of Contents

Abbreviations

AOG	Aluminium oxygen getter
CASTEP	Cambridge Serial Total Energy Package
CB	Conduction band
CCD	Charged coupled device
CIF	Crystallographic information file
DFT	Density functional theory
DOS	Density of states
DRS	Diffuse reflectance spectroscopy
ICSD	Inorganic crystal structure database
LDA	Local density approximation
MPMS	Magnetic property measurement system
ND	Neutron diffraction
PDOS	Partial density of states
PND	Powder neutron diffraction
PPMS	Physical property measurement system
PXRD	Powder X-ray diffraction
RMM	Relative molecular mass
SAED	Selected area electron diffraction
SQUID	Superconducting quantum interference device
TA	TOPAS Academic
TEM	Transmission electron microscopy
TOF	Time-of-flight

VB	Valence band
XRD	X-ray diffraction

Declaration & Statement of Copyright

The work described in this thesis is entirely my own, except where I have acknowledged help from, or collaboration with, a named person, or given reference to a published source or thesis.

The research presented was performed in the Department of Chemistry, Durham University, between October 2013 and December 2016, the result of which have not been submitted for a degree in this or any other university.

Acknowledgments

I would like to start by saying a big thank you to Rachel, my significantly better half. You made personal sacrifices which allowed me to start studying for a PhD at Durham and for that I will be forever in your debt (though perhaps I can repay you in Curly Wurly chocolate bars!).

The first few months of my PhD felt quite intimidating as I had so much to learn. I am very grateful in particular to Andrew Tuxworth who answered my incessant questions during this period with a smile (even though you were trying to write your own thesis at the time) and to Matt Tate for always being more than willing to help.

This thesis would not have possible without the help and expertise from numerous people outside of the group, including Budhika Medhis (TEM), Leon Bowen (SEM), Mark Raine (PPMS), Andrew Duckworth (DRS) and Ales Stefanic (SQUID). I would also like to thank the oxychalcogenide related 4th year project students and summer students, Jack Blandy, Vicky Lazarus, Sam Champion, Jamie Baird and Abby Haworth, for their invaluable contributions.

A special mention should go out to Ivana Evans. Although you are not my direct supervisor, I have been very fortunate to have your additional expertise and support. Спасибо.

I would also like to thank James Lewis and Luiza "Rosie" de Araujo for continued friendship that I consider to be special. Before I started at Durham, I never would have imagined that my new best friends would include a southerner with a Chunky Vegetable soup addiction and a 4 foot tall Brazilian with a Malted Milk biscuit addiction!

A specific mention should also go to Chun-Hai Wang, I was very fortunate to have been able to work alongside you for two years. Not only for your guidance and contributions towards the work, which at times were nothing short of genius, but also to have known you as a person. You are as pure at heart as anybody I have ever met and I feel knowing you made me a better person.

That just leaves me with one more specific thank you, to my supervisor John Evans. I feel infinitely lucky to have landed you as a PhD supervisor. You have an ability to manage each student as an individual in order to create an environment for them to best achieve. Your staggering intellectual capabilities and willingness to devote time to keep the work moving forward meant that I never felt constrained as to what could be achieved. This has made my time at Durham a refreshing period of my life. You are a true professional and I only hope you are as proud of the work in this thesis as I am.

Last but not least, a huge thank you should go out to all members of the Evans group as a whole, past and present. I have met some amazing people who have enriched my life over the past $3^{1}/_{4}$ years and I take fond memories away with me.

Chapter 1: Introduction and Literature Review

1.1 Overview

Oxychalcogenides are mixed anion compounds containing both oxide ions and anions of another group 16 element, typically S, Se or Te. Recently, superconductivity has been reported in $Bi_4O_4S_3$ (T_c up to 8.6 K),[1-3] $LnO_{1-x}F_xBiS_2$ (Ln = La, Ce, Pr, Nd, Yb; T_c 1.9 – 4.6 K),[4,5] $LaO_{0.5}F_{0.5}BiSe_2$ (T_c 2.6 K),[6] $Bi_3O_2S_3$ (T_c 4.0 - 5.8 K)[7,8] and $Eu_3Bi_2S_4F_4$ (T_c 1.5 K)[9]. Although superconductivity is the primary driver for the study of oxychalcogenides, many have been shown to have interesting electronic, magnetic and optical properties. Throughout this thesis, oxychalcogenides will be written as $A_aO_bM_cCh_d$, where "*A*" will indicate a trivalent rare-earth metal ion (or a Sr^{2+} in certain doped cases), *M* will indicate a transition metal ion, and *Ch* a chalcogenide ion (S, Se or Te).

The two anions in oxychalcogenides are markedly different in terms of both their ionic radii and chemistries. The bonding of the smaller more electronegative oxygen anion is usually predominantly ionic in nature, while the larger, more polarisable chalcogenide ion (S, Se or Te) bonds with more covalent character. For this reason oxychalcogenides often form 2-dimensional layered structures which separate the different anions. They are also able to stabilise some unusual geometries.

The quaternary ZrCuSiAs-type phases are by far the most studied oxychalcogenides, and contain fluorite-type lanthanide-oxide layers and anti-fluorite-type metal-chalcogenide layers. Cu containing compounds of this type have received most attention due to their interesting electronic and optical properties.[10-13] They are highly stable, in part due to the complementary sizes of the constituent A_4O and $CuCh_4$ tetrahedra, and in part due to the soft nature of Cu and hard nature of the lanthanide ions, which causes preferential bonding to Se and O respectively.

In recent years a group of closely related ZrCuSiAs-type phases containing transition metals in the +2 oxidation state (as opposed to +1 with Cu), leading to half occupancy of the sites has also emerged. This has led to the discovery of some exotic transition metal ordering.[14-17] The main focus of this review will be on the synthesis, structural properties, and physical properties of these quaternary ZrCuSiAs-type materials (and materials closely related), as this is most relevant to the work being presented in this thesis. In 2008, Clarke *et al.* published a review of other known layered oxychalcogenide (and oxypnictide) phases.[18]

1.2 Quaternary $A_2O_2M_2Ch_2$ Materials with the ZrCuSiAs Structure

The ZrCuSiAs structure type is adopted by a large number of oxychalocogenides. It is built from alternating layers of fluorite-like $[A_2O_2]^{2+}$ sheets and antifluorite-like $[M_2Ch_2]^{2-}$ sheets, which are constructed from distorted edge-sharing A_4O and MCh_4 tetrahedra. These layers stack alternatively along the *c*-axis, space group *P4/nmm*, as shown in Figure 1.1. The *A* cation sits in an 8 coordinate AO_4Ch_4 square antiprism environment.

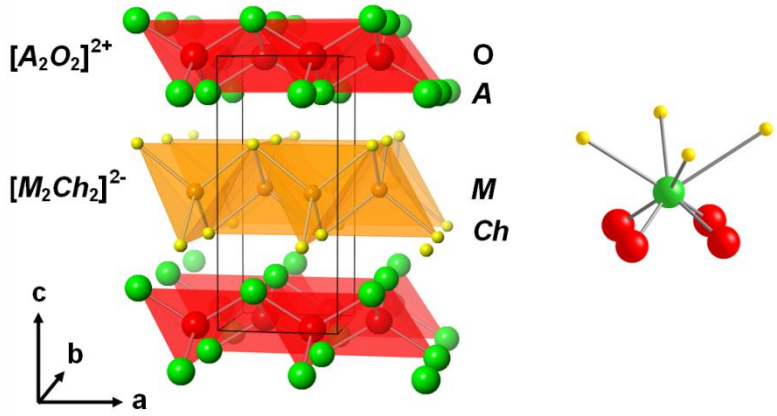

Figure 1.1. Left, ZrCuSiAs-type structure of AOMCh, P4/nmm symmetry, A = green, O = red, M = orange, Ch = yellow. Right, A cation 8 fold AO_4Ch_4 square antiprism site.

The ZrCuSiAs structure is adopted by a wide range of Cu containing compounds in the $A_2O_2Cu_2Ch_2$ series: S^{2-} (La-Eu, Bi); Se^{2-} (La-Nd, Sm-Er, Y, Bi); and Te^{2-} (La, Ce, Nd, Bi).[11,19-24] The physical properties of these materials will be discussed later in this review. There is also a smaller range of analogous Ag containing compounds with composition $A_2O_2Ag_2Ch_2$ (A = La, Ce).[25-27]

This structure type is also adopted by the insulating LaOFeAs; this superconducts below 26 K for F doped $LaO_{1-x}F_xFeAs$ ($0.07 < x < 0.12$)[28] and oxygen deficient $LaO_{1-x}FeAs$ ($x \sim 0.15$).[29] Substitution of the lanthanide for a smaller species raises T_c with reported values of 50 K for both $PrO_{0.85}F_{0.15}FeAs$[30] and $NdO_{0.85}F_{0.15}FeAs$[31]. T_c is raised to its highest value of 55 K in the oxygen deficient $SmO_{0.85}FeAs$[32]. Hole doping in these materials failed to induce superconductivity when Ca^{2+} was substituted for La^{3+}, however Sr doping proved more successful, with the compound $La_{0.88}Sr_{0.12}OFeAs$ superconducting below 25 K.[33]

1.2.1 Electronic, Optical and Magnetic Properties in $A_2O_2Cu_2Ch_2$ Materials

$A_2O_2Cu_2Ch_2$ materials have garnered particular interest as they show promise as transparent *p*-type semiconductors; for example, the well-studied compound $La_2O_2Cu_2S_2$ has a band gap of 3.1 eV which lies outside the visible region and also makes blue photoluminescence possible.[34-36] Because of the highly anisotropic nature of the crystal structures the compound has been described as containing “quantum wells”, in which there is a potential charge carrying chalcogenide layer separated by an insulating oxide layer.[12,37,38] Band structure calculations for $La_2O_2Cu_2S_2$ reveal the valence band (hatched) maxima to consist of antibonding Cu 3d and S 3p states, while the conduction band (unhatched) minima consists of antibonding Cu 4s states, Figure 1.2.[39]

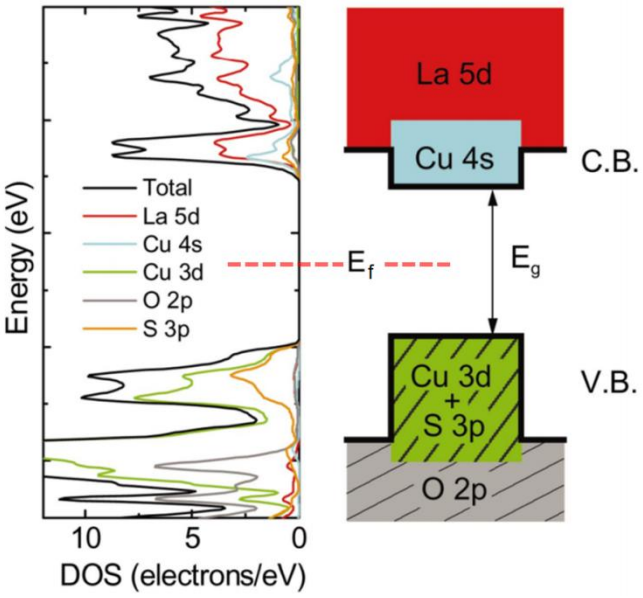

Figure 1.2. Left, total/partial DOS plot, right, schematic illustration of the band structure of stoichiometric $La_2O_2Cu_2S_2$. V.B. (hatched) and C.B. (unhatched) are the valence band and conduction band respectively. E_g and E_f are the band gap and Fermi level respectively.[39]

Band gap engineering can be achieved in $A_2O_2Cu_2Ch_2$ materials by varying the rare-earth and chalcogen. A decrease in electronegativity values from S^{2-} (2.58) to Se^{2-} (2.55) leads to a valence band maximum with greater hybridisation, hence the band gap is decreased from $La_2O_2Cu_2S_2$ (3.1 eV), to $La_2O_2Cu_2Se_2$ (2.8 eV).[10,40] In $La_2O_2Cu_2Te_2$, the bandgap is decreased even further (2.3 eV) and becomes a degenerate semiconductor, because of the higher energy of the Te 5p level relative to the S 3p and Se 4p levels.[41]

Changing the *A* site ion for a smaller rare-earth leads to a reduction in the band gap caused by unit cell shrinkage, from $La_2O_2Cu_2S_2$ (3.1 eV) to $Nd_2O_2Cu_2S_2$ (3.05 eV) to $Sm_2O_2Cu_2S_2$ (2.8 eV).[42,43] The lanthanide ions do not affect the valence maxima and conduction band minima directly; reduction of the *A* radii reduces the size of the $[A_2O_2]^{2-}$ layer, and in turn the $[Cu_2Ch_2]^{2-}$ layer. This acts to reduce the Cu-*Ch* bond length, increasing the hybridisation between Cu 3d and *Ch* *n*p, leading to a higher valence band maximum and decreased bandgap.

It is also possible to substitute *Ln* ions by trivalent Bi ions and this results in a significant decrease in the band gap (1.5 eV in BiOCuS). However this effect is attributed to the lower energy of the Bi 6*p* orbitals which form the conduction band minimum.[44]

Quaternary oxychalcogenides with the ZrCuSiAs structure often exhibit unique optical properties. Many are transparent *p*-type conductors (i.e. *p*-type doped semiconductors having a bandgap larger than ~3 eV)[10,45,46] and exhibit intense blue to near-ultraviolet light emission.[15,47] This arises from excitons which are sufficiently stable to produce room temperature emission. In LaOCuSe, the high carrier transport and light-emitting properties have been utilised to demonstrate a room temperature excitonic blue light-emitting diode.[47] Bi containing compounds have much smaller bandgaps (for reasons discussed above), and as a result are not suited to these optoelectric applications.

Magnetic susceptibility measurements on $A_2O_2Cu_2Ch_2$ materials (*A* = Pr, Nd, Sm, Eu) reveals that they remain paramagnetic down to low temperature, while in LaOCu*Ch*, La^{3+} ions are diamagnetic.[42,48-50]

1.2.2 $Ce_2O_2Cu_2Se_2$

There have been numerous publications on $Ce_2O_2Cu_2S_2$ in recent years, with conflicting reported unit cell volumes from different groups for the same apparent material.[11,27] This was clarified in 2009 by Clarke *et al.*, who demonstrated that the compound is capable of accepting a Cu deficiency as a charge compensation mechanism for the oxidation of Ce from +3 to +4. It was also demonstrated that the relationship between Cu site occupancy and unit cell volume is approximately linear. This is shown in Figure 1.3, where samples 1, 2 and 3 have accurately determined Cu stoichiometries via neutron diffraction (green and black data points[13]). Samples synthesised by other groups are also shown (blue[51], white[46] and red[27] data points), where labels indicate what they believed the composition to be, and with the actual Cu stoichiometry estimated from their cell volume. Sample 3 is near stoichiometric, olive green in colour, and in line with the lanthanide contraction, while sample 2 is jet black.[13]

Clarke *et al.* also demonstrated how a high-cell-volume green sample can be oxidised at room temperature, to a low cell volume black sample by a flow of moist O_2 gas, accompanied by the formation of low crystallinity CuO. The reverse can be achieved by heating the same black oxidised sample to 400 ˚C in a flow of H_2/N_2 gas, providing sufficient CuO is present. The change in cell volume from a near-stoichiometric compound to the most Cu deficient reported is ~5%. Near-stoichiometric $Ce_2O_2Cu_2S_2$ was prepared using a stoichimetric mixture of $CeCuS_2$, CeO_2 and Cu with a 0.5 molar equivalent of dried KCl added as flux. The mixture was loaded into an alumina crucible, sealed in an evacuated silica tube, and then heated to 900 ˚C for 10 days.[13]

Formation of a Cu deficiency in $Ce_2O_2Cu_2S_2$ could lead to oxidation of Ce^{3+} or to oxidation of the antibonding states at the top of the Cu-3*d*/S-3*p* band (which forms the readily depleted valence band in LaOCuS, as discussed later in this chapter). Calculations by Chan *et al.* show that the Ce-4*f* states lie close to the Fermi level and above Cu-3*d*/S-3*p* states,[27] implying that copper deficiency should result in mixed-valence Ce; this is in agreement with the results of others.[13,52]

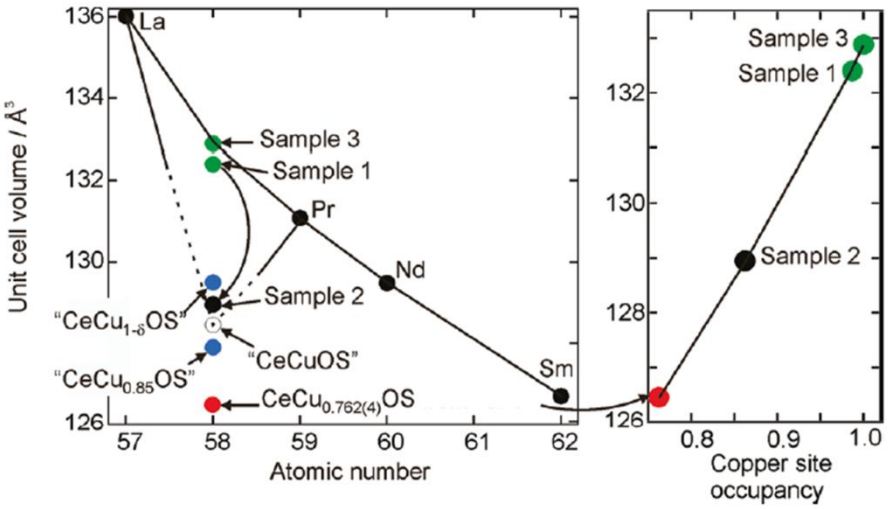

Figure 1.3. Left, unit cell volume of various $Ce_2O_2Cu_2S_2$ samples prepared by different groups, in relation to other compounds containing different lanthanides. Right, the linear dependency of Cu site occupancy on unit cell volume.[13]

1.2.3 Sr-doped $A_2O_2Cu_2Ch_2$ Materials

As the states at the top of the valence band in *Ln*OCu*Ch* are antibonding, these compounds are readily *p*-type doped producing transparent *p*-type conductors. There are numerous reported attempts to modify the physical properties of $A_2O_2Cu_2Ch_2$ materials by Sr^{2+} doping on the A^{3+} site. An insulator-metal transition was driven in the $(La_{2-x}Sr_x)O_2Cu_2S_2$ solid solution, by introducing holes into the valence band. $La_2O_2Cu_2S_2$ has a electrical resistivity at room temperature of ~10^4 Ω cm, with a temperature dependence which suggests semiconductive behaviour. The electrical resistivity of $(La_{2-x}Sr_x)O_2Cu_2S_2$ decreases with x, with $x \geq 0.04$ samples being metallic down to 4.2 K (with a 10,000 fold decrease in resistivity relative to undoped samples), Figure 1.4 left.[53]

The electrical properties of $(La_{2-x}Sr_x)O_2Cu_2Se_2$ (x = 0 to 0.2) have also been investigated. The temperature dependence of the conductivity (measured only from 373 to 673 K) indicated that non-doped $La_2O_2Cu_2Se_2$ was a *p*-type degenerate semiconductor due to a small number of Cu vacancies, while Sr-doped materials with x = 0.05 to 0.2 were *p*-type metals. The electrical conductivity increased with increasing Sr concentration up to x = 0.1, suggesting that the effective hole carriers increase with increasing Sr content up to x = 0.1.[54]

The bandgap in Bi materials is much lower than analogous La materials due to lowering of the conduction band maxima, though this is not directly very relevant to conductivity in *p*-type compounds. The effect of Sr-doping in $Bi_2O_2Cu_2Se_2$ based compounds has been recently reported. The substitution of Bi^{3+} by Sr^{2+} across $(Bi_{2-x}Sr_x)O_2Cu_2Se_2$ induces a strong decrease in the electrical resistivity up to the solubility limit of x = 0.35 (with a 100-fold decrease in resistivity relative to undoped samples), Figure 1.4 right. This is due to a strong increase of the hole carrier concentration. The resistivity is roughly two orders of magnitude lower in Bi materials compared to analogous La materials.[55]

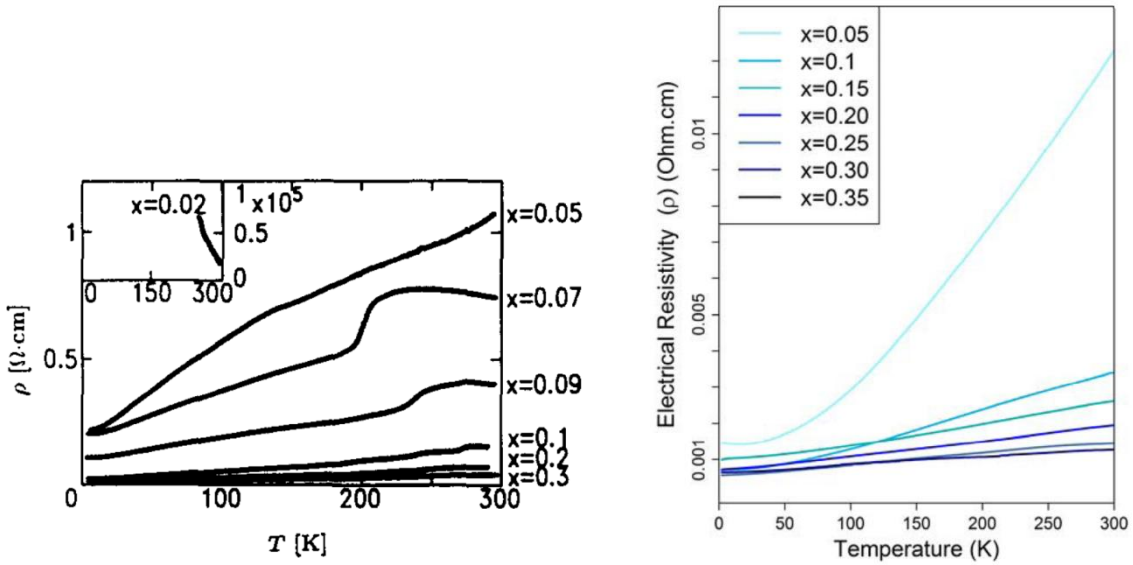

Figure 1.4. Temperature dependences of the electrical resistivity across the $(La_{2-x}Sr_x)O_2Cu_2S_2$ (left) and $(Bi_{2-x}Sr_x)O_2Cu_2Se_2$ (right) solid solutions at 0 T. The x = 0.00 non-doped samples show a 10,000-fold and 100-fold increase in resistivity respectively relative to the most doped samples.[53,55]

Thermoelectric materials are receiving increasing attention because of their possible applications in power generation and electronic cooling. The efficiency of such materials is determined by the dimensionless figure of merit zT:

$$zT = \frac{\alpha^2 \sigma}{k} T$$

Equation 1.1

where α, σ, k and T are the Seebeck coefficient (or thermopower, a measure of the amount of voltage generated per unit of temperature difference, with units of μV/K), electrical conductivity (Ω cm), thermal conductivity (W/m*K) and absolute temperature (K) respectively. Therefore a high figure of merit, hence an efficient thermoelectric material, requires maintaining high electrical conductivity and large thermopower while simultaneously limiting thermal conductivity.

After *p*-type Sr doping of BiOCuSe, the compound exhibits excellent electrical conductivity while keeping a high Seebeck coefficient. Coupled with a low thermal conductivity, Sr doped BiOCuSe can achieve zT values up to 0.76 at 873 K for $Bi_{0.925}Sr_{0.075}OCuSe$.[56,57] Sr doped LaOCuSe has also been investigated as a candidate thermoelectric material. Although Sr doping led to a drastic increase in zT, which is at its highest value of 0.04 at 873 K for $La_{0.95}Sr_{0.05}OCuSe$, this is still relatively low compared to Bi containing materials.[54]

1.3 Quaternary $A_2O_2MCh_2$ Materials derived from the ZrCuSiAs Structure

There is also a range of compounds known which are closely related to the $A_2O_2M_2Ch_2$ compounds yet with a subtle difference; the monovalent transition metal cations are substituted for divalent transition metal cations, giving composition $A_2O_2MCh_2$. This results in a structure with fluorite-like $[A_2O_2]^{2+}$ layers separated by anti-fluorite-like $[MCh_2]^{2-}$ layers, with half occupied transition metal sites. When the work in this thesis began, only $Ce_2O_2MnSe_2$,

$Ce_2O_2FeSe_2$, $La_2O_2CdSe_2$ and $La_2O_2ZnSe_2$ had been reported in the literature. Each has a unique arrangement of the transition metals within the $[MSe_2]^{2-}$ layer.[14,58-60]

1.3.1 $Ce_2O_2MnSe_2$

$Ce_2O_2MnSe_2$ was first reported by Ibers *et al.*, and structure solution was performed by single crystal diffraction. The single crystal synthesis involved the reaction of Ce, Mn, Se and SeO_2 (added as a source of oxygen) in a KCl flux to promote crystal growth. The reagents were intimately mixed, sealed in an evacuated silica tube, heated to 950 ˚C for 5 days, cooled at 0.05 ˚C min^{-1} to 650 ˚C min^{-1}, then the furnace turned off. The yield of $Ce_2O_2MnSe_2$ crystals was ~5%; the researchers were unable to prepare bulk samples.[14]

$Ce_2O_2MnSe_2$ was reported as having a transition metal ordering pattern which is random, with 50% statistical occupancy on each site. This arrangement leads to the tetragonal space group *P4/nmm*, as found in the $A_2O_2M_2Ch_2$ series of compounds. The structure is shown in Figure 1.5.[14]

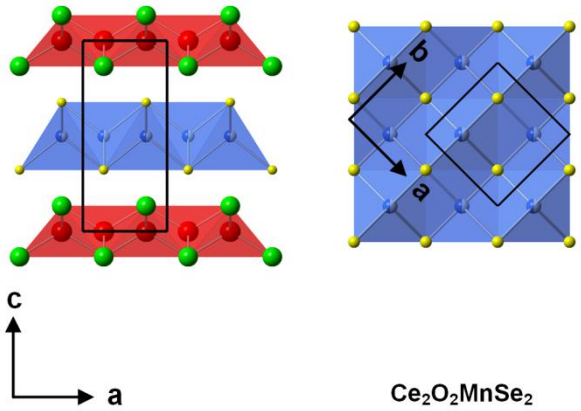

Figure 1.5. Left, ZrCuSiAs-type structure adopted by $Ce_2O_2MnSe_2$ with fluorite-like sheets of edge-sharing Ce_4O tetrahedra (red) and antifluorite-like sheets of $MnSe_4$ tetrahedra, with Mn sites half occupied in a disordered manner (blue), P4/nmm symmetry with a = b = 4.02620(7) Å, c = 9.107(2) Å. Right, view down [001] of $Ce_2O_2MnSe_2$ showing disordered Mn^{2+} sites.

Research which was done concurrently with the work presented in this thesis by fellow group member Dr Chun-Hai Wang, shows that this random distribution of transition metals is incorrect. Transition metal ordering is shown to be present by superstructure reflections in powder and single crystal X-ray diffraction (PXRD) and powder neutron diffraction (ND) data, and this ordering is incommensurate in nature. These reflections were not identified in the single crystal experiments of Ibers *et al.*.[14] This could have been due to fine scale twinning in the single crystals, or perhaps the superstructure peaks were simply overlooked; either way it shows the importance of powder diffraction data on phase-pure samples in structural work. Regardless of this, the disordered model provides a useful parent or “subcell” model in which to initially identify ZrCuSiAs related compounds, and from which to consider structural relationships with other materials. The optical bandgap of $Ce_2O_2MnSe_2$ was measured by Ibers et al. to be 2.01 eV, while work by Dr Chun-Hai Wang on the magnetic properties revealed the Mn moments to order antiferromagnetically below T_N = 150 K, and Ce moments order below ~70 K.[14,61]

1.3.2 $Ce_2O_2FeSe_2$

$Ce_2O_2FeSe_2$ was first reported within our group by McCabe *et al.*, when a polycrystalline sample was prepared via the reaction of CeO_2, Se and Fe powders. Stoichimetric quantities of reagents were intimately ground and placed in an alumina crucible. Al powder (10% molar excess) was placed in a second crucible to act as an oxygen getter, forming Al_2O_3 during the reaction. The crucibles were then heated in an evacuated, sealed quartz tube at 1050 ˚C for 12 hours, then furnace cooled. ~97% phase purity was obtained, with a ~3% Ce_2O_2Se impurity phase.[16]

$Ce_2O_2FeSe_2$ has an enlarged orthorhombic unit cell of $\sim\sqrt{2}a_{\text{subcell}} \times \sim\sqrt{2}a_{\text{subcell}} \times \sim 2c_{\text{subcell}}$ relative to the disordered $Ce_2O_2MnSe_2$ structure, crystallising in space group *Imcb*, as shown in Figure 1.6. The $[FeSe_2]^{2-}$ layers contain 1-D chains of edge-sharing $FeSe_4$ tetrahedra along the slightly shorter *a*-axis of the material.

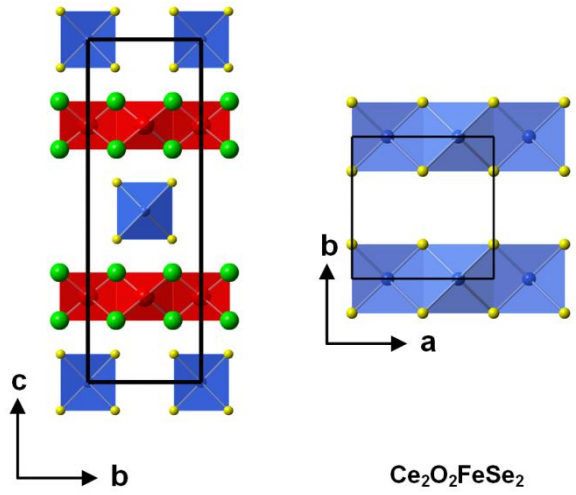

Figure 1.6. Left, structure adopted by $Ce_2O_2FeSe_2$ with fluorite-like sheets of edge-sharing Ce_4O tetrahedra (red) and chains of $FeSe_4$ edge-sharing tetrahedra (blue), Imcb symmetry with a = 5.70040(3), b = 5.71946(3) Å, c = 17.31342(9) Å. Right, view down [001] in $Ce_2O_2FeSe_2$ showing the stripe pattern formed by chains of edge sharing $FeSe_4$ tetrahedra.

$Ce_2O_2FeSe_2$ was reported to be a semiconductor with an electronic bandgap of 0.64 eV. Magnetic ordering occurs below T_N = 171 K, with ferromagnetic chains of Fe^{2+} along [100], and moments orientated perpendicular to the chain direction. The interaction between chains is anti-ferromagnetic.[16]

1.3.3 $La_2O_2CdSe_2$

$La_2O_2CdSe_2$ was first reported by Hiramatsu *et al.*. The single phase synthesis of polycrystalline $La_2O_2CdSe_2$ was achieved via the reaction of La_2O_3, La_2Se_3 and CdSe powders at 950 ˚C. It was noted how the synthesis of a single phase sample is largely dependent on controlling the stoichiometry of the reagent mixture during the high temperature reaction process. That is, it is critically important to keep the reaction vessel within a uniform temperature region during the reaction. A temperature gradient in the sample causes chemical vapour transport of Cd and Se from higher to lower temperature

regions, resulting in compositional deviations from stoichiometry. This results in La_2O_2Se being a common impurity.[15]

$La_2O_2CdSe_2$ has an enlarged unit cell of $\sim a_{subcell} \times \sim a_{subcell} \times \sim 2c_{subcell}$ relative to the disordered structure, crystallising in space group *P4₂/nmc*, as shown in Figure 1.7. The $[CdSe_2]^{2-}$ layers contain a checkerboard-like arrangement of exclusively corner-sharing $CdSe_4$ tetrahedra.[15]

The optical bandgap of $La_2O_2CdSe_2$ is reported to be 3.3 eV, which is somewhat larger than the 1.8 eV bandgap of CdSe. The increased bandgap of $La_2O_2CdSe_2$ can likely be ascribed to the 2D nature of the material.[15,38]

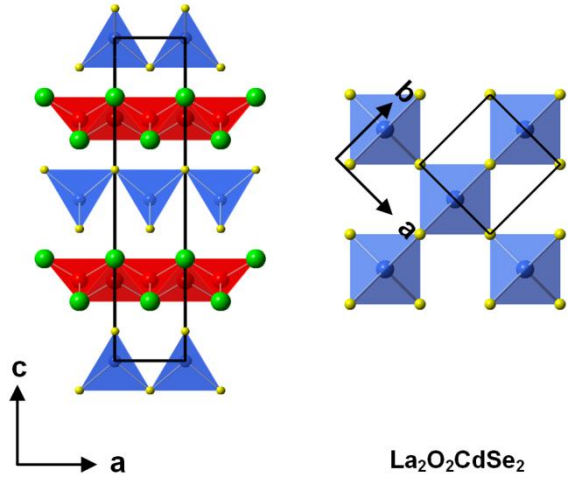

Figure 1.7. Left, structure adopted by $La_2O_2CdSe_2$ with fluorite-like sheets of edge-sharing Ce_4O tetrahedra (red) and corner-sharing $CdSe_4$ tetrahedra (blue), $P4_2/nmc$ symmetry with a = b = 4.0660(6) Å, c = 18.634(1) Å. Right, view down [001] in $La_2O_2CdSe_2$ showing checkerboard arrangement of corner-sharing $CdSe_4$ tetrahedra.

1.3.4 $La_2O_2ZnSe_2$

$La_2O_2ZnSe_2$ was first reported within the group by Tuxworth *et al.* Single phase polycrystalline samples were prepared by reacting stoichiometric quantities of La_2O_3, Se and Zn powders at 1100 ˚C. Single crystals were also grown by cooling a polycrystalline sample from 1300 ˚C to 800 ˚C at 0.12 ˚C min^{-1} in a sealed silica tube under 1 × 10^{-2} atm of Ar.[60]

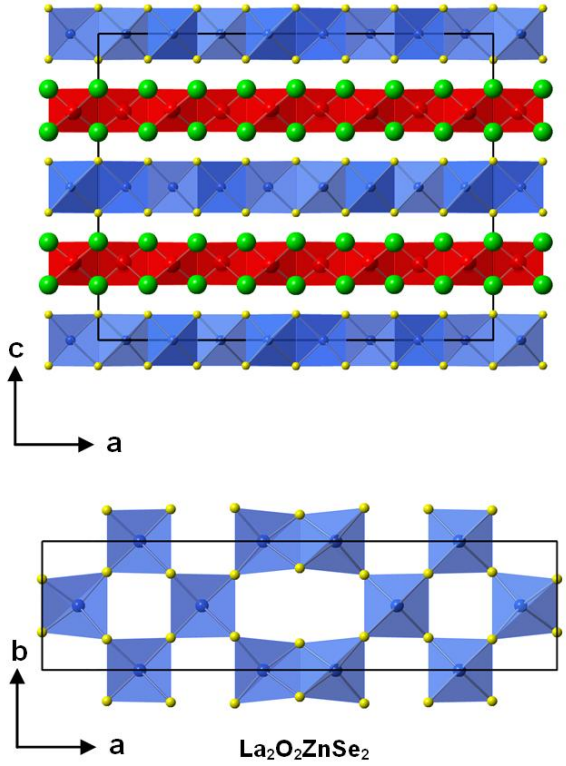

Figure 1.8 Top, structure adopted by $La_2O_2ZnSe_2$ with fluorite-like sheets of edge-sharing La_4O tetrahedra (red) and $ZnSe_4$ tetrahedra (blue), Bmab symmetry with a = 22.9332(2) Å, b = 5.73241(6) Å, c = 17.80043(6) Å. Bottom, view down [001] in $La_2O_2ZnSe_2$ showing a mix of stripe-like edge-sharing $ZnSe_4$ tetrahedra and checkerboard-like corner-sharing $ZnSe_4$ tetrahedra.

$La_2O_2ZnSe_2$ has an enlarged orthorhombic unit cell of $\sim 4\sqrt{2}a_{\text{subcell}} \times \sim\sqrt{2}a_{\text{subcell}} \times \sim 2c_{\text{subcell}}$ relative to the disordered structure, crystallising in space group *Bmab*, as shown in Figure 1.8. The $[ZnSe_2]^{2-}$ layers contain sections of both $Ce_2O_2FeSe_2$-like edge-sharing $ZnSe_4$ tetrahedra (stripes), and $La_2O_2CdSe_2$-like corner-sharing $ZnSe_4$ tetrahedra (checkerboards) along the *a*-axis of the material. Structure solution was done via symmetry adapted distortion mode analysis using the web based ISODISTORT software.[60,62]

The Tuxworth *et al.* publication also presents selected area electron diffraction (SAED) images which were used to derive unit cell dimensions; these are shown in Figure 1.9. Figure 1.9*a* and Figure 1.9*b* are taken down the $[001]$ zone axis. The strong reflections are consistent with the *P4/nmm* parent subcell, however weak superstructure reflections are observed along the $[1\bar{1}0]$ but not $[110]$ direction. These prove the loss of tetragonal symmetry in the superstructure. These additional reflections were indexed as 200, 400, *h*00 (*h* = 2*n*) in a $\sim 4\sqrt{2}a_{\text{subcell}} \times \sim\sqrt{2}a_{\text{subcell}} \times \sim 2c_{\text{subcell}}$ unit cell. Figure 1.9*c* shows the diffraction pattern taken down the $[110]$ zone axis; weak superstructure reflections (highlighted in red) are again observed, indicating the increased unit cell in the *ab* plane.[17]

$La_2O_2ZnSe_2$ was reported to be a direct gap semiconductor with an optical bandgap of 3.4 eV, consistent with electronic structure calculations.[17] This bandgap is much larger than the 2.67 eV value observed for the binary ZnSe. As was discussed for $La_2O_2CdSe_2$[15], this increase is likely due to band narrowing due to the layered structure of $La_2O_2ZnSe_2$.[17]

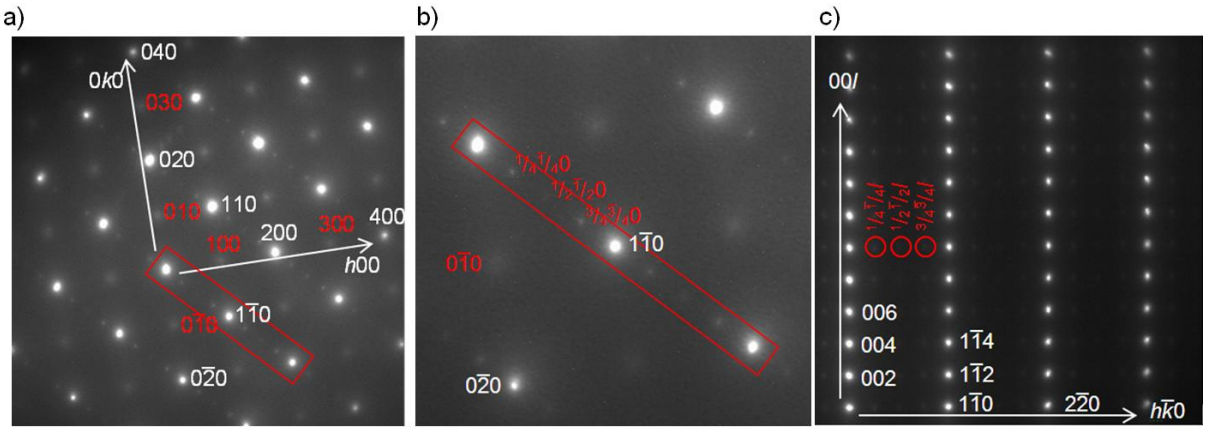

Figure 1.9. Selected area electron diffraction patterns for $La_2O_2ZnSe_2$ taken down (a) [001] zone axis and (b) enlarged region showing superstructure reflections and (c) [110] zone axis. Zone axes and hkl indices are given relative to the parent P4/nmm unit cell. Those that are consistent with the P4/nmm structure are shown in white, while those that are inconsistent are shown in red.[17]

1.3.5 Formal Naming System for Layered $Ln_2O_2MSe_2$-type Materials

The findings of this thesis has made it necessary to introduce a formal naming system by which to identify different transition metal ordering patterns in 2D $Ln_2O_2MSe_2$-type materials. This involves quantifying the number of corner-sharing (C, checkerboard-like) and edge-sharing (E, stripe-like) tetrahedra along the *a* direction (110 direction in $La_2O_2CdSe_2$), or from left to right as the ordering is depicted in Figure 1.10. Therefore, $Ce_2O_2FeSe_2$ can be described as 0C-1E, $La_2O_2CdSe_2$ as 1C-0E, and $La_2O_2ZnSe_2$ as 3C-1E.[15-17] It will become apparent in Chapter 4 why this naming system is required.

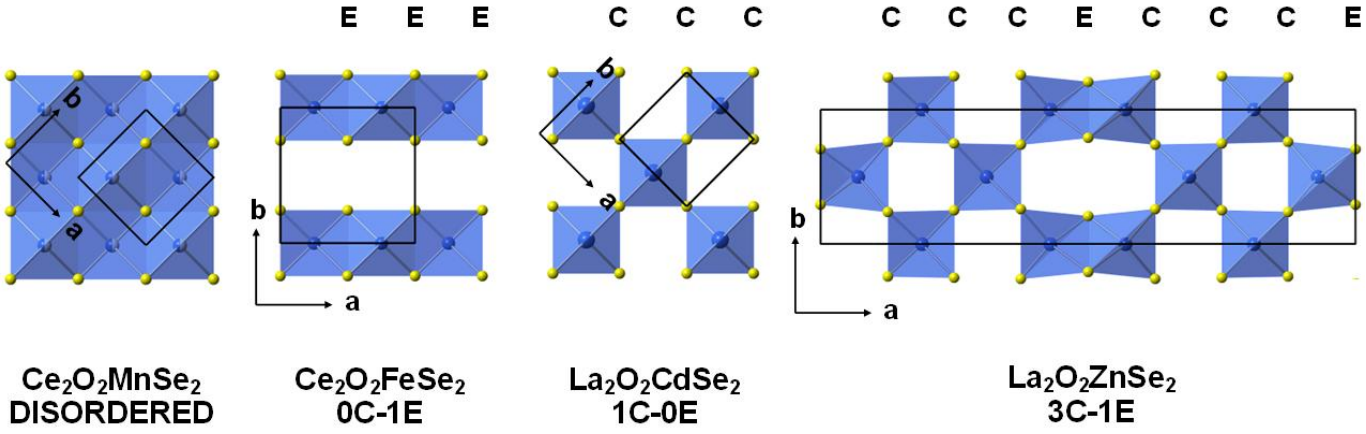

Figure 1.10. Formal naming system for layered $Ln_2O_2MSe_2$-type oxychalcogenides.

1.4 *β*-$La_2O_2MSe_2$ (*M* = Fe, Mn) 3-D Materials

The majority of $Ln_2O_2MSe_2$-type materials crystallise with 2D layered structures, as discussed above. However there are a few cases where materials with composition $La_2O_2MSe_2$ (*M* = Fe, Mn) form a 3D structure, space group *Ama2*. These 3-D materials were first synthesised by previous group members, and labelled as the *β*-structure type[63] (also referred to as the oP- $Ln_2O_2MSe_2$ polymorph by others).[64,65]

The structure of *β*-$La_2O_2MSe_2$ (*M* = Fe, Mn) contains extended ribbons of A_4O and A_3MO edge-sharing tetrahedra 4 units in width (red units in Figure 1.11). These are connected by an octahedrally coordinated MSe_4O_2 transition metal (Fe or Mn), which form edge-sharing MSe_4O_2 chains themselves along *c* (blue units in Figure 1.11). These MSe_4O_2 chains are connected by a tetrahedrally coordinated MSe_4 unit, leading to alternating chains of MSe_4O_2 and MSe_4 along *c*.[63]

Both $La_2O_2FeSe_2$ and $La_2O_2MnSe_2$ were synthesised in the same manner as $La_2O_2ZnSe_2$ (1100 °C for 12 hours), however $La_2O_2FeSe_2$ had to be quenched in ice water in order to avoid significant Fe impurities. $La_2O_2FeSe_2$ is a semiconductor from 150 – 300 K with an optical bandgap of 0.7 eV, while $La_2O_2MnSe_2$ is an insulator at 300 K with an optical bandgap of 1.6 eV. In terms of the magnetic properties, both are antiferromagnetically ordered at low temperatures, with T_N = 91 and 27 K for $La_2O_2FeSe_2$ and $La_2O_2MnSe_2$ respectively.[63]

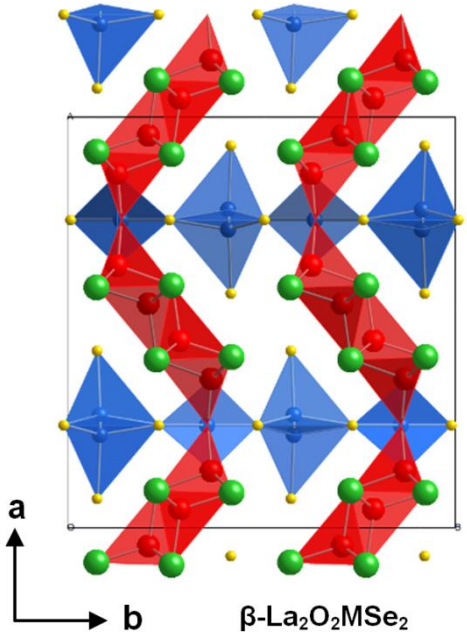

Figure 1.11. Structure of β-$La_2O_2MSe_2$ (M = Fe, M) space group Ama2; La = green, M = blue, Se = yellow, O = red.

1.5 Conclusions and Project Aims

Even though there is a large number of known oxychalcogenides, this literature review has focussed mainly on quaternary layered structures, and discussed the features that are common between them, as well as their subtle differences. Most attention has been given to

known layered $A_2O_2Cu_2Ch_2$-type and $Ln_2O_2MSe_2$-type materials, wherein the transition metal sites are fully occupied and half occupied respectively, as they are most relevant to the work presented in later chapters.

The aim of the project described in this thesis is to synthesise new $Ln_2O_2MSe_2$-type materials, and understand the driving force behind the different transition metal ordering patterns observed, which has hitherto seemed somewhat random. Thereafter, the aim is to use this understanding to target new, more complex materials. Studies on the physical properties (electronic, magnetic and optical) of some materials are also reported. The long term goal would be to use such an in depth understanding of the structural behaviour in these compounds, and relate this behaviour to the physical properties, hence allowing the design of better materials for specific applications.

Figure 1.12 is a thesis map, to help the reader navigate through the chapters presented, and understand how all the compounds relate. It is colour coded to act as a visual aid, and each chapter has its own colour scheme, which can be easily tracked back to the corresponding colour on the thesis map. A detachable thesis map is also provided with the thesis for easy reference. Chapter 3 discusses a single point on the map: a new quaternary layered oxychalcogenide, $Ce_2O_2ZnSe_2$, with Zn^{2+} cations in a new ordered arrangement. Chapter 4 reports a range of subtly evolving $Ln_2O_2(M_{1-y}M'_y)Se_2$ (*Ln* = La, Ce, *M*/*M'* = Fe/Zn, Zn,Mn, Mn/Cd) solid solutions on the right hand edge of Figure 1.12, and reveals the origins of transition metal ordering. Chapter 5 describes a new family of compounds containing both +1 and +2 transition metal ions in the $La_2O_2Cu_{2-2x}Cd_xSe_2$ family, which have complex long-range superstructures in the 3rd (stacking) dimension. Chapter 6 takes one compound from the $La_2O_2Cu_{2-2x}Cd_xSe_2$ solid solution (x = 0.5) from Chapter 5, and attempts to modify the electronic properties by Sr doping on the La site (green point of Figure 1.12). Chapter 7 extends Chapter 5 by exploring the main body of Figure 1.12 and discusses three more solid solutions analogous to $La_2O_2Cu_{2-2x}Cd_xSe_2$, but replacing Cd with Fe, Zn and Mn (lines 7a, 7b, 7c). It also investigates the effect of systematically varying the +2 transition metal size in two $La_2O_2Cu_{2-2x}(M_{1-y}M_y)_xSe_2$-type (*M*/*M'* = Fe/Zn, Zn,Mn, Mn/Cd) solid solutions (lines 7d, 7e). Chapter 8 attempts to summarise and link the work described in Chapters 3 to 7. The reader may find it useful to read this before and after the other chapters.

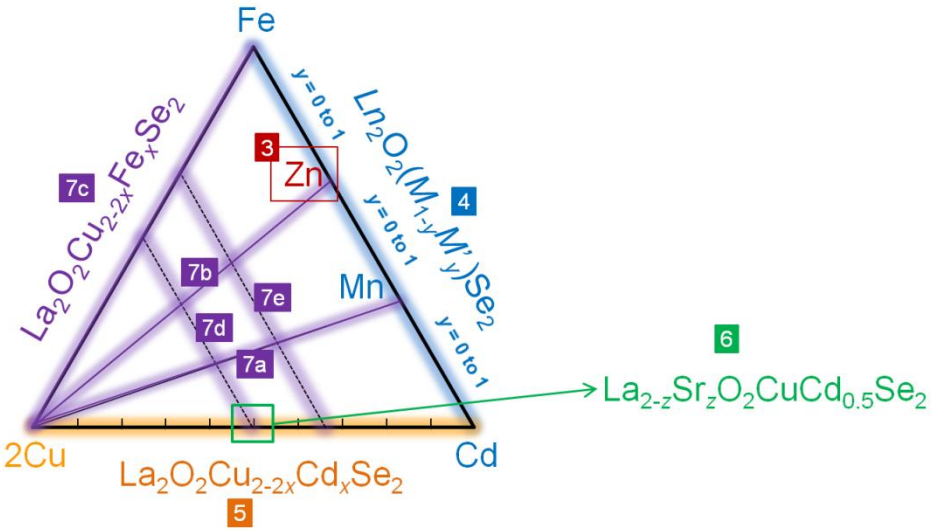

Figure 1.12. Thesis map highlighting the areas of work covered in the various chapters of the thesis.

1.6 References

(1) Mizuguchi, Y.; Fujihisa, H.; Gotoh, Y.; Suzuki, K.; Usui, H.; Kuroki, K.; Demura, S.; Takano, Y.; Izawa, H.; Miura, O. *Phys. Rev. B* **2012**, *86*, 5.

(2) Singh, S. K.; Kumar, A.; Gahtori, B.; Shruti; Sharma, G.; Patnaik, S.; Awana, V. P. S. *J. Am. Chem. Soc.* **2012**, *134*, 16504.

(3) Tan, S. G.; Li, L. J.; Liu, Y.; Tong, P.; Zhao, B. C.; Lu, W. J.; Sun, Y. P. *Physica C: Superconductivity* **2012**, *483*, 94.

(4) Yazici, D.; Huang, K.; White, B. D.; Chang, A. H.; Friedman, A. J.; Maple, M. B. *Philosophical Magazine* **2012**, *93*, 673.

(5) Thakur, G. S.; Selvan, G. K.; Haque, Z.; Gupta, L. C.; Samal, S. L.; Arumugam, S.; Ganguli, A. K. *Inorg. Chem.* **2015**, *54*, 1076.

(6) Krzton-Maziopa, A.; Guguchia, Z.; Pomjakushina, E.; Pomjakushin, V.; Khasanov, R.; Luetkens, H.; Biswas, P. K.; Amato, A.; Keller, H.; Conder, K. *J. Phys-condens. Mat.* **2014**, *26*, 5.

(7) Li, L.; Parker, D.; Babkevich, P.; Yang, L.; Ronnow, H. M.; Sefat, A. S. *Phys. Rev. B* **2015**, *91*.

(8) Shao, J. F.; Liu, Z. H.; Yao, X.; Pi, L.; Tan, S.; Zhang, C. J.; Zhang, Y. H. *Physica Status Solidi-Rapid Research Letters* **2014**, *8*, 845.

(9) Zhai, H. F.; Zhang, P.; Wu, S. Q.; He, C. Y.; Tang, Z. T.; Jiang, H.; Sun, Y. L.; Bao, J. K.; Nowik, I.; Felner, I.; Zeng, Y. W.; Li, Y. K.; Xu, X. F.; Tao, Q.; Xu, Z. A.; Cao, G. H. *J. Am. Chem. Soc.* **2014**, *136*, 15386.

(10) Ueda, K.; Hosono, H. *Thin Solid Films* **2002**, *411*, 115.

(11) Ueda, K.; Takafuji, K.; Hosono, H. *Journal of Solid State Chemistry* **2003**, *170*, 182.

(12) Ueda, K.; Hiramatsu, H.; Hirano, M.; Kamiya, T.; Hosono, H. *Thin Solid Films* **2006**, *496*, 8.

(13) Pitcher, M. J.; Smura, C. F.; Clarke, S. J. *Inorg. Chem.* **2009**, *48*, 9054.

(14) Ijjaali, I.; Mitchell, K.; Haynes, C. L.; McFarland, A. D.; Van Duyne, R. P.; Ibers, J. A. *J. Solid State Chem.* **2003**, *176*, 170.

(15) Hiramatsu, H.; Ueda, K.; Kamiya, T.; Ohta, H.; Hirano, M.; Hosono, H. *J. Mater. Chem.* **2004**, *14*, 2946.

(16) McCabe, E. E.; Free, D. G.; Evans, J. S. O. *Chem. Commun.* **2011**, *47*, 1261.

(17) Tuxworth, A. J.; McCabe, E. E.; Free, D. G.; Clark, S. J.; Evans, J. S. O. *Inorg. Chem.* **2013**, *52*, 2078.

(18) Clarke, S. J.; Adamson, P.; Herkelrath, S. J. C.; Rutt, O. J.; Parker, D. R.; Pitcher, M. J.; Smura, C. F. *Inorg. Chem.* **2008**, *47*, 8473.

(19) Charkin, D. O.; Akopyan, A. V.; Dolgikh, V. A. *Russian Journal of Inorganic Chemistry* **1999**, *44*, 833.

(20) Liu, M. L.; Wu, L. B.; Huang, F. Q.; Chen, L. D.; Ibers, J. A. *Journal of Solid State Chemistry* **2007**, *180*, 62.

(21) Hiramatsu, H.; Yanagi, H.; Kamiya, T.; Ueda, K.; Hirano, M.; Hosono, H. *Chem. Mater.* **2008**, *20*, 326.

(22) Ohtani, T.; Hirose, M.; Sato, T.; Nagaoka, K.; Iwabe, M. *Japanese Journal of Applied Physics Part 1-Regular Papers Short Notes & Review Papers* **1993**, *32*, 316.

(23) Kusainova, A. M.; Berdonosov, P. S.; Akselrud, L. G.; Kholodkovskaya, L. N.; Dolgikh, V. A.; Popovkin, B. A. *Journal of Solid State Chemistry* **1994**, *112*, 189.

(24) Pitcher, M. J.; Smura, C. F.; Clarke, S. J. *Inorganic Chemistry* **2009**, *48*, 9054.

(25) Palazzi, M.; Carcaly, C.; Flahaut, J. *J. Solid State Chem.* **1980**, *35*, 150.

(26) Palazzi, M.; Jaulmes, S. *Acta Crystallogr. B* **1981**, *37*, 1337.

(27) Chan, G. H.; Deng, B.; Bertoni, M.; Ireland, J. R.; Hersam, M. C.; Mason, T. O.; Van Duyne, R. P.; Ibers, J. A. *Inorg. Chem.* **2006**, *45*, 8264.

(28) Kamihara, Y.; Watanabe, T.; Hirano, M.; Hosono, H. *J. Am. Chem. Soc.* **2008**, *130*, 3296.

(29) Ren, Z. A.; Che, G. C.; Dong, X. L.; Yang, J.; Lu, W.; Yi, W.; Shen, X. L.; Li, Z. C.; Sun, L. L.; Zhou, F.; Zhao, Z. X. *Europhysics Letters* **2008**, *83*.
(30) Ren, Z. A.; Yang, J.; Lu, W.; Yi, W.; Che, G. C.; Dong, X. L.; Sun, L. L.; Zhao, Z. X. *Mater. Res. Innov.* **2008**, *12*, 105.
(31) Ren, Z. A.; Yang, J.; Lu, W.; Yi, W.; Shen, X. L.; Li, Z. C.; Che, G. C.; Dong, X. L.; Sun, L. L.; Zhou, F.; Zhao, Z. X. *Europhysics Letters* **2008**, *82*.
(32) Ren, Z. A.; Lu, W.; Yang, J.; Yi, W.; Shen, X. L.; Li, Z. C.; Che, G. C.; Dong, X. L.; Sun, L. L.; Zhou, F.; Zhao, Z. X. *Chinese. Phys. Lett.* **2008**, *25*, 2215.
(33) Hai-Hu, W.; Gang, M.; Lei, F.; Huan, Y.; Xiyu, Z. *EPL (Europhysics Letters)* **2008**, *82*, 17009.
(34) Kamioka, H.; Hiramatsu, H.; Hirano, M.; Ueda, K.; Kamiya, T.; Hosono, H. In *6th International Conference on Excitonic Processes in Condensed Matter (EXCON 04)*; Elsevier Science Bv: Cracow, POLAND, 2004; Vol. 112, p 66.
(35) Kamiya, T.; Ueda, K.; Hiramatsu, H.; Kamioka, H.; Ohta, H.; Hirano, M.; Hosono, H. *Thin Solid Films* **2005**, *486*, 98.
(36) Ramasubramanian, S.; Rajagopalan, M.; Kumar, J.; Thangavel, R. *J. Appl. Phys.* **2009**, *106*.
(37) Hosono, H. *Thin Solid Films* **2007**, *515*, 6000.
(38) Vajenine, G. V.; Hoffmann, R. *Inorg. Chem.* **1996**, *35*, 451.
(39) Ueda, K.; Hiramatsu, H.; Ohta, H.; Hirano, M.; Kamiya, T.; Hosono, H. *Phys. Rev. B* **2004**, *69*.
(40) Allred, A. L. *Journal of Inorganic & Nuclear Chemistry* **1961**, *17*, 215.
(41) Liu, M. L.; Wu, L. B.; Huang, F. Q.; Chen, L. D.; Ibers, J. A. *J. Solid State Chem.* **2007**, *180*, 62.
(42) Llanos, J.; Pena, O. *J. Solid State Chem.* **2005**, *178*, 957.
(43) Hiramatsu, H.; Kamioka, H.; Ueda, K.; Hirano, M.; Hosono, H. *J. Ceram. Soc. Jpn.* **2005**, *113*, 10.
(44) Sheets, W. C.; Stampler, E. S.; Kabbour, H.; Bertoni, M. I.; Cario, L.; Mason, T. O.; Marks, T. J.; Poeppelmeier, K. R. *Inorg. Chem.* **2007**, *46*, 10741.
(45) Ueda, K.; Inoue, S.; Hirose, S.; Kawazoe, H.; Hosono, H. *Appl. Phys. Lett.* **2000**, *77*, 2701.
(46) Ueda, K.; Takafuji, K.; Hiramatsu, H.; Ohta, H.; Kamiya, T.; Hirano, M.; Hosono, H. *Chem. Mater.* **2003**, *15*, 3692.
(47) Hiramatsu, H.; Ueda, K.; Ohta, H.; Kamiya, T.; Hirano, M.; Hosono, H. *Appl. Phys. Lett.* **2005**, *87*, 211107/1.
(48) Llanos, J.; Cortes, R.; Guizouarn, T.; Pena, O. *Mater. Res. Bull.* **2006**, *41*, 1266.
(49) Llanos, J.; Cortes, R.; Sanchez, V. *Mater. Res. Bull.* **2008**, *43*, 320.
(50) Nakao, H.; Takano, Y.; Takase, K.; Sato, K.; Hara, S.; Ikeda, S.; Takahashi, Y.; Sekizawa, K. *J. Alloy. Compd.* **2006**, *408*, 104.
(51) Charkin, D. O.; Akopyan, A. V.; Dolgikh, V. A. *Zh. Neorg. Khim.* **1999**, *44*, 895.
(52) Sato, H.; Nishimoto, S.; Takase, K.; Nakao, H.; Yoshikawa, K.; Higashi, M.; Taniguchi, M.; Negishi, H.; Negishi, S.; Takahashi, Y.; Takano, Y.; Sekizawa, K. In *Physica Status Solidi C - Current Topics in Solid State Physics, Vol 3, No 8*; Stutzmann, M., Ed. 2006; Vol. 3, p 2884.
(53) Takano, Y.; Yahagi, K.-i.; Sekizawa, K. *Physica B: Condensed Matter* **1995**, *206*, 764.
(54) Yasukawa, M.; Ueda, K.; Hosono, H. *J. Appl. Phys.* **2004**, *95*, 3594.
(55) Barreteau, C.; Bérardan, D.; Amzallag, E.; Zhao, L.; Dragoe, N. *Chem. Mater.* **2012**, *24*, 3168.
(56) Zhao, L.; Berardan, D.; Pei, Y.; Byl, C.; Pinsard-Gaudart, L.; Dragoe, N. *Appl. Phys. Lett.* **2010**, *97*, 092118.
(57) Vaqueiro, P.; Al Orabi, R. A. R.; Luu, S. D. N.; Guelou, G.; Powell, A. V.; Smith, R. I.; Song, J. P.; Wee, D.; Fornari, M. *Phys. Chem. Chem. Phys.* **2015**, *17*, 31735.
(58) McCabe, E. E.; Free, D. G.; Evans, J. S. *Chem Commun (Camb)* **2011**, *47*, 1261.

(59) Hiramatsu, H.; Ueda, K.; Kamiya, T.; Ohta, H.; Hirano, M.; Hosono, H. *Journal of Materials Chemistry* **2004**, *14*, 2946.
(60) Tuxworth, A. J.; McCabe, E. E.; Free, D. G.; Clark, S. J.; Evans, J. S. *Inorg Chem* **2013**, *52*, 2078.
(61) Wang, C.-H.; Ainsworth, C. M.; Gui, D.-Y.; McCabe, E. E.; Tucker, M. G.; Evans, I. R.; Evans, J. S. O. *Chem. Mater.* **2015**, *27*, 3121.
(62) Campbell, B. J. H. T. Stokes, D. E. Tanner and D. M. Hatch, *J. Appl. Cryst.,* **2006**, *39*, 607-614.
(63) McCabe, E. E.; Free, D. G.; Mendis, B. G.; Higgins, J. S.; Evans, J. S. O. *Chem. Mater.* **2010**, *22*, 6171.
(64) Nitsche, F.; Niklaus, R.; Johrendt, D. *Z. Anorg. Allg. Chem.* **2014**, *640*, 2897.
(65) Peschke, S.; Nitsche, F.; Johrendt, D. *Z. Anorg. Allg. Chem.* **2015**, *641*, 529.

Chapter 2: Synthesis, Experimental and Analytical Methods

2.1 Introduction

This chapter describes the synthetic methods and analytical techniques used to prepare and analyse the materials reported in this thesis. Polycrystalline samples were studied mainly by powder x-ray diffraction (PXRD) using laboratory and synchrotron x-ray sources, and, where needed, by powder neutron diffraction (PND). Structural information was extracted from the obtained data mainly by Rietveld Refinement. Selected area electron diffraction (SAED) was used to study subtle superstructure, Diffuse Reflectance Spectroscopy (DRS) to measure optical bandgaps, SQUID magnetometry to study magnetic properties, and a Physical Property Measurement System (PPMS) to measure electronic conductivity as a function of temperature.

2.2 Experimental Details

Preparation of the Ln_xO_y rare earth starting materials was required before the attempted synthesis of target materials. Table 2.1 shows a list of all the reagents used in the project. All were X-rayed prior to use.

	Reagent	Supplier	Purity
Ln_xO_y	La_2O_3	Sigma Aldrich	99.99%
	CeO_2	Alfa Aesar	99.99 %
	Pr_6O_{11}	Alfa Aesar	99.99 %
	Nd_2O_3	Electronic Materials	99 %
Ln dopant	SrO	Sigma Aldrich	99.9 %
M	Fe	Sigma Aldrich	99.9 %
	Zn	Alfa Aesar	99.9 %
	Mn	Koch-Light	99.9 %
	Cd	Alfa Aesar	99.5 %
	Cu	Alfa Aesar	99.9 %
Ch	Se	Alfa-Aesar	99.999 %
Oxygen getter	Al	Alfa Aesar	99.5 %
	Ti	Alfa Aesar	99.5 %

Table 2.1. Table of reagents used in the project.

2.2.1 Preparation of the Ln_xO_y Starting Materials

Solid La_2O_3, CeO_2 and Nd_2O_3 powders were placed in an alumina crucible, and heated at 1000 ˚C in air for 10 hours to remove any adsorbed H_2O or CO_2. The subsequent materials were analysed by PXRD to confirm purity, and stored in an evacuated desiccator between uses.

A pure Pr_2O_3 sample was prepared by a previous group member, via reduction of Pr_6O_{11} in a tube furnace under a gas stream of 5 % hydrogen in 95 % nitrogen at 1000 ˚C for 12 hours,

before cooling to room temperature. The sample was stored in a nitrogen filled glovebox, and PXRD was used to confirm it was still pure before use.

2.2.2 Synthesis of $Ce_2O_2ZnSe_2$

To prepare 0.6 g of $Ce_2O_2ZnSe_2$, stoichiometric amounts of CeO_2 (0.3857 g), Zn (0.0732 g), and Se (0.1769 g) were weighed out to within ±0.0001 g, and intimately ground using an agate pestle and mortar. The resulting powder was placed into a high density alumina crucible of 7 mm diameter, and this crucible placed into a silica tube of 11 mm inner diameter, flame sealed at one end. A second 7 mm diameter alumina crucible containing Al was placed on top of the first, to act as an oxygen getter, forming Al_2O_3 during the reaction (in this report, the aluminium oxygen getter will be abbreviated to AOG). The amount of AOG used for each synthesis ranged from 90 % – 110 % stoichiometric percentage for the various different syntheses (Table 2.2). The quartz tube was evacuated to a pressure of $<7x10^{-3}$ mbar, flame sealed, and heated in a muffle furnace under the following conditions: ramp at 1 ˚C min^{-1} to 600 ˚C and dwell for 12 hours, ramp at 0.5 ˚C min^{-1} and dwell for 1 hour, ramp at 1 ˚C min^{-1} to the final dwell temperature (between 1100 ˚C and 1225 ˚C for the various different syntheses) with final dwell times between 1 and 24 hours. Figure 2.1 shows the experimental setup. After reaction, ampoules were cooled to room temperature in the furnace (~8 hours) before being broken open with a hammer. The contents of the lower crucible were then reground, and the resulting powder analysed using PXRD. The sample code, PXRD code, mass amount of AOG, molar percentage of AOG, final dwell temperature and final dwell time for each compound synthesised is shown in Table 2.2. The stoichiometric equation for the reaction if 100 % phase purity is obtained is given by Equation 2.1.

$$2CeO_2 + Zn + 2Se + \tfrac{4}{3}Al \rightarrow Ce_2O_2ZnSe_2 + \tfrac{2}{3}Al_2O_3$$

Equation 2.1

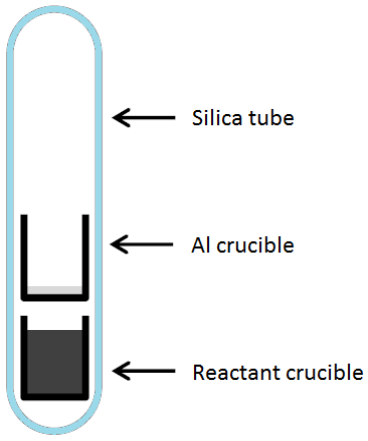

Figure 2.1. Experimental setup for the $Ce_2O_2ZnSe_2$ syntheses.

Experiment code	Al / g	Al / %	Final dwell temperature / ˚C	Final dwell time / hours
CMA006_1100C	0.0443	110	1100	12
CMA006_1150C	0.0443	110	1150	12
CMA006_1175C	0.0443	110	1175	12
CMA006_1200C	0.0443	110	1200	12
CMA006_1225C	0.0443	110	1225	12
CMA006_1hrs	0.0443	110	1200	1
CMA006_3hrs	0.0443	110	1200	3
CMA006_6hrs	0.0443	110	1200	6
CMA006_9hrs	0.0443	110	1200	9
CMA006_1200C	0.0443	110	1200	12
CMA006_24hrs	0.0443	110	1200	24
CMA006_1200C	0.0443	110	1200	12
CMA006_105%Al	0.0423	105	1200	12
CMA006_100%Al	0.0403	100	1200	12
CMA006_95%Al	0.0383	95	1200	12
CMA006_90%Al	0.0363	90	1200	12

Table 2.2. Table showing the experimental code, mass of AOG used, stoichiometric percentage of AOG used, final dwell temperature and final dwell time for each compound synthesised. Duplicates of one experiment (shown in red) are included for clarity.

For PND experiments at ISIS a large (~2.4 g) sample was made. Attempts to synthesise more than 0.6 g at 1200 ˚C in a single silica tube led to the tube swelling and ultimately bursting. This was attributed to higher pressure build up from the increase in the amount of initial reactants, coupled with the softening of the silica at the high temperatures required for reaction. Therefore, four 0.6 g samples were prepared as per experiment CMA006_1200C, intimately ground together, and reheated for a further 12 hours with 0.002 g of Se in the quartz tube. In this report, the sample will be referred to as the "ISIS sample" (CMA006_ISIS4).

2.2.3 Synthesis of $Ln_2O_2(M_{1-y}M'_y)Se_2$ (*Ln* = La, Ce, *M* = Fe, Zn, Mn, Cd) and $(La_{2-z}Ce_z)O_2MSe_2$ (*M* = Fe, Zn, Mn, Cd) Materials

For all $Ln_2O_2(M_{1-y}M'_y)Se_2$ and $(La_{2-z}Ce_z)O_2MSe_2$ materials, 0.6 g of sample was prepared by weighing stoichiometric amounts of Ln_xO_y (La_2O_3 or CeO_2), *M* (Fe, Zn, Mn, Cd), and Se. These were intimately ground using an agate pestle and mortar, placed in a quartz tube along with the oxygen getter (predominantly 110% stoichiometric percentage of Al, though in some cases 105% stoichiometric percentage of Ti), as per the method described in Section 2.2.2. The quartz tube was evacuated to a pressure of $<7x10^{-3}$ mbar, flame sealed, and heated in a muffle furnace under the following conditions: ramp at 1 ˚C min^{-1} to 600 ˚C and dwell for 12 hours, ramp at 0.5 ˚C min^{-1} to 800 ˚C and dwell for 1 hour, ramp at 1 ˚C min^{-1} to the final dwell temperature (1000 ˚C, 1100 ˚C or 1200 ˚C) and held for a set time (12, 24 or 48 hours). Specific experimental conditions for all samples are tabulated in Table 2.3, Table 2.4 and Table 2.5.

$La_2O_2(Fe_{1-y}Zn_y)Se_2$		$La_2O_2(Zn_{1-y}Mn_y)Se_2$		$La_2O_2(Mn_{1-y}Cd_y)Se_2$	
y	Conditions	*y*	Conditions	*y*	Conditions
0	1100˚C 12hr Al	0	1100˚C 12hr Al	0	1100˚C 12hr Al
0.125	1100˚C 12hr Al	0.1	1100˚C 12hr Al	0.025	1100˚C 12hr Al
0.25	1100˚C 12hr Al	0.2	1100˚C 12hr Al	0.05	1100˚C 12hr Al
0.275	1100˚C 12hr Al	0.3	1100˚C 12hr Al	0.1	1100˚C 12hr Al
0.325	1100˚C 12hr Al	0.4	1100˚C 12hr Al	0.15	1100˚C 12hr Al
0.35	1100˚C 12hr Al	0.5	1100˚C 12hr Al	0.2	1100˚C 12hr Al
0.375	1100˚C 12hr Al	0.6	1100˚C 12hr Al	0.25	1100˚C 12hr Al
0.5	1100˚C 12hr Al	0.7	1100˚C 12hr Al	0.3	1100˚C 12hr Al
0.625	1100˚C 12hr Al	0.8	1100˚C 12hr Al	0.35	1100˚C 12hr Al
0.75	1100˚C 12hr Al	0.9	1100˚C 12hr Al	0.4	1100˚C 12hr Al
0.875	1100˚C 12hr Al	0.95	1100˚C 12hr Al	0.45	1100˚C 12hr Al
1	1100˚C 12hr Al	0.975	1100˚C 12hr Al	0.5	1100˚C 12hr Al
		0.9875	1100˚C 12hr Al	0.6	1100˚C 12hr Al
		1	1100˚C 12hr Al	0.7	1100˚C 12hr Al
				0.8	1100˚C 12hr Al
				0.9	1100˚C 12hr Al
				1	1100˚C 12hr Al

Table 2.3. Synthetic conditions (final dwell temperature/final dwell time/oxygen getter type) for $La_2O_2(M_{1-y}M'_y)Se_2$ *samples.*

$Ce_2O_2(Fe_{1-y}Zn_y)Se_2$		$Ce_2O_2(Zn_{1-y}Mn_y)Se_2$		$Ce_2O_2(Mn_{1-y}Cd_y)Se_2$	
y	Conditions	*y*	Conditions	*y*	Conditions
0	1100˚C 12hr Al	0	1200˚C 12hr Al	0	1100˚C 24hr Al
0.03	1100˚C 12hr Al	0.2	1100˚C 12hr Al	0.05	1100˚C 12hr Al
0.0625	1100˚C 12hr Al	0.4	1100˚C 12hr Al	0.1	1100˚C 12hr Al
0.125	1100˚C 12hr Al	0.6	1100˚C 12hr Al	0.125	1100˚C 12hr Al
0.25	1100˚C 12hr Al	0.8	1100˚C 12hr Al	0.15	1100˚C 12hr Al
0.375	1100˚C 12hr Al	0.833	1100˚C 12hr Al	0.2	1100˚C 12hr Al
0.5	1100˚C 12hr Al	0.9	1100˚C 12hr Al	0.25	1100˚C 12hr Al
0.625	1100˚C 12hr Al	1	1100˚C 12hr Al	0.3	1100˚C 12hr Al
0.75	1100˚C 12hr Al			0.4	1100˚C 12hr Al
0.8125	1100˚C 12hr Al			0.5	1100˚C 12hr Al
0.875	1100˚C 12hr Al			0.6	1100˚C 12hr Al
0.9375	1100˚C 12hr Al			0.7	1100˚C 12hr Al
0.97	1100˚C 12hr Al			0.8	1100˚C 12hr Al
1	1200˚C 12hr Al			0.9	1100˚C 12hr Al
				1	1100˚C 12hr Al

Table 2.4. Synthetic conditions for $Ce_2O_2(M_{1-y}M'_y)Se_2$ *samples.*

$(La_{2-z}Ce_z)O_2FeSe_2$		$(La_{2-z}Ce_z)O_2ZnSe_2$		$(La_{2-z}Ce_z)O_2MnSe_2$		$(La_{2-z}Ce_z)O_2CdSe_2$	
z	Conditions	*z*	Conditions	*z*	Conditions	*z*	Conditions
0	1100˚C 12hr Al	0	1200˚C 12hr Al	0	x2 1150˚C 24hr Ti	0	1100˚C 12hr Al
0.5	1100˚C 12hr Al	0.2	1200˚C 12hr Al	0.1	x2 1150˚C 24hr Ti	0.5	1100˚C 12hr Al
1	1100˚C 12hr Al	0.6	1200˚C 12hr Al	0.2	x2 1150˚C 24hr Ti	1	1100˚C 12hr Al
1.5	1100˚C 12hr Al	1	1200˚C 12hr Al	0.4	x2 1150˚C 24hr Ti	1.5	1100˚C 12hr Al
2	1100˚C 12hr Al	1.4	1200˚C 12hr Al	0.6	x2 1150˚C 24hr Ti	2	1100˚C 12hr Al
		1.8	1200˚C 12hr Al	0.8	x2 1150˚C 24hr Ti		
		2	1200˚C 12hr Al	1	x2 1150˚C 24hr Ti		
				1.2	x2 1150˚C 24hr Ti		
				1.4	x2 1150˚C 24hr Ti		
				1.6	x2 1150˚C 24hr Ti		
				1.8	x2 1150˚C 24hr Ti		
				1.9	x2 1150˚C 24hr Ti		
				2	x2 1150˚C 24hr Ti		

Table 2.5. Synthetic conditions for ($La_{2-z}Ce_z)O_2MSe_2$ samples.

The stoichiometric equation for the reaction using Al and Ti as an oxygen getter, if 100% phase purity is obtained, is given by Equation 2.2 and Equation 2.3.

$$(1-\tfrac{z}{2})La_2O_3 + zCeO_2 + yM + (1-y)M' + 2Se + \left(\tfrac{2}{3}+\tfrac{1}{3}z\right)Al \rightarrow (La_{2-z}Ce_z)O_2(M_{1-y}M'_y)Se_2 + \left(\tfrac{1}{3}+\tfrac{1}{6}z\right)Al_2O_3$$

Equation 2.2

$$(1-\tfrac{z}{2})La_2O_3 + zCeO_2 + Mn + 2Se + \left(\tfrac{1}{2}+\tfrac{1}{4}z\right)Ti \rightarrow (La_{2-z}Ce_z)O_2MnSe_2 + \left(\tfrac{1}{2}+\tfrac{1}{4}z\right)TiO_2$$

Equation 2.3

For PND experiments at ISIS, large (~2.4 g) samples of $Ce_2O_2Fe_{3/4}Zn_{1/4}Se_2$, $Ce_2O_2Fe_{1/8}Zn_{7/8}Se_2$, $Ce_2O_2Zn_{1/6}Mn_{5/6}Se_2$ and $La_2O_2Zn_{1/10}Mn_{9/10}Se_2$ were made. For each composition, four 0.6 g samples were prepared at a final dwell temperature of 1100 °C for 12 hours using 110% stoichiometric percentage of Al. The four samples were then intimately ground together, and reheated at 1100 °C for a further 12 hours.

2.2.4 Synthesis of $La_2O_2Cu_{2-2x}Cd_xSe_2$ Materials

0.6 g samples were prepared across the $La_2O_2Cu_{2-2x}Cd_{2x}Se_2$ solid solution by weighing stoichiometric amounts of La_2O_3, Cu, Cd and Se. These were intimately ground using an agate pestle and mortar, placed in a quartz tube along with an AOG of 110% stoichiometric percentage, as per the method described in Section 2.2.2. The evacuated quartz tube was heated in a muffle furnace under the following conditions: ramp at 1 ˚C min^{-1} to 600 ˚C and dwell for 12 hours, ramp at 0.5 ˚C min^{-1} and dwell for 1 hour, ramp at 1 ˚C min^{-1} to a final dwell temperature of 1100 ˚C and held for 12 hours. The stoichiometric equation for the reaction if 100% phase purity is obtained, is given by Equation 2.4.

$$La_2O_3 + (2–2x)Cu + xCd + 2Se + \frac{2}{3}Al \rightarrow La_2O_2Cu_{2–2x}Cd_xSe_2 + \frac{1}{3}Al_2O_3$$

Equation 2.4

2.2.5 Synthesis of $La_2O_2Cu_{2–2x}M_xSe_2$ (*M* = Fe, Zn, Mn) and $La_2O_2Cu_{2-2x}(M_{1-y}M'_y)_xSe_2$ (*M*/*M*' = Fe/Zn, Zn/Mn, Mn/Cd) Materials

0.6 g samples were prepared across the $La_2O_2Cu_{2–2x}M_xSe_2$ and $La_2O_2Cu_{2–x}(M_{1–y}M'_y)_xSe_2$ solid solutions by weighing stoichiometric amounts of La_2O_3, Cu, Fe, Zn, Mn, Cd and Se. These were intimately ground using an agate pestle and mortar, placed in a quartz tube along with an AOG of 110% stoichiometric percentage, as per the method described in Section 2.2.2. The evacuated quartz tube was heated in a muffle furnace under the following conditions: ramp at 1 ˚C min^{-1} to 600 ˚C and dwell for 12 hours, ramp at 0.5 ˚C min^{-1} and dwell for 1 hour, ramp at 1 ˚C min^{-1} to a final dwell temperature of 1100 ˚C and held for 12 hours. The stoichiometric equation for the reaction if 100% phase purity is obtained is given by Equation 2.5 and Equation 2.6.

$$La_2O_3 + (2–2x)Cu + xM + 2Se + \frac{2}{3}Al \rightarrow La_2O_2Cu_{2–2x}M_xSe_2 + \frac{1}{3}Al_2O_3$$

Equation 2.5

$$La_2O_3 + (2–2x)Cu + (1-y)M + yM' + 2Se + \frac{2}{3}Al \rightarrow La_2O_2Cu_{2–2x}(M_{1–y}M'_y)_xSe_2 + \frac{1}{3}Al_2O_3$$

Equation 2.6

2.2.6 Synthesis of $La_{2–z}Sr_zO_2CuCd_{0.5}Se_2$ Materials

0.6 g samples were prepared across the $La_{2–z}Sr_zO_2CuCd_{0.5}Se_2$ (z = 0 – 1) solid solution by weighing stoichiometric amounts of La_2O_3, SrO, Cu, Cd and Se. These were intimately ground using an agate pestle and mortar, placed in a quartz tube along with an AOG of 110% stoichiometric percentage, as per the method described in Section 2.2.2. The evacuated quartz tube was heated in a muffle furnace under the following conditions: ramp at 1 ˚C min^{-1} to 600 ˚C and dwell for 12 hours, ramp at 0.5 ˚C min^{-1} and dwell for 1 hour, ramp at 1 ˚C min^{-1} to a final dwell temperature of 1100 ˚C and held for 12 hours. The stoichiometric equation for the reaction if 100% phase purity is obtained is given by Equation 2.7. This equation is making the assumption that the charge compensation mechanism for the substitution of La^{3+} for Sr^{2+} is the introduction of *p*-type holes by oxidising Cu^{1+} to Cu^{2+}.

$$(1–\frac{z}{2})La_2O_3 + zSrO + Cu + \frac{1}{2}Cd + 2Se + \left(\frac{2}{3}–\frac{1}{3}z\right)Al \rightarrow La_{2–z}Sr_zO_2CuCd_{0.5}Se_2 + \left(\frac{1}{3}–\frac{1}{6}z\right)Al_2O_3$$

Equation 2.7

2.3 Diffraction

Diffraction is perhaps the most important analytical technique in the study of crystalline materials, and can provide information such as unit cell dimensions and the position of atoms within the unit cell. On a more basic level, it can be a quick method of phase identification and phase purity determination. This section will discuss the theory behind

diffraction (theory which can be applied to X-rays, electrons and neutrons), before describing more complex theory on diffraction from incommensurate materials.

2.3.1 Diffraction from Commensurate Materials

Diffraction is an interference phenomenon which occurs when waves interact with a suitable grating, causing them to act as if emanating from a point source. These emanating waves then interfere with each other, both constructively (in phase) to increase their amplitude, and destructively (out of phase) to decrease their amplitude. As crystalline materials are composed of repeating arrays of atoms, they can be considered diffraction gratings if the wavelength of the radiation being scattered is comparable to the distances between atoms. Such radiation can include X-rays, neutrons and electrons.

Although diffraction is an interference phenomenon whereby atoms act as point sources of radiation, it is often simpler to think of the process as reflections from imaginary lattice planes. It should be stressed that although this is not strictly true, this type of a model allows the derivation of the reflection condition which is equivalent to that obtained via a more rigorous treatment. The lattice planes are labelled using Miller indices, *hkl*, which intercept the three unit cell axes at *a/h*, *b/k* and *c/k*. A single *hkl* defines a family of lattice planes separated by a constant distance, termed d_{hkl}. Constructive interference can occur when an integer number (*n*) of wavelengths of the incident beam equals the path difference ($2d_{hkl}\sin\theta$) of X-rays reflected from adjacent planes. When this is satisfied, intensity is observable in the diffraction pattern. Figure 2.2 shows this occurrence pictorially.

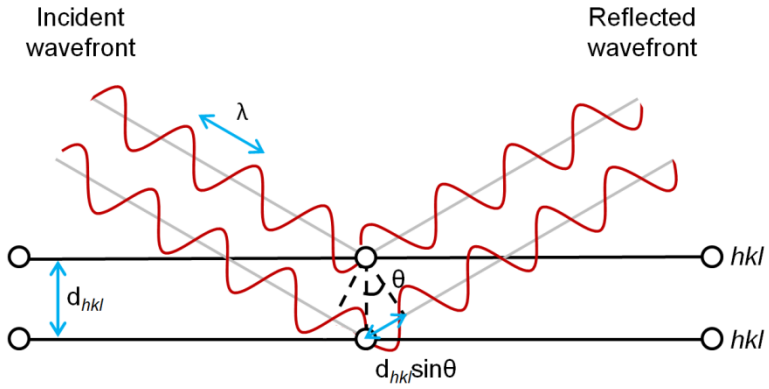

Figure 2.2. A schematic representation of Bragg's law.

It is only necessary to consider the case where *n* = 1 leading to Bragg's law, Equation 2.8, which mathematically describes the scattering of X-rays from imaginary lattice planes of crystalline materials.

$$\lambda = 2d_{hkl}sin\theta_{hkl}$$

Equation 2.8

This can then be related to the unit cell dimensions by Equation 2.9, where d_{hkl} is the spacing between a given set of planes, *a*, *b* and *c* unit cell dimensions and *h*, *k* and *l* Miller indices. It should be noted that Equation 2.9 can only be used for an orthorhombic, tetragonal or cubic unit cell, and takes slightly different forms for other crystal classes.

$$\frac{1}{d^2} = \frac{h^2}{a^2} + \frac{k^2}{b^2} + \frac{l^2}{c^2}$$

Equation 2.9

The structure factor equation, Equation 2.10, is related to the intensity of a given reflection from the unit cell contents, summed over all atoms. The structure factor relates the positions of individual atoms (*xyz*), the Miller indices (*hkl*) and the atomic scattering factors (f_j) to the observed intensities.

$$F_{hkl} = \sum_j f_j \exp\left[2\pi i\left(hx_j + ky_j + lz_j\right)\right]$$

Equation 2.10

The observed intensity is proportional to the square of the structure factor. For an ideal powder sample, it is modified by the experimental factors L (Lorentz factor), P (polarisation factor) and A (absorption). It is also modified by a scale factor (c), and multiplicity (j_{hkl}, number of symmetry equivalent reflections). This is shown in Equation 2.11.

$$I_{hkl} = c\mathrm{L}(2\theta)\mathrm{P}(2\theta)\mathrm{A}(2\theta)j_{hkl}|F_{hkl}|^2$$

Equation 2.11

2.3.2 Diffraction from Incommensurate Materials

A crystal can be defined as “a material that has essentially a sharp diffraction pattern”.[1] Crystallographers have classified 4 structural types with long range order that show sharp diffraction peaks; structures with translational symmetry (described in Section 2.3.1), incommensurately modulated structures, incommensurate composite crystals and quasicrystals. This section will discuss incommensurately modulated structures only.

The atomic arrangement of an incommensurately modulated structure has a function describing the modulation from a simple parent structure, which can have a non-integral relationship with the lattice periodicity. This is illustrated in Figure 2.3 where the modulation wave is such that atoms are displaced in the *x* direction by the negative of the wave amplitude. If we first consider a commensurate modulation, as shown in Figure 2.3, where atomic displacement leads to periodicity equal to 2*a*, the structure can be described by a unit cell doubled in the *a* direction, repeated in 2D using only translations.[2]

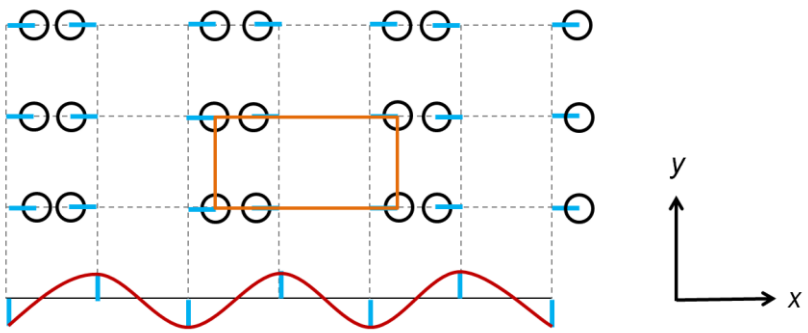

Figure 2.3. Atomic displacement in a crystal structure along x whereby the modulation function gives twice the lattice periodicity, described as a twofold superstructure. Dashed line is the original 2D unit cell (or subcell), red line is a displacive modulation wave with a period of double the lattice period, blue lines are the atomic displacement distances, black circles are new atomic positions and the orange rectangle the new unit cell (or supercell).

Incommensurately modulated structures are those where the periodicity of the modulation is not an integral multiple of lattice periodicity, as shown in Figure 2.4. These structures still contain long range order and give rise to sharp diffraction patterns.

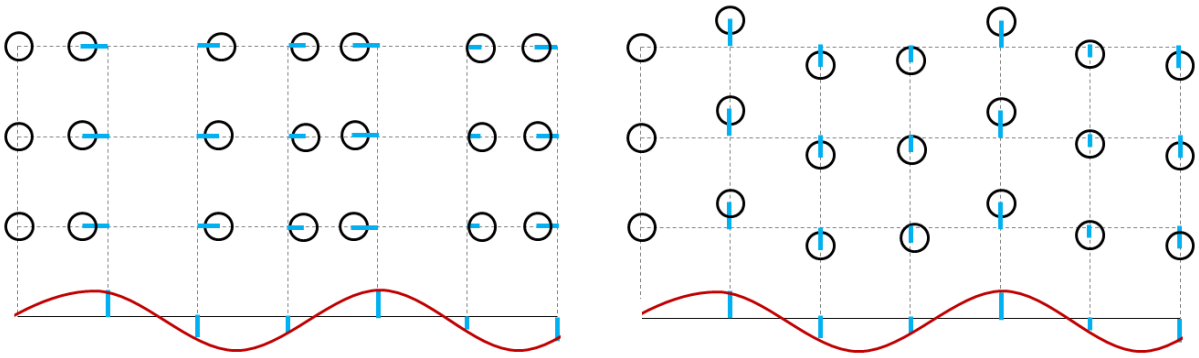

Figure 2.4. Incommensurately modulated structure with displacive modulation wavelength (red) equal to a non-integer number of lattice periods, leading to transverse (left) or longitudinal (right) atomic displacements.

In order to describe incommensurately modulated structures, one must apply the concepts of superspace, where there can be 1 (3+1), 2 (3+2) or 3 (3+3) additional dimensions orthogonal to the 3 physical space dimensions. This is represented in Figure 2.5 for one physical space dimension and one superspace dimension. The modulation along *a* is rotated about each basic lattice point becoming orthogonal to physical space, generating a periodic structure of “strings” in superspace. The points where these strings intersect with physical space are atomic positions. Hence, an atom in superspace is a wave one period in length, which within superspace repeats by purely translational displacements.[2]

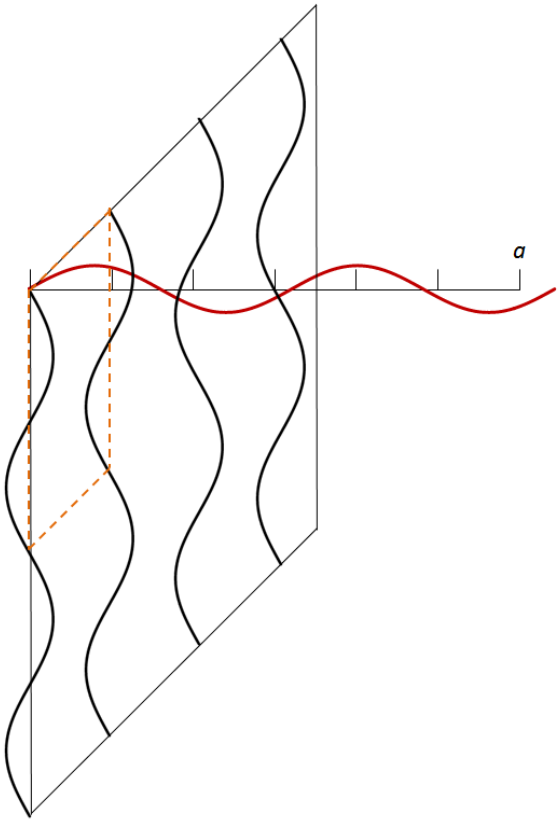

Figure 2.5. Illustration of one horizontal physical space dimension (a) orthogonal to a superspace dimension. The red wave along a is incommensurately modulated, with corresponding positions in superspace directions in black. Basic lattice points are shown by vertical marks, and the orange dashed box represents the unit which translates periodically in superspace.

For weakly modulated structures, Bragg reflections of the basic structure will be observed surrounded by satellite reflections in a regular pattern spaced at distances of ± the index of the modulation (m) × the modulation vector (*q*). It is common to only observe low order satellite reflections as amplitudes of modulations are weak; in the work presented in this thesis, only first order satellite reflections are observed experimentally. In structures with multi-dimensional modulations, the modulation wave vectors are not independent, but related by symmetry, making structural solution more challenging.[2] In this thesis, only one-dimensional modulations need to be considered (3+1). The generally accepted notation used to describe the indices in physical and superspace are *hklmnp*, and just as all 230 space groups have been tabulated in The International Tables of Crystallography, recently all the possible superspace groups have too. There are 775 (3+1)-dimensional superspace groups, and significantly more for (3+2) and (3+3)-dimensions.[2-4]

2.4 X-ray Powder Diffraction

Single crystal X-ray diffraction is considered the most powerful X-ray diffraction technique for structure determination due to its ability to give an accurate 3-dimensional description of electron density within a unit cell; however it is not always practical. For some materials, growing single crystals can prove difficult or even impossible, and instead they form small

crystals known as crystallites. Powder X-ray diffraction (PXRD) is therefore an invaluable technique for such samples.

A powder can be considered to be an effectively infinite number of crystallites arranged randomly in space. This leads to cones of intensity in PXRD, shown in Figure 2.6, as opposed to spots in single crystal X-ray diffraction. Data is collected across a 1D slice through these cones, and measures the intensity of peaks as a function of diffraction angle (2θ). The drawback of a 1D PXRD pattern compared to 3D single crystal X-ray data is the loss of information due to peak overlap. This makes structure solution more difficult, and a more common approach with PXRD is to use a starting model and refine this to fit the experimental data. Such a refinement is known as a Rietveld refinement,[5] discussed later in this chapter.

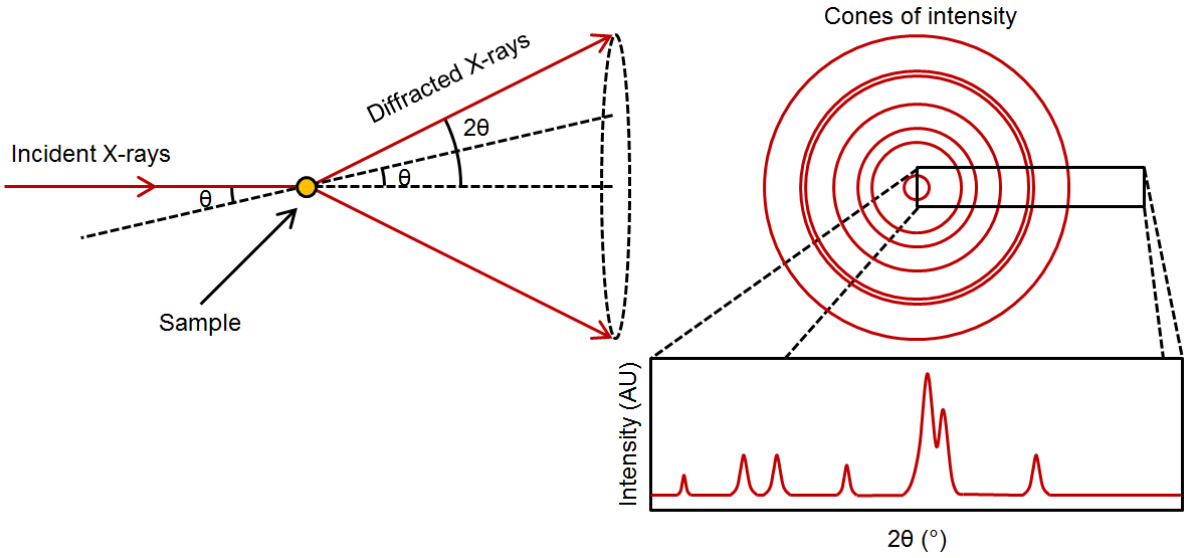

Figure 2.6. Cones of intensity producing powder X-ray diffraction.

In a PXRD pattern, peak positions can be used to deduce the unit cell size and shape, while peak intensity gives information about atomic positions. Peak widths can give information on crystallite size and strain, and the background can yield information relating to short range order within the structure. There is a set of peaks observed for every crystalline phase present and their relative intensities can be used to deduce sample composition.

2.4.1 Instrumentation and Sample Preparation - Bruker D8 Advance ("d7")

The "d7" was used in Bragg-Brentano geometry for routine phase analysis using Diffrac EVA[6] (30 minute scans) and for high quality data collection for Rietveld analysis[5] (14 hour scans), both at room temperature. The X-ray beam is passed through a Soller slit and a programmable variable divergent slit, before interaction with the sample. The diffracted X-ray beam is then stripped of its CuK_β radiation by a Ni filter before enetering a Lynx-eye detector, capable of rapidly collecting high resolution diffraction patterns with its 192 silicon strip detectors. Bruker-supplied software was used to control the diffractometer and visually inspect PXRD patterns.[7]

Samples were ground into a fine powder using a pestle and mortar, before being passed through a sieve of 120 mesh onto a silicon slide, pre-prepared with a thin layer of Vaseline®

to act as an adhesive. The slide is cut from a single crystal of silicon, parallel to the 511 crystallographic plane, thereby eliminating any diffracted intensity from the sample holder. It is set within a plastic housing designed to fit into the sample changer of a Bruker D8 Advance PXRD instrument. A prepared sample is shown in Figure 2.7.

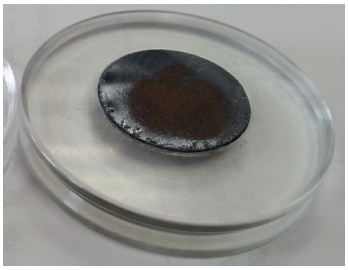

Figure 2.7. A prepared powder sample, ready to be loaded onto the Bruker D8 Advance instrument. The silicon slide is ~3 cm in diameter.

2.5 Neutron Powder Diffraction

The diffraction of neutrons is also possible when they interact with a suitable diffraction grating, such as crystalline materials for neutrons with wavelengths ~1 Å. Much of the theory behind the diffraction of X-rays is applicable to neutrons, however there is a significant difference: X-rays are scattered by electrons while neutrons are scattered by atomic nulclei. As a result, the scattering power is not proportional to the atomic number as in X-ray diffraction, but varies somewhat irregularly across the periodic table. This makes neutron diffraction able to distinguish between ions with a similar number of electrons, and be sensitive to lighter species such as H^+ and O^{2-} in the presence of heavier ones.

2.5.1 ISIS Neutron Source and Time-of-Flight (TOF) Neutron Diffractometers

All powder neutron diffraction (PND) data presented were collected at ISIS in the UK. At ISIS, neutrons are produced by a process called spallation, shown in Figure 2.8. H^- ions are first stripped of their electrons to produce protons before entry to a synchrotron ring, where the protons are accelerated to speeds of ~2.5×10^8 m s^{-1}. These high energy protons are then directed to a tungsten target in pulses, and the subsequent bombardment (the spallation process), releases pulses of neutrons. Moderators are used to select those neutrons with suitable energies for diffraction, which are directed towards a particular instrument.

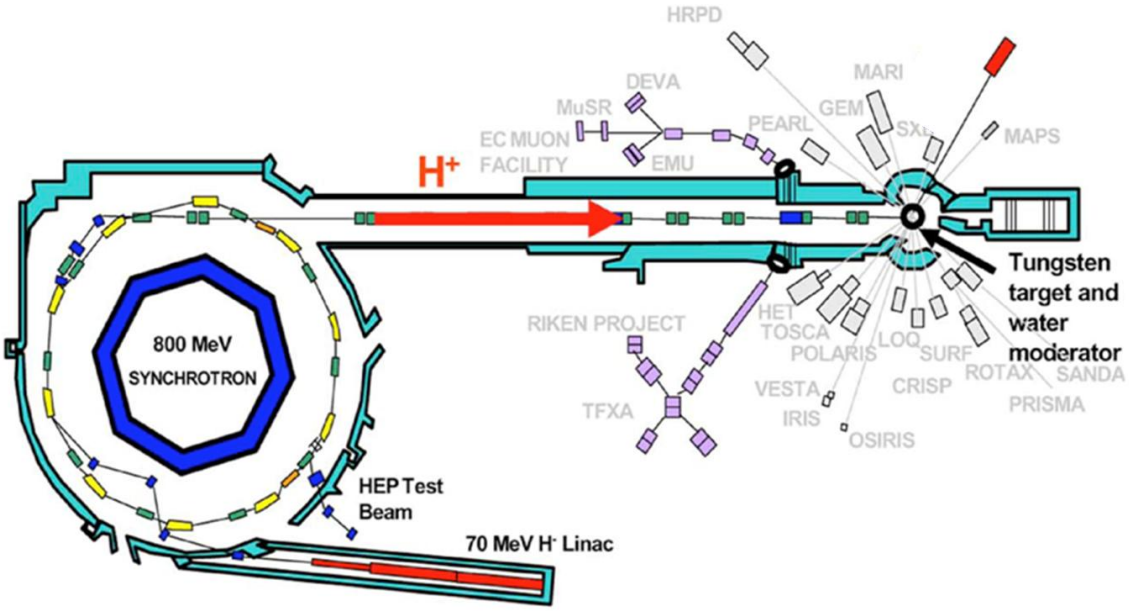

Figure 2.8. Schematic diagram showing the production of neutrons at ISIS, UK, via a spallation process.

During the spallation and moderation processes, neutrons with a wide range of energies are produced, hence a wide range of wavelengths. This is shown by the de Broglie relationship, Equation 2.12, where λ = wavelength, h = Planck's constant, p = momentum, m = mass and v = velocity. This can be substituted into the Bragg equation, as per Equation 2.13, which shows that protons travelling at different speeds will interact with a suitable diffraction grating differently. The instrumental setup therefore consists of detectors situated at a fixed angle to the sample, capable of detecting all neutrons that reach them. Their energy (or wavelength) is measured via their time-of-flight (TOF), Equation 2.14, the time taken for a neutron to travel the known distance from the tungsten target to the detector.

$$\lambda = \frac{h}{p}$$

(where $p = mv$)

Equation 2.12

$$\frac{h}{mv} = 2d_{hkl}sin\theta$$

Equation 2.13

$$v = \frac{distance}{TOF}$$

Equation 2.14

2.5.2 General Materials (GEM) Diffractometer

The General Materials Diffractometer or GEM is housed at the ISIS spallation source in Oxfordshire, UK, and was used to carry out all TOF neutron diffraction studies. GEM has multiple banks of detectors positioned over a wide range of scattering angles (1˚ - 171˚), giving a total detector array of 7.270 m^2. Each detector is constructed of individual ZnS/ ^{6}Li scintillators.[8] The setup is shown in Figure 2.9.

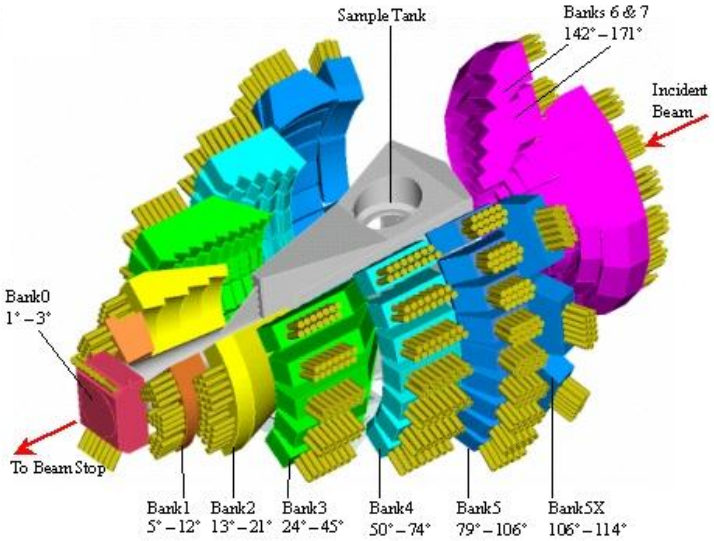

Figure 2.9. Schematic diagram of the GEM diffractometer at ISIS.[9]

The measured samples ($Ce_2O_2ZnSe_2$, $Ce_2O_2Fe_{3/4}Zn_{1/4}Se_2$, $Ce_2O_2Fe_{1/8}Zn_{7/8}Se_2$, $Ce_2O_2Zn_{1/6}Mn_{5/6}Se_2$, and $La_2O_2Zn_{1/10}Mn_{9/10}Se_2$) were loaded into cylindrical vanadium cans of diameter 6 mm. The samples were then lowered into the neutron beam through the sample tank and measurements carried out at room temperature. Vanadium is an ideal sample holder material due to its low neutron scattering cross section.

2.6 Synchrotron X-ray Diffraction

Synchrotron X-ray diffraction offers high intensity and excellent peak resolution (sharp peaks) when compared to laboratory X-ray sources. This was exploited during this work to determine microstructure across the $La_2O_2Cu_{2-2x}Cd_xSe_2$ solid solution samples, namely the quantification of stacking faults, which would have been near impossible without such high quality data. It was also useful to accurately determine cell volume trends across a range of solid solutions.

2.6.1 Synchrotron radiation

When electrons are accelerated to near the speed of light and their trajectory changed, synchrotron radiation is emitted tangentially at a variety of wavelengths, some of which can be used for diffraction studies of crystalline materials. This process begins by injecting electrons into a linear accelerator before moving them to a booster ring, where they are accelerated close to the speed of light. The electrons are transferred periodically to a larger storage ring, which is under high vacuum to prevent energy loss, and the electron path is controlled by a series of bending magnets. Electron acceleration of this sort causes the

emission of photons, which are directed towards target stations through a series of optics including slits, mirrors and monochromators. This process is shown schematically in Figure 2.10. The specific setup of the optics determines the radiation wavelength and collimation, and these vary from one synchrotron facility to the next. If bending magnets alone do not produce sufficient intensity, undulators and wigglers can be used which change the direction of the accelerated electron beam sinusoidally.

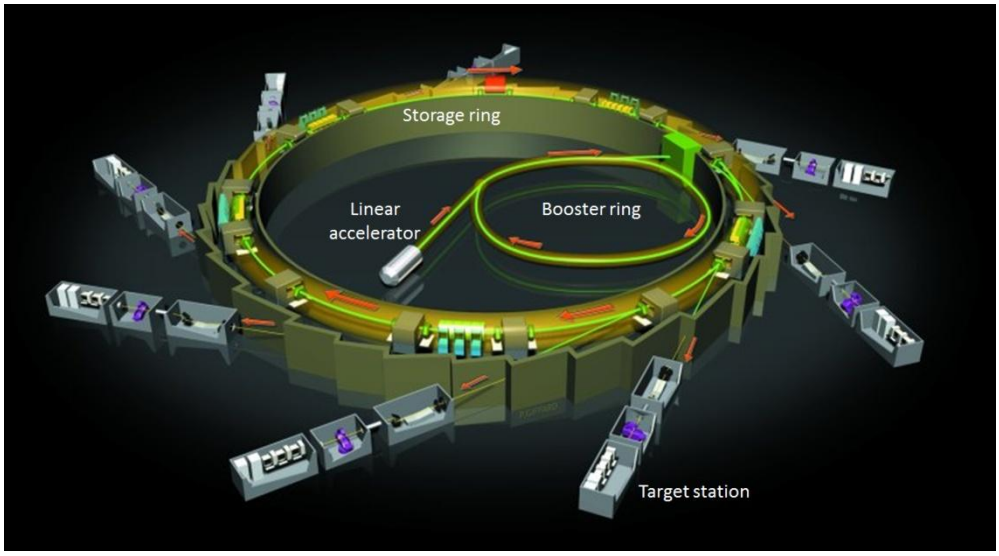

Figure 2.10. Schematic diagram of a typical synchrotron ring.[10]

2.6.2 Powder Diffraction Beamline at the Australian Synchrotron

The Powder Diffraction Beamline at the Australian Synchrotron is located on a bending magnet source and operates over the energy range 5-30 keV. Contained within the first hutch are optics, including mirrors and a double crystal monochromator. The centre hutch contains the primary end station, where most powder diffraction experiments take place. There are three detectors available for use; the Mythen microstrip detector was used for experiments in this thesis.

This beamline was used for the collection of data across the $La_2O_2Cu_{2-2x}Cd_xSe_2$ solid solution at a wavelength of 0.6354462(7) Å, and other closely related series where Cd is replaced by Fe, Zn and Mn at a wavelength of 0.6355792(5) Å. Samples were loaded into 0.5 mm capillaries, and data collected using the Mythen microstrip detector from 1-81° 2θ. To cover gaps between detector modules, 2 data sets were collected with the detector set 0.5° apart and then merged to a single data set using in-house data processing software, PDViPeR.

2.6.3 I11 Beamline at Diamond

The I11 beamline at Diamond operates over the energy range 5-25 keV. Similar to the Australian Beamline, it has three hutches. The optics hutch contains several slit systems, beam diagnostics, monochromator and harmonic rejection mirrors. Experimental hutch 1 (EH1) houses a large heavy duty diffractometer, where samples in capillaries, flat-plate holders or small sample cells can be mounted and measured. Larger sample cells and stages can be mounted on a large moveable sample table. High sample throughput (up to 200 capillary samples) is available via a robotic arm. For high resolution measurements,

there are 5 multi-analysing crystal (MAC) detectors with a total of 45 individual Si crystals and photomultiplier based detectors. There is also a Mythen microstrip detector with a 90º window for fast data collection.

This beamline was used for the collection of data across the $La_{2-z}Sr_zO_2CuCd_{0.5}Se_2$ (x = 0 - 1) solid solution at a wavelength of 0.825921(10) Å. Samples were loaded into 0.5 mm capillaries, and data collected using both the MAC and Mythen microstrip detector from 0-150° and 0-92° 2θ respectively.

2.7 Analysis of Diffraction Data

The analysis of the X-ray and neutron data collected was done primarily via Rietveld refinement, a tool which has become invaluable for the structural analysis of powder diffraction data. This will be discussed, along with Pawley refinement.

2.7.1 Rietveld Refinement

A Rietveld refinement attempts to fit experimental powder diffraction intensity values (y_i) using a least squares method to minimise the difference between a calculated diffraction pattern and the experimental data.[5] Such a refinement can yield a wealth of structural information about a compound, provided a good starting model is available. The starting model should contain information relating to the lattice parameters, space group, atomic coordinates, site occupancies, and a peak shape description. These can then be adjusted to best fit the experimental data, with the exception of the space group, which may or may not be correct. If the starting model is too dissimilar to the structure being refined, convergence may not be achieved.

The least squares refinement aims to minimise the quantity S_y, defined in Equation 2.15, where y_i is the observed intensity at 2θ point i, y_{ci} the calculated intensity at point i, and w_i the weighting factor.

$$S_y = \sum_i w_i (y_i - y_{ci})^2$$

Equation 2.15

A range of phase specific parameters (e.g. lattice parameters, atomic coordinates, scale factor, thermal parameters, preferred orientation, sample contribution to peak shape) and global parameters (e.g. background, instrumental profile, specimen displacement) can be refined. Sufficient parameters are needed in the structural model for the observed pattern to be reproduced, with care being taken to ensure that the refined parameters lead to a chemically sensible structure.

Residual factors (*R*-factors) give a measure of the fit quality to the data. R_{wp} (weighted *R*-factor) is often considered the most valuable of these as it directly relates to S_y, the quantity being minimized. It gives a quantitative measure of the difference between the calculated pattern and experimental data, as per Equation 2.16.

$$R_{wp} = \left\{ \frac{\sum w_i (y_i - y_{ci})^2}{\sum w_i (y_i)^2} \right\}^{\frac{1}{2}}$$

Equation 2.16

R_{exp} is a measure of the expected fit possible based on statistics, shown in Equation 2.17, where N is the total number of data points, and P the total number of refined parameters.

$$R_{exp} = \left\{ \frac{(N - P)}{\sum w_i {y_i}^2} \right\}^{\frac{1}{2}}$$

Equation 2.17

Another commonly quoted agreement factor is χ^2. This is derived from the ratio of R_{wp} to R_{exp}, and shown in Equation 2.18.

$$\chi^2 = \left[\frac{R_{wp}}{R_{exp}} \right]^2$$

Equation 2.18

All refinements in this thesis were performed in TOPAS Academic (TA).[11-13] Rietveld plots will be formatted consistently such that the observed data curve is shown in blue, calculated data curve in red and difference curve in grey.

2.7.2 Pawley Refinement

A Pawley refinement calculates a list of allowed reflections based on the space group and unit cell size specified.[14] Upon refinement the intensity of these reflections is varied until the best fit to the experimental data is obtained, hence no information on the unit cell contents is required, nor can it be inferred. It is common to first refine in the space group of lowest symmetry in the given crystal class, as all possible reflections will be present. It is then possible to get closer to the true space group by considering systematic absences and determining the highest symmetry space group consistent with the reflections observed.

2.8 Electron Diffraction

Electron diffraction can be used to study crystalline solids, and involves directing electrons at a sample and recording the resulting interference pattern. It therefore has similarities to X-ray and neutron diffraction, and is frequently used to complement such data. Usually performed in a transmission electron microscope (TEM), electrons are accelerated to a known energy (hence known wavelength) before interaction with the sample. As with other diffraction techniques, a crystalline solid acts as a diffraction grating and scatters electrons in a characteristic manner.

Diffraction patterns of a given crystal orientation measure one plane of reciprocal space. If the sample is tilted with respect to the incident electron beam, diffraction patterns from several different crystal orientations can be recorded and the reciprocal lattice of the crystal mapped in three dimensions. As the de Broglie wavelength of the electrons is short, only

small diffraction angles need to be measured and a large number of reflections can be recorded at each Bragg angle. Therefore the tilting required is minimal. One complication of the technique is the need for very thin samples, as the highly charged electrons interact with matter through strong Coulombic forces leading to non-kinematic diffraction.

Samples were prepared by suspending the powder in acetone and dispersing over a holey carbon grid. Electron diffraction was carried out on a JEOL 2100F FEG TEM in transmission mode operating at 200 eV, and images viewed/captured using a CCD (charged coupled device) camera.

2.9 Diffuse Reflectance Spectroscopy (DRS)

An Ocean Optics Maya Pro 2000 spectrometer was used to collect diffuse reflectance spectra of various $Ce_2O_2ZnSe_2$ samples. Samples were dispersed in NaCl in a roughly 1:3 mass ratio, and placed in a 20 mm diameter sample vial; NaCl was also used as the white standard. The samples were illuminated in the sample vial using an Energetiq LDLS EQ99 broadband lamp, with collection at 20° to the excitation. Integration times were varied across the measured samples to allow maximum response of the spectrometer without detector saturation. The data output is intensity (arbitrary units) as a function of wavelength (nm), whereby Reflectance (R) can be calculated by dividing the intensity of the sample by the intensity of the reference at any given wavelength, Equation 2.19. Kubelka-Munk treatment can then be used to determine the optical band gap of a material. The Kubelka-Munk function (F) is first calculated, Equation 2.20, then F plotted against energy; the optical band gap is given by the extrapolated *x*-intercept of the functions slope.[15,16]

$$R = \frac{I_{sample}}{I_{reference}}$$

Equation 2.19

$$F = \frac{(1-R)^2}{2R}$$

Equation 2.20

2.10 SQUID Magnetometry

A Quantum Design Magnetic Property Measurement System (MPMS) was used to measure the magnetic properties of $Ce_2O_2ZnSe_2$. A SQUID magnetometer consists of a superconducting magnet, a superconducting detection coil (a gradiometer), and a SQUID (which is connected to the detection coil). As superconducting materials are used the system is cooled to very low temperatures, usually by liquid helium. The detection coil is placed within a uniform region of the magnetic field of the superconducting magnet. As the detection coil couples inductively to the sample it can detect the magnetic properties of a material. Any changes in the detection coil caused by the sample are transmitted to the SQUID as changes in current, which is observed as changes to the SQUID's output voltage. The SQUID consists of a superconducting ring containing 2 parallel Josephson junctions, Figure 2.11. These act as small insulating gaps, through which superconducting electrons can tunnel.

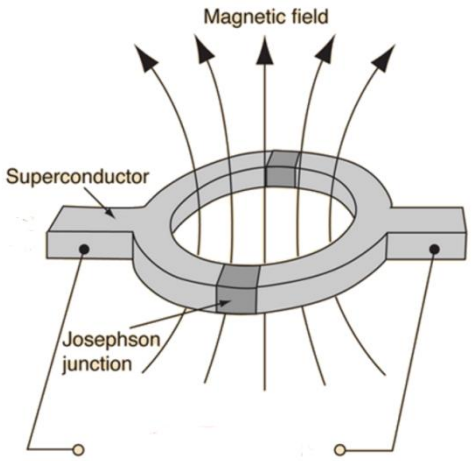

Figure 2.11. A schematic diagram of a SQUID.[17]

The sample (~0.1 g) was loaded into the larger end of a gelatin capsule, and then the smaller end upturned and inserted to hold the sample in place. The capsule was then mounted within a plastic straw, Figure 2.12, before being mounted within the SQUID magnetometer. These materials are selected as they give a minimal diamagnetic contribution to the overall magnetic signal.

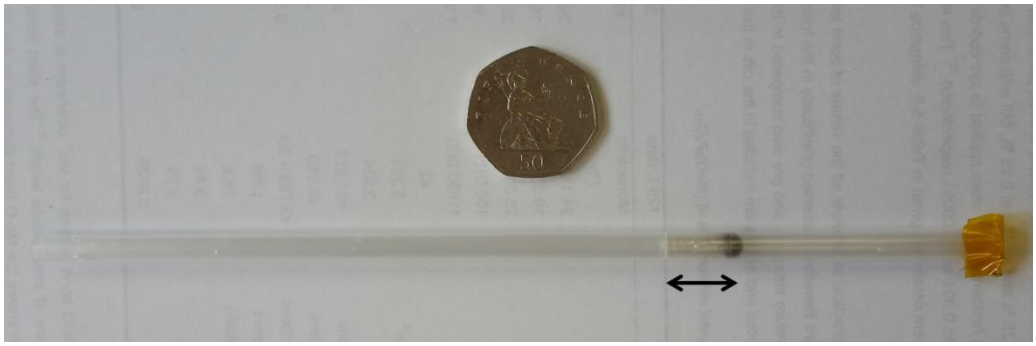

Figure 2.12. Sample setup for SQUID magnetometry, showing the black $Ce_2O_2ZnSe_2$ sample within the gelatin capsule (marked by a double headed arrow), within the straw.

The output data is recorded as "Long Moment" (emu), which can be converted to molar susceptibility (χ_{mol}), the sample magnetisation compared to the field, using Equation 2.21, where "Long Moment" (emu) and field (Oe) are recoded in the output data file and RMM is the relative molecular mass of the sample. For a material that shows Curie-Weiss behaviour, the Curie constant (C) is given by the reciprocal of the gradient for a linear plot of χ_{mol}^{-1} versus T. C can then be used in Equation 2.22 to calculate the moment, μ_{eff}.

$$\chi_{mol} = \frac{Long\ moment}{\left(\frac{mass}{RMM}\right) \times field}$$

Equation 2.21

$$\mu_{eff} = 2.828\sqrt{C}$$

Equation 2.22

2.11 Physical Property Measurement System (PPMS) – Resistivity Option

A Quantum Design PPMS with resistivity option was used to perform resistivity measurements between 300 and 5 K. The Resistivity option adds a configurable resistance bridge board to the PPMS controller. Powder samples (~0.4 g) across the $La_2O_2Cu_{2-2x}Cd_xSe_2$ solid solution were pressed into pellets using a 5 mm KBr die under 1 tonne of pressure. The resulting pellets were placed in evacuated quartz tubes at a pressure < $7x10^{-3}$ mbar, flame sealed, and sintered in a muffle furnace by ramping at 5 ˚C min^{-1} to 1100 ˚C and dwelling for 12 hours. The samples were then allowed to cool slowly to room temperature in the furnace (~8 hours) before the quartz tube was broken open. Sintered pellets were then cut into ~4 mm × ~2 mm × ~2 mm blocks and the surfaces abraded using emery paper, before being mounted onto Resistivity sample pucks, as shown in Figure 2.13. Four 0.2 mm Cu wires of purity 99.9% were first attached to the sample puck contacts using 60/40 tin/lead solder. Using silver conductive paint (supplied by Metalor) the outer I+ and I- wires were attached to the ends of the sample block ~4 mm apart, and the V+ and V- wires attached on top of the sample block ~2.5 mm apart. Up to three samples may be mounted on a single resistivity puck.

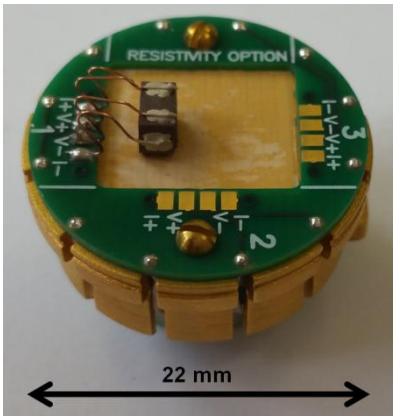

Figure 2.13. A mounted sample puck used for PPMS resistivity measurements.

In a four-probe resistance measurement, current is passed through a sample via two current leads, and two separate voltage leads measure the potential difference across the sample. The voltmeter has high impedance, so the voltage leads draw very little current (in theory, a perfect voltmeter draws no current). Therefore, by using the four-wire method, it is possible to accurately determine both the current and the voltage drop across the sample. This allows calculation of the resistance via Ohm's law, Equation 2.23, where I is the current (amperes), V is the voltage (volts), and R is the resistance (ohms).

$$I = \frac{V}{R}$$

Equation 2.23

2.12 Density Functional Theory (DFT) Calculations

DFT calculations were performed in Materials Studio 6.1 using the CASTEP (Cambridge Serial Total Energy Package) code.[18] CASTEP uses DFT with a plane wave basis set to

calculate the electronic properties of materials, including crystalline solids, from first principles. As well as being able to yield information such as electronic band structure and density of states (DOS) of a material, it can also be used for optimising the atomic geometry of a system. The calculations performed for this thesis all used the LDA (local density approximation) functional with a 6x6x1 k-point grid, 12 empty bands and 440 eV energy cutoff. The total density of states and partial DOS (PDOS) were calculated.

DFT calculations were initially performed on $La_2O_2Cu_2S_2$ to compare with DOS plots already published for this material, to check that the method being used is comparable. Two different methods were used. The first method took a Rietveld determined structural model from the literature,[19] performed a geometry optimisation with the unit cell size fixed, then performed a second geometry optimisation allowing the unit cell size to optimise (to help repeat these calculations on other structures, all the choices made are shown in Figure 2.14). After geometry optimisation, a DOS calculation was performed (all the choices made are shown in Figure 2.15. The DOS plot produced using this method is shown in Figure 2.16 (top) and was very similar to published data[20] ($La_2O_2Cu_2S_2$ DOS plot is given earlier in this chapter).

The second method simply did a straight energy band structure calculation using the Rietveld determined structural model from the literature.[19] The DOS plot produced using this method is shown in Figure 2.16 (bottom) and is almost identical to published data. As there is little difference between DOS plots with and without geometry optimisation, is was decided to optimise the geometry of all structures prior to DOS calculation for consistency across all structures. This method is used in Chapter 6 to calculate the DOS of $La_2O_2CuCd_{0.5}Se_2$, $La_2O_2Cu_2Se_2$ and $La_2O_2CdSe_2$.

It should be noted that the method used underestimates the band gap, though DFT calculations are renowned for this. Corrections are often made to calculate the bandgap correctly, however the purpose of these calculations was to determine the relative position of the partial bands, hence corrections were not applied. Plots should be compared to Figure 1.2.

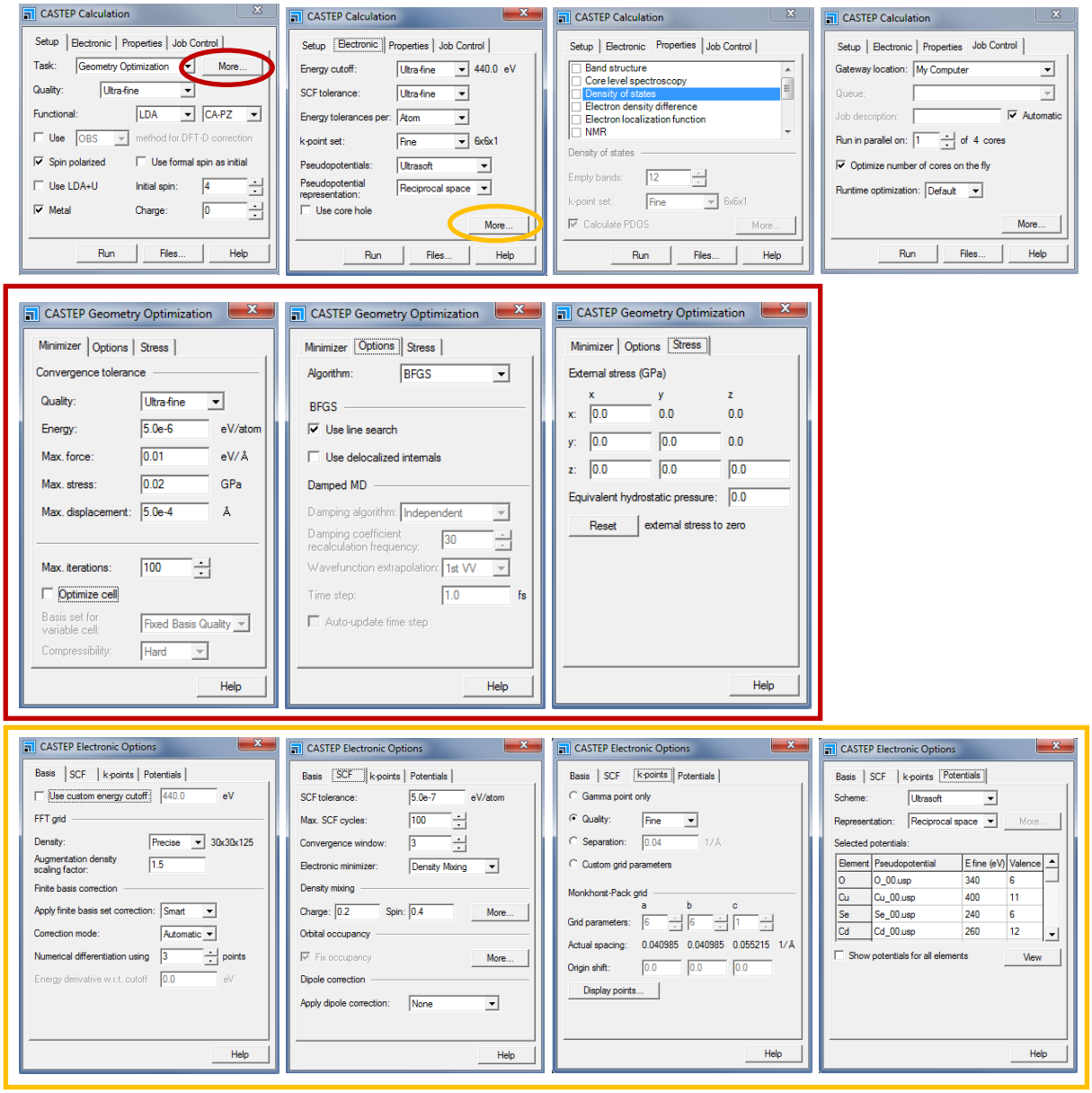

Figure 2.14. CASTEP choices for geometry optimisation calculations. The "optimise cell" box is initially unchecked for the first step of geometry optimisation, then checked for the second step.

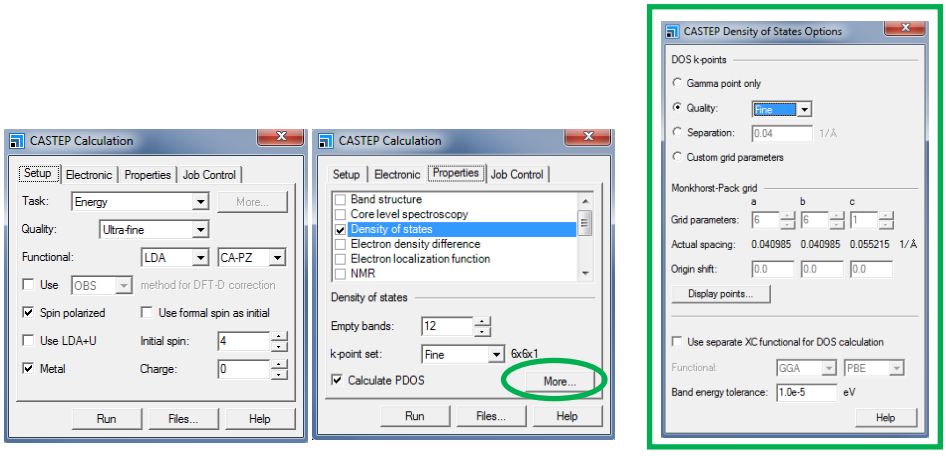

Figure 2.15. CASTEP choices for DOS calculations, performed after geometry optimisation. All other choices remain as above.

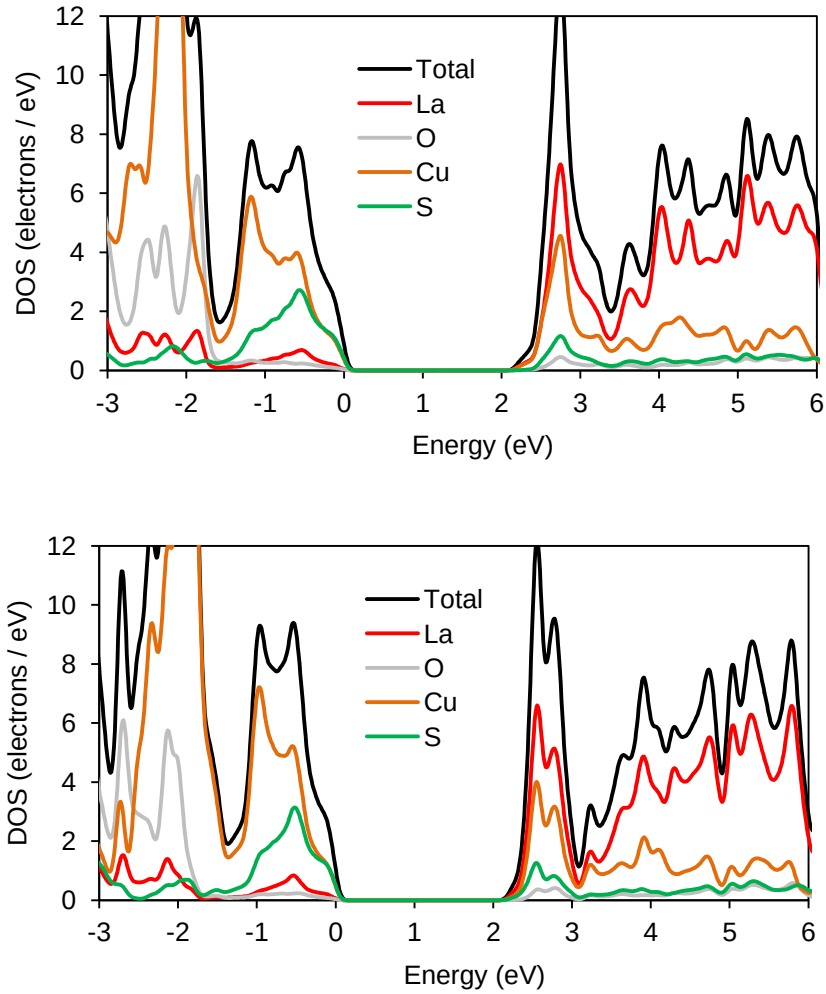

Figure 2.16. Total/partial DOS of $La_2O_2Cu_2S_2$ near the Fermi energy using a published structure determined by Rietveld refinement (top) and a geometry optimised structure (bottom).

2.13 References

(1) *Acta Crystallographica Section A.* **1992**, *48*, 922.
(2) Smaalen, S. V. *Incommensurate Crystallography*; Oxford University Press, 2007.
(3) Hahn, T. *International Tables for Crystallography*, 1993.
(4) Stokes, H. T.; Campbell, B. J.; van Smaalen, S. *Acta Crystallogr. A* **2011**, *67*, 45.
(5) Rietveld, H. M. *J. Appl. Crystallogr.* **1969**, *2*, 65.
(6) *Bruker AXS, Diffrac^{plus} Basic Evaluation Package: EVA 10.0, Karlsruhe*, 2004.
(7) Bruker-AXS *Diffrac.Suite v2.27: Software for Controlling Bruker Diffractometers*, 2011.
(8) Hannon, A. C. *Nuclear Instruments & Methods in Physics Research Section a-Accelerators Spectrometers Detectors and Associated Equipment* **2005**, *551*, 88.
(9) ISIS http://wwwisis2.isis.rl.ac.uk/disordered/gem/gem_home.htm, (accessed July 2016).
(10) Docsciences http://www.docsciences.fr/Galerie-Synchrotron.html, (accessed July 2016).
(11) Coelho, A. A. *J. Appl. Crystallogr.* **2003**, *36*, 86.
(12) Coelho, A. A. *TOPAS Academic: General Profile and Structure Analysis Software for Powder Diffraction Data*; 5th ed.; Bruker AXS: Karlsruhe, Germany, 2012.
(13) Coelho, A. A.; Evans, J. S. O.; Evans, I. R.; Kern, A.; Parsons, S. *Powder Diffr.* **2011**, *26*, S22.
(14) Pawley, G. S. *J. Appl. Cryst*., **1981**, *14*, 357-361.
(15) Kortum, G.; Braun, W.; Herzog, G. *Agnew. Chem., Int. Ed.* **1963**, *2 (7)*, 333.
(16) Tandon, S. P.; Gupta, J. P. *Phys. Status Solidi* **1970**, *38*, 363.
(17) Hyperphysics http://hyperphysics.phy-astr.gsu.edu/hbase/solids/imgsol/squide.gif, (accessed July 2016).
(18) Clark, S. J.; Segall, M. D.; Pickard, C. J.; Hasnip, P. J.; Probert, M. J.; Refson, K.; Payne, M. C. *Z. Kristallogr.* **2005**, *220*, 567.
(19) Hiramatsu, H.; Yanagi, H.; Kamiya, T.; Ueda, K.; Hirano, M.; Hosono, H. *Chem. Mater.* **2008**, *20*, 326.
(20) Ueda, K.; Hiramatsu, H.; Hirano, M.; Kamiya, T.; Hosono, H. *Thin Solid Films* **2006**, *496*, 8.

Chapter 3: Synthesis and Characterisation of a new ZrCuSiAs-related Material, $Ce_2O_2ZnSe_2$

3.1 Introduction

The work discussed in Chapter 3 is the area highlighted red on the thesis map, shown in Figure 3.1. The chapter presents the synthesis and characterisation of a previously unreported layered quaternary oxychalcogenide, $Ce_2O_2ZnSe_2$. Subtle changes to the synthetic method not only have an effect on phase purity, but also influence the structural and physical properties of the material. Reducing the amount of aluminium oxygen getter used during the reaction leads to an increase in oxidation of the Ce from +3 to +4. This leads to a decrease in the cell volume of the sample. At the highest, intermediate and lowest cell volumes the colour is yellow-ochre, brown and black respectively.

$Ce_2O_2ZnSe_2$ adopts a ZrCuSiAs-related structure with Zn^{2+} cations in a new ordered arrangement within the $[ZnSe_2]^{2-}$ layers, which is revealed by electron diffraction and distortion mode analysis. Diffuse reflectance spectroscopy (DRS) shows the material is a semiconductor at all cell volumes with experimental optical band gaps of 2.2, 1.4 and 1.3 eV for high, intermediate and low cell volume samples respectively. SQUID measurements show $Ce_2O_2ZnSe_2$ to be paramagnetic from 2–300 K with a negative Weiss temperature of θ = -10 K suggesting weak antiferromagnetic interactions.

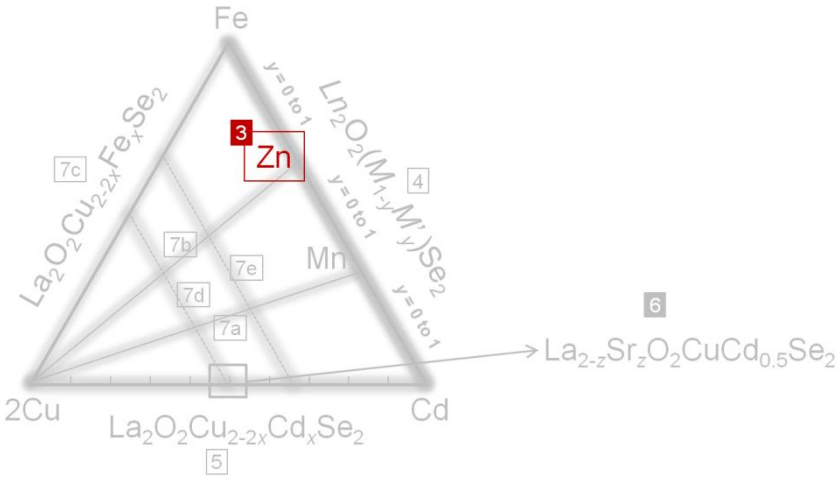

Figure 3.1. Thesis map highlighting the area of work discussed in Chapter 3.

3.2 Synthesis and Phase Purity

Samples of $Ce_2O_2ZnSe_2$ were initially synthesized from stoichiometric amounts of CeO_2, Zn, and Se. They were reacted for 12 hours in a sealed quartz tube with an aluminium oxygen getter (AOG) molar amount of 110% at 1100 ˚C, 1150 ˚C, 1175 ˚C, 1200 ˚C and 1225˚C. PXRD data showed a ZrCuSiAs-related phase had formed in varying amounts with a unit cell with a ≈ 4.01 Å, c ≈ 8.86 Å (the subcell), explaining the main peaks in the PXRD pattern, as shown in Figure 3.2, top, for the 1200 ˚C sample. Weak additional reflections are observed at low angles which could not be attributed to known impurity phases, Figure 3.2, bottom. It is shown in this chapter that these are due to a superstructure.

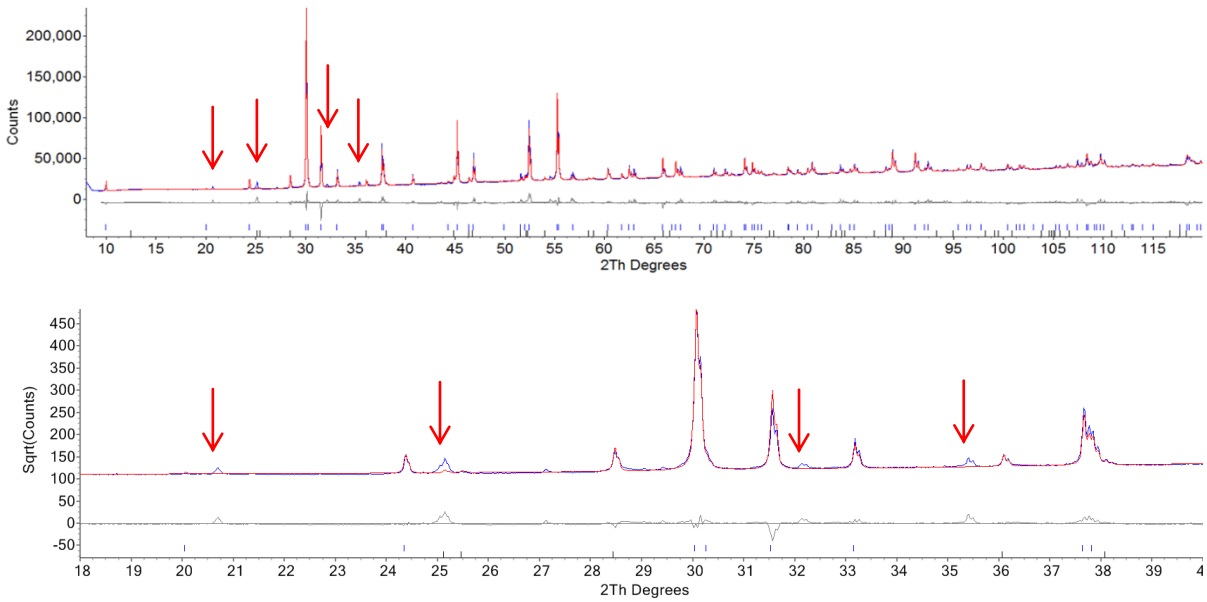

Figure 3.2. Top, Rietveld refinement profile using ZrCuSiAs structural model, space group P4/nmm, a ≈ 4.01 Å, c ≈ 8.86 Å, of PXRD data. Bottom, low angle region (on square root scale) showing superstructure reflections not predicted by this cell. Observed, calculated and difference profiles are shown in blue, red and grey respectively. Tick marks show positions of main phase (blue ~95% by weight) and Ce_2O_2Se (black ~5% by weight).

Figure 3.3a shows the phase purity of samples made at 1100 ˚C, 1150 ˚C, 1175 ˚C, 1200 ˚C and 1225˚C (phase purity was determined by Rietveld fitting of all phases, with the subcell used to estimate the amount of $Ce_2O_2ZnSe_2$ present). The highest phase purity was obtained at 1200 ˚C. The purest samples were yellow-ochre in color, whilst the least pure sample changed from red to black on standing in air. These samples contain a large Ce_2O_2Se impurity (~80% and ~50% in 1100 ˚C and 1150 ˚C samples respectively), which is reported to oxidise in ambient air to $Ce_2O_{2+x}Se$, changing colour from red to black while doing so.[1]

Attempts were made to increase the phase purity by varying the final dwell time, while maintaining the AOG molar amount at 110% and dwell temperature at 1200 ˚C, shown in Figure 3.3b. Above 3 h the dwell time makes little difference, producing samples of similar phase purity, all yellow-ochre in colour.

The effect of reducing the AOG molar ratio was also investigated at 1200 ˚C, Figure 3.3c. Phase purity is consistent (~97 wt%) between 110% and 100% AOG, and then drops at 95% and 90%. One important aspect of this experiment is the generation of different minor impurity phases with varying AOG, as emphasized in Figure 3.3d. At 110% and 105% AOG, Ce_2O_2Se is the only impurity produced and contains Ce in the 3+ oxidation state. Below 105% AOG the Ce_2O_2Se amount decreases and is replaced by $Ce_4O_4Se_3$ and CeO_2, where Ce is in a +3/+4 and +4 oxidation state respectively, and ZnSe. The increase in the oxidation state of Ce in these impurities is likely to be due to the increase in oxygen available when the AOG falls below the stoichiometric ratio.

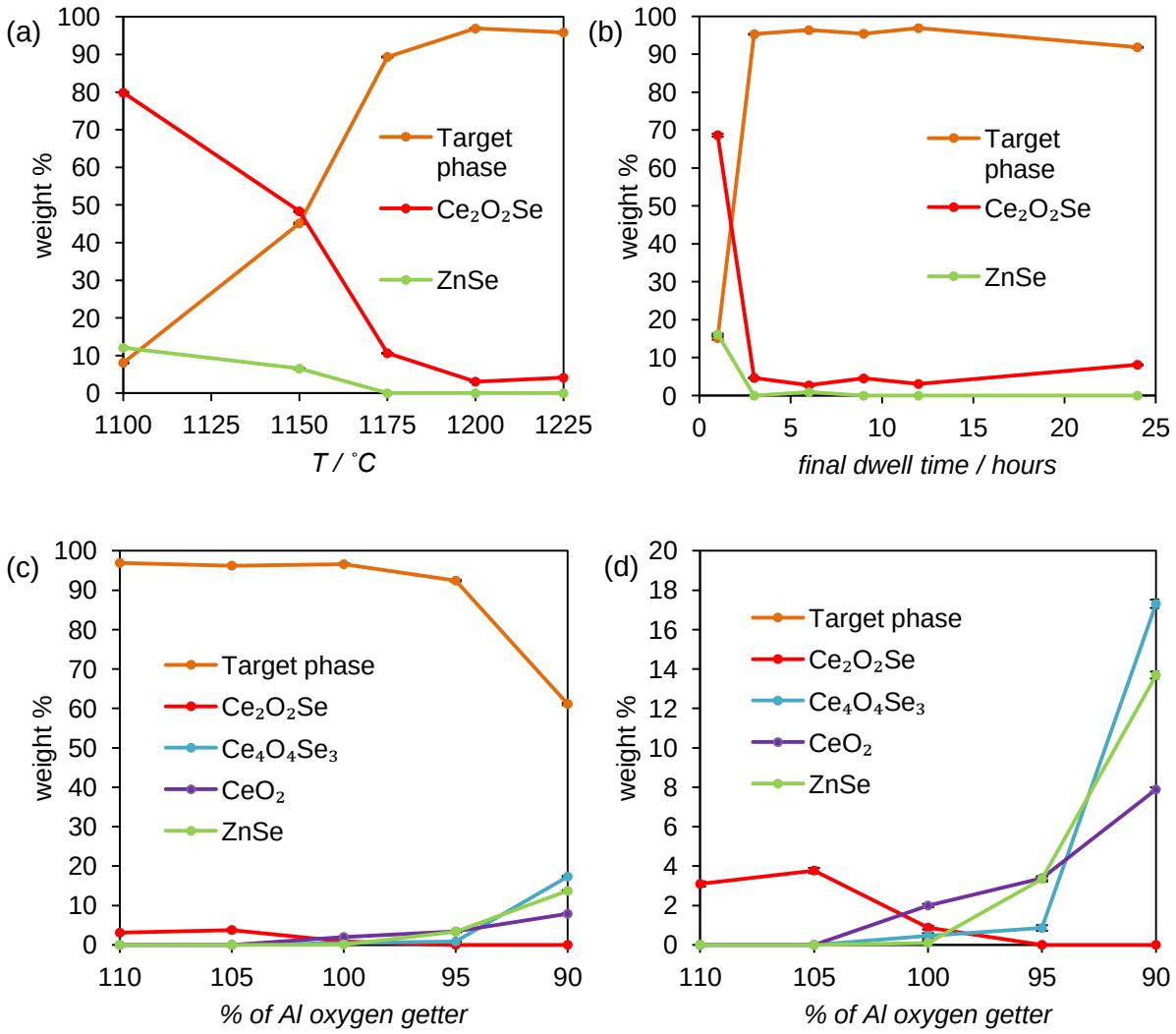

Figure 3.3. (a) Effect of temperature on the weight % of $Ce_2O_2ZnSe_2$ formed, with the time and AOG molar amount fixed at 12 h and 110% respectively. (b) Effect of dwell time on the $Ce_2O_2ZnSe_2$ weight fraction (1200 ˚C and 110% AOG). (c) Effect of AOG molar ratio on $Ce_2O_2ZnSe_2$ weight % (1200 ˚C, 12 h). (d) y-scale from 0-20% to show impurity phase weight fractions more clearly. Rietveld error bars are hidden by data points. More realistic error bars are around ±2%.

During the synthesis a small amount of an orange crystalline material (Figure 3.4), estimated at ~<0.005 g, 0.8% of the starting reagent mass, was typically observed on the quartz tube; PXRD revealed it to be ZnSe. This explains why the expected ZnSe impurity is often not present in the PXRD pattern when a small Ce_2O_2Se impurity is present.

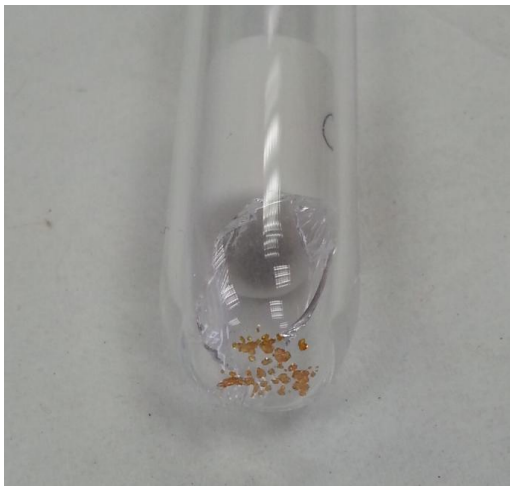

Figure 3.4. Bottom of a quartz tube after reaction, showing the build-up of ZnSe. This is representative of all $Ce_2O_2ZnSe_2$ samples synthesized.

3.3 Effects of Synthetic Conditions on Structural and Physical Properties

Figure 3.5a shows the effect of final dwell temperature on cell volume. All samples have a similar cell volume, and the same yellow-ochre colour (disregarding samples made at 1100 ˚C and 1150 ˚C where the phase purity is low). Figure 3.5b shows the effect of final dwell time on cell volume. As before, all samples have a similar cell volume and the same yellow-ochre colour (disregarding the 1 h sample). Figure 3.5c shows the effect of the AOG quantity. This has a large effect on cell volume, and the change is accompanied by a gradual change in colour, with samples being yellow-ochre, brown and black at high-, intermediate- and low-cell volume respectively, as shown in Figure 3.6. At 90% AOG the cell volume has increased relative to the 95% AOG sample, which is against the trend. Figure 3.5c suggests that at this low AOG ratio, the production of more oxidized impurity phases is favoured over changes in the target phase. The sample made for PND measurements (see below) was black and had a cell volume of 2848.7(6) $Å^3$. This is comparable to the lowest cell volume sample prepared with 95% AOG, as indicated by the red arrow in Figure 3.5c.

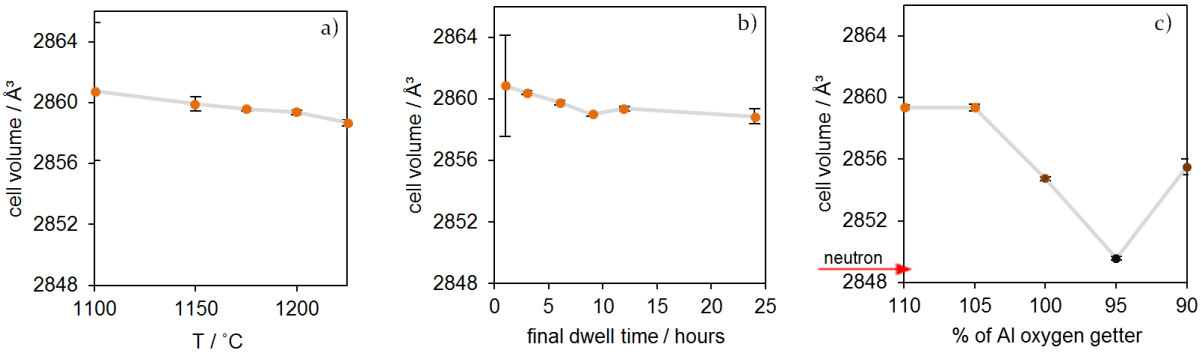

Figure 3.5. (a) Effect of synthesis temperature on cell volume (12 hours and 110% AOG). (b) Effect of dwell time on cell volume (1200 ˚C and 110% AOG). (c) Effect of AOG ratio on cell volume (12 hours, 1200 ˚C). The red arrow indicates the cell volume of the sample prepared for NPD experiments. The colour of data symbols represents sample colour. Cell volumes are refined from PXRD data using a ~28.4 Å × 5.7 Å × 17.7 Å unit cell in space group Imcb, which is later shown to be the correct space group.

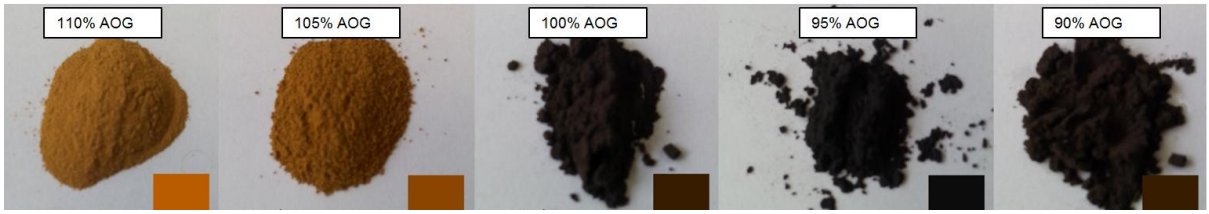

Figure 3.6. Powder samples synthesized with a range of AOG ratios at 1200 ˚C for 12 hours. Samples are yellow-ochre, brown and black at relative high, intermediate and low cell volume respectively.

The most likely cause of the contraction in cell volume is the partial oxidation of Ce from +3 to +4. This effect has been seen in the related compound $CeOCu_{1-x}S$, which has been studied by several different groups.[2-4] Charge compensation for Ce^{4+} formation in this system is achieved via loss of Cu^{1+}, with reported samples ranging from near stoichiometric CeOCuS (dark olive green) to $CeOCu_{0.762}Se$ (jet black), with a reduction in cell volume of around 5%. If $Ce_2O_2ZnSe_2$ charge compensates via loss of Zn^{2+}, the Zn loss is expected to be significantly lower. Firstly, the reduction in cell volume is only around 0.4% in $Ce_2O_2ZnSe_2$ between the highest and lowest cell volumes synthesized. Secondly, the loss of only one Zn^{2+} ion is required to compensate for the oxidation of two Ce atoms. We can speculate that as the cell volume reduction in $Ce_2O_2ZnSe_2$ is less than 10% that observed in $CeOCu_{0.762}Se$, and as Zn^{2+} loss can compensate for the oxidation of two Ce atoms, the lowest cell volume sample would have a Zn content of >0.98.

Further support that this contraction is caused by partial oxidation of Ce comes from work on solid solutions of various $Ln_2O_2MSe_2$-type phases (see Chapter 4). We find that changing the lanthanide leads to an approximately isotropic change in all lattice parameters, whereas substitution of *M* leads to a change mainly in the c direction, perpendicular to the layers. This is attributed to a relatively rigid *Ln*-O layer and a more flexible *M*-Se layer which adapts to the size demands of the *Ln*-O layer. Figure 3.7 shows the relative changes in cell parameters as a function of AOG quantity, when refined in the correct orthorhombic cell, space group *Imcb* with unit cell dimensions of ~28.4 Å × ~5.7 Å × ~17.7 Å. The change of all cell parameters by roughly equal amounts as AOG quantity is reduced suggests a contraction occurs in the *Ln*-O layer, as expected for partial oxidation of the Ce, and that this dominates over Zn^{2+} loss in the more flexible *M*-Se layer.

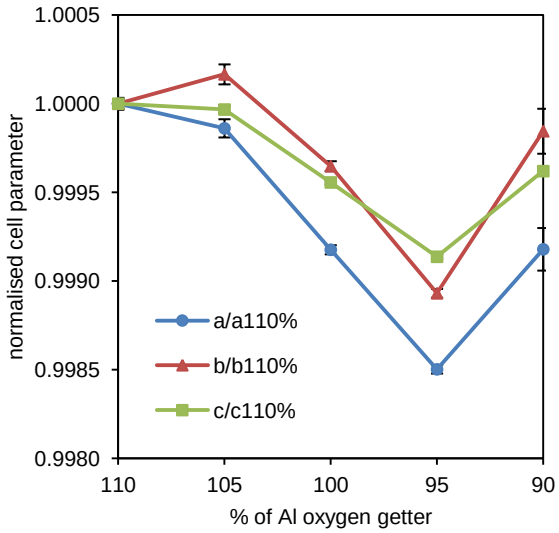

Figure 3.7. Effect of AOG molar quantity on cell parameters, normalised against the 110% AOG sample.

3.4 Superstructure Investigation by Electron Diffraction

Selected area electron diffraction (SAED) images were collected on the black, low cell volume NPD sample, Figure 3.8, and confirm the presence of the superstructure reflections suggested from the PXRD patterns. Intense reflections consistent with the parent *P4/nmm* parent structure are labelled in white in Figure 3.8b; weak superstructure reflections are observed along $[1\bar{1}0]$ and indexed in green. These are not present along $[110]$, suggesting the tetragonal symmetry has been lost. Figure 3.8*c* shows $[110]$ zone axis data. It reveals no superstructure reflections along $[001]$ or $[110]$, only reflections consistent with the parent structure are observed.

SAED images of $La_2O_2ZnSe_2$[5] revealed similar superstructure reflections, also exclusively along $[1\bar{1}0]$, though at $\frac{1}{4}\frac{\bar{1}}{4}0$, $\frac{1}{2}\frac{\bar{1}}{2}0$, and $\frac{3}{4}\frac{\bar{3}}{4}0$. These additional reflections were indexed as 200, 400, *h*00 (*h* = 2*n*) in a $4\sqrt{2}a_{\text{subcell}} \times \sqrt{2}a_{\text{subcell}} \times 2c_{\text{subcell}}$ unit cell. It therefore seemed likely that the $Ce_2O_2ZnSe_2$ structure may be related to the *P4/nmm* parent by a $5\sqrt{2}a_{\text{subcell}} \times \sqrt{2}a_{\text{subcell}} \times 2c_{\text{subcell}}$ unit cell. To confirm this supercell, Pawley refinements were attempted in the orthorhombic space group *P222* with unit cell dimensions ~28.35 Å × ~5.67 Å × ~17.71 Å. This unit cell successfully accounts for all observed reflections in the powder data of the black, low cell volume NPD sample, Figure 3.9.

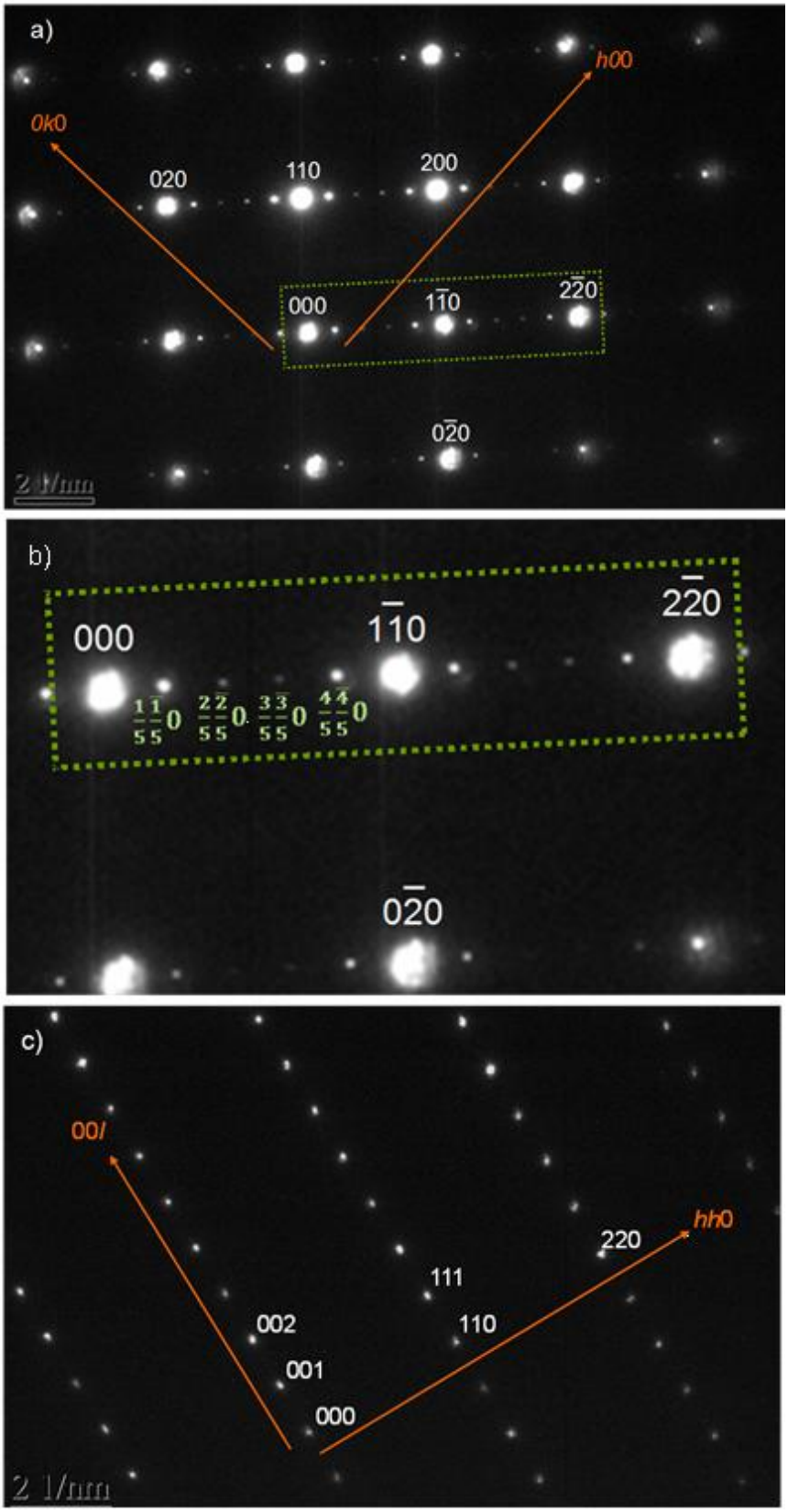

Figure 3.8. Selected area electron diffraction of $Ce_2O_2ZnSe_2$ taken down the (a) [001] zone axis, (b) enlarged [001] zone axis showing superstructure reflections, (c) [110] zone axis. Zone axes and hkl indices are given relative to the parent P4/nmm tetragonal cell. Reflections consistent with the parent structure are labelled white, superstructure reflections are labelled green.

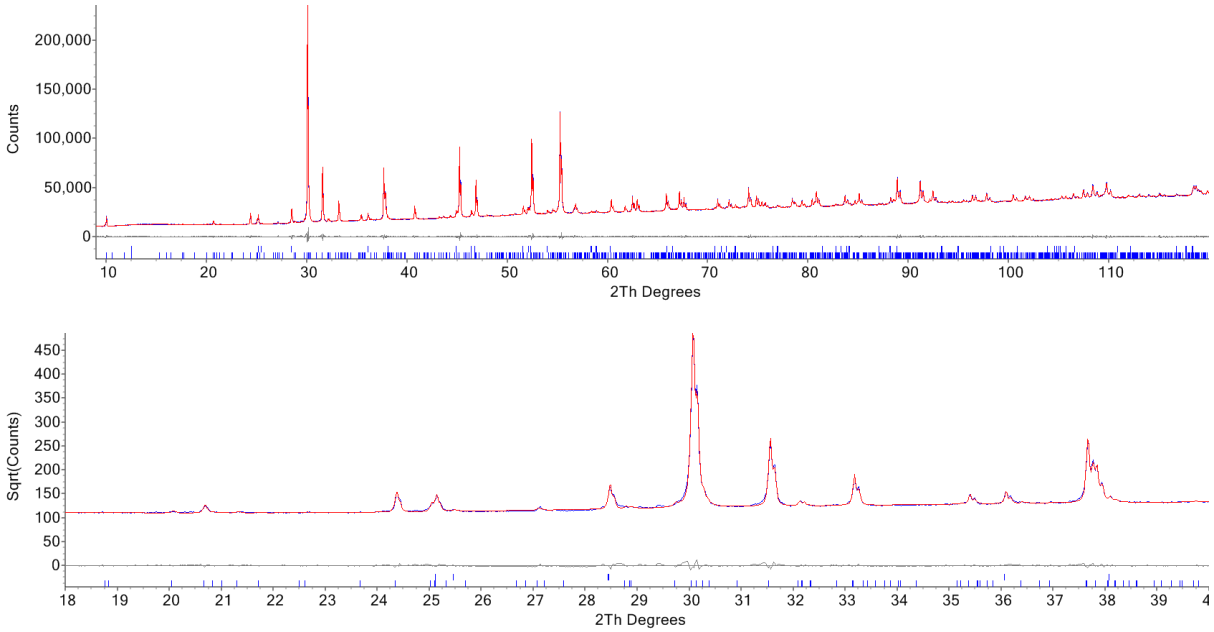

Figure 3.9. Top, Pawley refinement profile in the orthorhombic space group P222 with unit cell dimensions ~28.35 Å × ~5.67 Å × ~17.71 Å. Bottom, low angle region (on square root scale) emphasising superstructure reflections. Tick marks show positions of main phase (blue ~95% by weight) and Ce_2O_2Se (black ~5% by weight).

3.5 Development of the Crystal Structure Model

The crystal structure of $Ce_2O_2ZnSe_2$ was solved with the help of the web-based ISODISTORT software.[6] ISODISTORT calculates symmetry adapted distortion modes (displacive, site ordering, magnetic) associated with irreducible representations at different **k**-points. A low symmetry structure can then be described in terms of the parent structure and the amplitudes of the different ordering and displacive symmetry modes. This allows systematic and rapid exploration of different child structures from a given parent.

Compared to the parent, electron diffraction shows supercell diffraction peaks at (1/5 1/5 *g*). Figure 3.8b and Pawley refinement confirms that they can be explained with a $5\sqrt{2}a_{\text{subcell}} \times \sqrt{2}a_{\text{subcell}} \times 2c_{\text{subcell}}$ cell. The distortion vector of $Ce_2O_2ZnSe_2$ relative to the parent structure is therefore ***S***(*α α* 1/2) with *α* = 1/5 or 1/10 (due to systematic absences) and the representative basis is (supercell):

$$\begin{bmatrix} 5 & 5 & 0 \\ -1 & 1 & 0 \\ 0 & 0 & 2 \end{bmatrix} \begin{bmatrix} a_{subcell} \\ b_{subcell} \\ c_{subcell} \end{bmatrix} = \begin{bmatrix} a_{supercell} \\ b_{supercell} \\ c_{supercell} \end{bmatrix}$$

There are 16 possible daughter models within 6 space groups: *Cmma* (S1 or S3), *Cmca* (S1, S2, S3 or S4), *Ccca* (S2 or S4) when *α* = 1/5 and *Imma* (S1 or S3), *Ibam* (S1, S2, S3 or S4), *Ibca* (S2 or S4) when *α* = 1/10. Refinements were performed (on the PXRD data of the black, low cell volume NPD sample) for each of these 16 daughter models in which the amplitudes of S ordering and displacive modes were refined. The R_{wp} obtained for each possible model is shown in Figure 3.10.

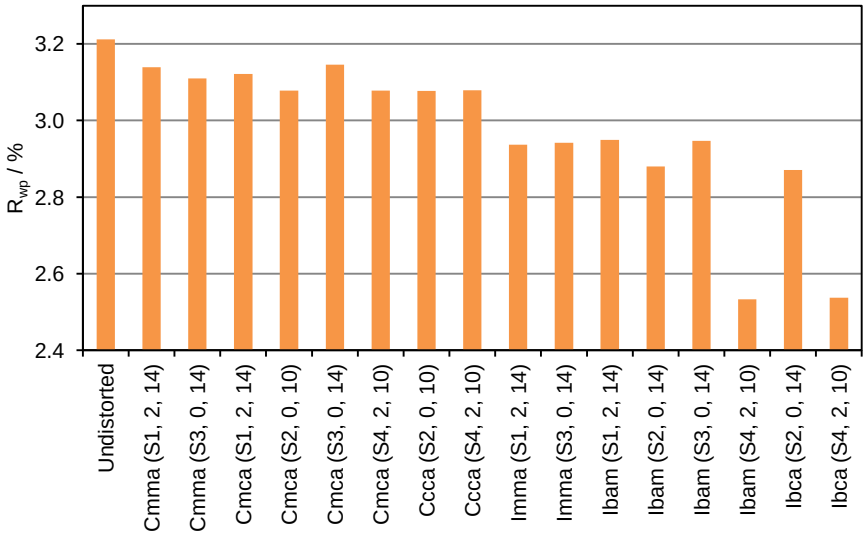

Figure 3.10. R_{wp} for the $Ce_2O_2ZnSe_2$ PXRD pattern using different distorted models. The values in brackets give the specific S distortion mode label and the number of refined primary ordering and displacive modes.

There are two distorted models based on S4 distortions, *Ibam* (72) and *Ibca* (73), which give significantly better agreement with the experimental data than others, both with R_{wp} = 2.53%. The ordering patterns of the Zn-Se layer in these two space groups are in Figure 3.11. Appendix 1 shows all allowed distortion modes for the *Ibam* (S4) and *Ibca* (S4) models respectively. In an *Ibam* (S4) model, Zn^{2+} sites can be either fully occupied or fully vacant while in the *Ibca* (S4) model, there is one Wyckoff site 50% occupied by Zn^{2+} (shown as a half sphere in Figure 3.11b).

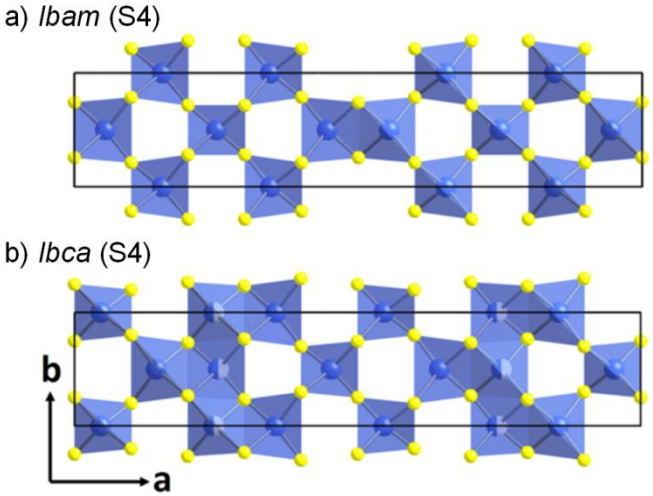

Figure 3.11. Zn ordering patterns in the Zn-Se layer of $Ce_2O_2ZnSe_2$ for (a) Ibam and (b) Ibca models from ISODISTORT refinement. Zn^{2+} cations are shown in blue and Se^{2-} anions are shown in yellow. The 50% occupied site is shown as a half sphere.

These two models are mathematically different though experimentally difficult to distinguish, even from "Rietveld quality" (14 h 8-120˚ 2θ) laboratory powder diffraction data. Simulations show that the largest difference in the X-ray data between the two models should be the weak 110 reflection at ~16.4˚ 2θ, with an intensity of ~0.25% of the most intense peak; this peak is systematically absent in the *Ibca* model (Figure 3.12).

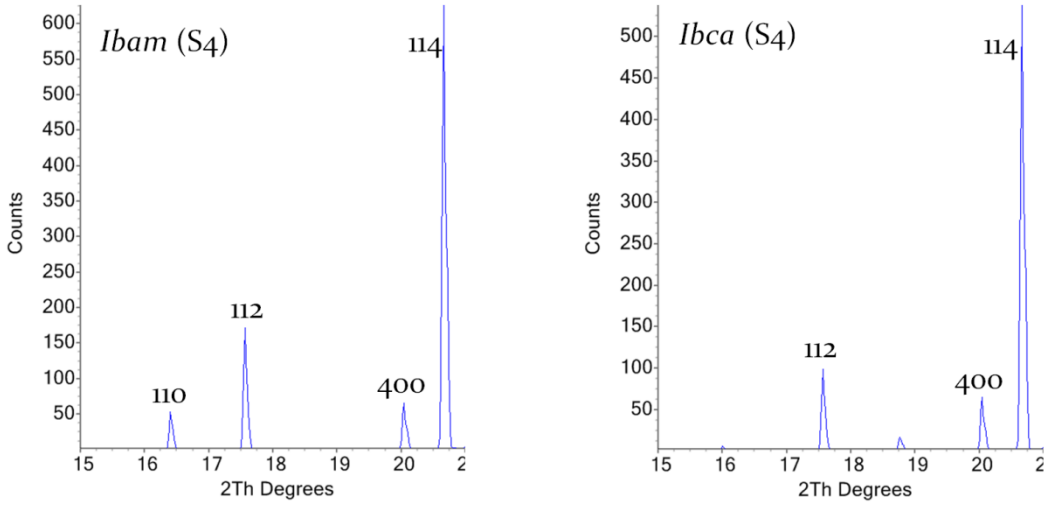

Figure 3.12. Simulated PXRD patterns over 2θ range 15–21˚ for the Ibam (S4) and Ibca (S4) distorted models.

A 54 hr scan over a 2θ range of 15–21˚ was therefore collected; this reveals weak intensity for the 110 reflection (Figure 3.13). A good fit to these limited data was achieved using the Rietveld-derived model discussed below. We therefore selected the ordered *Ibam* (S4) model for final Rietveld refinement.

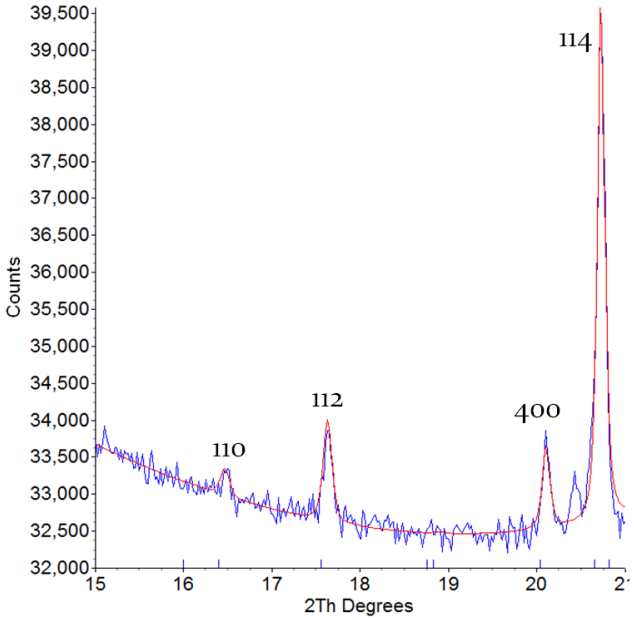

Figure 3.13. Rietveld refinement profile of $Ce_2O_2ZnSe_2$ PXRD data (54 hr scan over 2θ range 15–21˚) fitted using the ordered Ibam model. Data are consistent with an ~0.25% intensity 110 reflection. The weak peak at ~20.5˚ is due to a ~< 0.3% impurity.

3.6 Structure Refinement and Description

Final Rietveld refinements were performed on the fully cation-ordered model in space group *Imcb* (non-standard setting of *Ibam* with the *c*-axis perpendicular to the layers for consistency with other structures of this type reported in the literature), against laboratory X-ray and neutron powder data (collected on Gem at ISIS) of the black, low cell volume PND sample; a total of 209 parameters were refined. Refinement of a single O, Zn and Se site occupancy gave a sample composition of $Ce_2O_2ZnSe_2$ within 3 standard uncertainties, hence no indication of partial occupancy of Zn as charge compensation for partial Ce^{4+} formation can be detected. All sites were therefore considered fully occupied within the quality of the data. Refining separate temperature factors for each site did not significantly reduce the R_{wp}, so a single temperature factor was refined for each atom type. Structural parameters are shown in Table 3.1. Rietveld refinement profiles are shown in Figure 3.14. Selected bond lengths and angles are shown in Table 3.2 and Table 3.3 respectively. Figure 3.15 illustrates the structure of $Ce_2O_2ZnSe_2$.

Site label	Wyckoff site	x	y	z	B / Å^2
Ce(1)	16k	0.1992(3)	0.741(1)	0.3191(4)	0.47(2)
Ce(2)	16k	0.3998(3)	0.770(1)	0.3188(4)	0.47(2)
Ce(3)	8j	0	0.777(1)	0.8200(6)	0.47(2)
O(1)	8g	0.75	0	0.2560(4)	0.63(3)
O(2)	16k	0.8504(3)	0.486(3)	0.2499(2)	0.63(3)
O(3)	16k	-0.0501(4)	-0.025(2)	0.2517(3)	0.63(3)
Zn(1)	8i	0.0551(3)	0.5	0	1.19(3)
Zn(2)	8h	0.1515(4)	0	0	1.19(3)
Zn(3)	4b	0.75	0	0.5	1.19(3)
Se(1)	16k	0.7002(4)	0.254(1)	0.0831(3)	0.87(2)
Se(2)	16k	0.8991(3)	0.2305(8)	0.0878(2)	0.87(2)
Se(3)	8j	0	0.725(1)	0.0845(5)	0.87(2)

Table 3.1. Structural parameters of $Ce_2O_2ZnSe_2$ from combined refinement using room temperature PXRD and NPD data. Space group Imcb, a = 28.3595(4) Å, b = 5.67087(8) Å, c = 17.71308(6) Å; Rwp = 1.848%, Rp = 1.081 % and χ^2 = 1.193. Occupancy for all sites is 1.

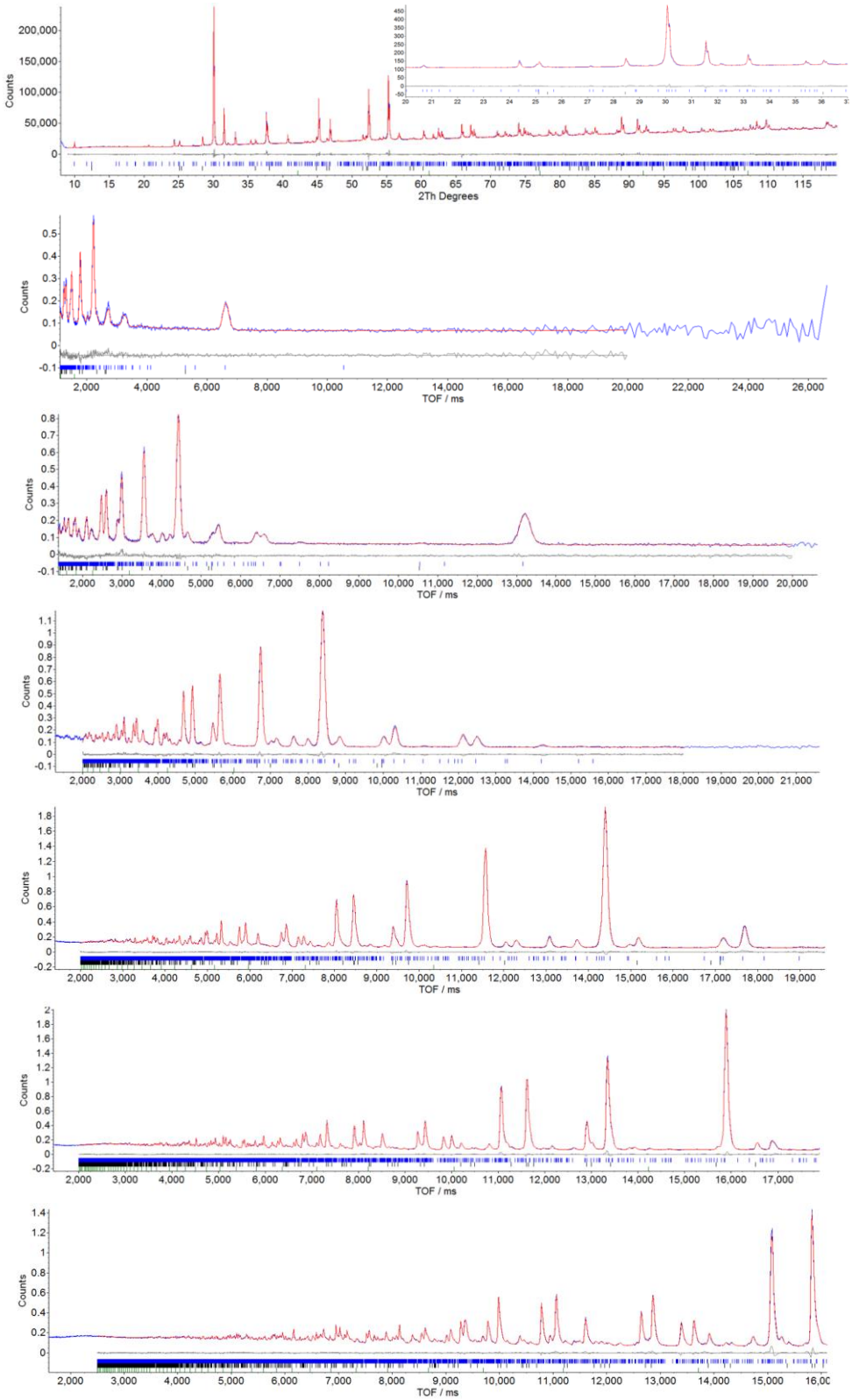

Figure 3.14. Rietveld refinement profiles from combined refinement of room temperature a) XRPD data (inset, low angle region on square root scale emphasising superstructure reflections) and b) 9˚ bank, c) 18˚ bank, d) 35˚ bank, e) 64˚ bank, f) 91˚ bank, g) 154˚ bank NPD data, for $Ce_2O_2ZnSe_2$, in space group Imcb. Tick marks show reflection positions for $Ce_2O_2ZnSe_2$ (blue), Ce_2O_2Se (black ~5% by weight) and vanadium (green, from sample can used in NPD data collection).

O(1) – Ce(1)	2 × 2.343(8) Å 2 × 2.389(9) Å	Zn(1) – Se(2)	2 × 2.539(7) Å
O(2) – Ce(1)	2.33(1) Å 2.36(1) Å	Zn(1) – Se(3)	2 × 2.512(8) Å
O(2) – Ce(2)	2.32(1) Å 2.36(1) Å	Zn(2) – Se(1)	2 × 2.48(1) Å
O(3) – Ce(2)	2.35(1) Å 2.35(1) Å	Zn(2) – Se(2)	2 × 2.487(9) Å
O(3) – Ce(3)	2.35(1) Å 2.37(1) Å	Zn(3) – Se(1)	4 × 2.470(7) Å

Table 3.2. Selected bond lengths in $Ce_2O_2ZnSe_2$.

Ce(1) – O(1) – Ce(1)	2 × 106.1(2)° 2 × 104.7(4)° 123.1(5)° 112.3(4)°	Se(1) – Zn(3) – Se(1)	2 × 111.3(3)° 2 × 110.3(4)° 2 × 106.8(3)°
Ce(1) – O(2) – Ce(1)	106.2(5)°	Se(1) – Zn(2) – Se(1)	112.3(6)°
Ce(1) – O(2) – Ce(2)	2 × 105.2(6)° 116.6(3)° 117.6(3)°	Se(1) – Zn(2) – Se(2)	2 × 112.8(2)° 2 × 104.8(2)°
Ce(2) – O(2) – Ce(2)	106.3(5)°	Se(2) – Zn(2) – Se(2)	109.6(5)°
Ce(2) – O(3) – Ce(2)	105.5(6)°	Se(2) – Zn(1) – Se(2)	118.4(5)°
Ce(2) – O(3) – Ce(3)	106.3(4)° 105.5(5)°	Se(2) – Zn(1) – Se(3)	2 × 112.2(2)° 2 × 105.0(2)°
Ce(3) – O(3) – Ce(3)	106.0(5)°	Se(3) – Zn(1) – Se(3)	103.1(4)°

Table 3.3. Selected bond angles in $Ce_2O_2ZnSe_2$.

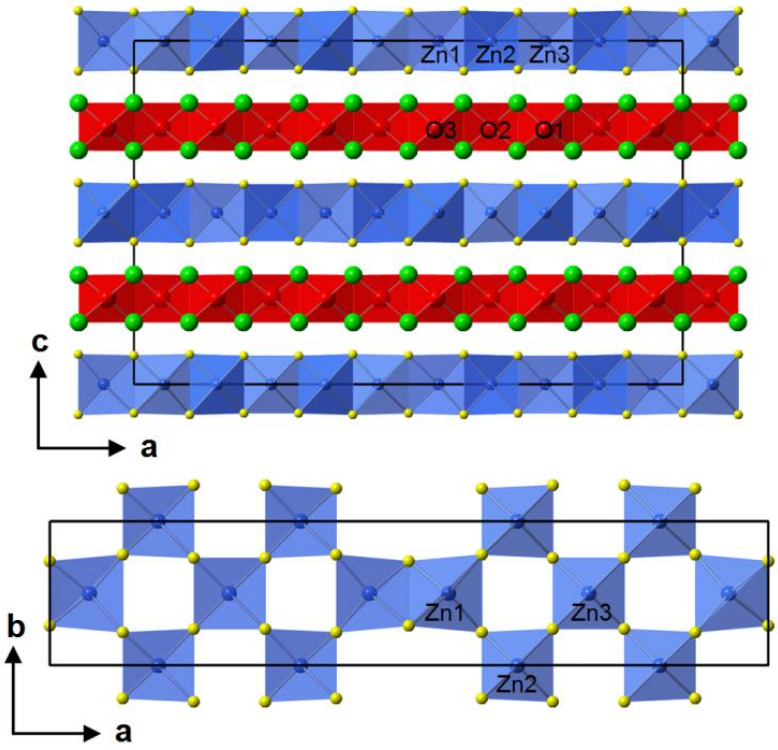

Figure 3.15. (Top) $Ce_2O_2ZnSe_2$ structure with sheets of edge-sharing Ce_4O (red) and $ZnSe_4$ tetrahedra (blue), viewed down [010]. (Bottom) view down [001] showing a mix of stripe-like edge-sharing $ZnSe_4$ tetrahedra and checkerboard-like corner-sharing $ZnSe_4$ tetrahedra (4C-1E), with an extended checkerboard-like section relative to $La_2O_2ZnSe_2$.

$Ce_2O_2ZnSe_2$ contains fluorite-like $[Ce_2O_2]^{2+}$ layers of Ce_4O tetrahedra, alternating with anti-fluorite-like $[ZnSe_2]^{2-}$ layers, perpendicular to the *c*-axis of the material. It is closely related to the *Ln*OCuCh-type structure, except the divalent nature of Zn^{2+} leads to half occupancy of the tetrahedral sites within the transition metal selenide layers.

The transition metal ordering pattern adopted in $Ce_2O_2ZnSe_2$ is novel, yet closely related to other divalent transition metal containing compounds. It contains both edge-sharing and corner-sharing $ZnSe_4$ tetrahedra, leading to alternating "checkerboard-like" and "stripe-like" regions along the *a*-axis. This is similar to the $La_2O_2ZnSe_2$ structure,[5] except $Ce_2O_2ZnSe_2$ has an extended checkerboard section. Using a simple nomenclature (Chapter 1.3.5) we can describe the Ce material as 4C-1E and La as 3C-1E. Both $Ce_2O_2ZnSe_2$ and $La_2O_2ZnSe_2$ can therefore be considered as intermediate structures between $Ce_2O_2FeSe_2$,[7] where all cations order in stripes of edge-sharing tetrahedra (0C-1E), and $La_2O_2CdSe_2$,[8] where all cations order in a checkerboard arrangement (1C-0E) of corner-sharing tetrahedra.

While Zn ordering is the main driver for the symmetry lowering, there are significant accompanying structural distortions, mainly in the Zn–Se tetrahedra shown in Figure 3.16 and Figure 3.17. These are most pronounced in the edge-shared $Zn1Se_4$ tetrahedra and reduce on moving from $Zn2Se_4$ tetrahedra to $Zn3Se_4$ in the centre of the corner-sharing block. As expected, the Zn–Zn separation in the edge-shared tetrahedra is significantly longer than an idealized structure [3.13(3) vs ~2.84 Å]. Similar distortions are observed in the Zn–Se tetrahedra of $La_2O_2ZnSe_2$, where the edge-shared Zn–Zn separation is even greater (3.22 Å).[5] The distortions in the OCe_4 tetrahedra are less pronounced, though still important. This is most evident in the $O1Ce_4$ tetrahedra, which lies below the centre of the corner-sharing block where $ZnSe_4$ tetrahedra are least distorted. This is highlighted in Table 3.4 which shows the standard deviation of bond angles around Zn and O sites. The distortion-mode analysis (described previously in this Chapter) shows that the 4 most significant structural distortions are S4 modes on Zn ([100] direction), Se, Ce and O (all [010] direction), shown in Figure 3.18. A table of all allowed distortion modes is given in Appendix 1)

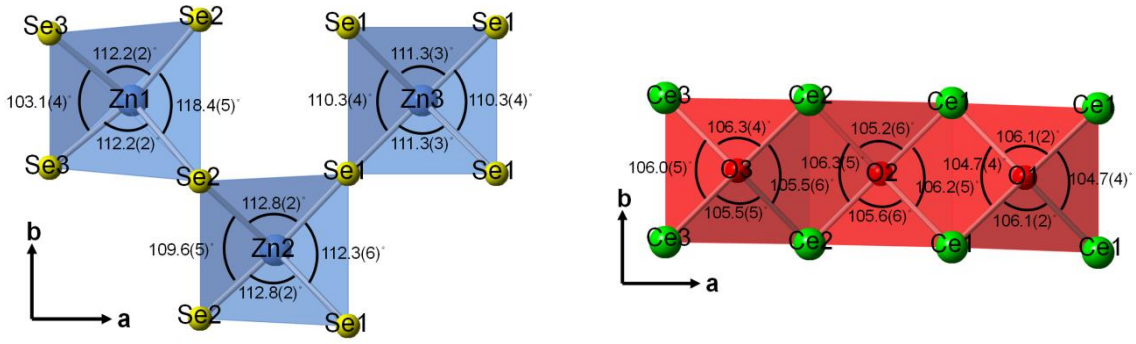

Figure 3.16. Coordination environments of Zn and O sites viewed down [001].

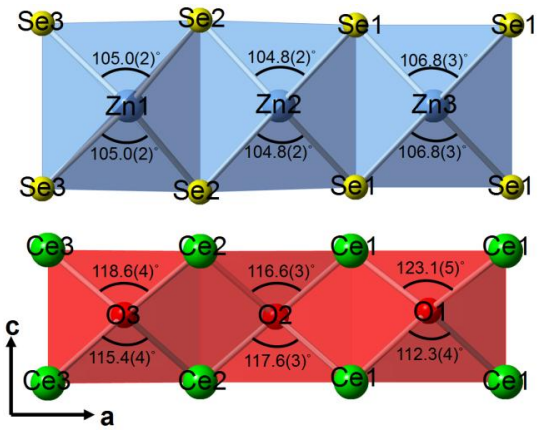

Figure 3.17. Coordination environments of Zn and O sites viewed down [010].

Zn1	Zn2	Zn3
5.9°	3.8°	2.1°

O3	O2	O1
5.9°	5.8°	7.2°

Table 3.4. Standard deviation of bond angles around Zn and O sites.

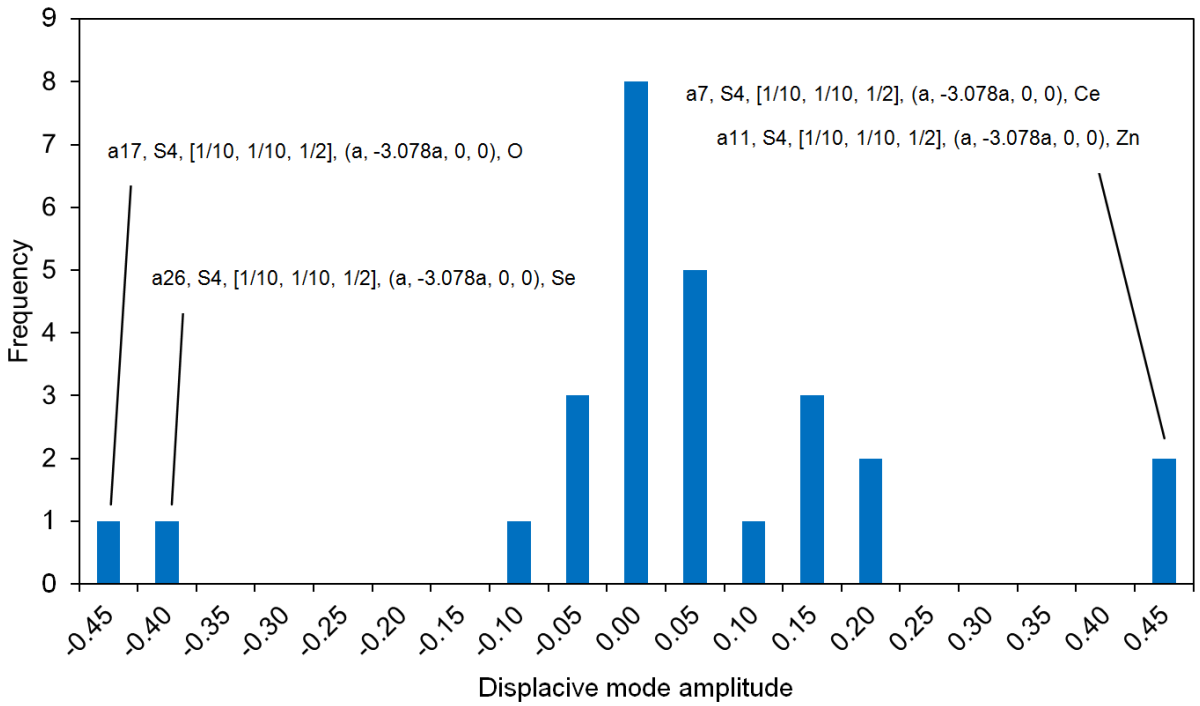

Figure 3.18. Histogram of amplitudes of the 27 possible displacive modes of $Ce_2O_2ZnSe_2$ relative to the P4/nmm parent. "Amplitude" is the root-summed-squared displacement of daughter atoms. The four large amplitude modes are all S4.

3.7 Cell Volume Dependence of the Zinc Ordering and Incommensurate Structures

The model presented above describes most of the $Ce_2O_2ZnSe_2$ samples synthesised; however it describes those with lower cell volume better than those with higher cell volume. Figure 3.19a shows the PXRD patterns of the sample synthesised with a 3 h final dwell at 1200 ˚C and 110% AOG molar amount. This is the highest cell volume sample synthesized with sufficient phase purity (>95%) to clearly observe superstructure reflections. The structural model does not accurately describe the superstructure reflections.

Figure 3.19b-d show the PXRD patterns of the samples synthesized with 105%, 100% and 95% AOG respectively (all at 1200˚C for 12 hours), which represent samples with systematically decreasing cell volume (Figure 3.5c). The structural model provides a progressively better fit to superstructure reflections as the cell volume decreases. Figure 3.19e shows the PXRD patterns of the sample synthesised for NPD experiments, which has the lowest cell volume and gives an excellent fit to the structural model presented.

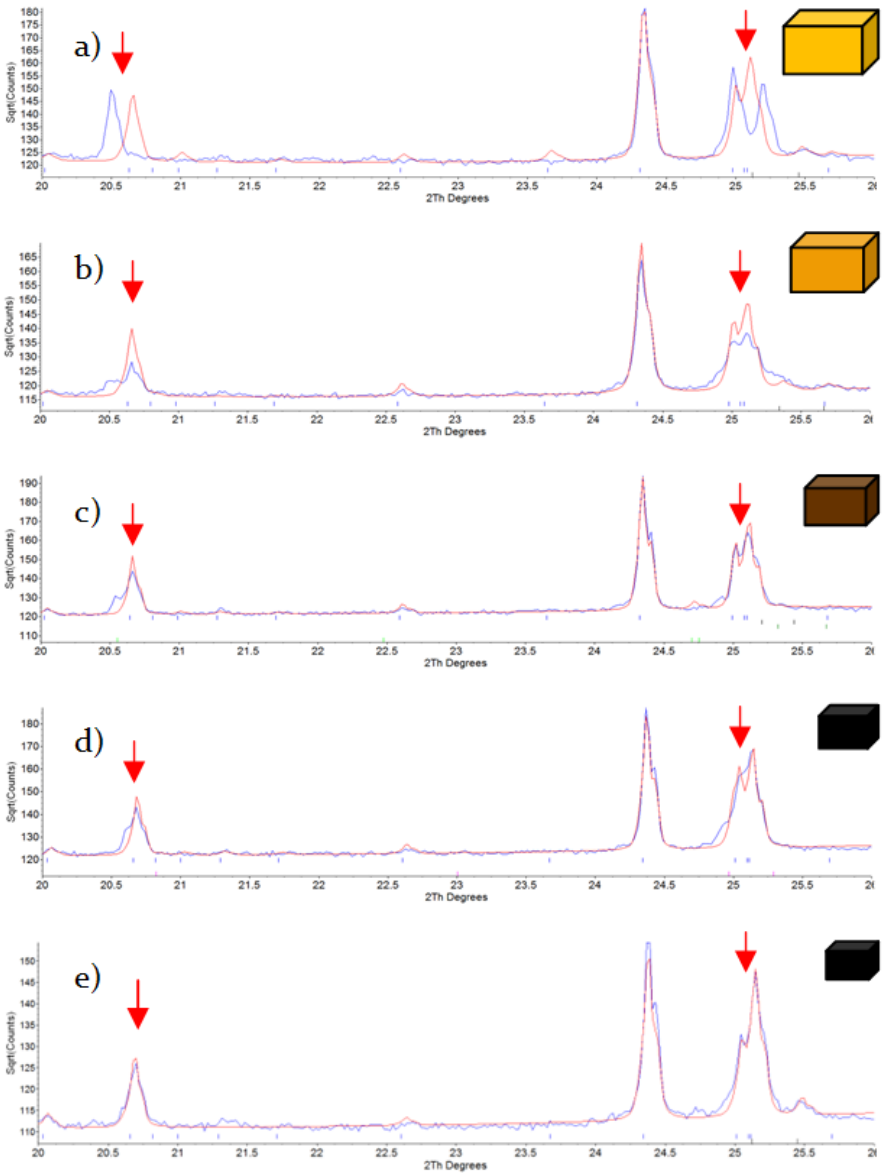

Figure 3.19. Rietveld fits of PXRD patterns of $Ce_2O_2ZnSe_2$ samples with systematically decreasing cell volume from (a) to (e), as shown by the cuboids, the colour of which shows the sample colour. The structural model proposed provides a good fit to superstructure reflections (marked by red arrows) for the minimum cell volume samples. Note that these peaks are very weak at ~5% intensity relative to the most intense peak.

Subsequent work on a range of related $Ln_2O_2MSe_2$-type solid solutions described in Chapter 4 revealed that superlattice peaks in samples (a) to (d) are incommensurately modulated due to a size mismatch between $[Ce_x^{4+}Ce_{2-x}^{3+}O_2]^{(2+x)+}$ and zinc selenide layers. For the low cell volume sample this locks in to the commensurate structure presented. For each of the samples reported in Figure 3.5c we have used a modulation approach to fit the weak unindexed satellite peaks observed in their powder pattern. This was performed by using the Pawley method to fit the subcell peaks and determine the subcell parameter (a typical fit is included in Chapter 4). Up to 34 of the strongest satellite reflections were simultaneously fitted using a pseudo-Voigt peakshape at positions constrained by refining the magnitude of α of the modulation vector $\mathbf{q} = \alpha\,\mathbf{a^*} + 0\mathbf{b^*} + 0.5\mathbf{c^*}$.

Figure 3.20 shows the value of α for samples (a) to (e). As the effective rare earth metal radius is decreased going from left to right (due to Ce oxidation), there is a decrease in α, before a lock-in region at $\alpha = 0.2$, as will be explained in Chapter 4. The lock-in region shows an energetic preference for commensurate ordering at $\alpha = 0.2$. Chapter 4 will explore in much greater detail how transition metal ordering is determined by the relative sizes of $[Ln_2O_2]^{2+}$ and $[MSe_2]^{2-}$ layers.

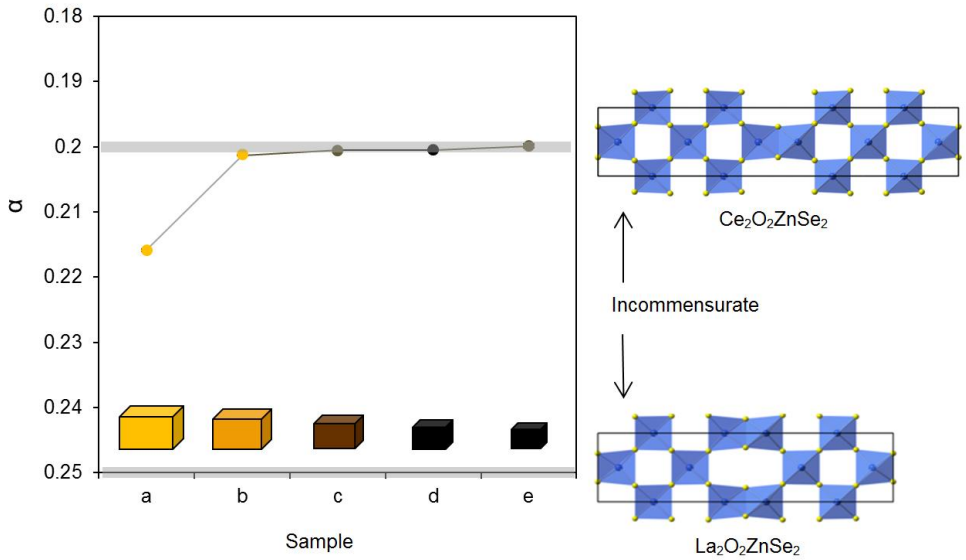

Figure 3.20. Modulation vector α for layered $Ce_2O_2ZnSe_2$ samples prepared with increasing levels of Ce oxidation, hence decreasing cell volume. Grey bands represent commensurate ordering. Rietveld-derived error bars are smaller than individual data points.

3.8 Diffuse Reflectance Spectroscopy

Diffuse reflectance spectroscopy (DRS) reveals different band gaps for high, intermediate and low-cell volume $Ce_2O_2ZnSe_2$ samples, which is unsurprising based on their different colours. The high-cell volume yellow ochre sample, intermediate-cell volume brown sample and low-cell volume black sample have band gaps of ~2.2 eV, ~1.4 eV and ~1.3 eV respectively, determined by Kubelka-Munk treatment[9,10] of data (described in Chapter 2), as shown in Figure 3.21. The narrowing of the band gap is not linearly dependant on cell volume. Measured band gaps are significantly smaller than for $La_2O_2ZnSe_2$ (3.4 eV)[5] and are strongly influenced by Ce(IV) content.

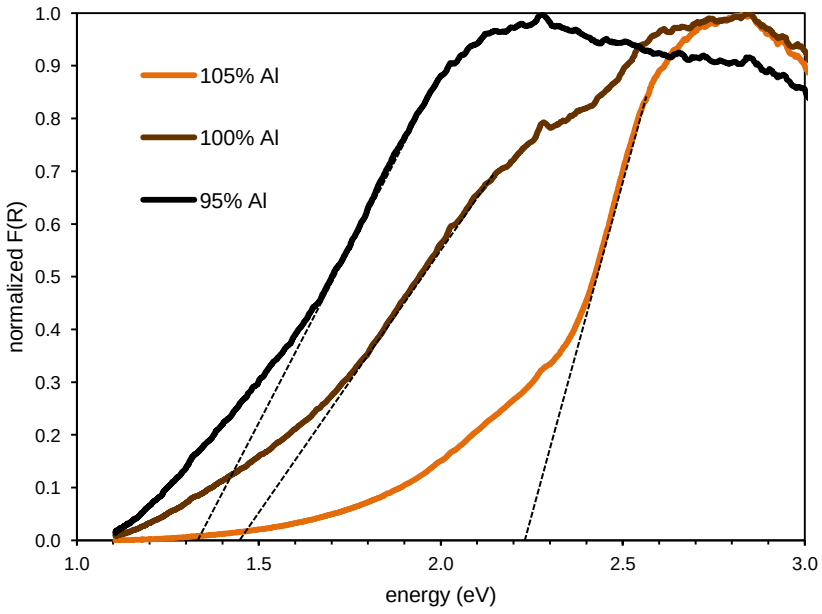

Figure 3.21. Normalised (against maximum F(R) value) diffuse reflectance spectra after Kubelka-Munk treatment for $Ce_2O_2ZnSe_2$ samples synthesized with 105% AOG (yellow), 100% AOG (brown) and 95% AOG (black), showing interband transitions corresponding to an optical band gap of ~2.2 eV, ~1.4 eV and ~1.3 eV respectively.

3.9 Magnetic Properties

The temperature dependence of the molar magnetic susceptibility (χ_{mol}) of $Ce_2O_2ZnSe_2$ (NPD sample) is shown in Figure 3.22. $Ce_2O_2ZnSe_2$ is a typical paramagnet, and obeys the Curie-Weiss law from 150 K to 300 K. By Curie-Weiss fitting $1/\chi_{mol} - T$ data from 150 -300 K, we obtain an effective magnetic moment of Ce_2O_2ZnSe of μ_{eff} = 3.43(1) μ_B, which equates to μ_{eff} = 2.42(1) μ_B for each $CeOZn_{0.5}Se$. In $Ce_2O_2ZnSe_2$, the magnetic properties come from the $4f^1$ open shell ion Ce^{3+}. The ground state of Ce^{3+} is $^2F_{5/2}$ with a theoretical effective magnetic moment μ_{eff} = 2.54 μ_B, however, most experiment results of Ce^{3+} show μ_{eff} ~ 2.4 μ_B. The Weiss constant θ is -10(2) K indicating local antiferromagnetic interactions, however we do not observe the onset of long range order down to 2 K. Similar behaviour has been reported for $Ln_4O_4Se_3$ (Ln = Ce and Nd) systems.[11]

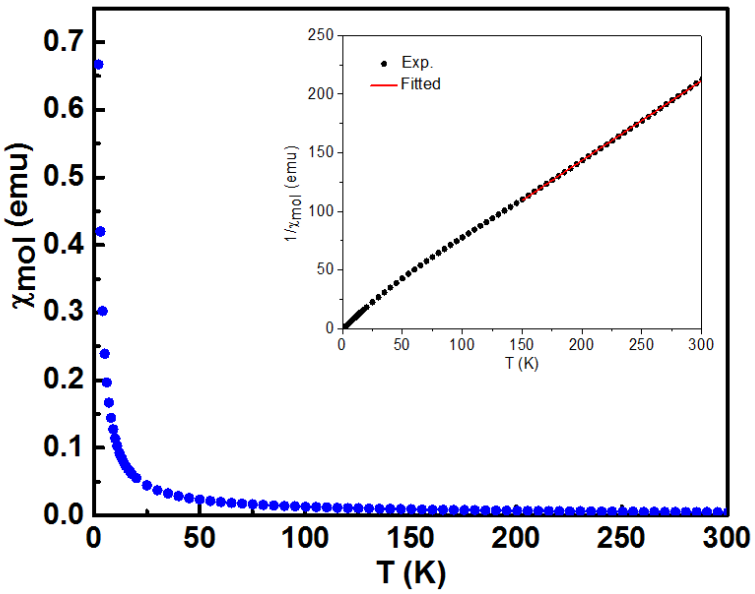

Figure 3.22. Molar susceptibility of $Ce_2O_2ZnSe_2$ at different temperatures.

3.10 Unsuccessful Syntheses

There have been previous attempts to synthesise $Ln_2O_2ZnSe_2$ (*Ln* = La, Ce, Pr, Nd) by other group members, all at 1100 ˚C. Although $La_2O_2ZnSe_2$ can be formed at this temperature, the Ce, Pr, and Nd compounds had proved unsuccessful.[12] As near single phase $Ce_2O_2ZnSe_2$ can be formed at 1200 ˚C it was believed that the Pr and Nd compounds may form at this temperature too. Unfortunately this was not the case, with the main products of the reactions being Ln_2O_2Se (*Ln* = Pr, Nd) and ZnSe. This is summarized in Table 3.5.

Target Compound	T / ˚C	Products
$Pr_2O_2ZnSe_2$	1100, 1200	Pr_2O_2Se, ZnSe
$Nd_2O_2ZnSe_2$	1100, 1200	Nd_2O_2Se, ZnSe

Table 3.5. Results of unsuccessful syntheses for two $Ln_2O_2ZnSe_2$ target phases.

3.11 Conclusions

In conclusion we describe the synthesis, structural characterization, optical measurements and magnetic measurements of the new material $Ce_2O_2ZnSe_2$. It adopts a ZrCuSiAs-related structure with ordering of Zn^{2+} cations over the tetrahedral sites in the $[ZnSe_2]^{2-}$ layers. The ordering pattern contains both corner-sharing and edge-sharing tetrahedra and is intermediate between ordering patterns observed for $Ce_2O_2FeSe_2$ and $La_2O_2CdSe_2$. It is similar to $La_2O_2ZnSe_2$ except that $Ce_2O_2ZnSe_2$ has extended corner-shared regions.

The colour of the compound and cell volume both change, which varies by ~0.4%. At the highest, intermediate and lowest cell volume the colour is yellow-ochre, brown and black respectively. This decrease is attributed to partial oxidation of the Ce from +3 to +4, the extent of which can be controlled by the synthetic conditions.

$Ce_2O_2ZnSe_2$ is a semiconductor in all cases with experimental optical band gaps of 2.2, 1.4 and 1.3 eV for the samples coloured yellow ochre, brown and black respectively. SQUID measurements show $Ce_2O_2ZnSe_2$ to be paramagnetic down to 2 K.

3.12 References

(1) Benacerraf, A.; Guittard, M.; Domange, L.; Flahaut, J. *Bull. Soc. Chim. Fr.* **1959**, 1920.

(2) Ueda, K.; Takafuji, K.; Hiramatsu, H.; Ohta, H.; Kamiya, T.; Hirano, M.; Hosono, H. *Chem. Mater.* **2003**, *15*, 3692.

(3) Chan, G. H.; Deng, B.; Bertoni, M.; Ireland, J. R.; Hersam, M. C.; Mason, T. O.; Van Duyne, R. P.; Ibers, J. A. *Inorg. Chem.* **2006**, *45*, 8264.

(4) Pitcher, M. J.; Smura, C. F.; Clarke, S. J. *Inorg. Chem.* **2009**, *48*, 9054.

(5) Tuxworth, A. J.; McCabe, E. E.; Free, D. G.; Clark, S. J.; Evans, J. S. O. *Inorg. Chem.* **2013**, *52*, 2078.

(6) Campbell, B. J.; Stokes, H. T.; Tanner, D. E.; Hatch, D. M. *J. Appl. Crystallogr.* **2006**, *39*, 607.

(7) McCabe, E. E.; Free, D. G.; Evans, J. S. O. *Chem. Commun.* **2011**, *47*, 1261.

(8) Hiramatsu, H.; Ueda, K.; Kamiya, T.; Ohta, H.; Hirano, M.; Hosono, H. *J. Mater. Chem.* **2004**, *14*, 2946.

(9) Kortum, G.; Braun, W.; Herzog, G. *Agnew. Chem., Int. Ed.* **1963**, *2 (7)*, 333.

(10) Tandon, S. P.; Gupta, J. P. *Phys. Status Solidi* **1970**, *38*, 363.

(11) Strobel, S.; Choudhury, A.; Dorhout, P. K.; Lipp, C.; Schleid, T. *Inorg. Chem.* **2008**, *47*, 4936.

(12) Tuxworth, A. J., *PhD thesis: Synthesis, Structure and Properties of Metal Oxychalcogenides*, Durham University, 2013.

Chapter 4: Infinitely Adaptive 2D Transition Metal Ordering in $Ln_2O_2MSe_2$-Type Oxychalcogenides

4.1 Introduction

Before the start of the work reported in this thesis there were only a limited number of known 2D $Ln_2O_2MSe_2$-type compounds, shown in Figure 4.1 alongside $Ce_2O_2ZnSe_2$ of Chapter 3. The origins of the different transition metal ordering in these compounds were unclear.

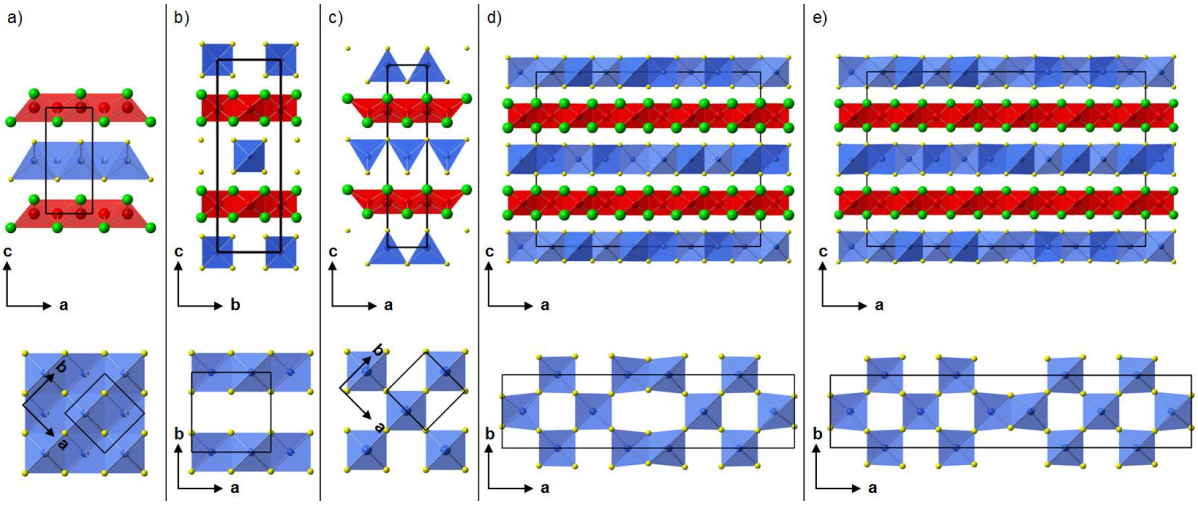

Figure 4.1. ZrCuSiAs-derived structures reported for (a) $Ln_2O_2MSe_2$, P4/nmm symmetry[1] (b) $Ce_2O_2FeSe_2$, Imcb symmetry[2] (c) $La_2O_2CdSe_2$, $P4_2/nmc$ symmetry[3] (d) $La_2O_2ZnSe_2$, Bmab symmetry[4] (e) $Ce_2O_2ZnSe_2$, Imcb symmetry.[5] Top figures show the fluorite-like sheets of edge-sharing Ln_4O tetrahedra (red) and antifluorite-like sheets of MSe_4 tetrahedra (blue). Bottom figures are the view down [001], showing the arrangement of MSe_4 tetrahedra. Ln^{3+} cations are shown in green, O^{2-} anions in red, M^{2+} cations in blue and Se^{2-} anions in yellow.

The work discussed in Chapter 4 is highlighted blue on the thesis map shown in Figure 4.2. It reports 60 new compositions across the $La_2O_2(Fe_{1-y}Zn_y)Se_2$, $La_2O_2(Zn_{1-y}Mn_y)Se_2$, $La_2O_2(Mn_{1-y}Cd_y)Se_2$, $Ce_2O_2(Fe_{1-y}Zn_y)Se_2$, $Ce_2O_2(Zn_{1-y}Mn_y)Se_2$, $Ce_2O_2(Mn_{1-y}Cd_y)Se_2$, $La_{2-z}Ce_zO_2FeSe_2$, $La_{2-z}Ce_zO_2ZnSe_2$, $La_{2-z}Ce_zO_2MnSe_2$, and $La_{2-z}Ce_zO_2CdSe_2$ solid solutions. By studying variations in cell volume/parameters and modulation vectors across the solid solutions, it is shown that the transition metal arrangement in $Ln_2O_2MSe_2$ (*Ln* = La & Ce, *M* = Fe, Zn, Mn & Cd) compounds is determined by the relative sizes of $[Ln_2O_2]^{2+}$ and $[MSe_2]^{2-}$ layers, and can be systematically controlled by either *Ln* or *M* substitution leading to an "infinitely adaptive" structural family. Detailed structural information is also reported for selected commensurate examples.

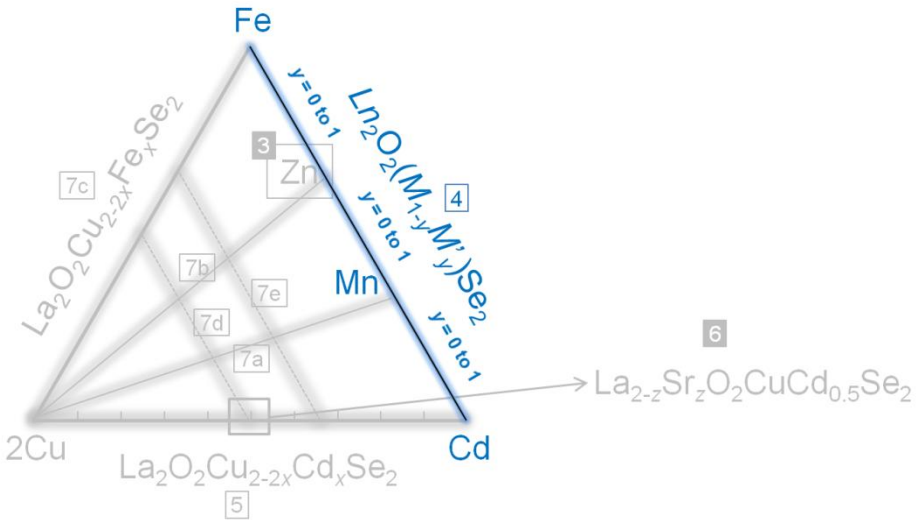

Figure 4.2. Thesis map highlighting the area of work discussed in Chapter 4.

4.2 Synthesis and Phase Purity

A range of $Ln_2O_2(M_{1-y}M'_y)Se_2$ and $La_{2-z}Ce_zO_2MSe_2$ (*Ln* = La & Ce, *M*/*M'* = Fe, Zn, Mn & Cd) solid solutions were prepared to investigate the effects of systematically changing the relative sizes of $[Ln_2O_2]^{2+}$ and $[MSe_2]^{2-}$ layers on transition metal ordering. Samples were synthesized for 12, 24 or 48 hours with an oxygen getter (OG) molar amount of 110 and 105% for Al and Ti respectively, at 1000, 1100 or 1200 ˚C. Specific synthetic conditions for each sample are tabulated in Chapter 2. PXRD showed that in most cases a layered ZrCuSiAs-related phase had formed with a unit cell $a = b \approx 4$ Å and $c \approx 9$ Å (the subcell), explaining the main peaks present. Weak additional reflections were observed at low angles for all samples which could not be attributed to known impurity phases. It is shown below that these arise from transition metal ordering.

The sample colour varied significantly across the solid solutions. The colours of all samples are shown in Table 4.1. In overview, the $La_2O_2(Fe_{1-y}Zn_y)Se_2$ samples are black/dark green, $La_2O_2(Zn_{1-y}Mn_y)Se_2$ pink/orange, $La_2O_2(Mn_{1-y}Cd_y)Se_2$ brick red/brown, $Ce_2O_2(Fe_{1-y}Zn_y)Se_2$ black, $Ce_2O_2(Zn_{1-y}Mn_y)Se_2$ dark red, $Ce_2O_2(Mn_{1-y}Cd_y)Se_2$ dark red/red, $La_{2-z}Ce_zO_2FeSe_2$ black, $La_{2-z}Ce_zO_2ZnSe_2$ black/ochre $La_{2-z}Ce_zO_2MnSe_2$ dark red/black, and $La_{2-z}Ce_zO_2CdSe_2$ ochre.

There are a few cases across the different solid solutions where the orthorhombic β-$Ln_2O_2MSe_2$ polymorph[6] (referred to as the *oP*-$Ln_2O_2MSe_2$ polymorph by others[7,8]) forms in preference to the layered ZrCuSiAs-related structure. We refer to this structure type as the "β phase" throughout, and the regions where it forms are indicated in Figure 4.3.

$La_2O_2(Fe_{1-y}Zn_y)Se_2$		$La_2O_2(Zn_{1-y}Mn_y)Se_2$		$La_2O_2(Mn_{1-y}Cd_y)Se_2$	
y	Colour	*y*	Colour	*y*	Colour
0		0		0	
0.125		0.1		0.025	
0.25		0.2		0.05	
0.275		0.3		0.1	
0.325		0.4		0.15	
0.35		0.5		0.2	
0.375		0.6		0.25	
0.5		0.7		0.3	
0.625		0.8		0.35	
0.75		0.9		0.4	
0.875		0.95		0.45	
1		0.975		0.5	
		0.9875		0.6	
		1		0.7	
				0.8	
				0.9	
				1	

$Ce_2O_2(Fe_{1-y}Zn_y)Se_2$		$Ce_2O_2(Zn_{1-y}Mn_y)Se_2$		$Ce_2O_2(Mn_{1-y}Cd_y)Se_2$	
y	Colour	*y*	Colour	*y*	Colour
0		0		0	
0.03		0.2		0.05	
0.0625		0.4		0.1	
0.125		0.6		0.125	
0.25		0.8		0.15	
0.375		0.833		0.2	
0.5		0.9		0.25	
0.625		1		0.3	
0.75				0.4	
0.8125				0.5	
0.875				0.6	
0.9375				0.7	
0.97				0.8	
1				0.9	
				1	

$La_{2-z}Ce_zO_2FeSe_2$		$La_{2-z}Ce_zO_2ZnSe_2$		$La_{2-z}Ce_zO_2MnSe_2$			$La_{2-z}Ce_zO_2CdSe_2$	
z	Colour	*z*	Colour	*z*	Colour		*z*	Colour
0		0		0			0	
0.5		0.2		0.1			0.5	
1		0.6		0.2			1	
1.5		1		0.4			1.5	
2		1.4		0.6			2	
		1.8		0.8				
		2		1				
				1.2				
				1.4				
				1.6				
				1.8				
				1.9				
				2				

Table 4.1. Colour of all samples in polycrystalline form. In $La_{2-z}Ce_zO_2MnSe_2$, the colour is given after x1 (left) and x2 (right) heating cycles.

$La_2O_2(Fe_{1-y}Zn_y)Se_2$		$La_2O_2(Zn_{1-y}Mn_y)Se_2$		$La_2O_2(Mn_{1-y}Cd_y)Se_2$	
y	2D/β/other	*y*	2D/β/other	*y*	2D/β/other
0	0.0/98.9/1.1	0	99.0/0.0/1.0	0	0.0/98.0/2.0
0.125	0.0/99.1/0.9	0.1	96.8/0.0/3.2	0.025	13.5/84.7/1.8
0.25	2.4/97.6/0.0	0.2	99.2/0.0/0.8	0.05	98.4/0.0/1.6
0.275	23.0/77.0/0.0	0.3	100.0/0.0/0.0	0.1	96.8/0.0/2.8
0.325	40.1/59.9/0.0	0.4	100.0/0.0/0.0	0.15	99.0/0.0/1.0
0.35	99.1/0.0/0.9	0.5	100.0/0.0/0.0	0.2	98.8/0.0/3.8
0.375	100.0/0.0/0.0	0.6	98.3/0.0/1.7	0.25	98.5/0.0/1.5
0.5	100.0/0.0/0.0	0.7	99.1/0.0/0.9	0.3	99.3/0.0/4.8
0.625	98.2/0.0/1.8	0.8	99.5/0.0/0.5	0.35	100.0/0.0/0.0
0.75	98.2/0.0/1.8	0.9	95.6/0.0/4.4	0.4	97.4/0.0/5.8
0.875	96.9/0.0/3.1	0.95	97.2/0.0/2.9	0.45	99.4/0.0/0.6
1	99.0/0.0/1.0	0.975	72.4/20.5/7.1	0.5	99.1/0.0/6.8
		0.9875	45.7/48.0/6.3	0.6	99.0/0.0/1.0
		1	0.0/98.0/2.0	0.7	99.0/0.0/7.8
				0.8	98.7/0.0/1.3
				0.9	99.2/0.0/8.8
				1	0.0/99.1/0.9

$Ce_2O_2(Fe_{1-y}Zn_y)Se_2$		$Ce_2O_2(Zn_{1-y}Mn_y)Se_2$		$Ce_2O_2(Mn_{1-y}Cd_y)Se_2$	
y	2D/β/other	*y*	2D/β/other	*y*	2D/β/other
0	100.0/0.0/0.0	0	96.9/0.0/3.1	0	88.4/0.0/11.6
0.03	98.2/0.0/1.8	0.2	95.8/0.0/4.2	0.05	98.3/0.0/1.7
0.0625	93.7/0.0/6.3	0.4	98.8/0.0/1.2	0.1	95.0/0.0/5.0
0.125	88.7/0.0/11.3	0.6	99.3/0.0/0.7	0.125	98.1/0.0/1.9
0.25	100.0/0.0/0.0	0.8	97.9/0.0/2.1	0.15	99.2/0.0/0.8
0.375	100.0/0.0/0.0	0.833	100.0/0.0/0.0	0.2	100.0/0.0/0.0
0.5	92.7/0.0/7.3	0.9	94.4/0.0/5.6	0.25	97.6/0.0/2.4
0.625	94.5/0.0/5.5	1	88.4/0.0/11.6	0.3	99.3/0.0/0.7
0.75	93.7/0.0/6.3			0.4	94.7/0.0/5.3
0.8125	99.2/0.0/0.8			0.5	95.8/0.0/4.2
0.875	98.4/0.0/1.6			0.6	97.4/0.0/2.6
0.9375	98.8/0.0/1.2			0.7	92.7/0.0/7.3
0.97	97.3/0.0/2.7			0.8	98.6/0.0/1.4
1	96.9/0.0/3.1			0.9	94.1/0.0/5.9
				1	95.7/0.0/4.3

Table 4.2. Weight percent of phases formed (2D/β/other) for $Ln_2O_2M_{1-y}M'_ySe_2$ samples. Weight percentages quoted are derived from Rietveld refinements and have a typical uncertainty of 2%.

$La_{2-z}Ce_zO_2FeSe_2$		$La_{2-z}Ce_zO_2ZnSe_2$		$La_{2-z}Ce_zO_2MnSe_2$		$La_{2-z}Ce_zO_2CdSe_2$	
z	2D/β/other	*z*	2D/β/other	*z*	2D/β/other	*z*	2D/β/other
0	0.0/100.0/0.0	0	98.3/0.0/1.7	0	0.0/100.0/0.0	0	99.1/0.0/0.9
0.5	99.5/0.0/0.5	0.2	98.5/0.0/1.5	0.1	0.0/100.0/0.0	0.5	99.6/0.0/0.4
1	98.7/0.0/1.3	0.6	97.5/0.0/2.5	0.2	0.0/100.0/0.0	1	99.7/0.0/0.3
1.5	98.9/0.0/1.1	1	93.4/0.0/6.6	0.4	47.6/40.4/12.0	1.5	99.7/0.0/0.3
2	100.0/0.0/0.0	1.4	90.7/0.0/9.3	0.6	84.5/10.5/5.0	2	95.7/0.0/4.3
		1.8	94.7/0.0/5.3	0.8	99.2/0.0/0.8		
		2	96.9/0.0/3.1	1	100.0/0.0/0.0		
				1.2	100.0/0.0/0.0		
				1.4	99.4/0.0/0.6		
				1.6	100.0/0.0/0.0		
				1.8	100.0/0.0/0.0		
				1.9	100.0/0.0/0.0		
				2	64.2/0.0/35.8		

Table 4.3. Weight percent of phases formed (2D/β/other) for $La_{2-z}Ce_zO_2MSe_2$ samples.

4.3 Unit Cell Volume Trends

The cell volume of layered ZrCuSiAs-related phases in all six $Ln_2O_2(M_{1-y}M'_y)Se_2$ solid solutions prepared are shown in Figure 4.3 (top). Series with common end members have been plotted continuously, and the plot is ordered Fe–Zn, Zn–Mn, Mn–Cd to reflect increasing effective transition metal radius for this structure type. For the small number of compositions reported previously, data points from the literature are included.[2-5,7-9] This gives one continuous plot for the three Ce solid solutions $Ce_2O_2(Fe_{1-y}Zn_y)Se_2$, $Ce_2O_2(Zn_{1-y}Mn_y)Se_2$ and $Ce_2O_2(Mn_{1-y}Cd_y)Se_2$, and for the three La solid solutions $La_2O_2(Fe_{1-y}Zn_y)Se_2$, $La_2O_2(Zn_{1-y}Mn_y)Se_2$ and $La_2O_2(Mn_{1-y}Cd_y)Se_2$.

Shannon's tables give ionic radii values of Fe = 0.63, Zn = 0.6, Mn = 0.66 and Cd = 0.78 Å, for 4 coordinate +2 oxidation states.[10] These values broadly account for the cell volume trends observed, though there are subtle anomalies observed. Firstly, the cell-volume gradient in Fe/Zn solid solutions is slightly positive; ionic radii consideration alone would suggest this should be negative. This could be caused by small amounts of Fe^{3+} being present, or by the changes in transition metal ordering discussed below. Secondly, the positive volume gradient of Zn–Mn and Mn–Cd containing solid solutions is roughly equal. This is somewhat surprising given the smaller difference in ionic radii between Zn and Mn compared to Mn and Cd (0.06 vs 0.12 Å).

For the Ce systems, Chapter 3 shows that the cell volume is influenced by the Ce^{3+}:Ce^{4+} ratio in the material (we presume the charge compensation mechanism is minor transition metal loss).[5] This can be controlled by the amount of OG used, which affects the amount of O available to the system. This effect was also observed in $La_{0.2}Ce_{1.8}O_2ZnSe_2$ (for example, the gray data points in Figure 4.3 are for samples synthesized with 100% and 95% Al molar amount), and will presumably occur in many/all of these systems. It is also the most likely reason for the higher scatter of Ce cell volumes across solid solutions (relative to La compounds) in Figure 4.3 (top). Attempts to deliberately change the cell volume of La-containing compounds by varying the OG amount were unsuccessful, consistent with the fixed +3 oxidation state of La.

The cell volumes of layered phases in the four $Ln_{2-z}Ce_zO_2MSe_2$ solid solutions studied are shown in Figure 4.3 (bottom). The gradient of all curves is negative, as expected from the lanthanide contraction. This effect will be enhanced by small levels of Ce oxidation. As in the $Ln_2O_2(M_{1-y}M'_y)Se_2$ solid solutions, Fe-containing compounds have a smaller cell volume than analogous Zn compounds.

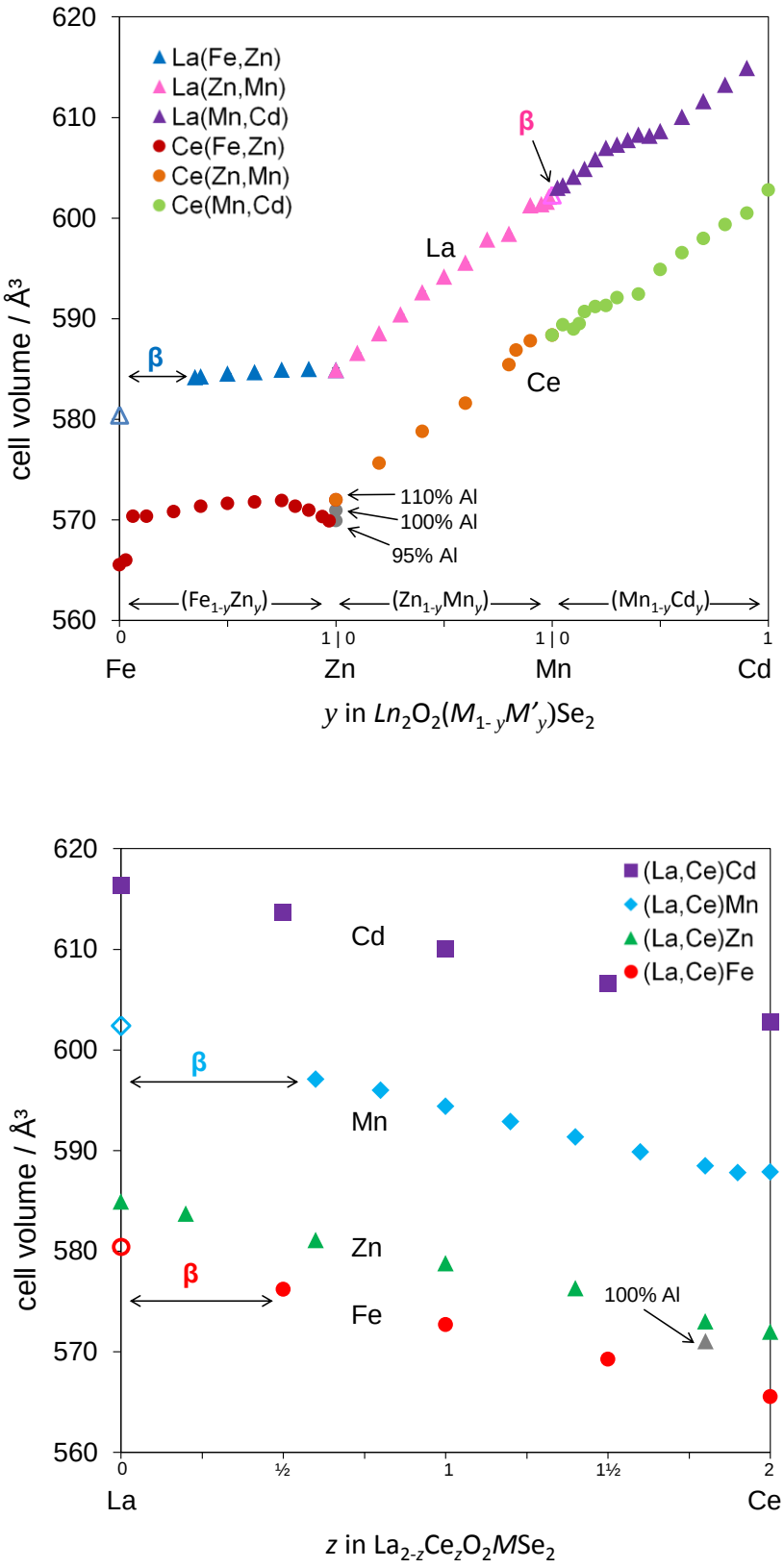

Figure 4.3. Cell volume of 2D ZrCuSiAs-related phases in $Ln_2O_2(M_{1-y}M'_y)Se_2$ (top) and $Ln_{2-z}Ce_zO_2MSe_2$ (bottom) solid solutions. The $La_2O_2FeSe_2$/ $La_2O_2MnSe_2$ data points (open symbols) are taken from the literature.[7,8] *Rietveld error bars are smaller than data points.*

Under the experimental conditions used, partial β phase formation occurs for $La_2O_2(Fe_{1-y}Zn_y)Se_2$ with $y < 0.33$, with near pure β phase formation for $y < 0.25$. $La_2O_2MnSe_2$ also preferentially forms the β phase, though only slight Zn or Cd doping is required ($y \approx 0.05$ and 0.1 respectively) for the layered structure to form. The β phase also begins to form in place of the layered structure in $La_{2-z}Ce_zO_2FeSe_2$ (for $z \lesssim 0.5$) and $La_{2-z}Ce_zO_2MnSe_2$ (onset $z \approx 0.7$). Recent work by another group on $Ln_2O_2FeSe_2$ and $Ln_2O_2MnSe_2$ (*Ln* = La, Ce) shows that single crystals of the La and Ce structures can be prepared in the 2D phase by careful control of the synthesis conditions.[7,8] Data from these works are shown with open points in Figure 4.3.

4.4 Cell Parameter Trends

The individual cell parameters of 2D phases in the six $Ln_2O_2(M_{1-y}M'_y)Se_2$ solid solutions are shown in Figure 4.4. These were derived using a $\sqrt{2}a_{\text{subcell}} \times \sqrt{2}b_{\text{subcell}} \times 2c_{\text{subcell}}$ unit cell. For comparison each has been normalised to the cell parameter of the zinc phase $Ln_2O_2ZnSe_2$.[4,5] By comparing this figure with Figure 4.3 (top), it is apparent that the majority of the volume change on *M* substitution is due to changes in the *c*-axis, perpendicular to the layers.

The cell parameters in the four $La_{2-z}Ce_zO_2MSe_2$ solid solutions are shown in Figure 4.5. In contrast to transition metal substitution, lanthanide substitution leads to significant changes in all cell parameters, with *a* and *b* changing at approximately twice the rate of the *c*-axis.

One explanation for the trends in both $Ln_2O_2(M_{1-y}M'_y)Se_2$ and $La_{2-z}Ce_zO_2MSe_2$ solid solutions would be that *Ln*-O layers are relatively rigid, and the *M*-Se layers relatively flexible. If this were true, as the transition metal size increased across the $Ln_2O_2(M_{1-y}M'_y)Se_2$ solid solutions, increases in unit cell size would have to be accommodated by changes only in *c* due to the *a* and *b* parameters being fixed in size by the rigid *Ln*-O layers; this is observed experimentally. As the lanthanide size decreases across $La_{2-z}Ce_zO_2MSe_2$ solid solutions, a decrease in all cell parameters could now be observed as ionic radii changes are being made directly to the rigid *Ln*-O layers; this is also observed experimentally. A more in depth discussion of this is below.

Tabulated values of cell volumes/parameters for all the compounds of Chapter 4 are given in Appendix 2.

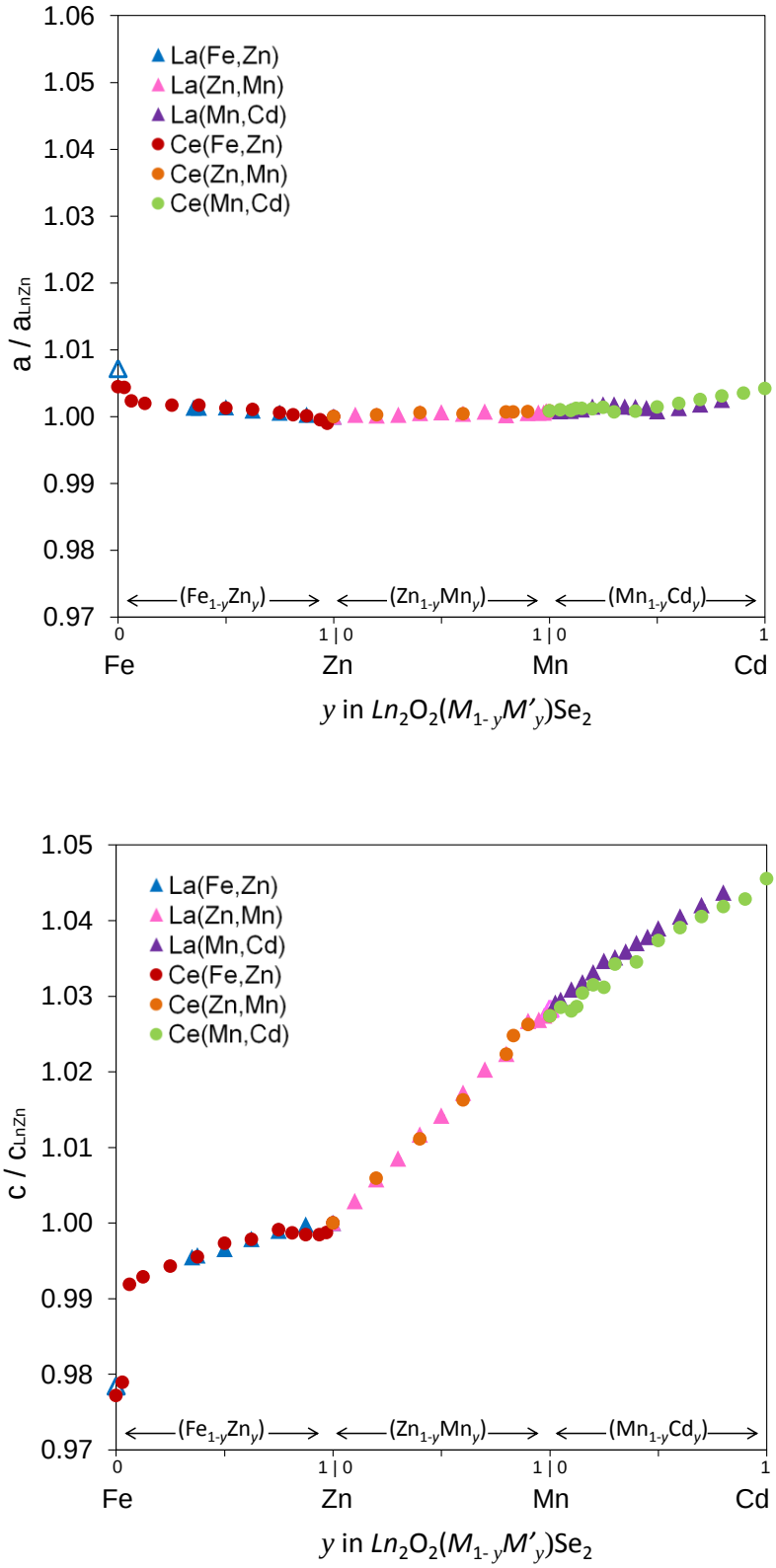

Figure 4.4. Relative cell parameters of 2D $Ln_2O_2(M_{1-y}M'_y)Se_2$ solid solutions. The a and b parameters are equated in all samples except $Ln_2O_2FeSe_2$ (La, Ce) where 0C-1E stripe-like ordering leads to subtle differences in a and b (~0.25%).[2] Rietveld error bars are smaller than data points.

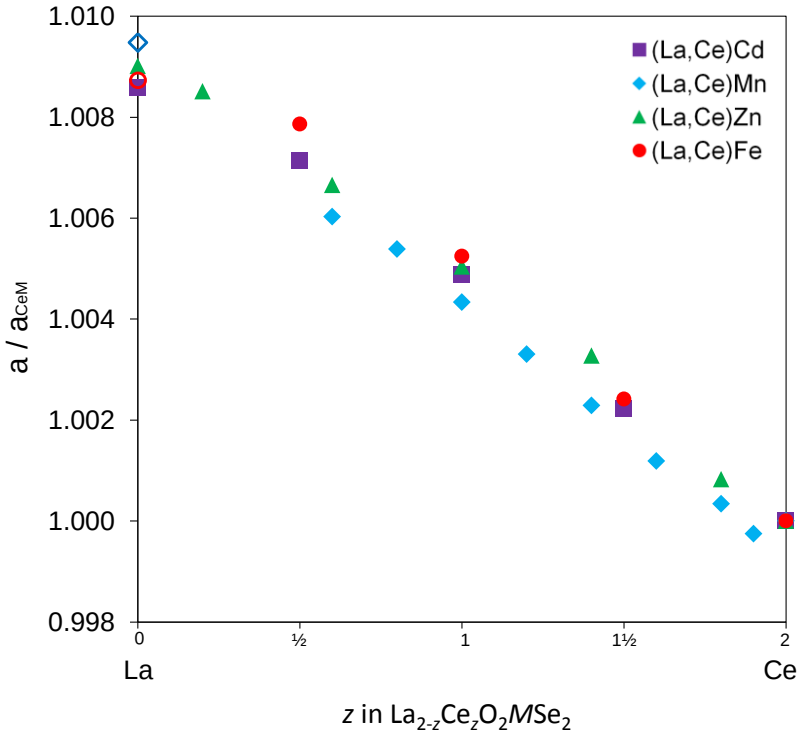

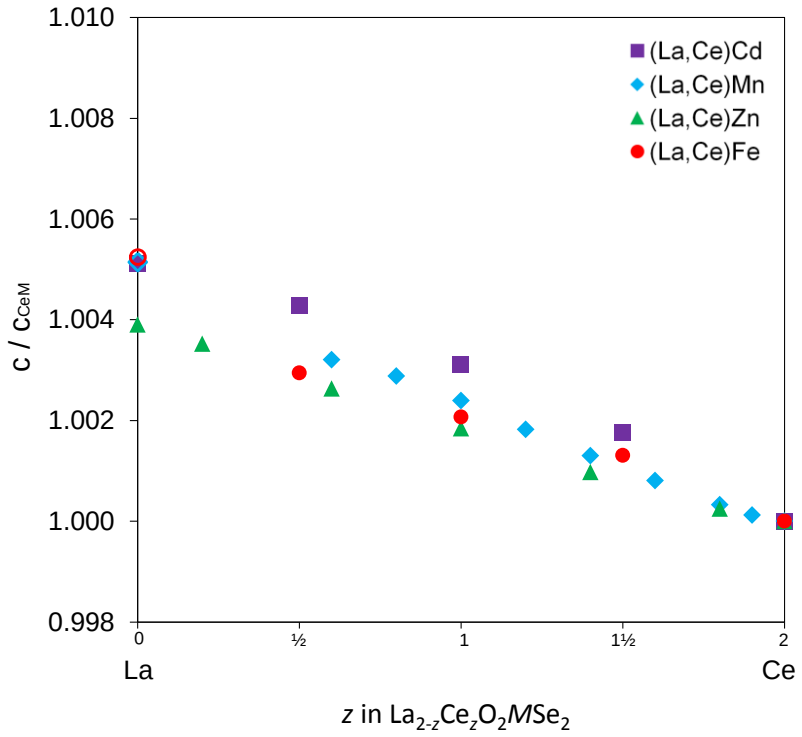

Figure 4.5. Relative cell parameters of 2D $Ln_{2-z}Ce_zO_2MSe_2$ solid solutions. The a and b parameters are equated in all samples except Fe containing compounds, where 0C-1E stripe-like ordering leads to subtle differences in a and b (~0.25%).[2] Rietveld error bars are smaller than data points.

4.5 Modulation Vector Investigation

For all the samples synthesised, the powder patterns contained weak additional supercell reflections at low angles which could not be fitted using a subcell model. Closer inspection of these supercell reflections showed a smooth variation in their 2θ position as the transition metal ionic radii increased. Figure 4.6 shows the progression of supercell reflections in the $La_2O_2(Zn_{1-y}Mn_y)Se_2$ solid solution, where the blue line indicates subcell peaks, and all others are supercell peaks. At $y = 0$ there are two supercell reflections at ~25° in 2θ. As y increases these supercell peaks move closer together and eventually overlap at $y = 0.9$ (note that at $y = 1$, $La_2O_2MnSe_2$, the β structure forms).

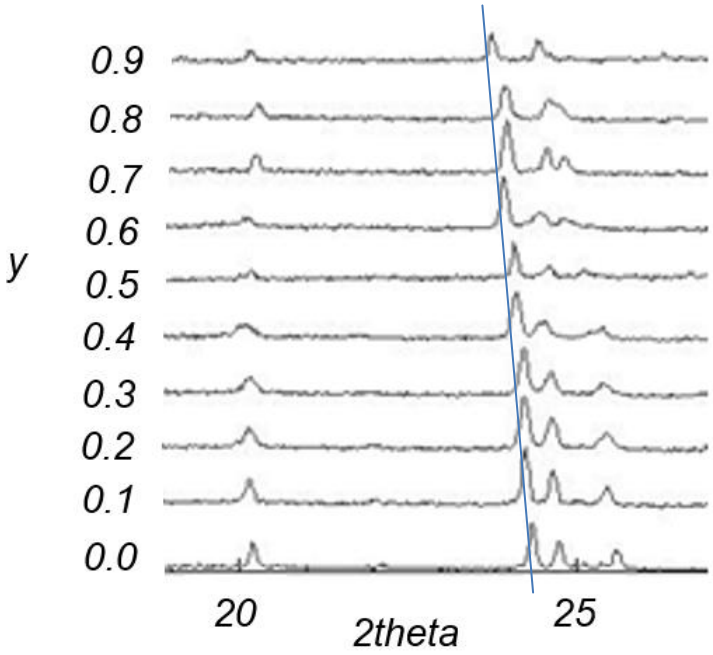

Figure 4.6. Variation of supercell peaks across the $La_2O_2(Zn_{1-y}Mn_y)Se_2$ solid solution. The peaks marked by a blue line are subcell peaks, while all others are supercell peaks.

All commensurately ordered $Ln_2O_2MSe_2$-type compounds that were known when we started this study can be described with a unit cell with dimensions $n\sqrt{2}a_{subcell} \times \sqrt{2}b_{subcell} \times 2c_{subcell}$, where n = 1 ($Ce_2O_2FeSe_2$,[2] 0C-1E), n = 4 ($La_2O_2ZnSe_2$,[4] 3C-1E), n = 5 ($Ce_2O_2ZnSe_2$,[5] 4C-1E) or n = 6 ($La_{0.44}Ce_{1.56}O_2MnSe_2$,[9] 5C-1E). These systems can therefore be described as an evolving series using a modulated approach based on a $\sqrt{2}a_{subcell} \times \sqrt{2}b_{subcell} \times 2c_{subcell}$ parent cell with a modulation vector of **q** = α**a*** + 0**b*** + ½**c*** and superspace group *Cmme*(α01/2)0*s*0. The corresponding **q**-vectors for the commensurate structures are α = 1 (0C-1E), α = 1/4 (3C-1E), α = 1/5 (4C-1E), α = 1/6 (5C-1E), as shown schematically in Figure 4.7. Note that for an *m*C-1E structure α = 1/(*m*+1).

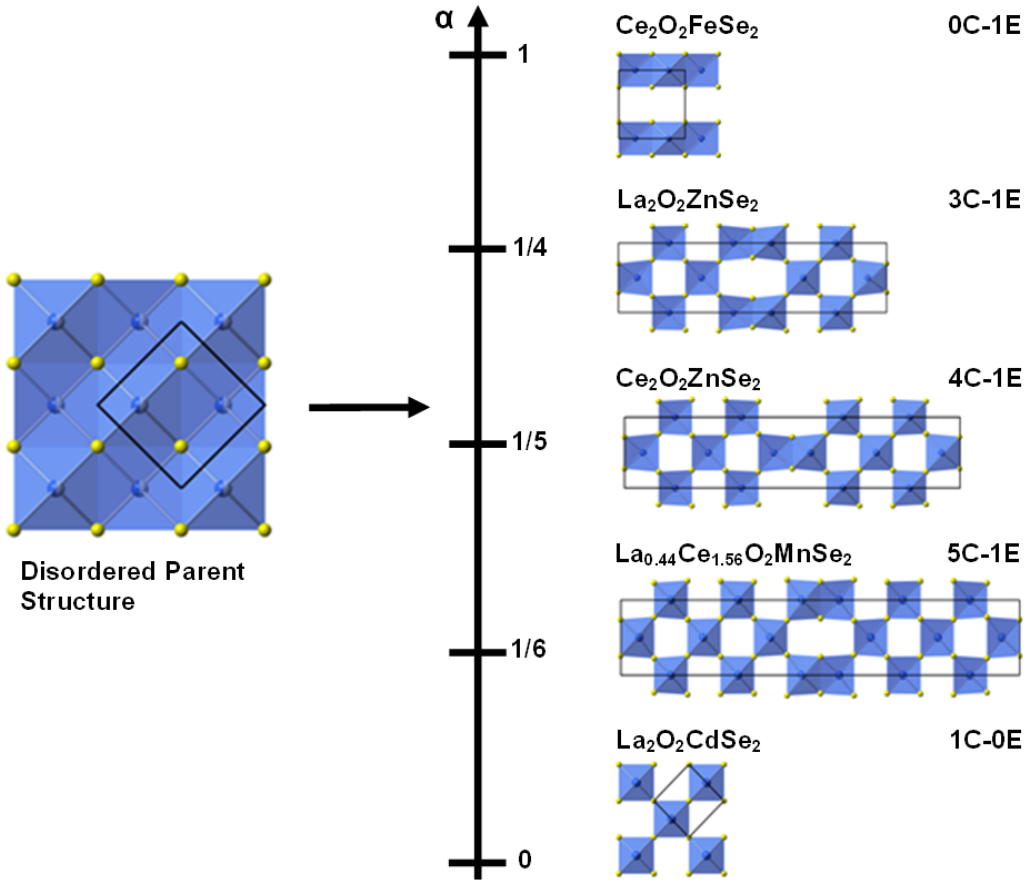

Figure 4.7. Relationship of transition metal ordering patterns in $Ln_2O_2MSe_2$ to α in ***q*** *= α**a*** + 0**b*** + ½**c***.*

For each of the samples reported in Figure 4.3 the modulation approach has been used to fit the weak unindexed satellite peaks observed in their powder pattern. This was performed by using the Pawley method to fit the subcell peaks and determine the subcell parameter. Up to 34 of the strongest satellite reflections were simultaneously fitted using a pseudo-Voigt peakshape at positions constrained by refining the magnitude of *α*. A typical fit is included in Figure 4.8. A snippet of the input file used to perform this is shown in Figure 4.9.

This was made possible by important collaborative work which was conducted alongside the work of Chapter 4 (by Dr Chun-Hai Wang). This work involved single crystal studies to provide a full structural solution for the incommensurate compound $Ce_2O_2MnSe_2$ using the modulation approach.[3] As this identified which superstructure peaks were prevalent in experimental data, Dr Wang was able to develop the Pawley-like modulation approach to the fitting of superstructure reflections described above.

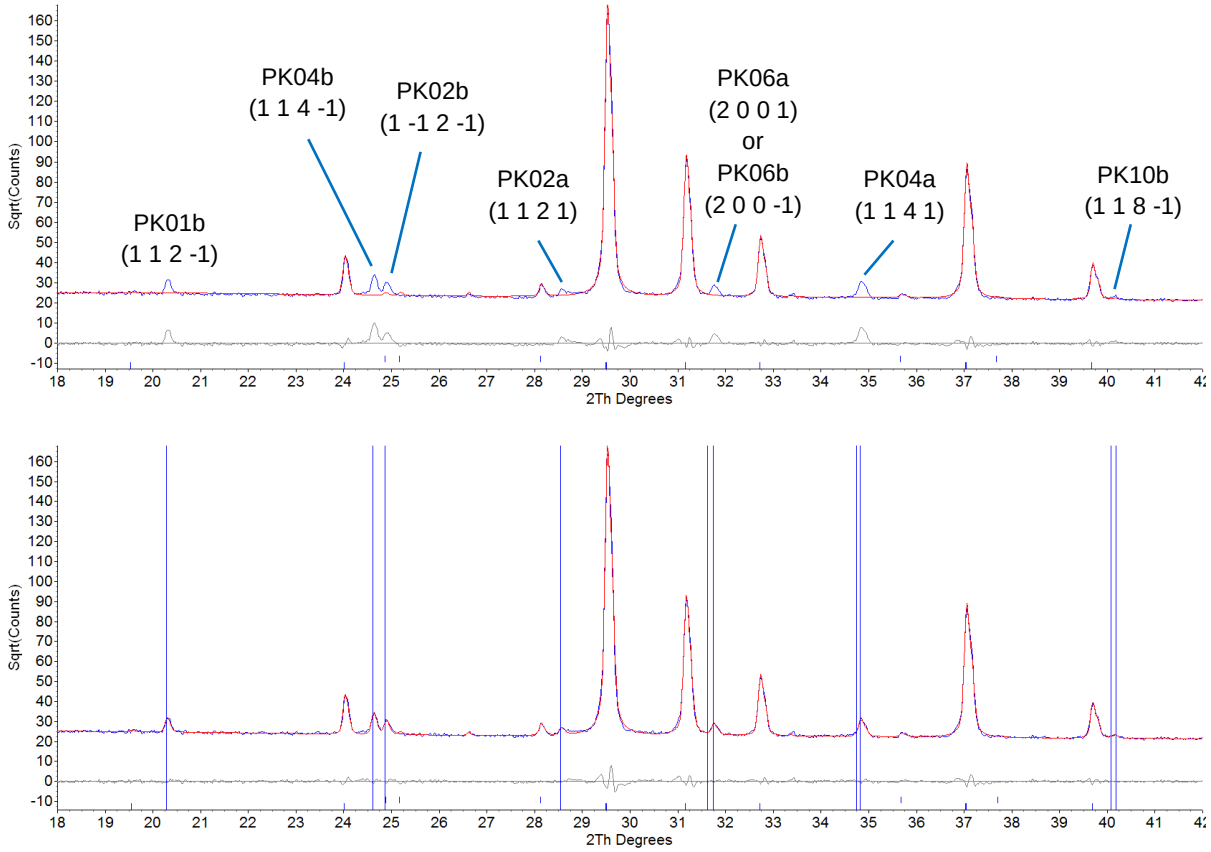

Figure 4.8. The modulation approach to fitting satellite peaks in $La_2O_2(Zn_{0.3}Mn_{0.7})Se_2$. The Pawley method was used to fit the strong subcell peaks and determine the subcell parameter (top). The position of the strongest satellite reflections were described by refining the modulation vector α (bottom).

```
#ifdef ic_peaks

prm !lam 1.540596
'Define k vector
prm !k_a 0
prm  k_b  0.21335`_0.00018
prm !k_c 1

macro get2th(h,k,l,lp_a,lp_b,lp_c)
{
(360/Pi)*ArcSin(lam/2*Sqrt((h)^2/(lp_a)^2+(k)^2/(lp_b)^2+(l)^2/(lp_c)^2));
} 'calculation of 2theta

'First order m = 1
prm IC_PK02a  = get2th(1+k_a,1+k_b,2+k_c,lpa,lpb,lpc)   '(1 1 2 1)
prm IC_PK04a  = get2th(1+k_a,1+k_b,4+k_c,lpa,lpb,lpc)   '(1 1 4 1)
prm IC_PK06a  = get2th(2+k_a,0+k_b,0+k_c,lpa,lpb,lpc)   '(2 0 0 1)

'First order m = -1
prm IC_PK01b  = get2th(1-k_a,1-k_b,2-k_c,lpa,lpb,lpc)   '(1 1 2 -1)
prm IC_PK02b  = get2th(1-k_a,-1-k_b,2-k_c,lpa,lpb,lpc)  '(1 -1 2 -1)
prm IC_PK04b  = get2th(1-k_a,1-k_b,4-k_c,lpa,lpb,lpc)   '(1 1 4 -1)
prm IC_PK06b  = get2th(2-k_a,0-k_b,0-k_c,lpa,lpb,lpc)   '(2 0 0 -1)
prm IC_PK10b  = get2th(1-k_a,1-k_b,8-k_c,lpa,lpb,lpc)   '(1 1 8 -1)

xo_Is
TCHZ_Peak_Type(pku,-0.00689`_0.00328, pkv,  0.01435`_0.00309,
pkw, -0.00744`_0.00066,!pkz, 0.0000, pky, 0.11988`_0.00155,!pkxz, 0.0000)
load xo I {

=IC_PK02a;:   28.539603`_0.00190582134   @  0.94298`_0.11038
=IC_PK04a;:   34.8236758`_0.00160535594  @  3.99955`_0.24813
=IC_PK06a;:   31.7185241`_0.000971337315 @  1.01627`_13818424.61485

=IC_PK01b;:   20.2728245`_0.00172182851  @  0.94663`_0.05835
=IC_PK02b;:   24.868687`_0.00216300221   @  1.50261`_0.09090
=IC_PK04b;:   24.5958181`_0.00143679824  @  2.20116`_0.10107
=IC_PK06b;:   31.7185241`_0.000971337315 @  1.01627`_13818424.61485
=IC_PK10b;:   40.0634603`_0.000990140638 @  0.54593`_0.22063

}
#endif
```

Figure 4.9. Snippet of input file used in the modulation approach to fitting the satellite reflections of Figure 4.8.

Figure 4.10 (top) shows the value of α over the six $Ln_2O_2(M_{1-y}M'_y)Se_2$ solid solutions, presented in the same sequence as Figure 4.3 (top). As the effective transition metal radius is increased going from left to right, there is a systematic decrease in α in both La and Ce series. A decrease in α corresponds to an increase in the ratio of corner:edge sharing tetrahedra in *m*C-1E.

For the smallest *M* = Fe case both the La and Ce 2D materials adopt the 0C-1E structure with $\alpha = 1$. Upon doping with a small amount of Zn ($y \leq 0.06$), $\alpha = 1$ (0C-1E) transforms to $\alpha = 1/4$ (3C-1E). The modulation vector appears to then lock in to this commensurate value, with $\alpha = 1/4$ over a range of y in both the La and Ce series. For the Ce series, as the average radius of M is increased further ($y > 0.5$ in $Fe_{1-y}Zn_y$) α changes smoothly from 1/4 to 1/5 (y~0.8) then locks in to this value up to ($Zn_{0.6}Mn_{0.4}$). α then changes smoothly before a small lock-in region at $\alpha = 1/6$. There appears to be no locking in to commensurate ordering beyond this point. Instead there is a rapid progression through compounds with a

continuously increasing ratio of corner- to edge-sharing $MSe_{4/2}$ tetrahedra. Very similar behaviour is seen for the La series but with a small "lag" relative to Ce due to the larger radius of La than Ce. The stability field of the $\alpha = 1/4$ structure is larger than for Ce, but there is no real evidence for a lock-in phase at $\alpha = 1/6$.

The evolution of α for $La_{2-z}Ce_zO_2MSe_2$ compounds is shown in Figure 4.10 (bottom). All pure Fe containing compounds show one extreme of ordering with $\alpha = 1$ (0C-1E), for all z. However, the $Ce_2O_2(Fe_{1-y}Zn_y)Se_2$ solid solution of Figure 4.10 (top) shows that 0C-1E ordering is lost upon ~5% Zn doping, suggesting that pure $FeSe_{4/2}$ layers are important for realizing exclusively edge-sharing tetrahedra. This suggests that Fe–Fe bonding could help stabilize this structure type. For Zn-containing compounds, $\alpha = 1/4$ for $0 < z \leq 1.4$. For $1.4 \leq z < 2$, α decreases gradually, then appears to be commensurate again at $z = 2$, with $\alpha = 1/5$. For the larger Mn compounds, the tendency to "lock in" to commensurate ordering is lower. Instead, a series of incommensurate compounds form, passing through an effectively commensurate example with $\alpha = 1/6$ at $z = 1.56$; $La_{0.44}Ce_{1.56}O_2MnSe_2$ can thus be described as having 5C-1E ordering. Exclusively Cd-containing compounds exhibit the second extreme of transition metal ordering, and contain purely corner sharing tetrahedra, 1C-0E.

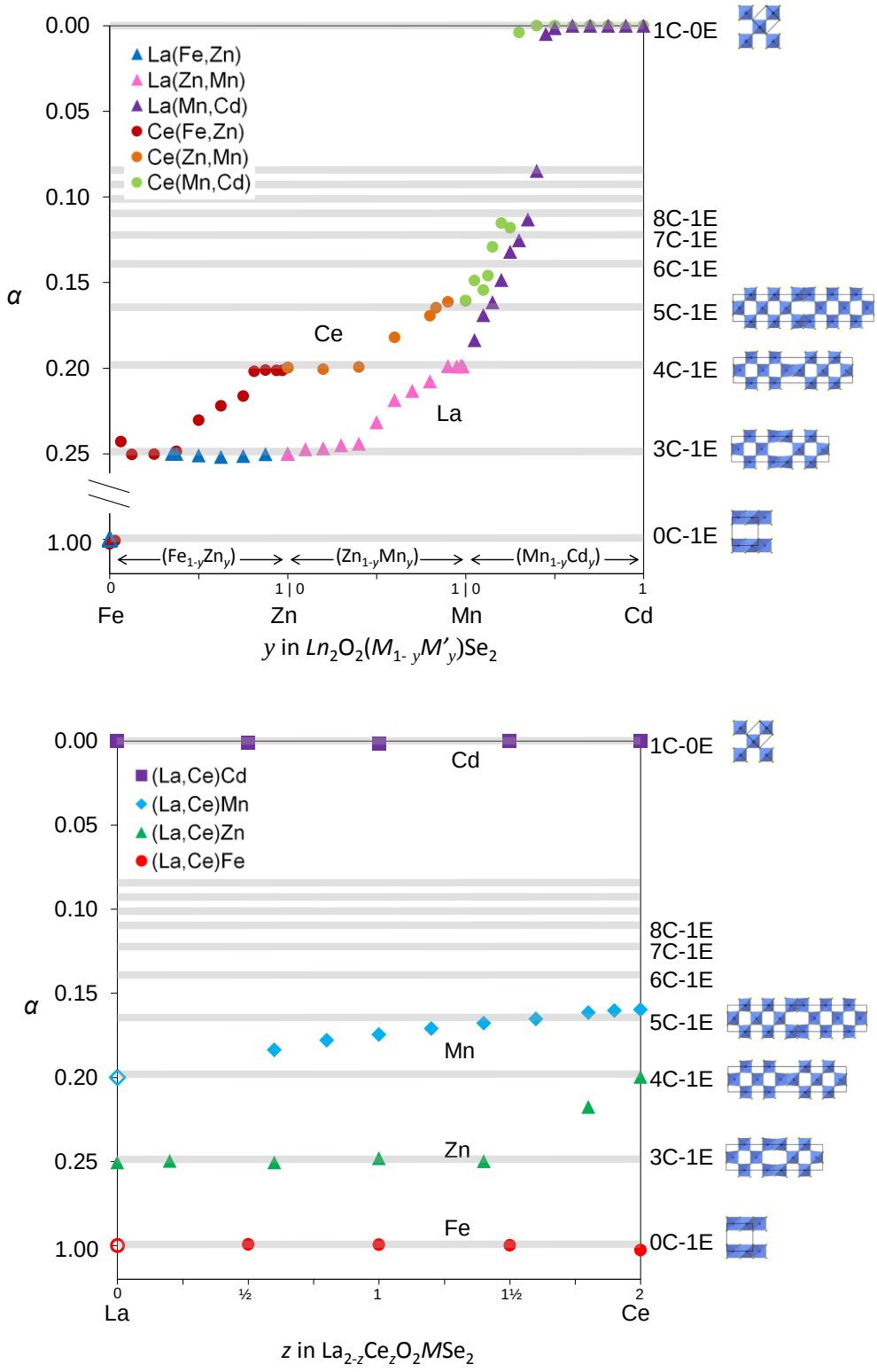

Figure 4.10. Modulation vector α for layered $Ln_2O_2(M_{1-y}M'_y)Se_2$ (top) and $Ln_{2-z}Ce_zO_2MSe_2$ (bottom) solid solutions. Grey bands represent commensurate ordering. The $La_2O_2FeSe_2$/$La_2O_2MnSe_2$ data points (open symbols) are taken from the literature.[7,8] Rietveld-derived error bars are smaller than individual data points.

4.6 Structural Models of Commensurate Examples

In order to fully understand all the structures shown in Figure 4.10, an incommensurate structure refinement would need to be done for many samples, ideally using single crystal methods. One such incommensurate refinement was performed by fellow group member Dr Chun-Hai Wang, on the compound $Ce_2O_2MnSe_2$.[11] This gave a high quality structural model for this phase, which is fully consistent with the arguments presented in this chapter. The atomic calculations observed also confirm the ideas of relatively rigid oxide and more flexible chalcogenide layers. To further confirm our structural model, we have selected four commensurate samples from the $Ln_2O_2(M_{1-y}M'_y)Se_2$ solid solutions for detailed X-ray and neutron structural studies. Each has an α value corresponding to a lock-in or commensurate structure. These were the Ce containing compounds $Ce_2O_2(Fe_{3/4}Zn_{1/4})Se_2$ (α = 1/4), $Ce_2O_2(Fe_{1/8}Zn_{7/8})Se_2$ (α = 1/5), and $Ce_2O_2(Zn_{1/6}Mn_{5/6})Se_2$ (α = 1/6) which represent 3C-1E, 4C-1E and 5C-1E structure types respectively, and the La containing compound $La_2O_2(Zn_{1/10}Mn_{9/10})Se_2$ (α = 1/5), a second example of 4C-1E. Non-standard space groups were used in all cases to keep the *c*-axis perpendicular to the layers for consistency with other structures of this type reported in the literature. These were *Bmeb* for the 3C-1E and 5C-1E structures, and *Imcb* for the 4C-1E structure. As discussed in Chapter 3 and elsewhere,[5,9] the structures could be described in lower symmetry settings, (with the loss of the mirror plane perpendicular to the *a*-axis), but this is beyond the information content of the powder diffraction data. A total of 27, 32, 37 and 32 structural variables were refined for $Ce_2O_2(Fe_{3/4}Zn_{1/4})Se_2$, $Ce_2O_2(Fe_{1/8}Zn_{7/8})Se_2$, $Ce_2O_2(Zn_{1/6}Mn_{5/6})Se_2$, and $La_2O_2(Zn_{1/10}Mn_{9/10})Se_2$ respectively along with parameters to describe peak shapes and background functions for the X-ray and 6 banks of neutron diffraction data. In all cases, transition metal sites were found to be fully occupied or fully empty within the quality of the data, and a single isotropic temperature factor was used for each atom type. In all cases an excellent fit to the powder data was obtained and the intensity and positions of key superstructure reflections were well described confirming our structural models. Full structural parameters and all refinement profiles can be found in Table 4.4 - Table 4.7 and Figure 4.11 - Figure 4.14. Rietveld plots of X-ray data highlighting regions with superstructure reflections are shown in Figure 4.15 for comparison.

Site label	Wyckoff site	*x*	*y*	*z*	B / Å^2	Occupancy
Ce(1)	8e	0.25	0.75	0.1830(4)	0.40(2)	1
Ce(2)	8f	0	0.2325(9)	0.8204(4)	0.40(2)	1
Ce(3)	16g	0.6252(3)	0.7338(6)	0.3192(3)	0.40(2)	1
O(1)	16g	0.6881(3)	0.492(2)	0.2471(1)	0.49(2)	1
O(2)	16g	0.4372(3)	0.4798(9)	0.2493(2)	0.49(2)	1
Fe(1)	8d	0.5661(1)	0	0	0.83(3)	0.75
Fe(2)	8d	0.8120(2)	0	0	0.83(3)	0.75
Zn(1)	8d	0.5661(1)	0	0	0.83(3)	0.25
Zn(2)	8d	0.8120(2)	0	0	0.83(3)	0.25
Se(1)	8e	0.25	0.75	0.4211(2)	0.64(2)	1
Se(2)	8f	0	0.2248(7)	0.5847(3)	0.64(2)	1
Se(3)	16g	0.6256(3)	0.7429(4)	0.0863(1)	0.64(2)	1

Table 4.4. Structural parameters of $Ce_2O_2(Fe_{3/4}Zn_{1/4})Se_2$ from combined refinement using room temperature PXRD and NPD data. Space group Bmeb, a = 22.7495(1) Å, b = 5.69246(3) Å, c = 17.63155(6) Å; R_{wp} = 1.909 %, R_p = 0.993 % and χ^2 = 2.501.

Site label	Wyckoff site	*x*	*y*	*z*	B / Å^2	Occupancy
Ce(1)	16k	0.2003(5)	0.744(2)	0.3201(4)	0.31(3)	1
Ce(2)	16k	0.4002(4)	0.770(1)	0.3159(3)	0.31(3)	1
Ce(3)	8j	0	0.772(2)	0.8225(6)	0.31(3)	1
O(1)	8g	0.75	0	0.2461(5)	0.33(4)	1
O(2)	16k	0.8492(4)	0.485(3)	0.2558(3)	0.33(4)	1
O(3)	16k	-0.0494(6)	-0.023(2)	0.2513(5)	0.33(4)	1
Fe(1)	8i	0.0554(3)	0.5	0	0.94(6)	0.125
Fe(2)	8h	0.1511(5)	0	0	0.94(6)	0.125
Fe(3)	4b	0.75	0	0.5	0.94(6)	0.125
Zn(1)	8i	0.0554(3)	0.5	0	0.94(6)	0.875
Zn(2)	8h	0.1511(5)	0	0	0.94(6)	0.875
Zn(3)	4b	0.75	0	0.5	0.94(6)	0.875
Se(1)	16k	0.6998(4)	0.259(2)	0.0811(3)	0.59(4)	1
Se(2)	16k	0.9009(4)	0.231(1)	0.0850(4)	0.59(4)	1
Se(3)	8j	0	0.732(2)	0.0918(5)	0.59(4)	1

Table 4.5. Structural parameters of $Ce_2O_2(Fe_{1/8}Zn_{7/8})Se_2$ from combined refinement using room temperature PXRD and NPD data. Space group Imcb, a = 28.3945(8) Å, b = 5.6792(2) Å, c = 17.7043(1) Å; R_{wp} = 2.858 %, R_p = 1.580 % and χ^2 = 5.462.

Site label	Wyckoff site	*x*	*y*	*z*	B / Å^2	Occupancy
Ce(1)	16g	0.5831(4)	0.231(1)	0.3162(4)	0.38(2)	1
Ce(2)	16g	0.6667(4)	0.742(1)	0.3185(4)	0.38(2)	1
Ce(3)	8f	0	0.717(2)	0.8167(6)	0.38(2)	1
Ce(4)	8e	0.25	0.75	0.1825(6)	0.38(2)	1
O(1)	16g	0.5415(3)	0.474(2)	0.2420(2)	0.28(2)	1
O(2)	16g	0.6244(4)	-0.015(2)	0.2490(3)	0.28(2)	1
O(3)	16g	0.7083(4)	0.494(4)	0.2490(3)	0.28(2)	1
Zn(1)	8d	-0.0451(6)	0	0	0.91(6)	0.166
Zn(2)	8d	0.7882(7)	0	0	0.91(6)	0.166
Zn(3)	8d	0.6251(7)	0	0	0.91(6)	0.166
Mn(1)	8d	-0.0451(6)	0	0	0.91(6)	0.833
Mn(2)	8d	0.7882(7)	0	0	0.91(6)	0.833
Mn(3)	8d	0.6250(7)	0	0	0.91(6)	0.833
Se(1)	8e	0.25	0.75	0.4126(6)	0.74(2)	1
Se(2)	8f	0	0.730(2)	0.5837(5)	0.74(2)	1
Se(3)	16g	0.6671(4)	0.739(1)	0.0891(4)	0.74(2)	1
Se(4)	16g	0.5832(4)	0.227(1)	0.0898(4)	0.74(2)	1

Table 4.6. Structural parameters of $Ce_2O_2(Zn_{1/6}Mn_{5/6})Se_2$ from combined refinement using room temperature PXRD and NPD data. Space group Bmeb, a = 34.0768(1) Å, b = 5.67696(3) Å, c = 18.12258(4) Å; R_{wp} = 1.849 %, R_p = 1.011 % and χ^2 = 2.082.

Site label	Wyckoff site	*x*	*y*	*z*	B / Å^2	Occupancy
La(1)	16k	0.1990(2)	0.743(1)	0.3175(3)	0.50(2)	1
La(2)	16k	0.3997(2)	0.7666(8)	0.3180(4)	0.50(2)	1
La(3)	8j	0	0.775(1)	0.8161(5)	0.50(2)	1
O(1)	8g	0.75	0	0.254(1)	0.49(4)	1
O(2)	16k	0.8501(8)	0.492(4)	0.2526(7)	0.49(4)	1
O(3)	16k	-0.0504(8)	-0.026(3)	0.2469(7)	0.49(4)	1
Zn(1)	8i	0.0537(5)	0.5	0.1	0.79(5)	0.1
Zn(2)	8h	0.1534(6)	0	0	0.79(5)	0.1
Zn(3)	4b	0.75	0	0.5	0.79(5)	0.1
Mn(1)	8i	0.0537(5)	0.5	0.1	0.79(5)	0.9
Mn(2)	8h	0.1534(6)	0	0	0.79(5)	0.9
Mn(3)	4b	0.75	0	0.5	0.79(5)	0.9
Se(1)	16k	0.7008(4)	0.258(2)	0.0861(5)	0.88(3)	1
Se(2)	16k	0.8987(4)	0.235(1)	0.0859(5)	0.88(3)	1
Se(3)	8j	0	0.724(2)	0.0914(6)	0.88(3)	1

Table 4.7. Structural parameters of $La_2O_2(Zn_{1/10}Mn_{9/10})Se_2$ from combined refinement using room temperature PXRD and NPD data. Space group Imcb, a = 28.6843(1) Å, b = 5.73465(3) Å, c = 18.27312(5) Å; R_{wp} = 1.764 %, R_p = 1.098 % and χ^2 = 1.537.

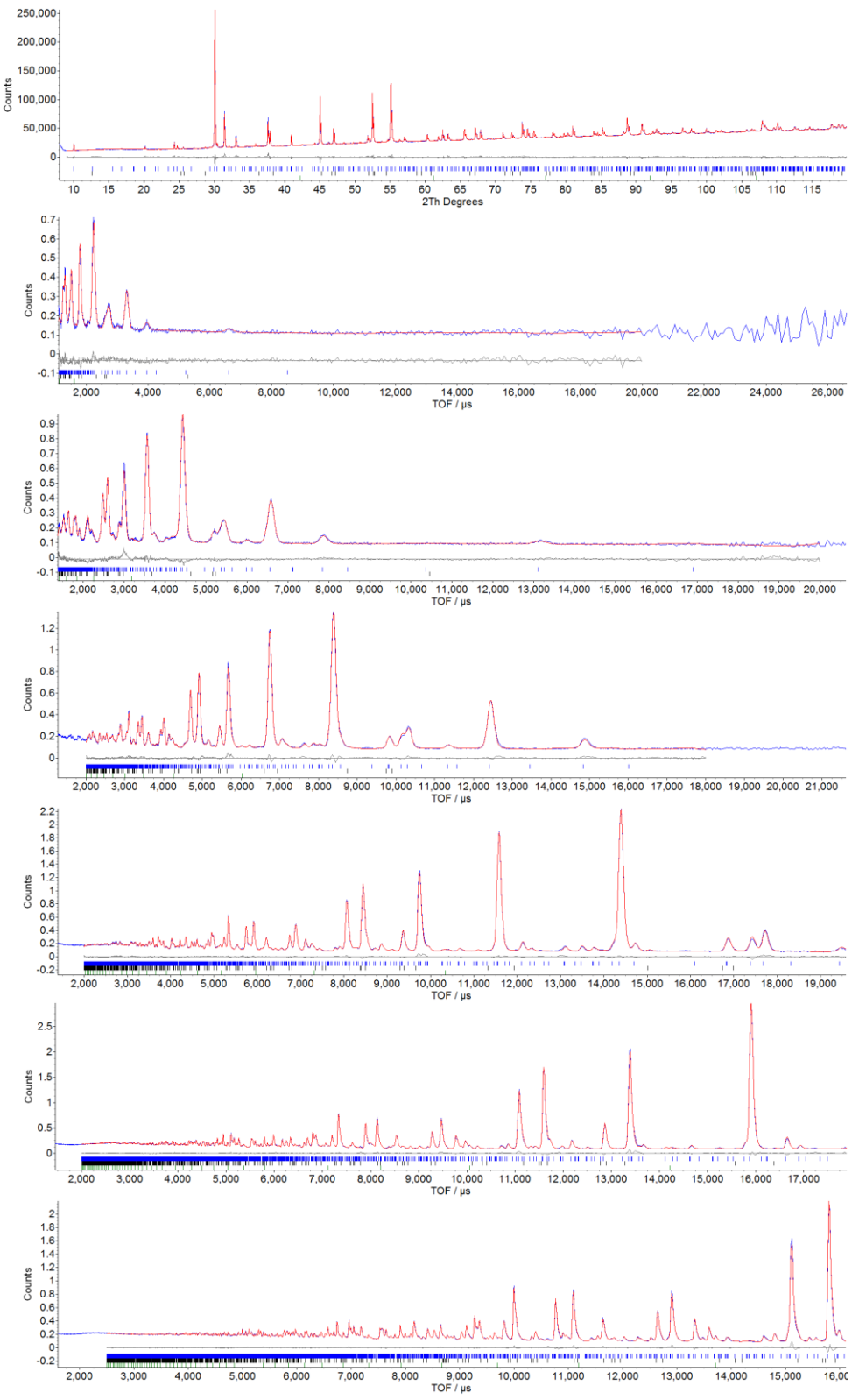

Figure 4.11. Rietveld refinement profiles from combined refinement of room temperature a) PXRD data and b) 9˚ bank, c) 18˚ bank, d) 35˚ bank, e) 64˚ bank, f) 91˚ bank, g) 154˚ bank NPD data, for $Ce_2O_2(Fe_{3/4}Zn_{1/4})Se_2$, in space group Bmeb (observed, calculated and difference profiles shown in blue, red and grey respectively). Tick marks show reflection positions for $Ce_2O_2(Fe_{3/4}Zn_{1/4})Se_2$ (blue), Ce_2O_2Se (black ~0.5% by weight) and vanadium (green, from sample can used in NPD data collection).

Figure 4.12. Rietveld refinement profiles from combined refinement of room temperature a) PXRD data and b) 9˚ bank, c) 18˚ bank, d) 35˚ bank, e) 64˚ bank, f) 91˚ bank, g) 154˚ bank NPD data, for $Ce_2O_2(Fe_{1/8}Zn_{7/8})Se_2$, in space group Imcb *(observed, calculated and difference profiles shown in blue, red and grey respectively). Tick marks show reflection positions for $Ce_2O_2(Fe_{1/8}Zn_{7/8})Se_2$ (blue), Ce_2O_2Se (black ~3% by weight) and vanadium (green, from sample can used in NPD data collection).*

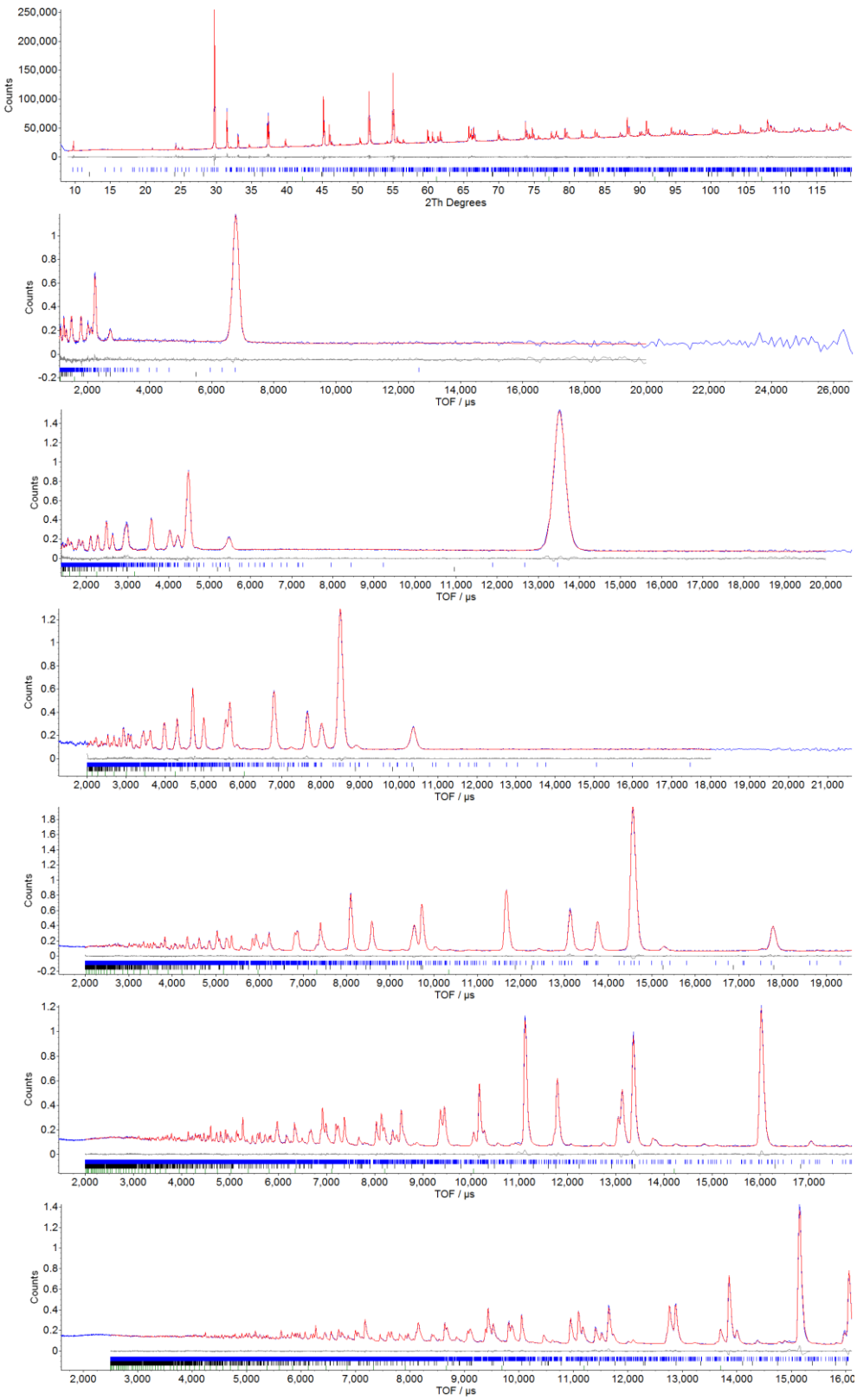

Figure 4.13. Rietveld refinement profiles from combined refinement of room temperature a) PXRD data and b) 9˚ bank, c) 18˚ bank, d) 35˚ bank, e) 64˚ bank, f) 91˚ bank, g) 154˚ bank NPD data, for $Ce_2O_2(Zn_{1/6}Mn_{5/6})Se_2$, in space group Imcb (observed, calculated and difference profiles shown in blue, red and grey respectively). Tick marks show reflection positions for $Ce_2O_2(Zn_{1/6}Mn_{5/6})Se_2$ (blue), Ce_2O_2Se (black ~0.5% by weight) and vanadium (green, from sample can used in NPD data collection).

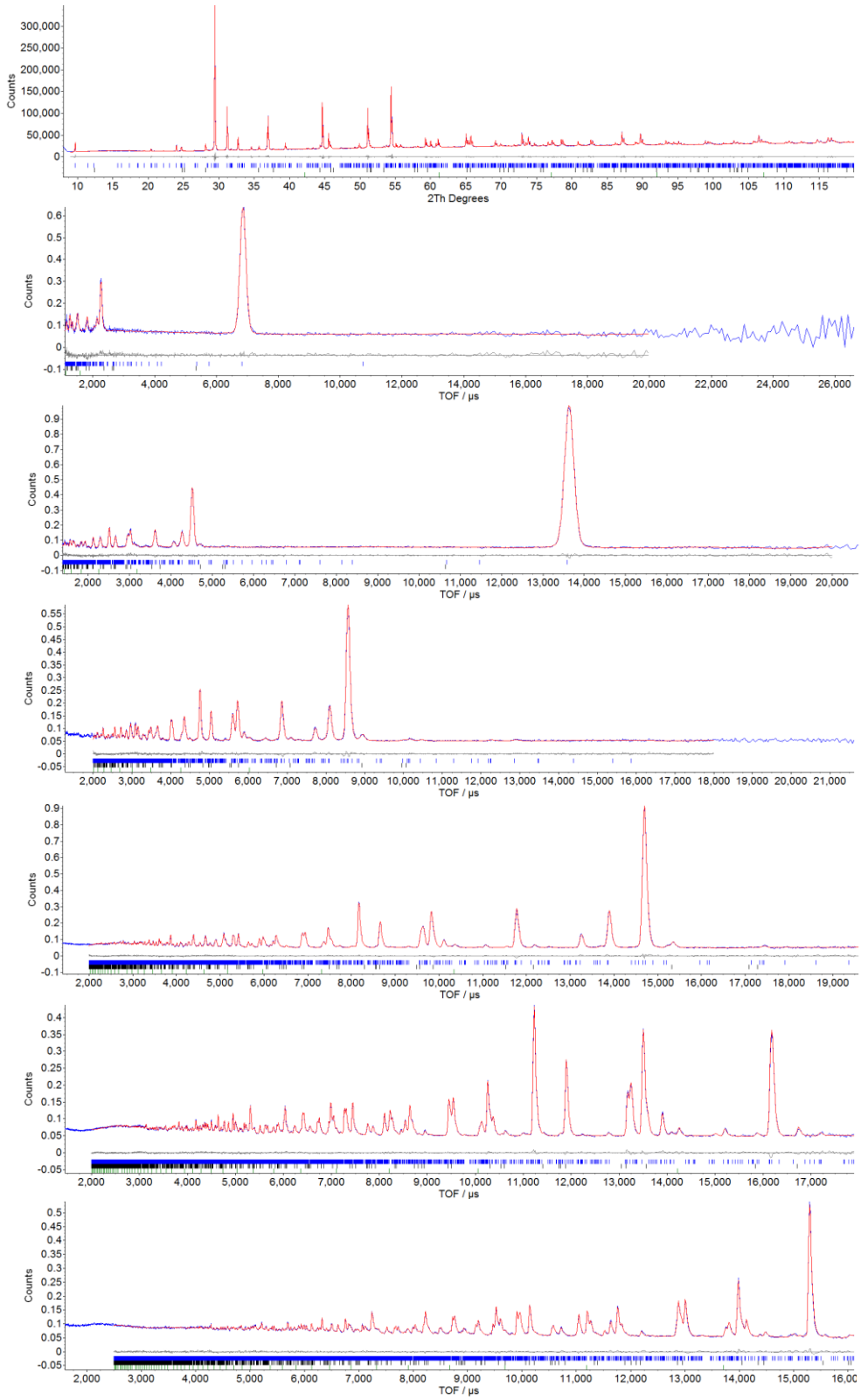

Figure 4.14. Rietveld refinement profiles from combined refinement of room temperature a) PXRD data and b) 9˚ bank, c) 18˚ bank, d) 35˚ bank, e) 64˚ bank, f) 91˚ bank, g) 154˚ bank NPD data, for $La_2O_2(Zn_{1/10}Mn_{9/10})Se_2$, in space group Imcb (observed, calculated and difference profiles shown in blue, red and grey respectively). Tick marks show reflection positions for $La_2O_2(Zn_{1/10}Mn_{9/10})Se_2$ (blue), La_2O_2Se (black ~4% by weight) and vanadium (green, from sample can used in NPD data collection).

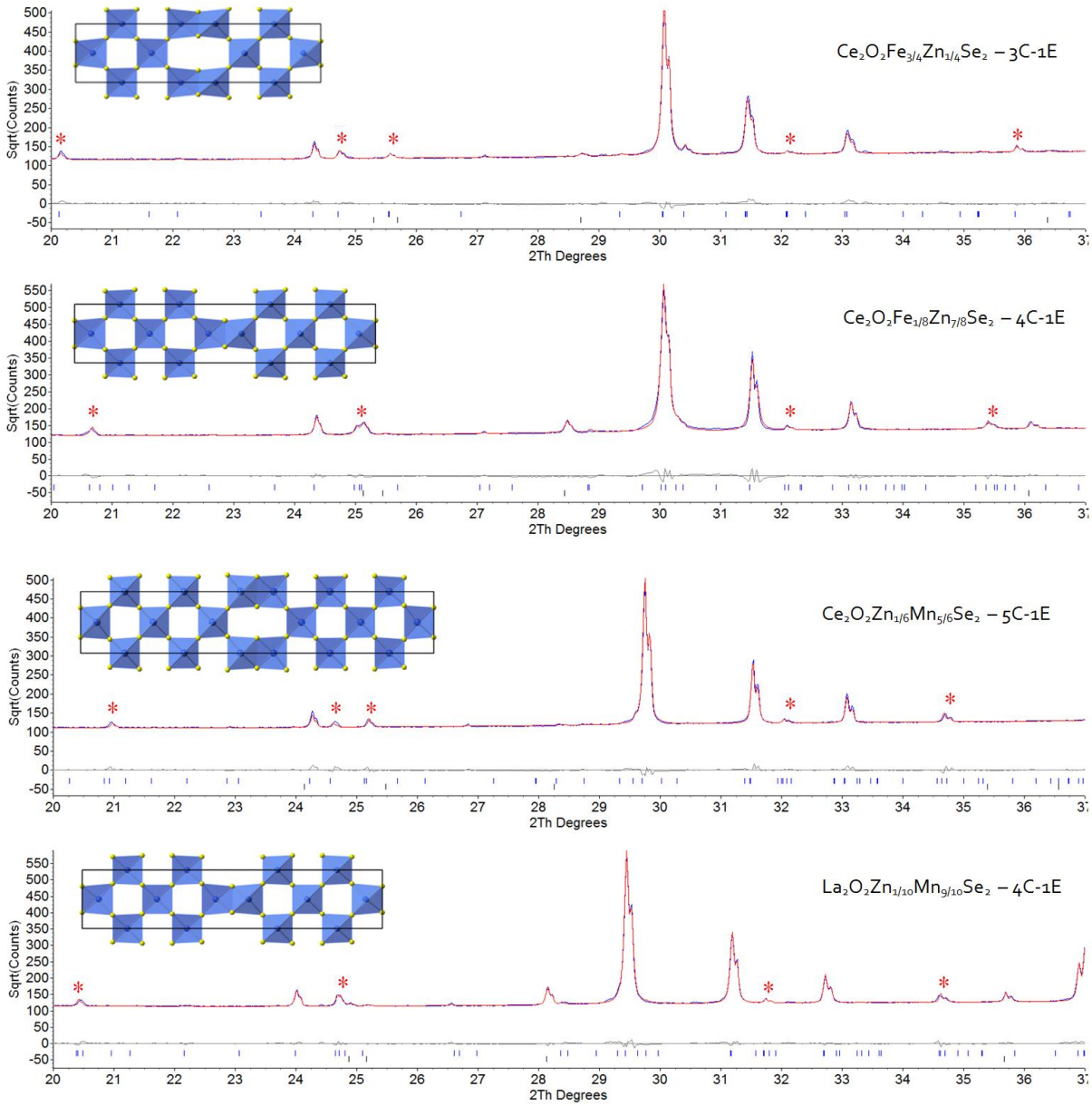

Figure 4.15. X-ray Rietveld profiles from combined X-ray and neutron refinements of selected commensurate samples from the $Ln_2O_2(M_{1-y}M'_y)Se_2$ series. Data are plotted on a $\sqrt{I}$ scale to emphasize weak supercell reflections, which are marked with an asterisk.

Synchrotron powder data were also collected for $Ce_2O_2CdSe_2$, a previously unreported quaternary oxychalcogenide. It is isostructural to $La_2O_2CdSe_2$,[3] space group $P4_2/nmc$, with $[CdSe_2]^{2-}$ layers containing exclusively corner-sharing $CdSe_{4/2}$ tetrahedra (α = 0, 1C-0E). A total of 10 structural variables were refined along with parameters to describe peak shapes and background functions. Transition metal sites were found to be fully occupied or fully empty within the quality of the data, and isotropic temperature factors were used for each atom type. Full structural parameters and the refinement profile can be found in Table 4.8 and Figure 4.16.

Site label	Wyckoff site	*x*	*y*	*z*	B / Å^2	Occupancy
Ce(1)	4d	0.5	0	0.18464(1)	0.71(2)	1
O(1)	4c	0	0	0.2489(1)	1.03(5)	1
Cd(1)	2a	0	0	0	1.26(3)	1
Se(1)	4d	0	0.5	0.59314(2)	1.04(2)	1

Table 4.8. Structural parameters of $Ce_2O_2CdSe_2$ from refinement using room temperature synchrotron XRPD data. Space group $P4_2/nmc$, a = 4.031950 (4) Å, c = 18.54850 (3) Å; R_{wp} = 3.597 %, R_p = 2.373 % and χ^2 = 10.062.

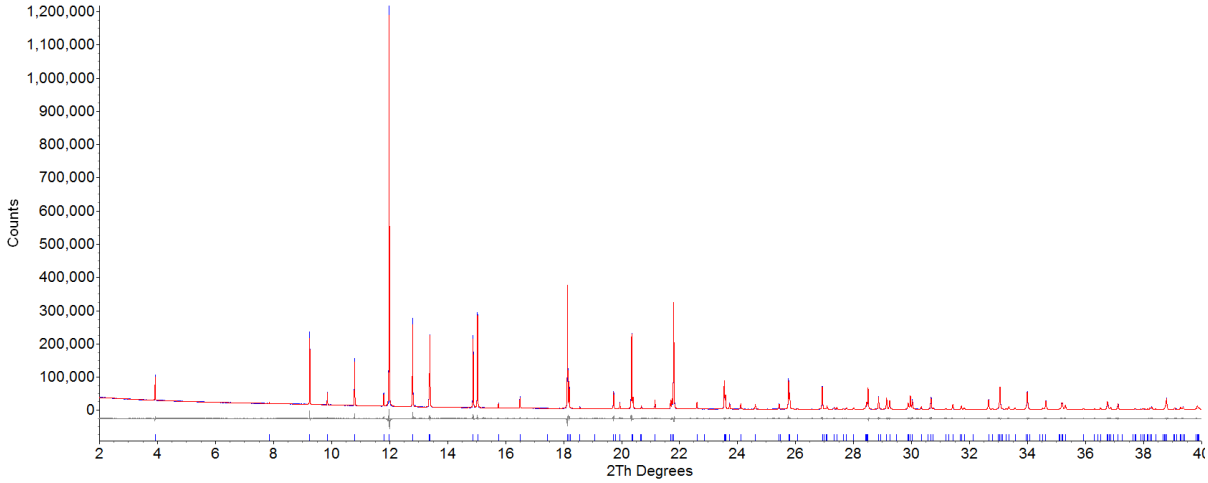

Figure 4.16. Rietveld refinement profiles from refinement of room temperature synchrotron XRPD data for $Ce_2O_2CdSe_2$, in space group P42/nmc (observed, calculated and difference profiles shown in blue, red and grey respectively). Blue tick marks show $Ce_2O_2CdSe_2$ reflection positions.

4.7 The Structural Chemistry of $Ln_2O_2MSe_2$ Materials

The information on the changes in unit cell parameters, modulation vector and detailed structure described above give significant insight into the structural chemistry of $Ln_2O_2MSe_2$ materials.

Firstly, it is clear from Figure 4.4 and Figure 4.5 that a given edge-sharing $[Ln_2O_2]^{2+}$ tetrahedral layer is relatively rigid, with its size and geometry insensitive to the transition metal layer to a first approximation. It is, however, important to note that the $OLn_{4/2}$ edge-shared tetrahedra are not ideal but significantly compressed along the *c*-axis. This is common to $Ln_2O_2MSe_2$ and related *LnOMCh* materials as shown by the tetrahedral bond angles summarized for end-member compounds in Table 4.9.[2-5,7,12-14] The $[Ln_2O_2]^{2+}$ rigidity means that as the radius of *M* is increased, the *a*/*b* cell parameters remain essentially unchanged, and the unit cell volume increase is largely due to a change in the *c*-axis as the $[Ln_2O_2]^{2+}$ layers move further apart.

	angle 1	angle 2		angle 1	angle 2		angle 1	angle 2
LaFe	118.2	105.2	CeFe	118.3	105.2	LaOCuSe	117.7	105.5
LaZn	117.3	105.7	CeZn	117.3	105.7			
LaMn	117.5	105.6	CeMn	117.7	105.5	LaOFeAs	117.0	105.9
LaCd	117.7	105.5	CeCd	117.9	105.4	CeOFeAs	117.4	105.7

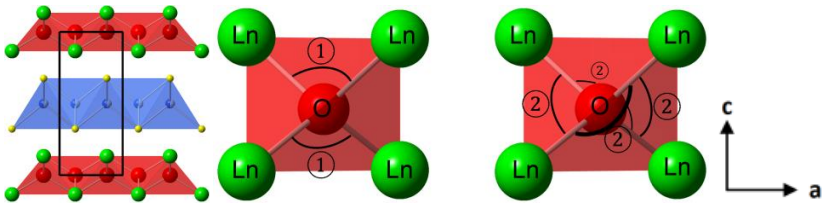

Table 4.9. Average bond angles around Ln–$O_{4/2}$ tetrahedra in a range of ZrCuSiAs-related compounds.

The fact that structural distortions occur primarily in the $[MSe_2]^{2-}$ layers can also be seen from Figure 4.17, which shows the thickness along the *c*-axis of *Ln*-O-*Ln*, Se-*Ln*-O-*Ln*-Se and Se-*M*-Se blocks for structurally characterized samples[2-5,7-9] with increasing sizes of *M*. The thickness of the $[Ln_2O_2]^{2+}$ and $[Ln_2O_2Se_2]^{2-}$ block shows little change across the series whereas there is a systematic and significant increase in the thickness of the $[MSe_2]^{2-}$ block.

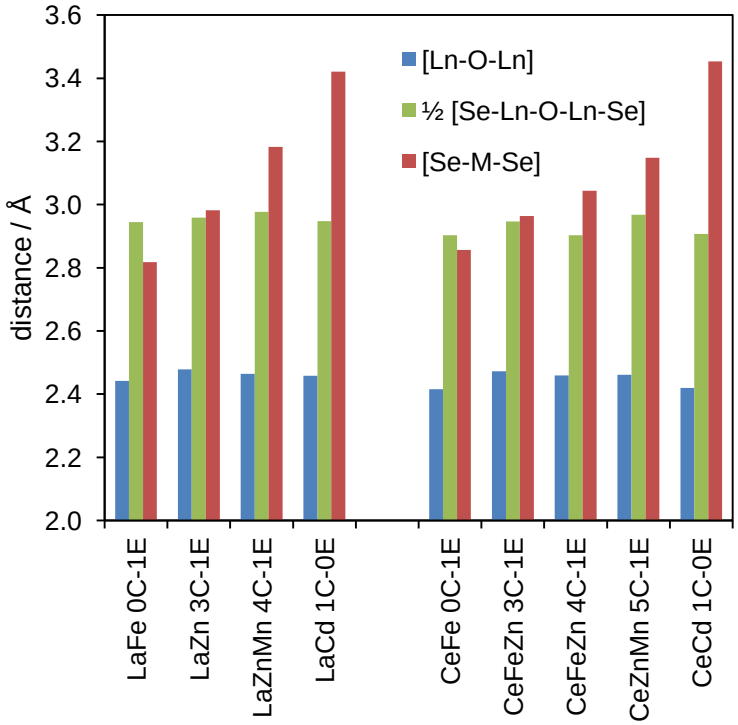

Figure 4.17. The thickness along the c-axis of Ln-O-Ln, Se-Ln-O-Ln-Se and Se-M-Se blocks for structurally characterized samples[2-5,7-9] with increasing sizes of M.

This flexibility reflects the fact that MSe_2 layers can respond to the fixed $[Ln_2O_2]^{2+}$ size in different ways. If we focus on the La($Zn_{1-y}Mn_y$) series, we observe a lock-in region for $0 < y < 0.5$ where the $\alpha = 1/4$ (3C-1E) structure is retained and the cell volume undergoes a gradual Vegard-like increase. The increase in the *c*-axis implies a gradual distortion of $MSe_{4/2}$ in this region. For $y > 0.5$, however, the change in modulation vector α ($\mathbf{q} = \alpha\mathbf{a^*} + 0\mathbf{b^*} + 0.5\mathbf{c^*}$) shows that the structure responds in a different way and that the ratio of corner- to edge-shared tetrahedra is systematically increased from 3C-1E to 4C1E (and to 5C-1E and

beyond as Cd is introduced). A similar effect is seen for the Ce series but the lock in region is α = 1/5 (4C-1E) for 0 < y < 0.5, rising to α = 0.158 (5.33C-1E) for y = 1.

The change in transition metal architecture can be explained by the fact that corner-shared tetrahedra are a more compact way of occupying 2-dimensional space than edge-shared tetrahedra. Therefore, as the size of the $[MSe_2]^{2-}$ block is increased relative to the $[Ln_2O_2]^{2+}$ block (either by increasing *M* or decreasing *Ln* radius) the proportion of corner-sharing tetrahedra will increase to compensate.

The local structural changes allowing the flexibility can be understood by considering the structure in terms of rows of Se atoms perpendicular to the *a*-axis of the modulated structures (e.g. 3C-1E and 4C-1E structures in Figure 4.2). These rows repeat every $a_{subcell}/\sqrt{2}$ ~ 2.82 Å. Typical values of edge- and corner-shared *M*–*M* distances are, for example, 3.1 Å and 4.0 Å in $Ce_2O_2ZnSe_2$[5] and 3.2 and 4.0 Å in $Ce_2O_2MnSe_2$.[9] A corner sharing $MSe_{4/2}$ arrangement leads to rows of transition metals along *a* separated by $M\text{-}M/\sqrt{2}$ ~ 2.82 Å, whereas edge-sharing leads to rows separated by ~3.1 Å. Introduction of edge-sharing tetrahedra, which distort due to *M*–*M* proximity, therefore allows the $[MSe_2]^{2-}$ layer to expand to size-match the $[Ln_2O_2]^{2+}$ layers.

Figure 4.3 shows that the volume change across the ($Zn_{1-y}Mn_y$) and ($Mn_{1-y}Cd_y$) solid solutions is approximately equal (or perhaps slightly higher for the former than the latter), despite the larger difference in ionic radius for the Mn/Cd pair; this goes against Vegard's law expectations. The modulation vector plot of Figure 4.10 (top) shows, however, that this can be explained by the constantly evolving value of α, and therefore constantly increasing proportion of smaller corner-sharing units in the (Mn/Cd) case.

As discussed above, the 0C-1E structure is favoured for pure-Fe containing samples. This suggests that Fe–Fe bonding could help stabilize this structure type, and is consistent with the known tendency of FeSe to adopt structures such as the superconducting PbO-type polymorph with layers of edge-sharing tetrahedra, and a NiAs-type polymorph with face-shared octahedra; both structures encourage Fe–Fe bonding.[15] The observation that the cell parameter parallel to the chain direction is smaller than that perpendicular (a < b) gives some support to this observation. It is also clear from Figure 4.3 that the cell volumes of 0C-1E structures are significantly lower than those with corner-sharing. Whilst it's tempting to ascribe this to Fe–Fe bonding, the main contribution to the volume reduction is a ~1% contraction of the *c*-axis relative to other structures, suggesting the origins are more complex.

The $Ln_2O_2MSe_2$ materials therefore emerge as an infinitely adaptive set of structures with the $[MSe_2]^{2-}$ layers responding to changes in rigid $[Ln_2O_2]^{2+}$ layers by either internal distortions (around lock in regions) or continual structural change. There is clearly a fine balance between strain energy terms and the energetic penalties of introducing edge-shared tetrahedra.

4.8 Conclusions

In summary, the origins of transition metal ordering in $Ln_2O_2MSe_2$ type oxychalcogenides have been revealed by investigating a range of solid solutions. Transition metal ordering is determined by the relative sizes of $[Ln_2O_2]^{2+}$ and $[MSe_2]^{2-}$ layers, and can be exquisitely

tuned by substitution in either layer. The two extremes of transition metal ordering contain $MSe_{4/2}$ tetrahedra that are exclusively edge-sharing (stripe-like) or exclusively corner-sharing (checkerboard-like). The proportion of the inherently smaller corner-shared motif increases as the transition metal size increases relative to the lanthanide oxide layers. Detailed structural information has been determined for the commensurate compounds $Ce_2O_2(Fe_{3/4}Zn_{1/4})Se_2$ (3C-1E), $Ce_2O_2(Fe_{1/8}Zn_{7/8})Se_2$ (4C-1E), $Ce_2O_2(Zn_{1/6}Mn_{5/6})Se_2$ (5C-1E), $La_2O_2(Zn_{1/10}Mn_{9/10})Se_2$ (4C-1E) and $Ce_2O_2CdSe_2$ (1C-0E).

4.9 References

(1) Ijjaali, I.; Mitchell, K.; Haynes, C. L.; McFarland, A. D.; Van Duyne, R. P.; Ibers, J. A. *J. Solid State Chem.* **2003**, *176*, 170.
(2) McCabe, E. E.; Free, D. G.; Evans, J. S. O. *Chem. Commun.* **2011**, *47*, 1261.
(3) Hiramatsu, H.; Ueda, K.; Kamiya, T.; Ohta, H.; Hirano, M.; Hosono, H. *J. Mater. Chem.* **2004**, *14*, 2946.
(4) Tuxworth, A. J.; McCabe, E. E.; Free, D. G.; Clark, S. J.; Evans, J. S. O. *Inorg. Chem.* **2013**, *52*, 2078.
(5) Ainsworth, C. M.; Wang, C.-H.; Tucker, M. G.; Evans, J. S. O. *Inorg. Chem.* **2015**, *54*, 1563.
(6) McCabe, E. E.; Free, D. G.; Mendis, B. G.; Higgins, J. S.; Evans, J. S. O. *Chem. Mater.* **2010**, *22*, 6171.
(7) Nitsche, F.; Niklaus, R.; Johrendt, D. *Z. Anorg. Allg. Chem.* **2014**, *640*, 2897.
(8) Peschke, S.; Nitsche, F.; Johrendt, D. *Z. Anorg. Allg. Chem.* **2015**, DOI 10.1002/zaac.201400603.
(9) Wang, C. H.; Ainsworth, C. M.; Gui, D. Y.; McCabe, E. E.; Tucker, M. G.; Evans, I. R.; Evans, J. S. O. *Chem. Mater.* **2015**, DOI 10.1021/acs.chemmater.5b00666.
(10) Shannon, R. *Acta Crystallogr. A* **1976**, *32*, 751.
(11) Wang, C.-H.; Ainsworth, C. M.; Gui, D.-Y.; McCabe, E. E.; Tucker, M. G.; Evans, I. R.; Evans, J. S. O. *Chem. Mater.* **2015**, *27*, 3121.
(12) Hiramatsu, H.; Yanagi, H.; Kamiya, T.; Ueda, K.; Hirano, M.; Hosono, H. *Chem. Mater.* **2008**, *20*, 326.
(13) Kamihara, Y.; Watanabe, T.; Hirano, M.; Hosono, H. *J. Am. Chem. Soc.* **2008**, *130*, 3296.
(14) Zhao, J.; Huang, Q.; de la Cruz, C.; Li, S. L.; Lynn, J. W.; Chen, Y.; Green, M. A.; Chen, G. F.; Li, G.; Li, Z.; Luo, J. L.; Wang, N. L.; Dai, P. C. *Nature Mater.* **2008**, *7*, 953.
(15) Hsu, F. C.; Luo, J. Y.; Yeh, K. W.; Chen, T. K.; Huang, T. W.; Wu, P. M.; Lee, Y. C.; Huang, Y. L.; Chu, Y. Y.; Yan, D. C.; Wu, M. K. *Proc Natl Acad Sci U S A* **2008**, *105*, 14262.

Chapter 5: 3D Transition Metal Ordering and Rietveld Stacking Fault Quantification of the New Oxychalcogenides $La_2O_2Cu_{2-2x}Cd_xSe_2$ $0 \leq x \leq 1$

5.1 Introduction

Chapter 4 described how combining rigid-geometry oxide building blocks with more flexible or adaptive chalcogenide layers can lead to infinitely adaptive structures with remarkable structural complexity (though governed by simple rules) within two dimensional layers. Chapter 5 shows that this complexity can be extended to 3 dimensions in a new family of mixed metal oxychalcogenides.

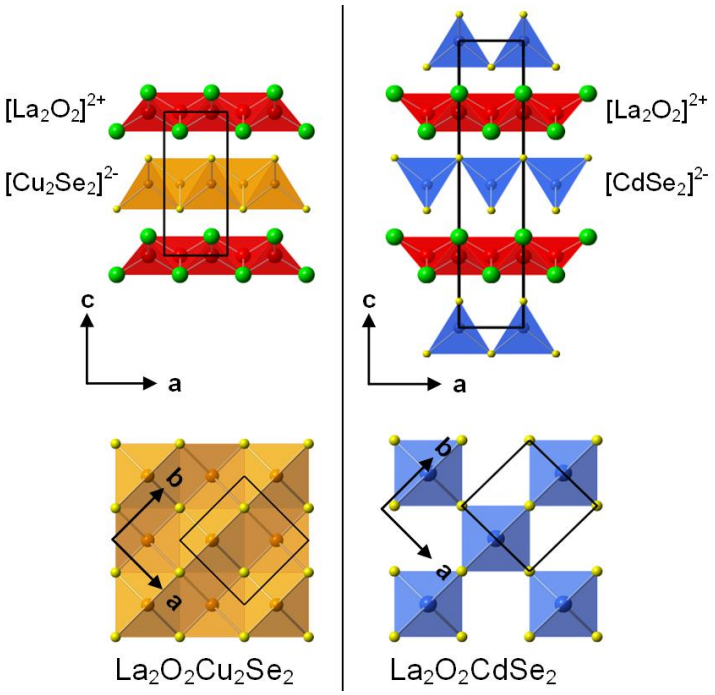

Figure 5.1. ZrCuSiAs-derived structures reported for (left) $La_2O_2Cu_2Se_2$, P4/nmm symmetry, (right) $La_2O_2CdSe_2$, $P4_2/nmc$ symmetry. Top figures show the fluorite-like sheets of edge-sharing Ln_4O tetrahedra (red) and antifluorite-like sheets of MSe_4 tetrahedra (orange/blue). Bottom figures are the view down [001], showing the arrangement of MSe_4 tetrahedra. La^{3+} cations are shown in green, O^{2-} anions in red, Cu^{1+} cations in orange, Cd^{2+} cations in blue and Se^{2-} anions in yellow.

The compounds reported in this chapter are structurally related to *Ln*OCu*Ch* (*Ln* = La–Nd, Bi; Ch = S, Se, Te) materials,[1,2] though the doubled $La_2O_2Cu_2Ch_2$ formula is more convenient for consistency with other materials (Figure 5.1, left). The oxidation state of Cu within these structures is +1, with full occupancy of the available tetrahedral sites. Chapters 3 and 4 (and related publications[3-11]) outlined the structures of a range of related compounds containing +2 metals, where charge balance leads to half the available metal sites in the tetrahedral layers being occupied and composition $Ln_2O_2MSe_2$. In the case of *M* = Cd this leads to the simple checkerboard ordering pattern (Figure 1, right) in which tetrahedra are exclusively corner-shared.[4]

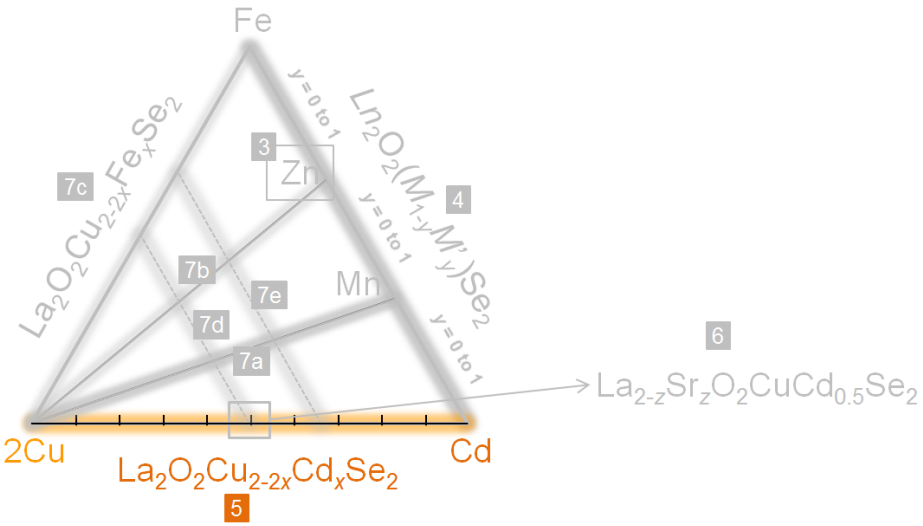

Figure 5.2. Thesis map highlighting the area of work discussed in Chapter 5.

In Chapter 5, the synthesis and characterisation of the first M^{1+}/M^{2+} systems is presented in the $La_2O_2Cu_{2-2x}Cd_xSe_2$ family, which represents the orange line in the thesis map shown in Figure 5.2. There is a remarkable degree of long-range cation ordering, this time along the *c*-axis of the structures, whereby it is possible to access each of the new structure types shown schematically in Figure 5.3 from x = 0 (all Cu) to x = 1 (all Cd). Obtaining full information on both the structure and microstructure of these materials has required development of a DIFFaX-like[12] approach to the treatment of stacking faults in a Rietveld refinement.

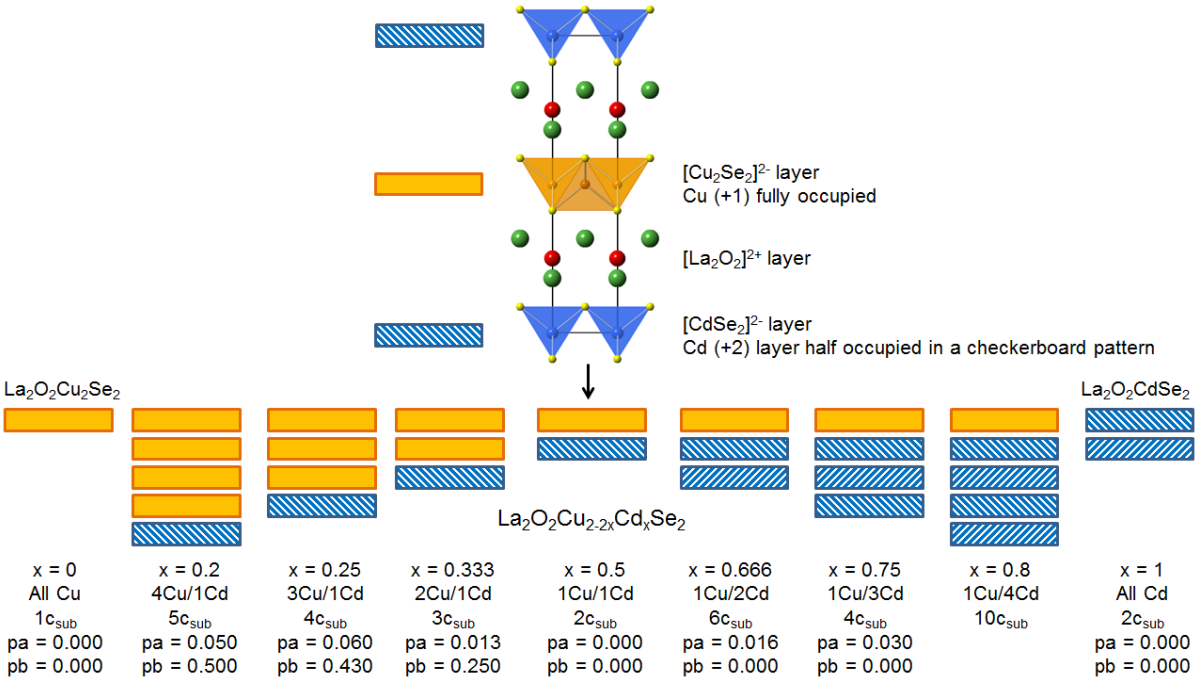

Figure 5.3. Schematic showing the unique crystallographic layers in samples prepared in the $La_2O_2Cu_{2-2x}Cd_xSe_2$ solid solution. The c-axis length relative to a $Ln_2O_2Cu_2Ch_2$ subcell model is shown along with the fraction of pa and pb-type faults present (discussed later in the text). Direction of blue hatching reflects different positions in the ab plane of Cd-centred tetrahedral layers.

5.2 Stacking Fault Methodology

The powder diffraction data of several of the new compounds described below showed significant *hkl*-dependence to peak widths and/or marked Warren-like[13] peak shapes which are suggestive of stacking faults.[14] Such faults are commonly found in layered materials, and whilst there have been various analytical and computational approaches to quantify them, readily accessible Rietveld-like approaches are limited. One implementation is the DIFFaX+ suite of Leoni et al. which places Treacy, Newsam and Deem's DIFFaX algorithm in a least squares framework to allow refinement of stacking fault probabilities, though the approach is computationally demanding.[15] A second is the FAULTS approach of Casas-Cabanas *et al*..[16]

To fully characterise these materials, extensive work was undertaken by Professor John Evans (PhD supervisor), Dr Alan Coelho (author of the TOPAS software) and James Lewis (a fellow PhD student) to develop a DIFFaX-like[12] methodology for Rietveld refinement in the TOPAS suite which offers significant speed and flexibility advantages over previous approaches. It allows analysis of stacking faults alongside all the other features of TOPAS (multi-phase, multi-dataset, user-defined fitting functions and convolutions, parametric refinements, symmetry mode refinements, magnetism, etc). The method builds on the supercell approach described by Ufer and co-workers[17-19] which has been applied in a Rietveld-like context for systems with a limited number of layers by Wang and Bette.[20,21] In this method the structure is described in terms of a stack of individual layers in a supercell defined along the *c*-axis of the basic crystallographic cell. Individual layers in this supercell may differ in terms of chemical composition, internal structure or overall position in *x*, *y* or *z* relative to a reference layer. For a perfect or unfaulted stacking sequence the calculated pattern from the supercell will be identical to a conventional crystallographic subcell description (as all supercell reflections will have zero intensity). As faults are introduced into the stack, the superposition of multiple closely-spaced supercell reflections will sum to produce the complex peak shapes observed experimentally. By embedding this in a Rietveld package such as TOPAS, one can obtain simultaneous information about structure and microstructure of new materials. In the implementation used in this work, the probabilities *pn* of layer-to-layer transitions are defined using a probability matrix of the format defined in the DIFFaX software package of Treacy et al.[12] A python routine reads this matrix and produces an input file suitable for Rietveld refinement in TOPAS. For structures containing layers of different chemical composition the user can control the overall composition.

One of the major issues with this approach has been the size of the supercell that can be used. There are many potential advantages of using a large supercell: low probability stacking faults can be identified, the closely-spaced *hkl* reflections better approximate the continuous diffuse scatter expected in reciprocal space, and an individual supercell description is likely to be a good statistical approximation of the ensemble of different crystallites contributing to the powder pattern. There are, however, significant computational bottlenecks associated with calculating the powder pattern from a large supercell, in particular the large number of reflections that must be summed to produce the calculated pattern, y_{calc}. In previous work this has required handling *00l* and *hk0* reflections separately for turbostratic systems,[18,19] or the use of relatively small supercells to approximate materials.[20,21] In this work we have introduced new approximations to the Rietveld method which circumvent this problem. The most significant of these impacts the peaks buffer (for computational efficiency phase peaks are calculated at predefined 2θ intervals in a "peaks

buffer" and in between peaks are determined by stretching and interpolating, which hugely reduces the number of peaks actually calculated). In cases where peak properties are *hkl* dependent, anisotropic peak broadening for example, TOPAS traditionally eliminated the peaks buffer and a new individual peak shape was calculated for each reflection regardless of any similarities in peak shapes. This process works well in typical Rietveld refinements where a few hundred to maybe a few thousand reflections are present. However in the present work, supercells can result in hundreds of thousands to even millions of *hkl* reflections each potentially having a unique peak shape due to a *hkl*-dependent aberration.

To speed up the process TOPAS now also allows tolerances for peaks which are *hkl* dependent, where peak shapes are only calculated for reflections at the start and end of a given 2θ range; between these ends peaks are interpolated or stretched to model intervening peaks. The net result is that a whole pattern can be described using hundreds rather than hundreds of thousands of peaks, allowing the synthesis of diffraction patterns in a fraction of the time with little or no loss in precision. Subsequent Rietveld refinement can therefore be performed with very little impact on the fit quality or the derived parameters. Of equal importance is the reduction in computer memory usage realized through the reduction in the size of the peaks buffer; Rietveld refinement without such a reduction in memory would not otherwise be possible.

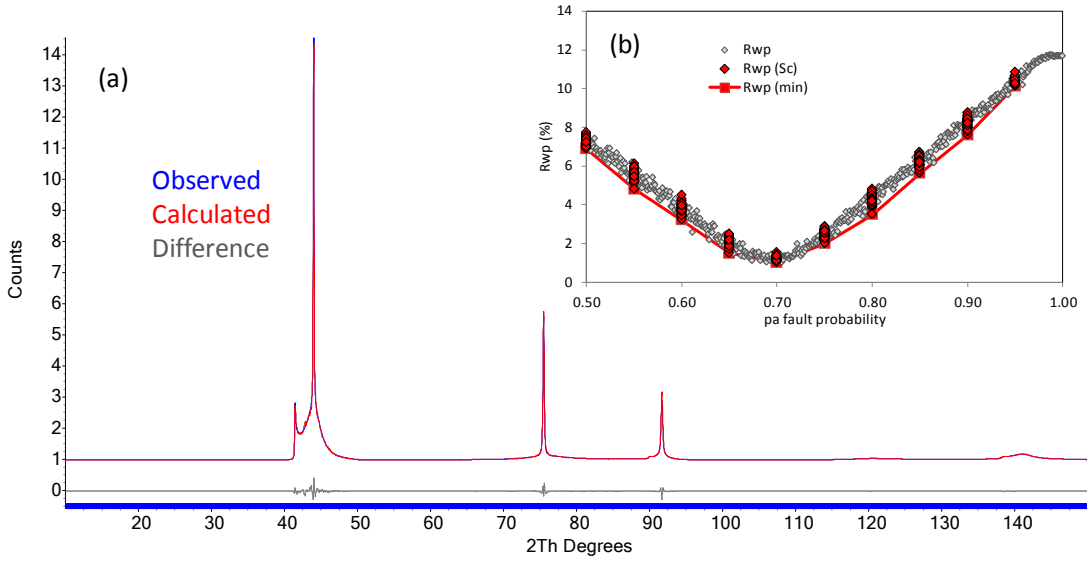

Figure 5.4. (a) Stacking mode Rietveld fit to a DIFFaX-simulated powder pattern of faulted cubic/hexagonal diamond. 5000 layers with a fault probability of 0.7 give excellent agreement to the simulated data. The blue "bar" at the bottom of the figure represents tick markers for each of the 236884 hkl reflections predicted over this 2θ range. (b) Dependence of R_{wp} on pa. Grey open points are a series of stacks with different pa; closed red points are a series of 100 repeat stacks at discrete pa values.

As an example of what this achieves, we used the test input file dia.dat distributed with the DIFFaX suite to calculate the expected powder pattern for a sample of stacking-faulted diamond containing intergrowths of the cubic diamond and hexagonal lonsdaelite forms with a 0.7 probability (*pa*) of ideal c–c and h–h stacking and a 0.3 probability (1–*pa*) of h–c or c–h faults. This example is discussed in the literature and produces the complex peak shapes shown in Figure 5.4.[12] These simulated data were fitted using our Rietveld approach with a supercell containing 5000 carbon layers. Using the peaks buffer approach the pattern could

be well approximated using just 285 *hkl* reflections as opposed to 236884, with no change in R_{wp}. Figure 5.4a shows the Rietveld fit for this model using just 7 refined parameters (1 scale, 2 isotropic peak shape parameters, 4 background terms) for a faulting probability of *pa* = 0.7. An excellent agreement is observed between the simulated data and the Rietveld fit, and the complex peak shapes are extremely well reproduced.

Figure 5.4b shows the Rietveld agreement factor R_{wp} as the stacking fault probability *pa* is systematically varied from 0.5 to 1.0. A clear minimum in R_{wp} is found at *pa* = 0.7 showing that the fault probability can be well quantified for this system. The scatter in R_{wp} (standard deviation 0.1 close to the *pa* minimum) shows that a 5000 layer stack gives a good statistical model for the infinite stack simulated by DIFFaX.

Using fewer layers in the Rietveld model gives an increase in the R_{wp} spread, but the minimum remains reasonably well defined even with only 100 layers. The increased spread of R_{wp} arises due to the different superstructure peak intensities from different specific layer sequences in the stacks. When investigating low probability faults in small stacks it is important to fit multiple stacks generated with a given set of transition probabilities to the diffraction data. The best fit to the data is typically achieved by averaging the calculated patterns of multiple models to better represent the ensemble of crystallites in a sample.[14] This approach was applied to the different $La_2O_2Cu_{2-2x}Cd_xSe_2$ phases prepared in this work. Example input files and accompanying Python script are included in the e-appendix.

It should be noted that further significant speed gains were made after the work of this chapter was completed. TOPAS can now average the calculated patterns of multiple model stacks (100's or even 1000's of models) internally in one step, leading to astronomical speed gains of ~10,000 relative to a traditional Rietveld approach.[22] For example performing all the refinements to generate Figure 5.4b (even with TOPAS peaks buffer improvements) took ~3 hours; the same curve can now be generated in <30 seconds. The R_{wp} surfaces of Figure 5.14 took ~15 hours whereas more discriminating surfaces can now be calculated in minutes.

5.3 Synthesis and Phase Purity

Samples across the $La_2O_2Cu_{2-2x}Cd_xSe_2$ solid solution were synthesized by heating for 12 hours at 1100 ˚C with an aluminium oxygen getter to control oxygen composition. $La_2O_2Cu_2Se_2$ and $La_2O_2CdSe_2$ were coloured khaki and sienna respectively, while all other samples were yellow-ochre. These colours are shown visually in Figure 5.5.

0 (all Cu)	0.2	0.25	0.333	0.5	0.666	0.75	0.8	1 (all Cd)

Figure 5.5. Sample colour across the $La_2O_2Cu_{2-2x}Cd_xSe_2$ solid solution.

Powder X-ray diffraction data showed that in all cases, layered ZrCuSiAs-related phases had formed with a unit cell $a = b \approx 4$ Å, $c \approx 9$ Å (the subcell), explaining the main peaks present. Weak additional reflections were observed at low angles for all samples (with the exception of $Ln_2O_2Cu_2Ch_2$, where full occupancy of the Cu site gives no supercell reflections), which could not be attributed to known impurity phases. It is shown below that these arise from transition metal ordering. The layered phases account for >98.5% weight percentage in all

the new compounds prepared. Typically a minor La_2O_2Se impurity phase is present in all samples (Table 5.1).

x	% of phases formed
0	$La_2O_2Cu_2Se_2$ 99.1%, La_2O_2Se 0.3%, Cu 0.6%
0.05	6Cu/1Cd 91.3%, $La_2O_2Cu_2Se_2$ 8.4%, La_2O_2Se 0.3%
0.1	4Cu/1Cd 95.3%, $La_2O_2Cu_2Se_2$ 4.4%, La_2O_2Se 0.3%
0.125	3Cu/1Cd 97.2%, $La_2O_2Cu_2Se_2$ 1.4%, La_2O_2Se 1.4%
0.15	2Cu/1Cd 59.6%, 3Cu/1Cd 40.1%, La_2O_2Se 0.3%
0.167	2Cu/1Cd 98.5%, La_2O_2Se 1.49%
0.2	1Cu/1Cd 77.0%, 2Cu/1Cd 23.0%
0.25	1Cu/1Cd 99.4%, La_2O_2Se 0.6%
0.3	1Cu/1Cd 28.8%, 1Cu/2Cd 71.1%, La_2O_2Se 0.1%
0.333	1Cu/2Cd 99.4%, La_2O_2Se 0.6%
0.35	1Cu/2Cd 59.7%, 1Cu/3Cd 40.2%, La_2O_2Se 0.1%
0.375	1Cu/3Cd 99.9%, La_2O_2Se 0.1%
0.4	1Cu/3Cd 49.6%, 1Cu/4Cd 50.2%, La_2O_2Se 0.2%
0.45	1Cu/4Cd 27.0%, 1Cu/6Cd 67.9%, $La_2O_2CdSe_2$ 5.0%, La_2O_2Se 0.1%
0.5	$La_2O_2CdSe_2$ 97.5%, $La_4O_4Se_3$ 2.2%, CdSe 0.3%

Table 5.1. Weight % of phases formed across the $La_2O_2Cu_{2-2x}Cd_xSe_2$ solid solution.

5.4 Cell Volume/Parameter Trends

Unit cell volumes (Figure 5.6) showed a smooth variation across the series suggesting a smooth change in structure with composition. The *a* cell parameter remains relatively unchanged across the series whilst the *c*-axis expands rapidly (Figure 5.7). As in related materials, this shows the high rigidity of Ln_2O_2 layers relative to M_nSe_2 layers. The compositions we discuss in detail below contained a single layered phase (the red points of Figure 5.6/Figure 5.7). For some other compositions we see evidence of phase segregation. For example at a nominal x = 0.9 we see three similar layered phases with cell volumes corresponding to x = 0.8, x = 0.92 and x = 1 in a ~5:14:1 ratio as indicated by the three vertical grey points for this nominal composition. This implies an inherent stability of the ordered structures discussed below.

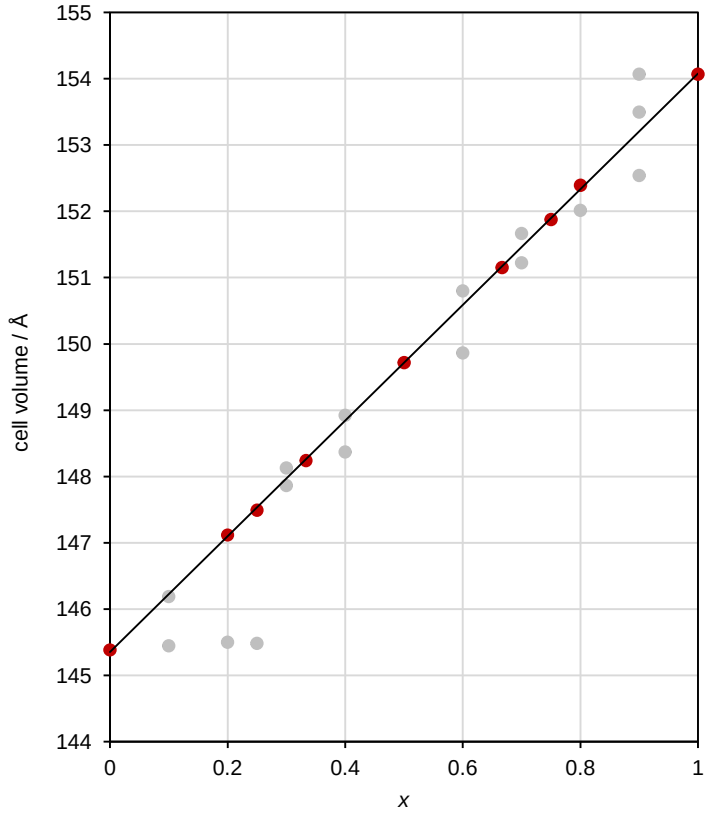

Figure 5.6. Variation in cell volume of phases formed across the $La_2O_2Cu_{2-2x}Cd_xSe_2$ solid solution. Multiple data points at a given value of x represents multiphase samples. Red and grey circles are explained in the text.

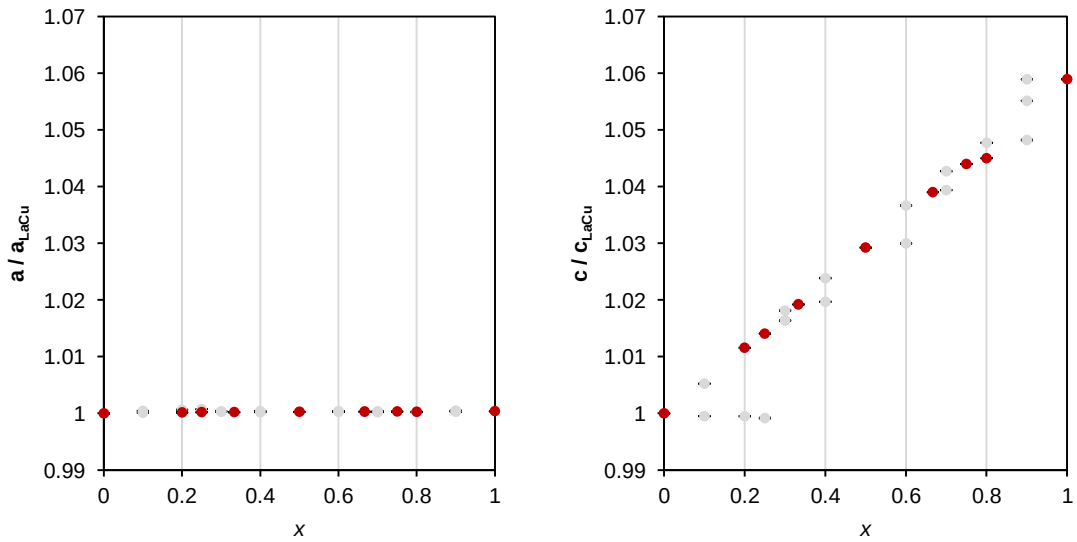

Figure 5.7. Variation in cell parameters of phases formed across the $La_2O_2Cu_{2-2x}Cd_xSe_2$ solid solution. Multiple data points at a given value of x represents multiphase samples. Red and grey circles are explained in the text.

5.5 *x* = 0 (all Cu) and x = 1 (all Cd)

$La_2O_2Cu_2Ch_2$ and $La_2O_2CdSe_2$ end members were synthesized and diffraction data were fully consistent with the structures previously reported in the literature and shown in Figure 5.1. PXRD data are included in Figure 5.16. Minor (2%) impurities are present in the Cd end member under these synthetic conditions. Fully pure samples can be made at 950 K[4]. For this work we deliberately chose a single set of synthesis conditions for all compositions.

5.6 *x* = 0.5 $La_2O_2CuCd_{0.5}Se_2$ (1Cu/1Cd layer)

Synchrotron data of the *x* = 0.5 composition showed that a layered ZrCuSiAs-related phase had formed with a unit cell *a* = *b* = 4.07 Å, *c* = 9.05 Å (the subcell), explaining the main peaks present. Figure 5.8a shows a $La_2O_2Cu_2Se_2$ model, *P4/nmm* (red) refined against the experimental data (blue). Weak additional reflections are clearly observed. Figure 5.8b shows a refined $La_2O_2CdSe_2$ model, space group $P4_2/nmc$, which fits some, but not all of the supercell reflections.

The ionic radii of Cu^{1+} and Cd^{2+} ions differ considerably; Shannon's tables give values of 0.6 and 0.78 Å for Cu^{1+} and Cd^{2+} respectively.[23] Models were therefore investigated which have Cu and Cd in distinct layers. If this occurs, a sample with composition $La_2O_2CuCd_{0.5}Se_2$ would need to have a 1:1 ratio of Cu^{1+} layers (tetrahedra fully occupied) to Cd^{2+} layers (half occupied). Perhaps the most likely structural model of this sort would have alternating Cu and Cd layers, with the Cd occupying alternate checkerboard sites either side of a given Cu layer. This model is shown in Figure 5.9 (left), and would have space group $P4_2/nmc$. Figure 5.8c shows this model refined against the experimental data, but it is clearly incorrect.

A second possible model would also have alternating Cu and Cd layers, but with the Cd occupying the same sites either side of a given Cu layer, shown in Figure 5.9 (right), space group *P*-4*m*2. Figure 5.8d shows this model refined against the experimental data. It provides an excellent fit. Full crystallographic details of the final model (and other conventional refinements in the chapter), as well as the Cu-Se and Cd-Se layer thicknesses as derived from conventional refinements for the *x* = 0.5 sample (as well as other compounds discussed in the chapter) are included later in the chapter (Figure 5.16 and Figure 5.17 respectively).

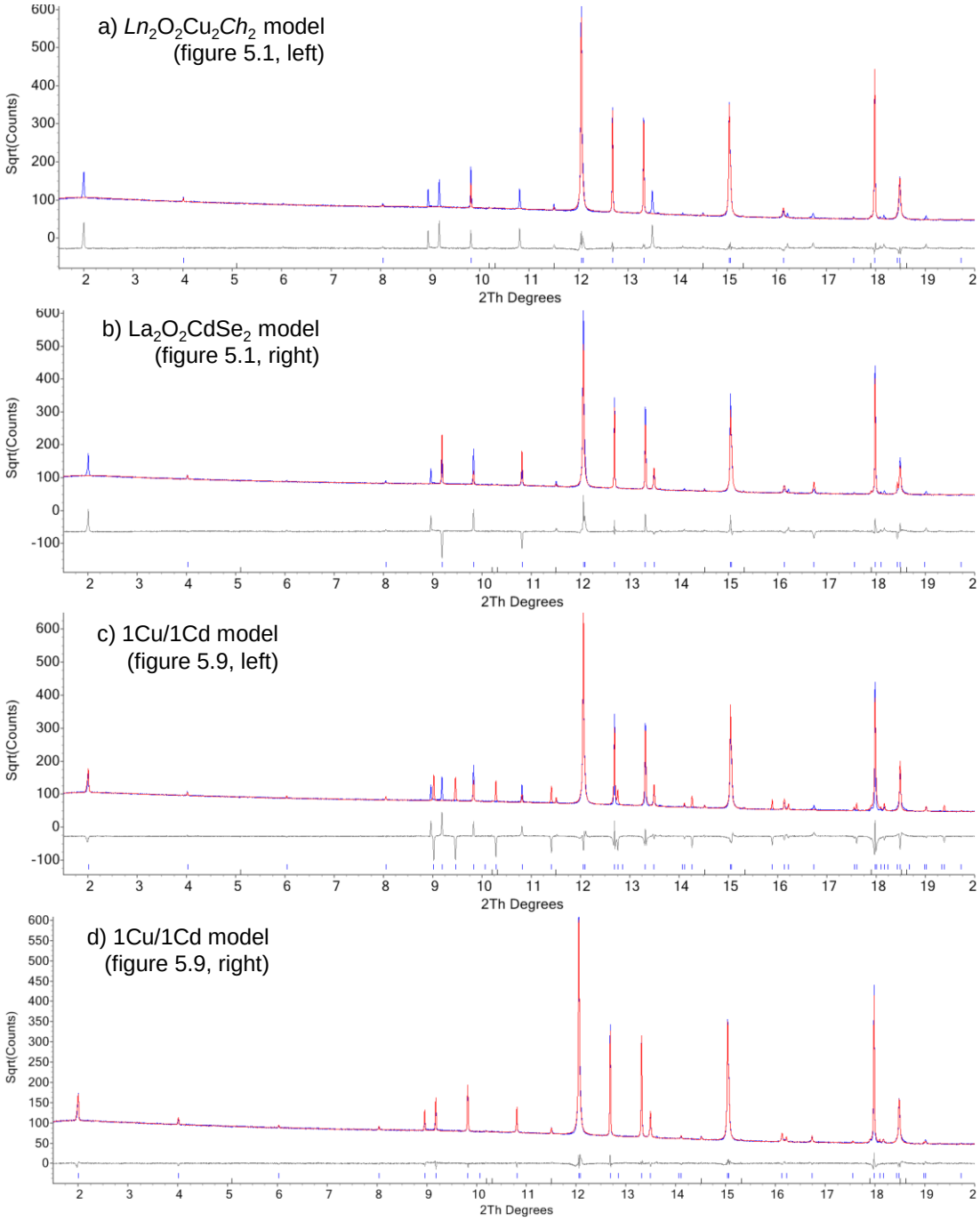

Figure 5.8. Rietveld refinement profiles of synchrotron powder diffraction data for $La_2O_2CuCd_{0.5}Se_2$ using the structural models discussed in the text. The correct model is that given in Figure 5.9, right. A $\sqrt{I}$ y-scale is used to emphasize the weak supercell reflections.

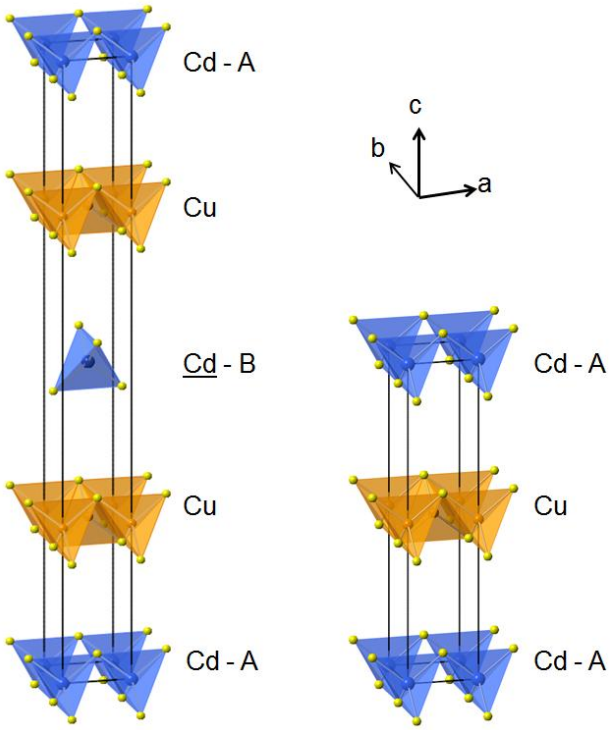

Figure 5.9. Two possible structural models for $La_2O_2CuCd_{0.5}Se_2$ with alternating layers of Cu and Cd. Underlined Cd layers represent those in layer position B in the ab plane, which will be useful when considering layer stacking sequences later in the chapter. The model with Cd occupying equivalent sites either side of a Cu layer (right) is the correct model. Cu^{1+} cations are shown in orange, Cd^{2+} cations in blue and Se^{2-} anions in yellow. $[La_2O_2]^{2+}$ layers are omitted for clarity.

5.7 Cd-rich samples: *x* = 0.667, 0.75, 0.8, 0.9 (1Cu/2Cd, 1Cu/3Cd, 1Cu/4Cd, 1Cu/9Cd)

Compounds expected to contain more Cd than Cu layers were investigated for *x* = 0.667, 0.75, 0.8 and 0.9. In all cases the formation of $La_2O_2Cu_2Se_2$-derived phases was clear from powder diffraction data. For *x* = 0.667 a model was constructed with a 1:2 ratio of Cu:Cd layers, with Cd occupying equivalent sites either side of a given Cu layer as suggested by the *x* = 0.5 structure, and opposite sites when in adjacent layers as found in $La_2O_2CdSe_2$ (Figure 5.10a). This leads to space group $P4_2/nmc$.

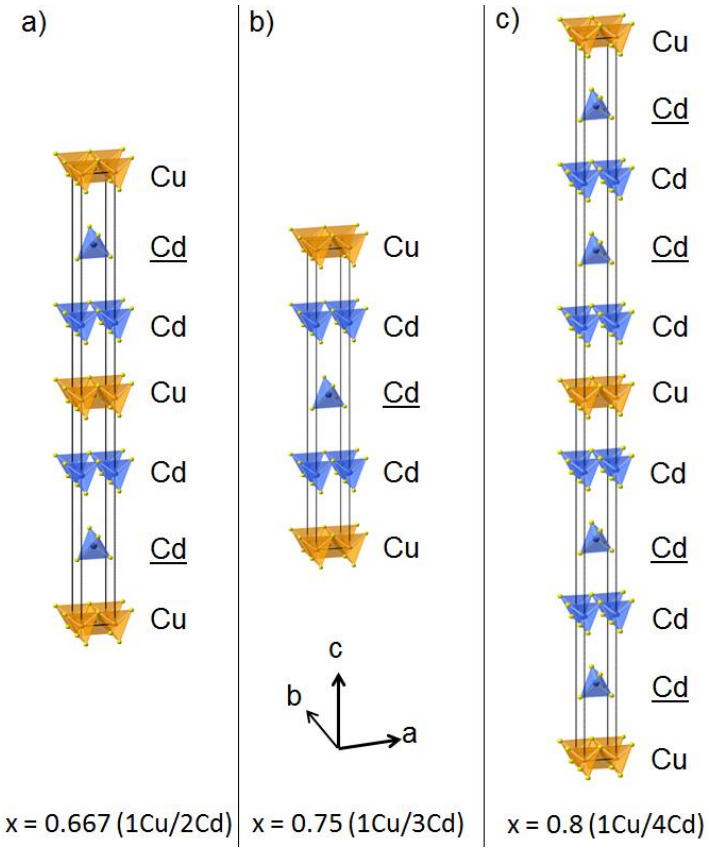

Figure 5.10. Structural models for (a) $La_2O_2Cu_{0.667}Cd_{0.667}Se_2$ (1Cu/2Cd), (b) $La_2O_2Cu_{0.50}Cd_{0.75}Se_2$ (1Cu/3Cd) and (c) $La_2O_2Cu_{0.40}Cd_{0.80}Se_2$ (1Cu/4Cd), space group $P4_2/nmc$, P-4m2 and $P4_2/nmc$ respectively. Cu^{1+} cations are shown in orange, Cd^{2+} cations in blue and Se^{2-} anions in yellow. $[La_2O_2]^{2+}$ layers are omitted for clarity.

On initial inspection, the refined model seems to provide a satisfactory fit to experimental data (Figure 5.11a), with R_{wp} = 5.92%. However, upon closer inspection, several of the weak supercell peaks show small but significant discrepancies in both peak intensity and widths (Figure 5.11b, peaks marked with arrows). Note that Figure 5.11 is drawn with a $\sqrt{I}$ scale such that these reflections are ~0.25% of the strongest subcell reflections.

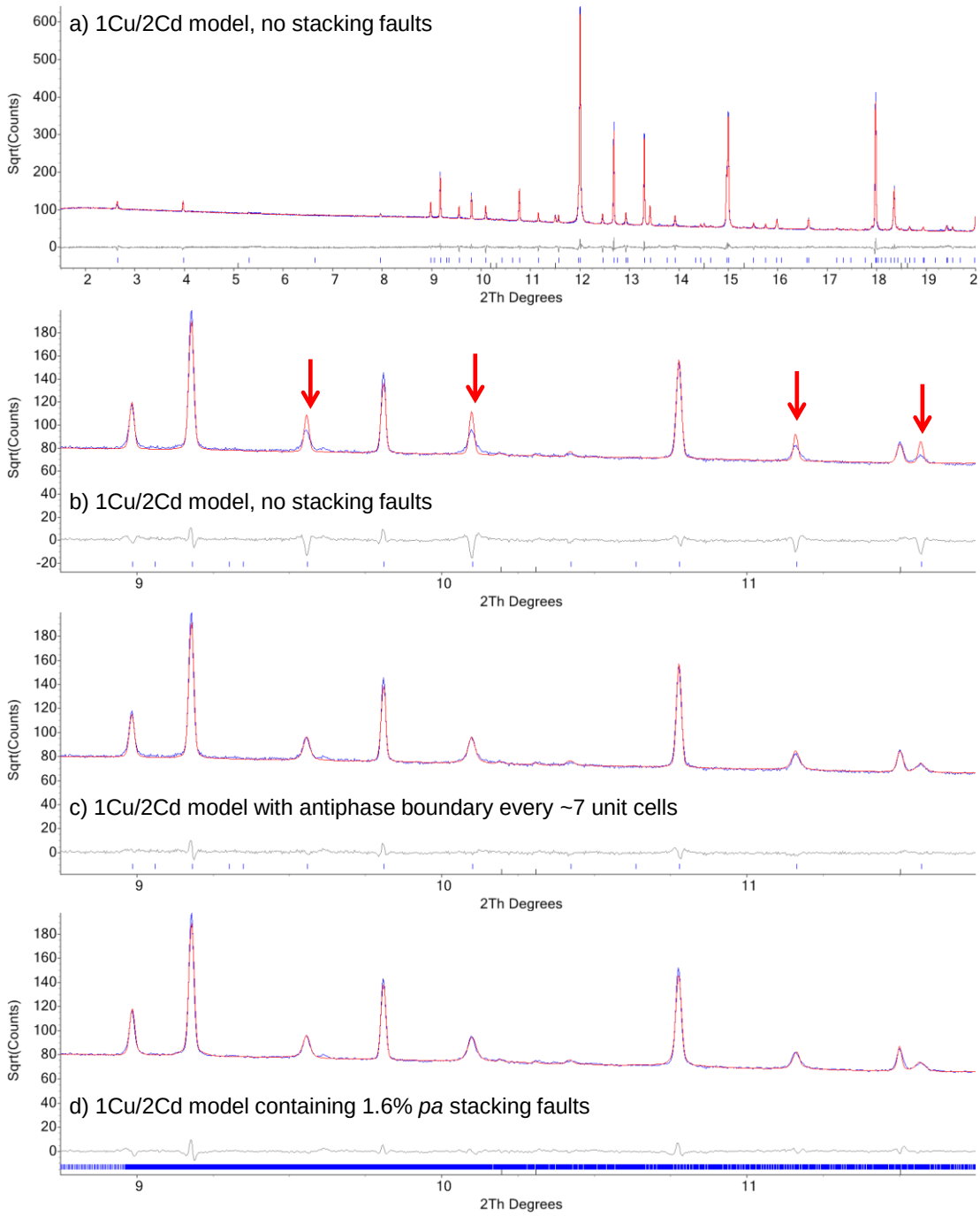

Figure 5.11. Rietveld refinement profiles of synchrotron powder diffraction data for $La_2O_2Cu_{0.66}Cd_{0.66}Se_2$ using the structural model proposed in Figure 5.10a, both without and with stacking faults. The correct model contains ~1.6% pa stacking faults. A $\sqrt{I}$ scale is used to emphasize the weaker supercell reflections.

Analysis of individual reflections showed a clear broadening of all *hkl* reflections where $l \neq 3n$. This is shown most clearly by a plot of the fwhm of individual PXRD reflections against 2θ (Figure 5.12). Therefore, an additional parameter was introduced to model antiphase domain walls perpendicular to c*, using the approach employed in the refinements of MgB_2H_8[24], but with an $l = 3n$ condition. This leads to an improved fit of supercell reflections (Figure 5.11c), R_{wp} = 5.01%, and refined fault domain size value of ~380 Å suggesting the presence of a fault every ~7 unit cells (42 layers).

Figure 5.12. Full width at half maximum of individual reflections in x = 0.667 sample. The (0,2,1) and (0,1,40) reflections are anomalies due to them being relatively weak and overlapping with other intense reflections.

Since the other members of the $La_2O_2Cu_{2-4x}Cd_xSe_2$ series discussed later in the chapter show more complex broadenings of the supercell reflections, we have applied our DIFFaX-Rietveld approach to these data. The alternating $[La_2O_2]^{2+}$ and either $[CdSe_2]^{2-}$ or $[Cu_2Se_2]^{2-}$ 2D units in these structures mean that we can easily describe the structure in terms of [LaOLaSe(Cu_2/Cd)Se] layers stacked along *c* and that two types of stacking fault are likely for *x* = 0.667 (Figure 5.13). Firstly one could break the (Cu|Cd|Cd) repeat by introducing an additional layer of either metal to form (Cu|Cu|Cd|Cd) or (Cu|Cd|Cd|Cd) local faults. This is called a *pa*-type fault throughout the chapter. These correspond to a local intergrowth of *x* = 0.5 and *x* = 0.75 phases, and chemical composition requirements mean that their number must be balanced. The cell volume plot of Figure 5.6 and single-phase nature of this sample provide strong evidence that the composition is that expected.

A second possibility is a fault of the type shown in Figure 5.9, left, where neighbouring Cd atoms layers are offset by ±(a/2, b/2) in the *ab* plane across a Cu layer. This is called a *pb*-type fault throughout the chapter. The structure of faulted *x* = 0.667 $La_2O_2Cu_{0.667}Cd_{0.667}Se_2$

can then be described by stacking 6 layers labelled Cd1, Cd2, Cu3, Cd4, Cd5, & Cu6 as shown in Figure 5.13, with transition probabilities from layer to layer as defined in the accompanying probability matrix. In this description an underlined Cd atomic layer is offset by (*a*/2, *b*/2). The ideal structure is generated by stacking (Cd1|Cd2|Cu3|Cd4|Cd5|Cu6)$_\infty$. A *pa* type fault can be introduced by an $m \rightarrow m+3$ transition and a *pb* fault by Cu3→Cd1 or Cu6→Cd4. In this description a *pa* fault after a Cd layer retains the Cd offset pattern observed in $La_2O_2CdSe_2$ and a *pa* fault after a Cu layer leads to Cd's retaining the *xy* position they would have within a given layer in an unfaulted stack; by setting *pa* to an $m \rightarrow m$ transition for Cu layers the alternate fault in which Cd position is mirrored across a *pa*-induced Cu double layer can be explored.

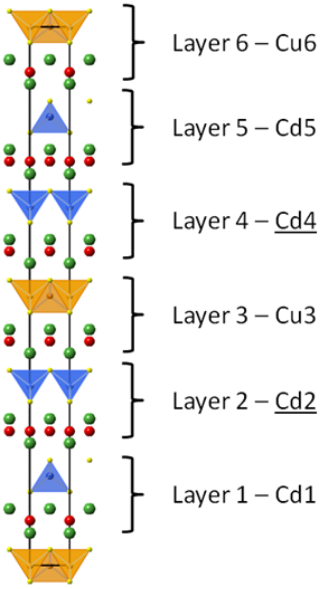

from layer *m*

to layer *n*

$$\begin{pmatrix} 0 & 0 & pb & pa & 0 & 1-pa-pb \\ 1-pa & 0 & 0 & 0 & pa & 0 \\ 0 & 1-pa & 0 & 0 & 0 & pa \\ pa & 0 & 1-pa-pb & 0 & 0 & pb \\ 0 & pa & 0 & 1-pa & 0 & 0 \\ 0 & 0 & pa & 0 & 1-pa & 0 \end{pmatrix}$$

Figure 5.13. Layer description and stacking probability matrix for x = 0.667. Each pa fault retains the Cd offset that would be adopted in an ideal stack.

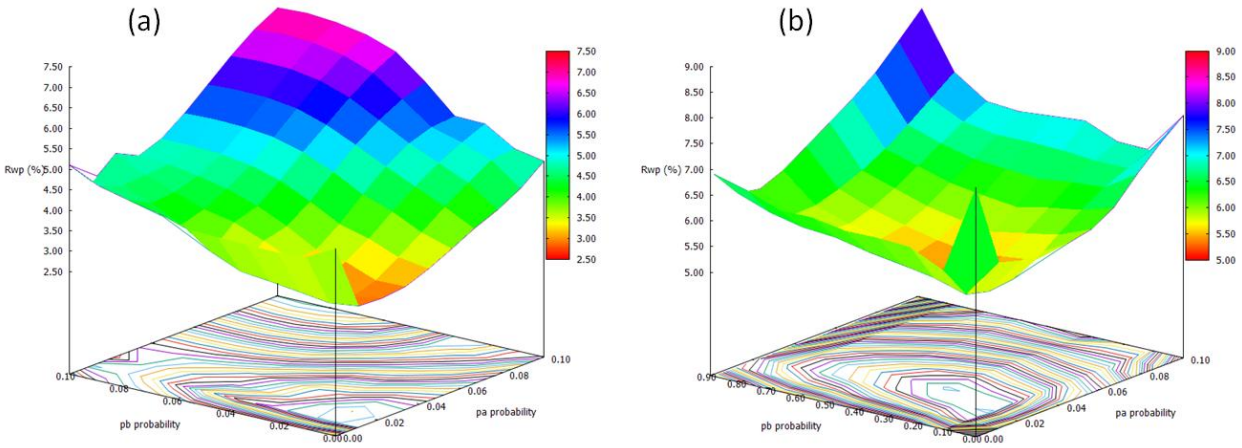

Figure 5.14. Dependence of R_{wp} on pa and pb for the x = 0.667 and x = 0.333 systems. Note different pb scale in (b).

The supercell was constructed by stacking 320 Cu and 640 Cd layers with internal geometries derived from the *x* = 0.5 refinement. The ideal thickness of each layer type along the *c*-axis can be estimated from the *c* cell parameter in *x* = 0 (Cu) and *x* = 1 (Cd) series end members as 8.7975 Å and 9.3160 (=18.6320/2) Å respectively. The thickness defines the displacement along *c* from one layer to the next. For rigid layers, the supercell should then have a *c*-axis of 320 × 8.7975 Å + 640 × 9.3160 Å = 8777.44 Å, implying a subcell parameter of 9.1432 Å. Experimentally the subcell parameter is 9.1410(3) Å, so ideal thicknesses were automatically scaled during the refinement to account for this very small discrepancy. This supercell model gave a good fit to the diffraction data with an R_{wp} only marginally higher than a standard crystallographic model (4.1 vs 3.9 % for 2–20° 2θ), despite having no refined structural parameters. The new peaks-buffer approach described earlier in the chapter means that the pattern is simulated using 1530 *hkl* reflections rather than the 54881 predicted for this supercell size and 2θ range. As expected, an identical R_{wp} is obtained for any unfaulted supercell containing 6*n* layers to a conventional description.

A grid search was then performed with both *pa* and *pb* allowed to vary from 0 to 0.1 and 100 trial stacks tested for each *pa*/*pb* pair (approximately 15 hours of computer time). Analysis of the R_{wp} surface (Figure 5.14) indicated a significant improvement in fit (R_{wp} = 2.78 %) for structures with ~18 *pa* faults in the stack and no *pb* faults, corresponding to a fault every ~490 Å or 54 layers. Figure 5.14 gives the lowest R_{wp} at a given *pa*/*pb* pair, while data for all 100 stacks trialled at each *pa*/*pb* pair is given in Appendix 3. As shown in Figure 5.11d, this model reproduces the shape and intensities of weak supercell reflections extremely well, with only one additional structural parameter (*pa* value). Refinement of parameters defining the relative thickness of Cu/Cd layers gave essentially no change in R_{wp} and refined values of 8.806/9.307 Å. Models with imposed correlation lengths between faults were investigated but we found that the best fits had uncorrelated faults. As well as the "extra layer" *pa* model a similar "missing layer" *pc* fault was investigated. It was found that similar fits to the data are possible with either fault type, but that the total number of *pa*/*pc* faults remains constant.

Rietveld fits for the *x* = 0.75 composition are included later in Figure 5.16. The powder diffraction data are essentially consistent with the structural model shown in Figure 5.10b, which contains blocks of 3 Cd's, within which the structural arrangement is the same as in $La_2O_2CdSe_2$, followed by a Cu layer. This model, however, significantly overestimates the

intensity of the weak 002 and 003 reflections at ~2 and ~3° 2θ as well as, for example, the 01*l*, $l \neq 2n$ reflections (in a conventional crystallographic refinement using an average model this effect is partially "mopped up" by the thickness of Cd and Cu layers distorting, Figure 5.17). A *pa*/*pb* grid search similar to that for the x = 0.66 sample was investigated and a significant reduction in R_{wp} (5.81 to 2.78 %, 2-20° 2θ) was achieved with approximately 25 *pa* faults in 960 layers. Introduction of *pb* faults caused an increase in R_{wp}. Refinement of the Cu/Cd slab thickness gave 8.861/9.248 Å, close to expected values. Details of the R_{wp} surface analysis is given in Appendix 3.

Inspection of the powder data for x = 0.8 and x =0.9 suggests similar basic structures with a $(Cu|Cd|Cd|Cd|Cd)_\infty$ repeat for x = 0.8, and similar *pa* type faults. The weak intensity of the superstructure peaks and the likelihood of partial phase separation preclude detailed analysis of the stacking faults. For x = 0.9 we see evidence for partial phase segregation to x = 0.8 and x = 1 compositions.

5.8 Cu-rich samples: x = 0.333, 0.25, 0.2, 0.1 (2Cu/1Cd, 3Cu/1Cd, 4Cu/1Cd, 9Cu/1Cd)

From powder diffraction data we can identify 3 new discrete structure types for Cu-layer-rich compositions. The basic structure types found are depicted in Figure 5.15, though we again see marked supercell peak broadening and significant peak asymmetry in the powder diffraction patterns. For x = 0.333 the supercell reflections are well fitted with *pa* ≈ 0.013 suggesting a similar number of layer-repeat faults to the Cd-rich phases. There are also a significant number of *pb*-type faults (*pb* ≈ 0.25) corresponding to 80 faults in the 960 layer stack, or a fault every 55 Å or 6 layers. A surface plot showing the dependence of R_{wp} on *pa* and *pb* is given in Figure 5.14b (data for all 100 stacks trialled at each *pa*/*pb* pair is given in Appendix 3).

As the number of Cu layers is increased, the proportion of *pb*-type faults increases. At x = 0.25 (Cu|Cu|Cu|Cd) *pb* is ≈ 0.43 implying an almost-random choice for the position of the Cd layers (further details in Appendix 3). This leads to the triangular or Warren-like peak shape seen for the 10*l*-related peaks from ~ 8.9° 2θ, shown in Figure 5.15. This sample also contains a significant number of *pa* type defects (*pa* ≈ 0.06). Without these defects 00*l* reflections have too high a peak height. In a conventional crystallographic refinement using an average model this effect is again partially "mopped up" by the thickness of Cd and Cu layers distorting, Figure 5.17.

For x = 0.2 we find *pb* = 0.5 gives the best fit to the data (Figure 5.15e) implying full disorder of the Cd atoms over the two sites available (further details in Appendix 3). For x = 0.1 (targeted to be 9Cu/1Cd), phase separation is observed, into x = 0.1 and x = 0 compositions.

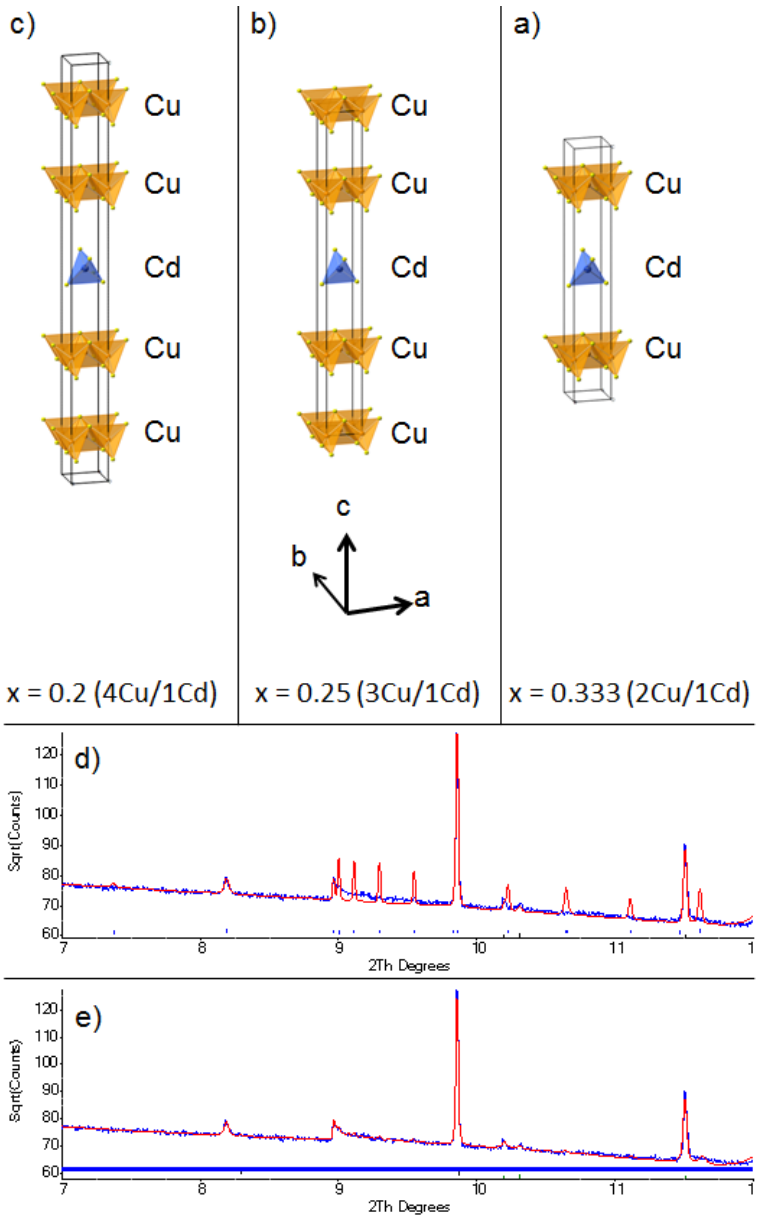

Figure 5.15. Structural models for (a) $La_2O_2Cu_{1.33}Cd_{0.33}Se_2$ (2Cu/1Cd), (b) $La_2O_2Cu_{1.50}Cd_{0.25}Se_2$ (3Cu/1Cd) and (c) $La_2O_2Cu_{1.60}Cd_{0.20}Se_2$ (4Cu/1Cd), all space group P-4m2. Cu^{1+} cations are shown in orange, Cd^{2+} cations in blue and Se^{2-} anions in yellow. $[La_2O_2]^{2+}$ layers are omitted for clarity. (d) and (e) show the Rietveld fit for x = 0.2 with no faults and 0.05/0.50 pa/pb faults respectively. The 2θ 8.2° peak has I~0.4% of the strongest reflection.

5.9 Discussion

Work on single-metal layered oxychalcogenides (Chapter 4) has shown that the combination of a rigid oxide layer and a more flexible chalcogenide layer can lead to structures with remarkable complexity and large superstructures in the *ab* plane.[9,10] In this chapter it has been shown that a similar level of complexity can be built into these materials along the stacking direction by using two metals, giving rise to the range of materials from 4Cd/1Cu to 1Cd/4Cu shown schematically in Figure 5.3. A conventional structural description has been used in this work for all compounds, with the space groups of each structure given in Table 5.2. However, it is also possible to describe all these structures in terms of a superspace group, *P4/nmm*(00g)s00*s* [129.4]. The tendency to adopt ordered superstructures of this

type is initially surprising, but again has its origin in the rigidity of the oxide layers in the *ab* plane. This rigidity forces two fixed Se–Se dimensions on the MSe_4 tetrahedra, and the planar layers means that they can only adjust to coordinate a given transition metal by elongation along their S_4 axis (parallel to *c*). Simple bond valence arguments[25,26] for a Cu^{1+} or Cd^{2+} in this environment imply Se–Se layer distances of ~3.0 and ~3.4 Å respectively. This large difference in geometry provides a strong driving force for segregation of Cu and Cd into separate layers.

Both our crystallographic models and stacking fault analyses show an initially counterintuitive arrangement of Cd sites in $CdSe_2$ layers separated by a Cu_2Se_2 block. In pure $La_2O_2CdSe_2$ the Cd ordering pattern can be derived from the parent Cu structure in terms of a Z_4^- ordering mode which leads to a checkerboard ordering within layers and adjacent layers with Cd positions offset by (½, ½, ½) such that layers repeat in an ABAB sequence along *c*. This arrangement would be expected purely on electrostatic grounds and is retained within the Cd blocks of all our materials. Figure 5.9, however, shows that Cd positions are mirrored across the single Cu_2Se_2 layers in the Cd-rich materials. As such, the Cd A(B)A stacking sequence [where (B) indicates the effective position of the Cu layer] is retained. We also find that the *pa* stacking fault for the x = 0.667 and x = 0.75 samples is best modelled such that Cd sites alternate across a double layer, again retaining the A(B)(A)B sequence through the fault. One possible explanation for this is that the *pa* fault occurs within column-like domains in a crystallite. The Cd ions immediately following a local double-Cu layer would then be in registry with other Cd sites within that layer following this type of fault. The only structure in which the ABAB sequence is not followed is the x = 0.333 2Cu/1Cd composition. Since the *pb* type disorder is high in the Cu rich sequences, our observations are consistent with Cd preferring a mirrored configuration across multiple Cu layers.

The powder diffraction data show that there is significant long range order along the *c*-axis of these materials, with a relatively low probability of faults (*pa*) in the Cu/Cd sequence. There is also a strong tendency for Cd sites to adopt ordered positions in the *ab* plane in Cd-rich materials but that this tendency is reduced as the $CdSe_2$ layers become separated by more than one Cu_2Se_2 layers. Stacking fault probabilities *pa* and *pb* for the whole series are given in Figure 5.3. The different types of faults lead to the characteristic changes in superstructure peak shapes and intensities across the series shown in Figure 5.16. It should be acknowledged that there may be other models that provide an equally good fit to the data.

Figure 5.17 shows the thickness of Se-Cu-Se and Se-Cd-Se layers from conventional Rietveld refinement. In compounds with no or minimal faults in the stacking sequence along *c*, the Se-Cu-Se and Se-Cd-Se layer thicknesses are reasonably well defined (x = 0.333, 0.5, 0.667). However in compounds with more severe faulting (x = 0.25, 0.75), layer thicknesses are clearly incorrect. This is happening as the least squares refinement gives the lowest R_{wp} with a significantly distorted structural model if stacking faults are not being modelled.

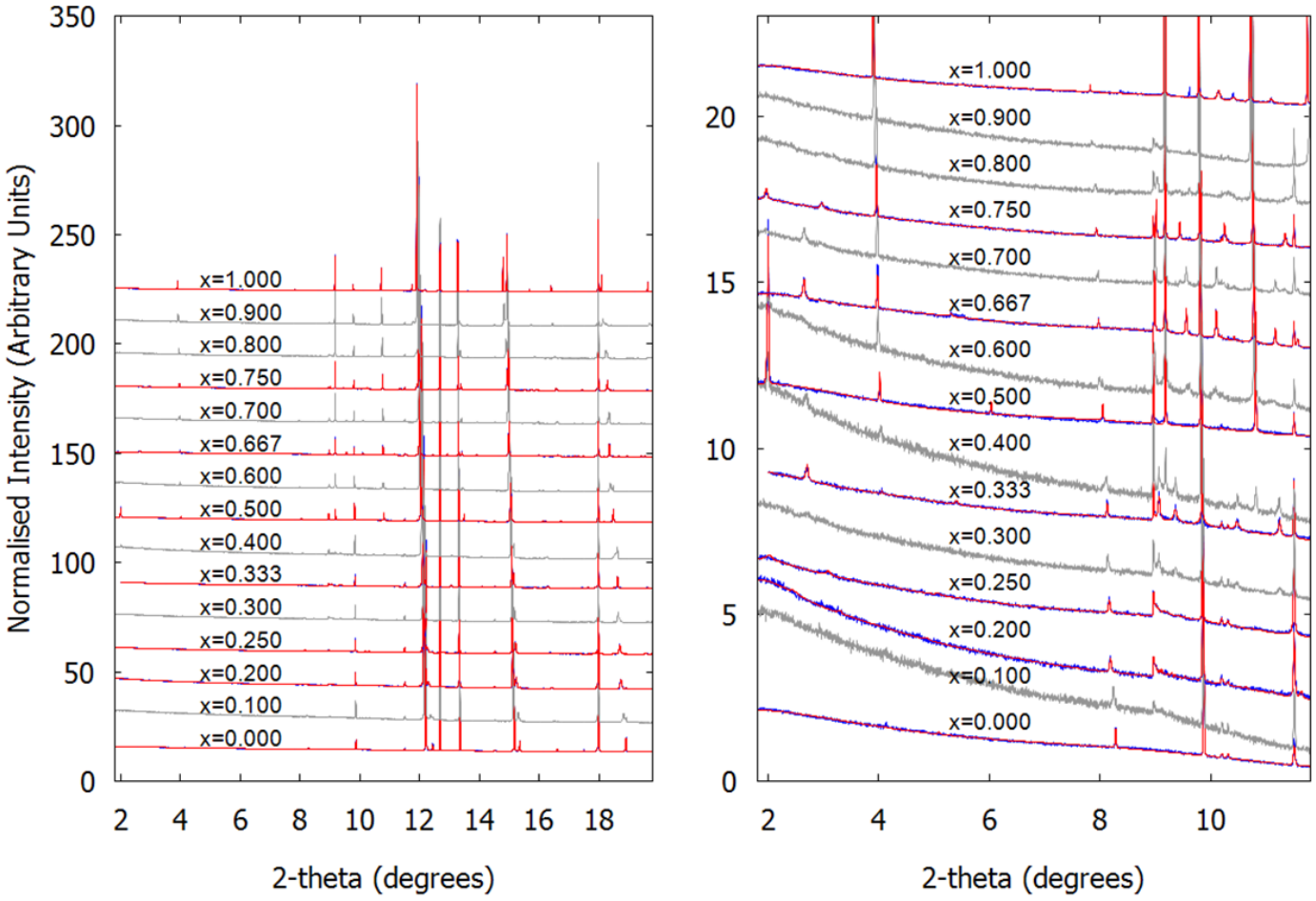

Figure 5.16. Rietveld fits for all compositions studied using the stacking fault approach. Left hand panel shows all data normalized on a 0–100 scale and offset vertically by 20 units for presentation. Right hand panel shows data over a low 2-theta range to emphasise the weak superstructure reflections which reveal metal ordering. Data sets are offset by 2 units along the y-axis. The differing backgrounds reflect different capillary packings. Rietveld fits of x = 0.667 and 0.5 are averages of 100 unique stacks.

x	0.25			0.333			0.5			0.667			0.75		
Sgrp	P-4m2			P-4m2			P-4m2			P42/nmc			P-4m2		
a/Å	4.0662(1)			4.0662(1)			4.0665(1)			4.0664(1)			4.0664(1)		
c/Å	35.6871(3)			26.9014(2)			18.1110(1)			54.8470(2)			36.7390(2)		
V/Å^3	590.041(6)			444.794(4)			299.496(1)			906.934(4)			607.495(5)		
# prms	54			42			38			41			49		
wRp %	7.67402			7.42851			5.1759			3.90622			4.6776		
R Bragg %	4.64301			4.35428			3.60904			2.20767			3.14275		
	x	y	z	x	y	z	x	y	z	x	y	z	x	y	z
La01	0.5	0	0.0934(1)	0	0.5	0.0457(1)	0.0	0.5	0.1890(1)	0.5	0	0.0584(1)	0.5	0	0.0929(1)
La02	0	0.5	0.1623(1)	0.5	0	0.2832(1)	0.5	0	0.3247(1)	0	0.5	0.1033(1)	0	0.5	0.1590(1)
La03	0.5	0	0.3419(1)	0	0.5	0.3744(1)				0.5	0	0.2277(1)	0.5	0	0.3442(1)
La04	0	0.5	0.4106(1)										0	0.5	0.4117(1)
O01	0	0	0.1191(9)	0	0	0	0	0	0.25	0.5	0.5	0.0832(4)	0	0	0.1314(6)
O02	0.5	0.5	0.1192(8)	0.5	0.5	0	0.5	0.5	0.25	0	0	0.0826(4)	0.5	0.5	0.1314(6)
O03	0	0	0.3795(10)	0	0	0.3296(9)				0.5	0.5	0.2491(2)	0	0	0.3777(7)
O04	0.5	0.5	0.3794(9)	0.5	0.5	0.3342(9)							0.5	0.5	0.3797(7)
Se01	0.5	0	-0.0465(2)	0.5	0	0.1080(2)	0.5	0	0.0944(1)	0	0.5	0.0281(1)	0	0.5	0.0464(2)
Se02	0.5	0	0.2093(2)	0	0.5	0.2204(1)	0	0.5	0.4174(1)	0.5	0	0.1349(1)	0.5	0	0.2066(2)
Se03	0	0.5	0.2947(2)	0.5	0	0.4377(1)				1	0.5	0.1962(1)	0	0.5	0.2973(2)
Se04	0.5	0	0.4582(2)										0.5	0	0.4574(2)
Cu01	0	0	0	0	0	0.1617(2)	0	0	0.5	0	0	0	0	0	0.0
Cu02	0.5	0.5	0	0.5	0.5	0.1634(2)	0.5	0.5	0.5	0.5	0.5	0	0.5	0.5	0.0
Cu03	0	0	0.2541(2)												
Cu04	0.5	0.5	0.2548(2)												
Cd01	0.5	0.5	0.5	0.5	0.5	0.5	0	0	0	0.5	0.5	0.1656(1)	0	0	0.2495(1)
Cd02													0.5	0.5	0.5

Table 5.2. Crystallographic information from conventional Rietveld refinement of more ordered systems.

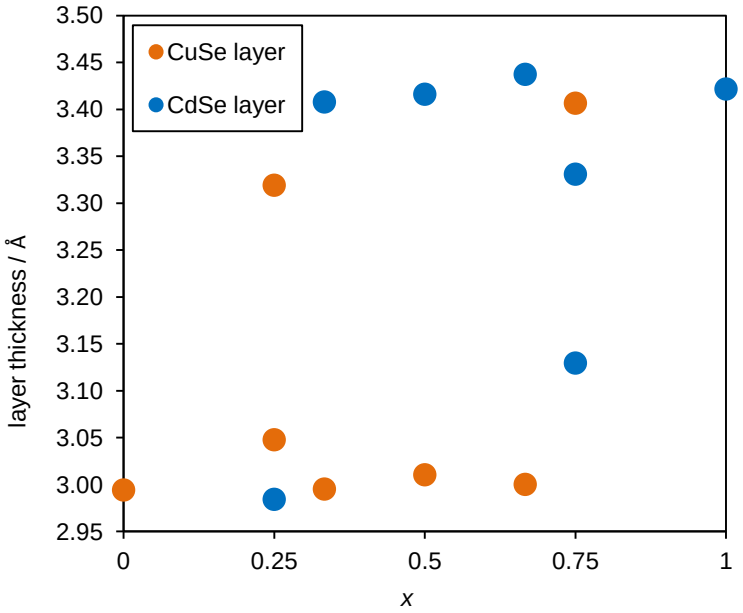

Figure 5.17. Thickness of Se–Cu–Se and Se–Cd–Se layers from conventional Rietveld refinement. Note that the more faulted samples at x = 0.25 and x = 0.75 show apparent distortions in the layer thicknesses using conventional refinement.

5.10 Conclusions

In conclusion, the design principle of combining rigid oxide blocks with more flexible chalcogenide blocks learnt from the 2D $Ln_2O_2MSe_2$ infinitely flexible materials can be taken, and used to produce cation-ordered materials over a large length scale in the 3rd dimension. This has allowed the production of materials with stacks of electronically-interesting Cu_2Se_2 layers where we can systematically change the number of adjacent layers and/or the separation between them in a controlled fashion. This gives access to a large new

oxychalcogenide family which can potentially be doped to give p-type conductors related to the important LaOCuSe and BiOCuSe families. This is explored further in Chapter 6. By using different metal chalcogenide layers there is also a possibility of combining electronic and magnetically active layers in a controllable structural family.

It is also shown that materials with low and high-probability stacking faults can be properly analysed within the Rietveld method for the first time. This allows us to simultaneously extract structural (by refining atomic coordinates) and microstructural (by analysing stacking fault probabilities) information on the samples. The ability to correctly fit complex peak shapes with a small number of structurally meaningful parameters means that reflection intensities are correctly modelled, which is essential for accurate structural information or accurate quantitative analysis. The method described is entirely general and will be applicable to the wide range of materials that exhibit stacking faults. Note that since the work of this chapter was performed, further improvements have been integrated into TOPAS giving overall speed gains of ~10,000 relative to a conventional Rietveld algorithm.

5.11 References

(1) Hiramatsu, H.; Yanagi, H.; Kamiya, T.; Ueda, K.; Hirano, M.; Hosono, H. *Chem. Mater.* **2008**, *20*, 326.
(2) Ueda, K.; Takafuji, K.; Hiramatsu, H.; Ohta, H.; Kamiya, T.; Hirano, M.; Hosono, H. *Chem. Mater.* **2003**, *15*, 3692.
(3) Ijjaali, I.; Mitchell, K.; Haynes, C. L.; McFarland, A. D.; Van Duyne, R. P.; Ibers, J. A. *J. Solid State Chem.* **2003**, *176*, 170.
(4) Hiramatsu, H.; Ueda, K.; Kamiya, T.; Ohta, H.; Hirano, M.; Hosono, H. *J. Mater. Chem.* **2004**, *14*, 2946.
(5) McCabe, E. E.; Free, D. G.; Evans, J. S. O. *Chem. Commun.* **2011**, *47*, 1261.
(6) Tuxworth, A. J.; McCabe, E. E.; Free, D. G.; Clark, S. J.; Evans, J. S. O. *Inorg. Chem.* **2013**, *52*, 2078.
(7) Ainsworth, C. M.; Wang, C. H.; Tucker, M. G.; Evans, J. S. O. *Inorg. Chem.* **2015**, *54*, 1563.
(8) Peschke, S.; Nitsche, F.; Johrendt, D. *Z. Anorg. Allg. Chem.* **2015**, *641*, 529.
(9) Wang, C.-H.; Ainsworth, C. M.; Gui, D.-Y.; McCabe, E. E.; Tucker, M. G.; Evans, I. R.; Evans, J. S. O. *Chem. Mater.* **2015**, *27*, 3121.
(10) Ainsworth, C. M.; Wang, C.-H.; Johnston, H. E.; McCabe, E. E.; Tucker, M. G.; Brand, H. E. A.; Evans, J. S. O. *Inorg. Chem.* **2015**, *54*, 7230.
(11) Nitsche, F.; Niklaus, R.; Johrendt, D. *Z. Anorg. Allg. Chem.* **2014**, *640*, 2897.
(12) Treacy, M. M. J.; Newsam, J. M.; Deem, M. W. *Proc. R. Soc. A* **1991**, *433*, 499.
(13) Warren, B. E. *Phys. Rev.* **1941**, *59*, 693.
(14) Proffen, T.; Neder, R. B. *Diffuse Scattering and Defect Structure Simulations: A Cook Book Using the Program DISCUS*; Oxford University Press: Oxford, 2008.
(15) Leoni, M.; Gualtieri, A. F.; Roveri, N. *J. Appl. Crystallogr.* **2004**, *37*, 166.
(16) Casas-Cabanas, M.; Rodriguez-Carvajal, J.; Canales-Vazquez, J.; Laligant, Y.; Lacorre, P.; Palacin, M. R. *J. Power Sources* **2007**, *174*, 414.
(17) Ufer, K.; Roth, G.; Kleeberg, R.; Stanjek, H.; Dohrmann, R.; Bergmann, J. *Z. Kristallogr.* **2004**, *219*, 519.
(18) Ufer, K.; Kleeberg, R.; Bergmann, J.; Dohrmann, R. *Clays Clay Miner.* **2012**, *60*, 535.
(19) Ufer, K.; Kleeberg, R.; Bergmann, J.; Dohrmann, R. *Clays Clay Miner.* **2012**, *60*, 507.
(20) Wang, X. D.; Li, J.; Hart, R. D.; van Riessen, A.; McDonald, R. *J. Appl. Crystallogr.* **2011**, *44*, 902.
(21) Bette, S.; Dinnebier, R. E.; Freyer, D. *J. Appl. Crystallogr.* **2015**, *48*, 1706.
(22) Coelho, A. A.; Evans, J. S. O.; Lewis, J. W. *J. Appl. Crystallogr.* **2016**, *49*, 1740.
(23) Shannon, R. *Acta Crystallogr. A* **1976**, *32*, 751.
(24) Her, J.-H.; Stephens, P. W.; Gao, Y.; Soloveichik, G. L.; Rijssenbeek, J.; Andrus, M.; Zhao, J.-C. *Acta Crystallogr. B* **2007**, *63*, 561.
(25) Brese, N. E.; O'Keeffe, M. *Acta Crystallogr. B* **1991**, *47*, 192.
(26) Brown, I. D. *Chem. Rev.* **2009**, *109*, 6858.

Chapter 6: Electronic Properties of Sr Doped $(La_{2-z}Sr_z)O_2CuCd_{0.5}Se_2$

6.1 Introduction

The work discussed in Chapter 6 is the area highlighted in green on the thesis map, Figure 6.1. It explores the effects of Sr doping on the La site of the compound $La_2O_2CuCd_{0.5}Se_2$ described in Chapter 5 (x = 0.5, 1Cu/1Cd). This was chosen over the other compounds in the series as it's the simplest parent system containing a single Cu layer and contains essentially no stacking faults. Sr doping has been performed on related compounds, such as $La_2O_2Cu_2S_2$,[1] $La_2O_2Cu_2Se_2$,[2] $Bi_2O_2Cu_2Se_2$[3], and leads to interesting and exploitable changes in the electronic properties of the materials. This occurs as charge compensation for the aliovalent substitution is achieved by the introduction of holes at the top of the valence band, which consists of Cu 3d and *Ch* *n*p states. This means that *p*-type conduction is largely contained within the $[Cu_2Ch_2]^{2-}$ layers, bound by $[A_2O_2]^{2+}$ insulating layers. Sr doping on $La_2O_2CuCd_{0.5}Se_2$ will give us the opportunity to see how layer-layer interactions and isolating layers influences conductivity.

In this chapter, sample purity and cell volumes/parameters are investigated across the $(La_{2-z}Sr_z)O_2CuCd_{0.5}Se_2$ solid solution to understand the Sr doping limit. Subsequently, the resistivity of various samples is measured from 3 – 300 K, in order to understand the effects of Sr doping on the electronic properties of the material. Density Functional Theory (DFT) calculations are also performed to understand the effect of the more complex structure on the band structure and conductivities.

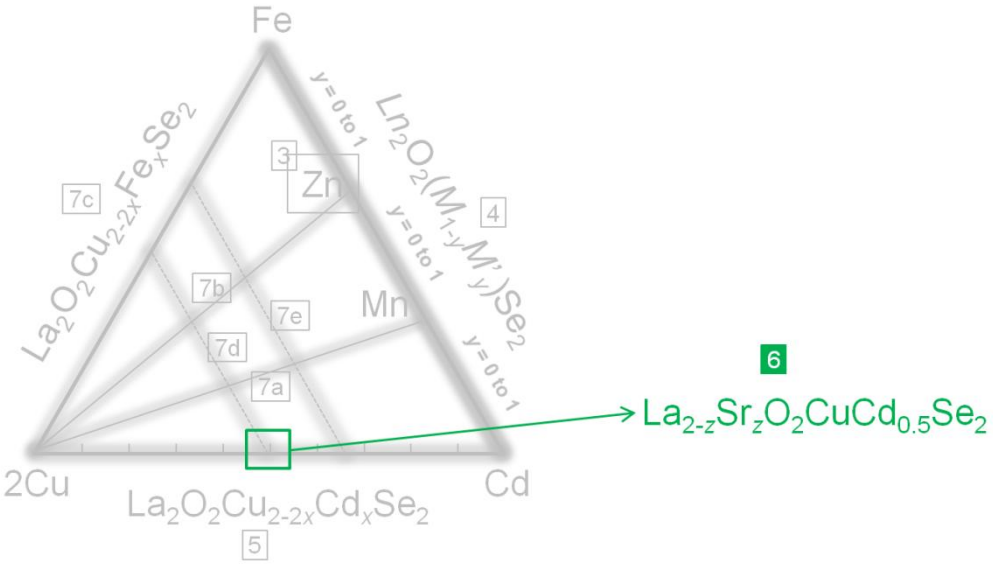

Figure 6.1. Thesis map highlighting the area of work discussed in Chapter 6.

6.2 Synthesis and Phase Purity

Samples across the $(La_{2-z}Sr_z)O_2CuCd_{0.5}Se_2$ (z = 0 to 1) solid solution were synthesized by heating reagents at 1100 ˚C for 12 hours, with an aluminium oxygen getter of 110% molar amount to control oxygen composition. Powder X-ray diffraction data were collected at the Diamond synchrotron source using beamline I11 (at a wavelength of 0.82592(1) Å).

The sample colours were cadmium yellow at z = 0, but changed to olive yellow at z = 0.05, brown beige at z = 0.1, tomato red at z = 0.15, wine red at z = 0.2 and black red at z = 0.3 and beyond. The colours are shown visually in Figure 6.2.

z	0	0.01	0.05	0.1	0.15	0.2	0.3	0.4	0.6	0.8	1
Doping %	0%	1%	2.5%	5%	7.5%	10%	15%	20%	30%	40%	50%
Colour											

Figure 6.2. Sample colour across the $(La_{2-z}Sr_z)O_2CuCd_{0.5}Se_2$ solid solution.

Rietveld fitting of the target phase was done using the 1Cu/1Cd model of $La_2O_2CuCd_{0.5}Se_2$ (presented in Chapter 5), space group *P*-4*m*2, with no stacking faults. Atomic positions and temperature factors were fixed at values determined in Chapter 5 for this compound, and other impurity phases were included in the model as required. The type and level of impurities encountered are shown for selected samples in Figure 6.3; these samples are highlighted red in Table 6.1. Where multiple samples were made at the same target percentage doping, the purest and/or best quality data is shown.

Table 6.1 and Figure 6.4 show the weight percent of phases formed across the range of doping levels attempted, determined from Rietveld fitting of powder X-ray diffraction data. From z = 0 - 0.2 (0% to 10% doping), a near pure (>98%) layered ZrCuSiAs-related phase formed. Phase purity declines gradually beyond z = 0.2 (10% doping), with CdSe and SrSe impurities emerging, as well as several other phases which at present cannot be identified. As the structure and composition of these phases is not known it is impossible to accurately determine their weight percentage. However to give an approximate indication, Table 6.1 estimates the weight percent from the relative peak intensity of the most intense peak of each unknown phase, relative to the most intense target phase peak. All weight percentages are summed and scaled to 100% total. The number of unknown phases is estimated by comparison of impurity peak intensities between different samples (using a stackplot such as that given in Figure 6.3, top).

For z = 0 we see an excellent fit to both the subcell reflections and the weaker supercell reflections which arise from ordering of the Cu/Cd layers and the ordered positions in the *xy* plane of the Cd checkerboard (mirrored across Cu layers). This is retained up to x = 0.05. However at x = 0.1 there is peak broadening observed in 00*l* and other supercell reflections; this effect gets progressively more severe for x = 0.15 and beyond. Similar observations could be made across the $La_2O_2Cu_{2-2x}Cd_xSe_2$ solid solution of Chapter 5, hence *pa*/*pb* type faulting is likely. Also, the asymmetric broadening and eventual loss of the peaks at around 12° 2θ resemble the Warren type peaks[4] observed in the more Cu rich samples of Chapter 5. Although the 001 reflection gets broader as z increases, it still remains up to z = 0.8 suggesting significant 1Cu/1Cd order has been retained. It is not until z = 1 that all intensity in the 001 reflection is lost. As discussed below, this could be caused by changes in the Cu:Cd ratio preventing layer ordering. Although we believe at present that unfitted peaks are due to unknown impurity phases, it cannot be ruled out that these could be superstructure reflections from another ordered arrangement. Their 2θ positions do not however point towards any of the other phases of Chapter 5, such as a 2Cu/1Cd composition.

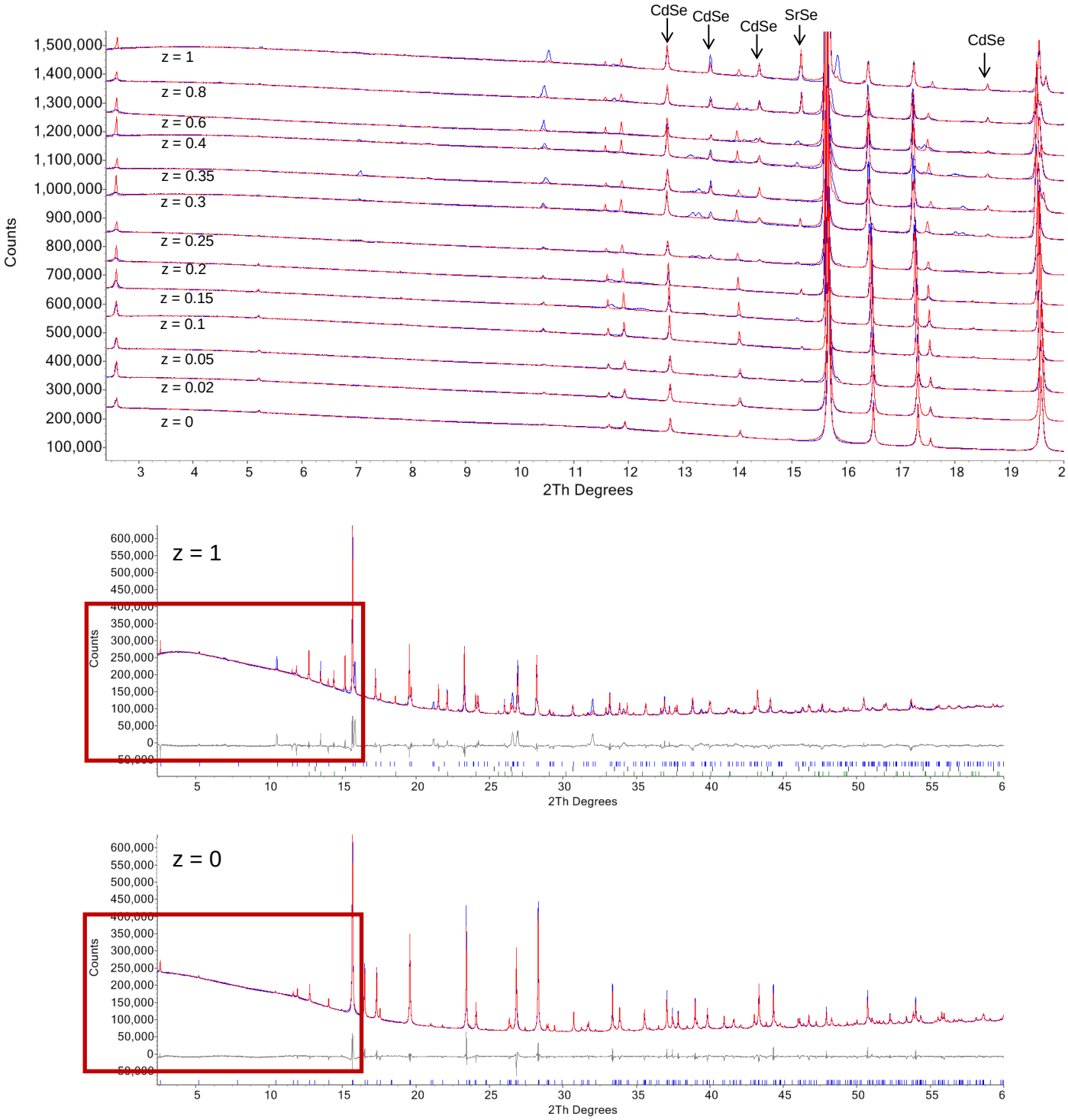

Figure 6.3. Top, zoomed-in Rietveld profiles from 2–20° 2θ using the 1Cu/1Cd model of $La_2O_2CuCd_{0.5}Se_2$. Up to z = 0.1 (5% Sr doping), the model provides a good structural description. Known impurity phases are indicated. Middle/bottom, full Rietveld fits from 2-60° 2θ of the z = 0 and 1 samples, where the red squares highlight the area shown in the top image.

z	Target phase %	La_2O_2Se phase %	SrSe phase %	CdSe phase %	Total unknown phase(s) %	Number of unknown phases
0.00	100	0	0	0	0	0
0.02	100	0	0	0	0	0
0.05	98	1	1	0	0	0
0.05	99	0	1	0	1	1
0.10	100	0	0	0	0	0
0.10	99	0	1	0	0	0
0.15	99	0	0	0	1	1
0.20	99	0	0	0	1	1
0.20	99	0	1	0	0	0
0.25	98	0	0	1	1	2
0.25	96	0	1	1	1	2
0.30	96	0	1	2	1	2
0.35	92	0	0	3	5	2
0.35	92	0	0	5	3	2
0.40	94	0	0	2	4	3
0.40	89	0	3	2	6	2
0.40	81	0	1	2	17	1
0.50	87	0	0	3	10	3
0.50	86	0	0	3	11	1
0.60	80	0	3	2	16	1
0.60	89	0	0	1	10	2
0.70	80	0	3	4	13	2
0.80	79	0	5	2	14	2
0.80	67	0	8	4	22	2
1.00	63	0	9	4	24	2
1.00	72	0	9	3	16	1

Table 6.1. Weight % of phases formed across $(La_{2-z}Sr_z)O_2CuCd_{0.5}Se_2$ series, including repeats. Rietveld-derived errors are negligibly small, and more realistic errors are ~2%. The "unknown" phase purity % is estimated by the method described in the text. Rietveld plots of the samples highlighted red are given in Figure 6.3.

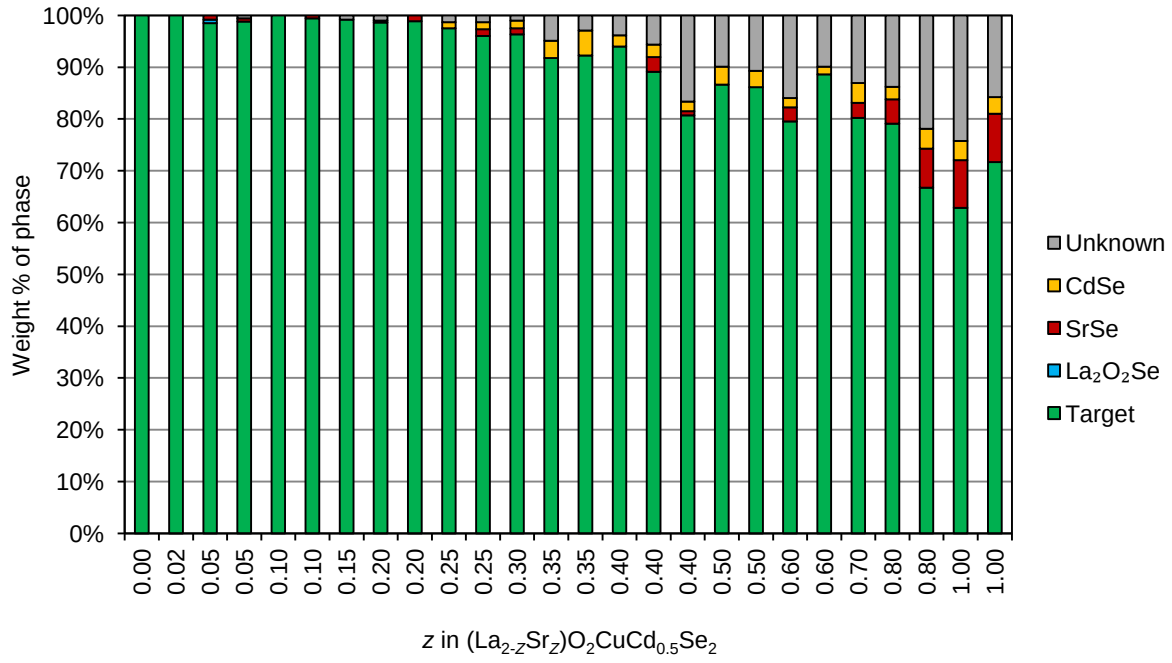

Figure 6.4. Weight % of phases formed across $(La_{2-z}Sr_z)O_2CuCd_{0.5}Se_2$, including repeats.

6.3 Cell Volume/Parameter Trends of $(La_{2-z}Sr_z)O_2CuCd_{0.5}Se_2$, $0 \leq z \leq 1$

Figure 6.3 left shows a progressive and smooth increase in cell volume between z = 0 and 0.3. This may be expected from the increase in ionic radii of Sr^{2+} (1.26 Å) relative to La^{3+} (1.16 Å)[5], and, with the high sample purity observed, is good evidence that Sr can be doped on the *Ln* site. Beyond z = 0.3, the cell volume is more scattered, even for repeat samples of the same target composition; despite this the cell volumes all still lie between those of the z = 0 to 0.4 samples. For comparison, Figure 6.5 (right) compares cell volumes of the $(La_{2-z}Sr_z)O_2CuCd_{0.5}Se_2$ solid solution with the $La_2O_2Cu_{2-2x}Cd_xSe_2$ solid solution of Chapter 5, and will be referred to in later discussion.

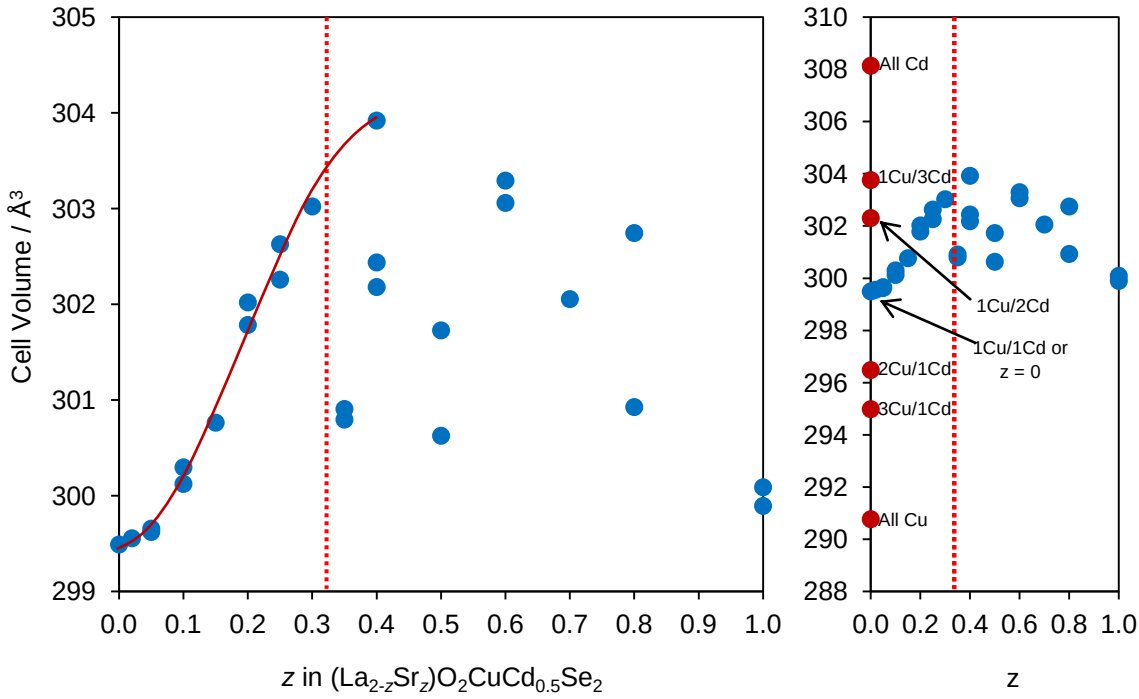

Figure 6.5. Left, cell volume of 2D ZrCuSiAs-related phases in the $(La_{2-z}Sr_z)O_2CuCd_{0.5}Se_2$ solid solution. Right, the same plot compared with cell volumes of the compounds of Chapter 5. Rietveld error bars are smaller than data points.

Investigation of the individual cell parameters offers further insight into the origin of the volume scatter. Figure 6.6 shows that there is a progressive increase in both the *a*-cell and *c*-cell parameter between z = 0 and 0.3, however the *c*-parameter shows a much smaller overall increase. This is further strong evidence that Sr is incorporated into the structure on the *Ln* site: Chapter 4 showed how *Ln* site doping led to changes in all cell parameters, with the *a*-parameter changing at roughly double the rate of the *c*-parameter, while doping on the transition metal site led to changes almost exclusively in the *c*-parameter.

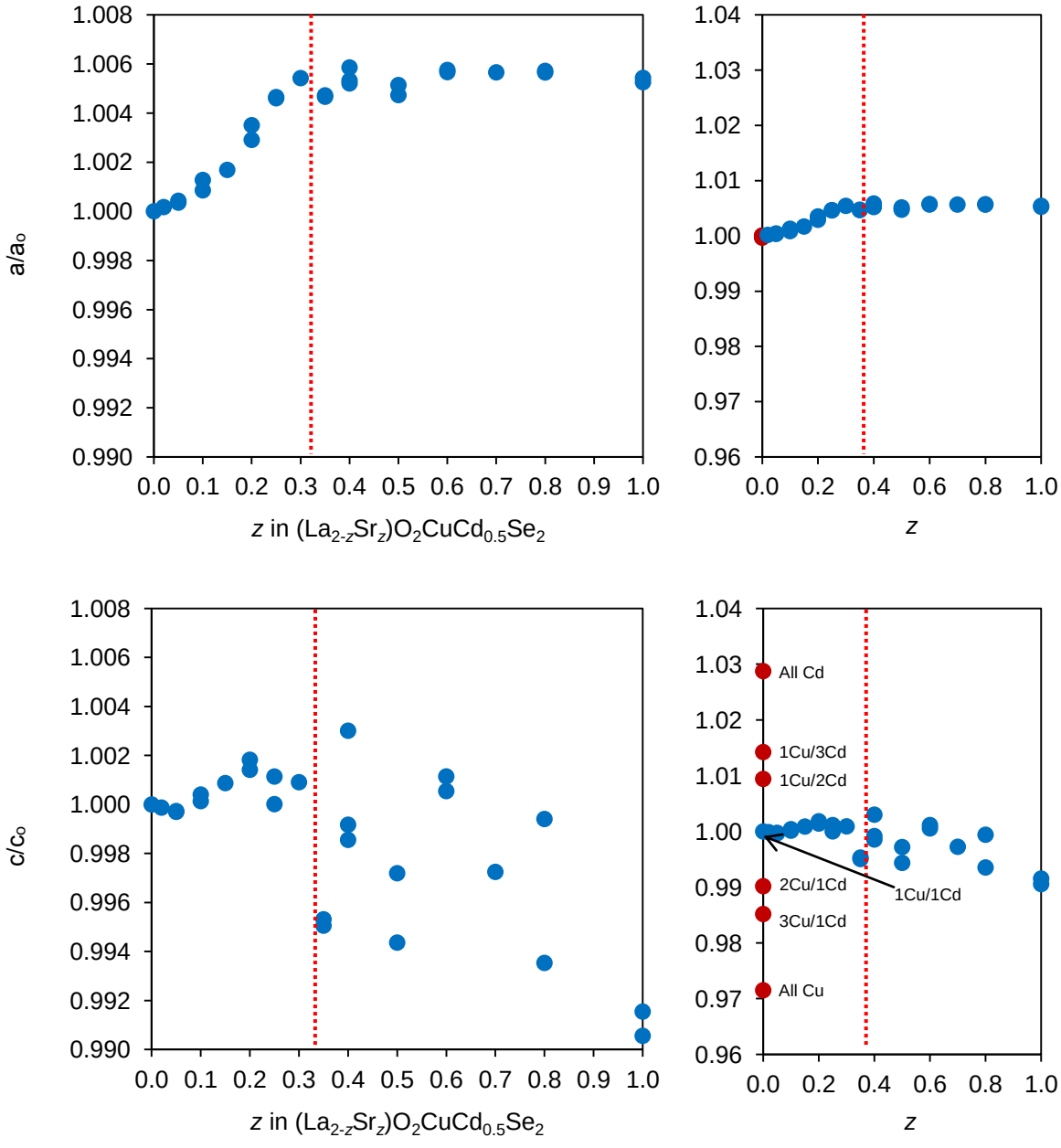

Figure 6.6. Left, cell parameters of 2D ZrCuSiAs-related phases in the $(La_{2-z}Sr_z)O_2CuCd_{0.5}Se_2$ solid solution. Right, the same plot compared with the compounds of Chapter 5 (all 7 red data points are on top of each other in top figure as a-paramter is equated). Rietveld error bars are smaller than data points.

Beyond z = 0.3, the *a*-parameter plateaus suggesting the sample is approaching the solid solution limit, while the *c*-parameter changes more erratically, showing that its behaviour is driving the scattered nature of the cell volume plot. One possible explanation for this is as follows: when the Sr saturation point is reached at z ~ 0.3, additional Sr forms SrSe or other unidentified Sr-containing phases. The excess Sr therefore removes elements which are required by the target phase, thereby both reducing the amount of target phase produced, and affecting its composition. In particular this could alter the relative ratio of Cu to Cd, which may lead to formation of other $La_2O_2Cu_{2-2x}Cd_xSe_2$ phases discussed in Chapter 5. For example, if a large amount of CdSe is formed, this could mean the relative ratio of Cu to Cd in the target phase results in a 2Cu/1Cd structure, which could explain the shorter *c*-axis. The introduction of excess Cu over Cd layers would also perturb the layer stacking sequence contributing to the peak broadenings observed in Figure 6.3. This is supported by the x = 0.6 and 0.8 samples of Figure 6.3 having relatively large *c*-axes and relatively sharp 001 reflections (pink and violet PXRD patterns of Figure 6.7). A second x = 0.8 sample had a smaller *c*-axis and broader peaks (green PXRD pattern of Figure 6.7). Other samples are also consistent with this trend.

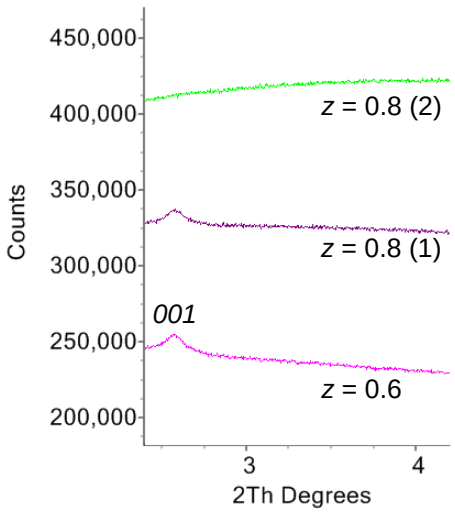

Figure 6.7. Selected low angle region of PXRD patterns of $(La_{2-z}Sr_z)O_2CuCd_{0.5}Se_2$ suggesting the introduction of excess Cu over Cd layers perturbing the layer stacking sequence, contributing to the peak broadening in the 001 reflection.

The trends in *a* and *c* across $(La_{2-z}Sr_z)O_2CuCd_{0.5}Se_2$ (z = 0 to 0.3) seem to follow what would be expected from ionic radii considerations.[5] Unusually the same trends are not observed in $(La_{2-z}Sr_z)O_2Cu_2S_2$ or $(La_{2-z}Sr_z)O_2Cu_2Se_2$.[1,2] In $(La_{2-z}Sr_z)O_2Cu_2S_2$, from z = 0 to 0.6, the *a*-parameter stays nearly constant while the *c*-parameter decreases linearly (~0.1% in total) up to z = 0.2, then remains constant up to z = 0.6. For z < 0.4, samples are near single phase, with trace impurities up to z = 0.6.[1] In $(La_{2-z}Sr_z)O_2Cu_2Se_2$, from z = 0 to 0.4, all samples are reported as phase pure and the *a* and *c*-parameter constant. Quite worryingly, the authors state that "this is probably due to almost equal ionic radii between La^{3+} and Sr^{2+} ions".[2] Chapter 4 of this thesis showed how the ionic radii of La (1.16 Å) compared to Ce(1.14 Å) are different enough to show clear and systematic changes to cell parameters with good data collection and careful analysis, hence Sr (1.26 Å) could be considered to have a markedly different ionic radii relative to La. Future work within the group will restudy

the $(La_{2-z}Sr_z)O_2Cu_2S_2$ and $(La_{2-z}Sr_z)O_2Cu_2Se_2$ solid solutions to see if these findings are reliable.

It should be noted that the ZrCuSiAs phase in the z = 0.3 (15% target Sr doping) sample certainly does not contain all the Sr available during reaction, due to the presence of a ~1% SrSe impurity. A simple calculation indicates that ~13.5% Sr doping is achieved, perhaps slightly less if the other unknown impurities also contain Sr. This effect may be present in other samples up to x = 0.3 (15% Sr doping) to a lesser extent, and is certainly present in samples beyond.

z	V / Å	a / Å	c / Å
0	299.49(1)	4.0665(1)	18.1111(1)
0.02	299.56(1)	4.0672(1)	18.1089(2)
0.05	299.66(1)	4.0682(1)	18.1057(1)
0.05	299.62(1)	4.0679(1)	18.1063(1)
0.1	300.30(2)	4.0717(1)	18.1136(6)
0.1	300.12(1)	4.0699(1)	18.1185(1)
0.15	300.76(1)	4.0733(1)	18.1270(1)
0.2	302.02(1)	4.0807(1)	18.1368(1)
0.2	301.78(1)	4.0783(1)	18.1442(1)
0.25	302.63(1)	4.0854(1)	18.1318(2)
0.25	302.26(1)	4.0852(1)	18.1114(4)
0.3	303.02(1)	4.0885(1)	18.1276(3)
0.35	300.91(2)	4.0857(1)	18.0263(5)
0.35	300.80(2)	4.0854(1)	18.0216(5)
0.4	302.18(1)	4.0876(1)	18.0850(3)
0.4	302.44(1)	4.0881(1)	18.0962(3)
0.4	303.92(1)	4.0903(1)	18.1657(2)
0.5	300.63(2)	4.0857(1)	18.0090(5)
0.5	301.73(1)	4.0874(1)	18.0603(5)
0.6	303.06(1)	4.0895(1)	18.1211(3)
0.6	303.29(1)	4.0899(1)	18.1319(2)
0.7	302.05(1)	4.0895(1)	18.0613(4)
0.8	302.74(1)	4.0897(1)	18.1004(4)
0.8	300.93(2)	4.0895(1)	17.9940(6)
1	299.89(1)	4.0886(1)	17.9401(5)
1	300.09(2)	4.0878(1)	17.9580(5)

Table 6.2. Cell volume/parameters of 2D ZrCuSiAs-related phases in the $(La_{2-z}Sr_z)O_2CuCd_{0.5}Se_2$ solid solution.

6.4 Resistivity Measurements

The resistivity of samples between z = 0 and 0.4 (0% to 20% Sr doping) were measured from 3 - 300 K using a Quantum Design Physical Property Measurement System (PPMS) and are shown in Figure 6.8. Overall, the data show progressive changes as z increases. The first interesting point to note is the interruption of data collection below certain temperatures. This was initially believed to be due to contact issues between the sample and the Cu wires attached to the PPMS puck (see Chapter 2), which was made using silver paint. Though when the sample was inspected after data collection, there were no visual problems with the contact. In the z = 0 sample, four Pt contacts were sputtered onto the pellet in an attempt to improve the contact between sample and Cu wires, though this made no difference. The problem is therefore believed to be caused by high resistivity values which are approaching the instrument limits. At z = 0, 0.05, 0.1, 0.15, 0.2, 0.3 and 0.4 measurements were possible down to ~260, 155, 13, 3, 3, 3 and 3 K respectively.

For z = 0 the sample was insulating/semiconducting (indicated by increasing ρ as the temperature decreases) with ρ(300 K) = 1.5×10^4 Ω cm. On doping, ρ(300 K) decreased significantly to 8.2×10^1 Ω cm at z = 0.05, reaching a minimum of ~6×10^{-1} Ω cm for z = 0.3. This is in agreement with cell parameter plots which suggest that at z = 0.3, the Sr doping limit is reached. A plot of ρ(300 K) vs z is given in Figure 6.9.

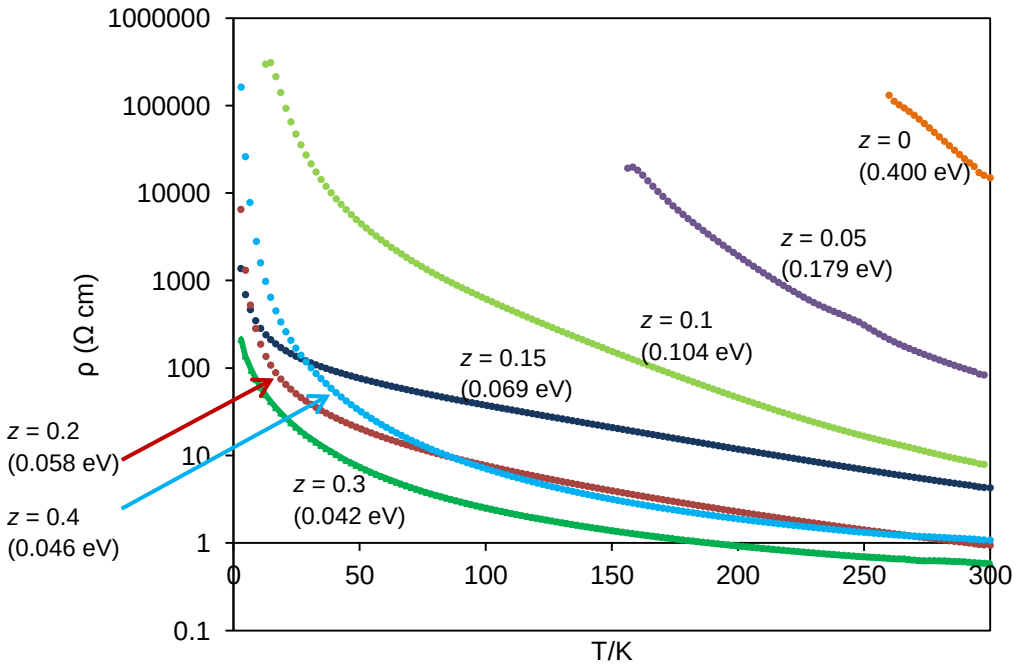

*Figure 6.8. Temperature dependence of electrical resistivity ρ for selected samples across the $(La_{2-z}Sr_z)O_2CuCd_{0.5}Se_2$ solid solution. The activation energy for each sample is given in parenthesis, and was determined from the gradient of a ln(T*conductivity) vs 1/T plot from 150 - 300 K.*

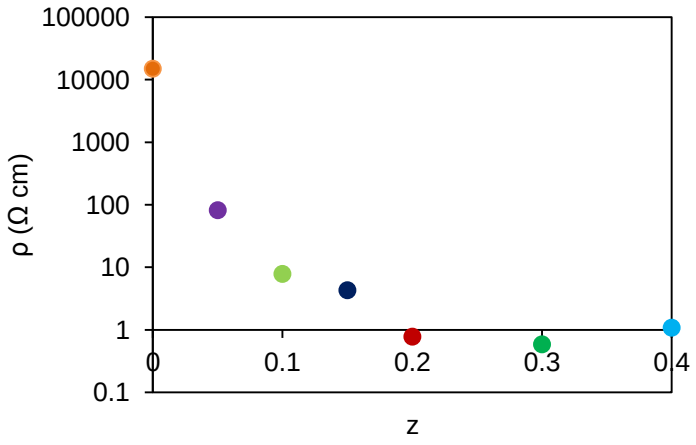

Figure 6.9. Plot of ρ(T = 300 K) vs *z for selected samples across the $(La_{2-z}Sr_z)O_2CuCd_{0.5}Se_2$ solid solution.*

6.5 Discussion/Band Structure Calculations

Resistivity measurements suggest similar conductivity changes to $La_2O_2Cu_2Se_2$ can be achieved by Sr doping, though samples do not reach metallic behaviour like in

$La_{2-z}Sr_zO_2Cu_2Se_2$ (z = 0.1 to 0.4).[6] This suggests that the band structures of $La_2O_2CuCd_{0.5}Se_2$ and $La_2O_2Cu_2Se_2$ are broadly similar. To confirm this we have performed DFT calculations using CASTEP[7] (embedded within Materials Studio) to determine the density of states (DOS) around the valence band (VB) and conduction band (CB) in $La_2O_2CuCd_{0.5}Se_2$, $La_2O_2Cu_2Se_2$ and $La_2O_2Cd_2Se_2$, using a local density approximation (LDA) functional. It should be noted that calculations performed on $La_2O_2Cu_2S_2$ (using the same method used for $La_2O_2CuCd_{0.5}Se_2$, $La_2O_2Cu_2Se_2$ and $La_2O_2Cd_2Se_2$) are analogous to those reported by Hosono *et al.* but with a smaller calculated bandgap, as discussed in Chapter 2.[6]

The DOS for $La_2O_2CuCd_{0.5}Se_2$ close to E_F is shown in Figure 6.10b. The valence band maximum consists of Cu 3d and Se 4p states, similar to that of $La_2O_2Cu_2Se_2$, Figure 6.10a. It is therefore reasonable to assume that Sr doping is charge compensated by the introduction of electronic holes within the Cu 3d and Se 4p states of the valence band, and therefore electronic conduction is confined to the $[Cu_2Se_2]^{2-}$ layers, as in hole doped $La_2O_2Cu_2Se_2$ and related materials.[1-3] One striking difference between the DOS for $La_2O_2CuCd_{0.5}Se_2$ relative to $La_2O_2Cu_2Se_2$ is how much broader the bands are. This band broadening is observed in $La_2O_2CdSe_2$ (Figure 6.10c) therefore this effect is likely caused by the introduction of Cd, even though the Cd states have little impact on the VB or CB.

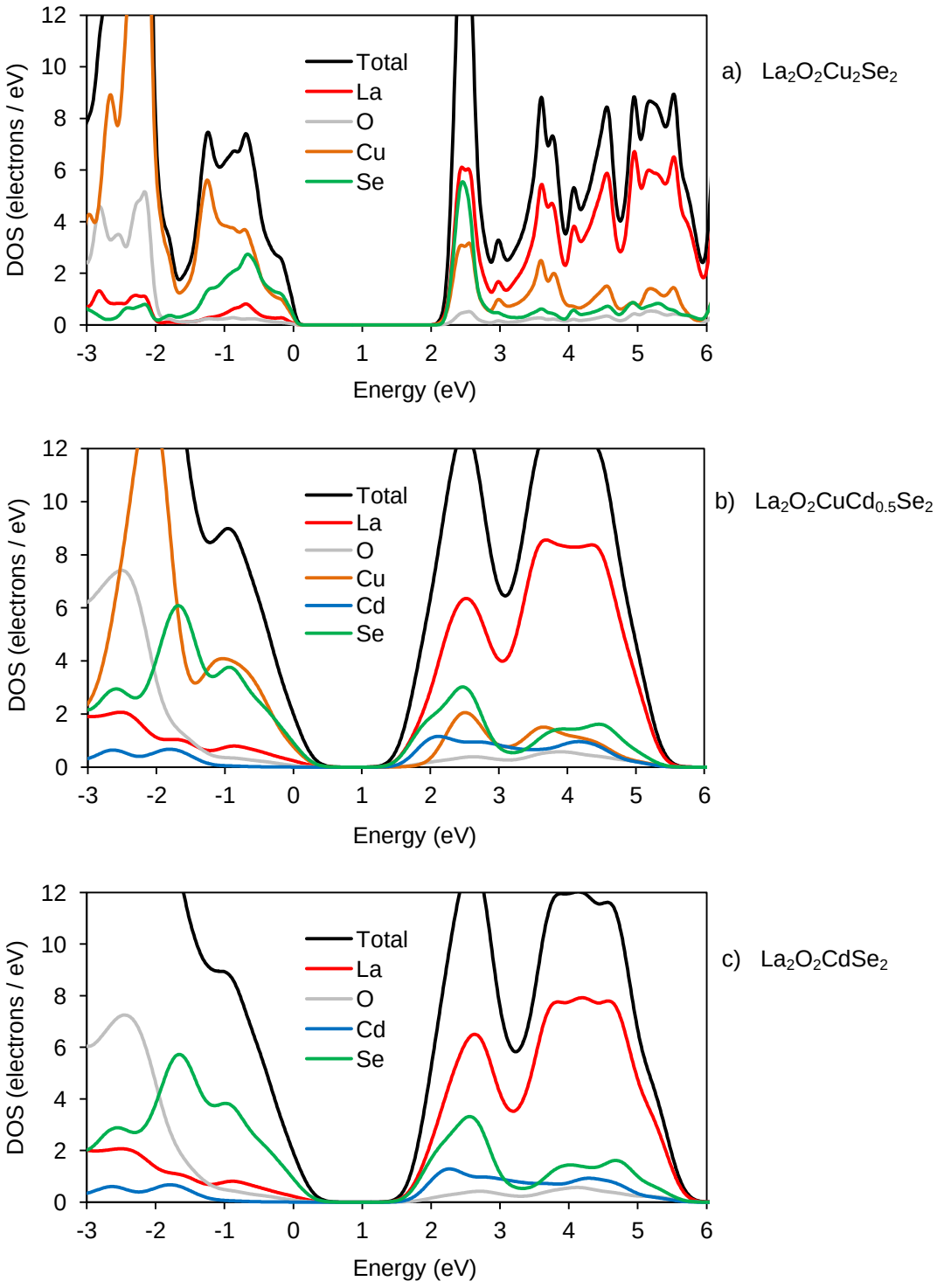

Figure 6.10. Total/partial DOS of (a) $La_2O_2CuCd_{0.5}Se_2$, (b) $La_2O_2Cu_2Se_2$ and (c) $La_2O_2CdSe_2$ near the Fermi energy.

6.6 Conclusions

This chapter shows that Sr can be successfully doped onto the La site of $(La_{2-z}Sr_z)O_2CuCd_{0.5}Se_2$, as has been possible in related systems. Cell volume/parameter plots show that the doping limit is z = 0.3 (15%). Undoped $La_2O_2CuCd_{0.5}Se_2$ shows insulating/semiconducting behaviour, while all samples between z = 0.05 and 0.3 (2.5% – 15% doping) show a systematic decrease in resistivity, such that samples approach the metallic regime. DFT calculations of $La_2O_2CuCd_{0.5}Se_2$ show that the valence band consists of Cu 3d and Se 4p states. Therefore charge compensation for Sr doping is likely achieved by the introduction of electronic holes into these states, hence electronic conduction is confined to the $[Cu_2Se_2]^{2-}$ layers.

6.7 References

(1) Takano, Y.; Yahagi, K.-i.; Sekizawa, K. *Physica B: Condensed Matter* **1995**, *206*, 764.
(2) Yasukawa, M.; Ueda, K.; Hosono, H. *J. Appl. Phys.* **2004**, *95*, 3594.
(3) Zhao, L.; Berardan, D.; Pei, Y.; Byl, C.; Pinsard-Gaudart, L.; Dragoe, N. *Appl. Phys. Lett.* **2010**, *97*, 092118.
(4) Warren, B. E. *Phys. Rev.* **1941**, *59*, 693.
(5) Shannon, R. *Acta Crystallogr. A* **1976**, *32*, 751.
(6) Ueda, K.; Hiramatsu, H.; Hirano, M.; Kamiya, T.; Hosono, H. *Thin Solid Films* **2006**, *496*, 8.
(7) Clark, S. J.; Segall, M. D.; Pickard, C. J.; Hasnip, P. J.; Probert, M. J.; Refson, K.; Payne, M. C. *Z. Kristallogr.* **2005**, *220*, 567.

Chapter 7: $La_2O_2Cu_{2-2x}M_xSe_2$ (*M* = Fe, Zn, Mn) and $La_2O_2Cu_{2-2x}(M_{1-y}M'_y)_xSe_2$-type (*M*/*M'* = Fe/Zn, Zn,Mn, Mn/Cd) Solid Solutions

7.1 Introduction

Chapter 7 (highlighted purple on the thesis map) extends the work of Chapter 5 by discussing three more solid solutions analogous to $La_2O_2Cu_{2-2x}Cd_xSe_2$. These are $La_2O_2Cu_{2-2x}Fe_xSe_2$, $La_2O_2Cu_{2-2x}Zn_xSe_2$ and $La_2O_2Cu_{2-x}Mn_xSe_2$, labelled as lines 7a, 7b and 7c respectively. It also investigates the effect of systematically varying the +2 transition metal size in the solid solutions $La_2O_2Cu(M_{0.5-y}M'_y)Se_2$ and $La_2O_2Cu_{0.667}(M_{0.667-y}M'_y)Se_2$ (*M*/*M'* = Fe/Zn, Zn/Mn & Mn/Cd) along the lines 7d and 7e. This is somewhat akin to the work of Chapter 4. It should be noted that the Chapter reports initial exploratory work on these compositions and that our understanding of their structure and properties is not at the same level as Chapters 3-6. However it will show that further complexity can be realised with such compositions, with evidence of mixing of Cu/*M* and time dependence to ordering, as well as the need for huge supercells for structural refinement, which make refinements more demanding due to computational limitations.

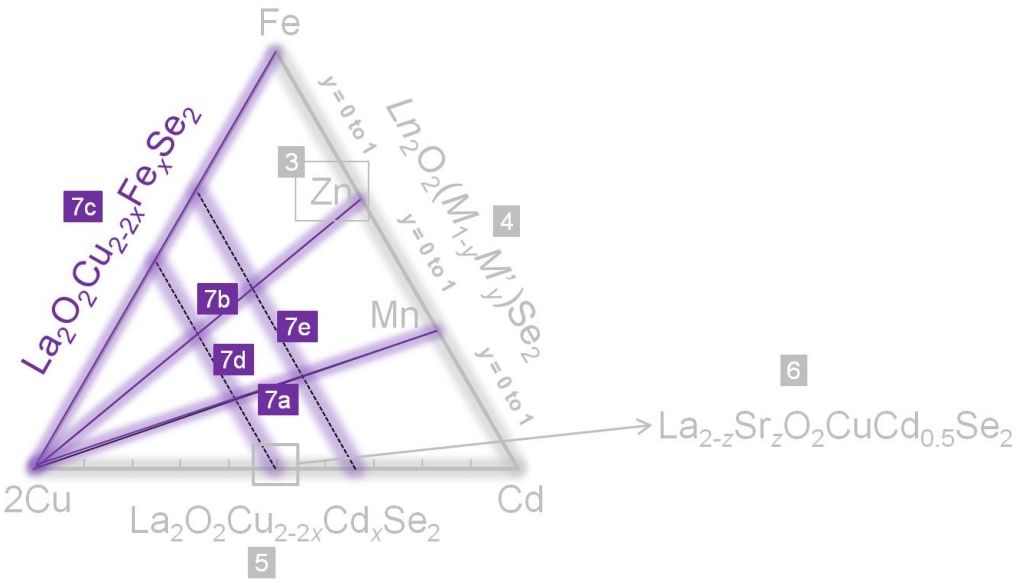

Figure 7.1. Thesis map highlighting the area of work discussed in Chapter 7.

7.2 Synthesis and Phase Purity

Samples across the $La_2O_2Cu_{2-2x}M_xSe_2$ (labelled as 7a, 7b and 7c in Figure 7.1 for *M* = Fe, Zn, Mn respectively) and $La_2O_2Cu_{2-2x}(M_{1-y}M'_y)_xSe_2$ (*M*/*M'* = Fe/Zn, Zn/Mn, Mn/Cd, labelled as 7d, 7e for *x* = 0.5 and 0.667 respectively) solid solutions were synthesized by heating for 12 hours at 1100 ˚C, with an aluminium oxygen getter of 110% molar amount to control oxygen composition. The colours varied across the solid solutions, and are shown visually in Table 7.1.

		All Cu	3Cu/1*M*	2Cu/1*M*	1Cu/1*M*	1Cu/2*M*	1Cu3*M*	All *M*
		x = 0	x = 0.25	x = 0.33	x = 0.5	x = 0.66	x = 0.75	x = 1
All Fe	*y* = 0							3D
	y = 0.2							
	y = 0.4							
	y = 0.6							
	y = 0.8							
All Zn	*y* = 1/0							
	y = 0.2							
	y = 0.4							
	y = 0.6							
	y = 0.8							
All Mn	*y* = 1/0							3D
	y = 0.2							
	y = 0.4							
	y = 0.6							
	y = 0.8							
All Cd	*y* = 1/0							

Table 7.1. Sample colour across the $La_2O_2Cu_{2-2x}(M_{1-y}M'_y)_xSe_2$ solid solutions. White cells represent samples which were not synthesised.

Powder X-ray diffraction data showed that in all cases, layered ZrCuSiAs-related phases had formed with a unit cell $a = b \approx 4$ Å, $c \approx 9$ Å (the subcell), explaining the main peaks present. Weak additional supercell reflections were observed at low angles for most samples with less than full occupancy of the transition metal sites, though the reflections varied greatly in intensity between the samples. Most samples contain a single phase (>95% purity) ZrCuSiAs-type layered compound, though in a limited number of cases two layered phases are clearly present. Two compositions formed the β or 3D structure type discussed in Chapter 1.4.

7.3 $La_2O_2Cu_{2-2x}M_xSe_2$ (*M* = Fe, Zn, Mn) Solid Solutions

7.3.1 Cell Volume/Parameter Trends

Three series of compounds were prepared which are analogous to the $La_2O_2Cu_{2-2x}Cd_xSe_2$ solid solution (discussed in Chapter 5). These were $La_2O_2Cu_{2-2x}Mn_xSe_2$, $La_2O_2Cu_{2-2x}Zn_xSe_2$ and $La_2O_2Cu_{2-2x}Fe_xSe_2$, corresponding to the purple lines 7a, 7b and 7c respectively in Figure 7.1. Samples were synthesised at x = 0, 0.25, 0.333, 0.5, 0.667, 0.75 and 1 for all three series. Unit cell volumes, Figure 7.2, showed a smooth variation across all series, suggesting a smooth change in structure with composition. The samples in the $La_2O_2Cu_{2-2x}Cd_xSe_2$ series of Chapter 5 are included for comparison, highlighted with a yellow line. The blue line represents the $La_2O_2(M_{1-y}M'_y)Se_2$ solid solutions of Chapter 4. Only one composition, x = 0.75 in $La_2O_2Cu_{2-2x}Fe_xSe_2$, shows obvious phase separation into two layered ZrCuSiAs-related phases. The *a*/*b* cell parameter remains relatively unchanged across the series, with almost all changes in cell volume due to contraction/expansion of the *c*-axis, Figure 7.3. As in related materials, this shows the high rigidity of Ln_2O_2 layers relative to M_nSe_2 layers. Note how the *a*-parameter shows subtle differences relative to the *b*-parameter in Fe containing compounds only, brought about by increasing 0C-1E stripe like

ordering as x increases (see below). This was also observed in the Fe containing compounds of Chapter 4.

One interesting aspect of the cell volume plot is the slight negative and positive gradient across the $La_2O_2Cu_{2-2x}Fe_xSe_2$ and $La_2O_2Cu_{2-2x}Zn_xSe_2$ solid solutions respectively. This suggests that the influence of replacing two Cu^+ ions with one Zn^{2+} ion acts to expand the lattice, while replacing two Cu^+ ions with one Fe^{2+} ion acts to contract the lattice. It is also clear that the effective ionic radii of Fe in these systems is smaller than Zn, as was identified in Chapter 4, even though Shannon's tables (Fe = 0.63, Zn = 0.6 Å for 4 coordinate +2 oxidation states) suggests it should be the other way around. This could be caused by small amounts of Fe^{3+} being present, or perhaps more likely by the transition metal ordering. Tabulated values for the cell volume/parameters of all samples are given in Appendix 4.

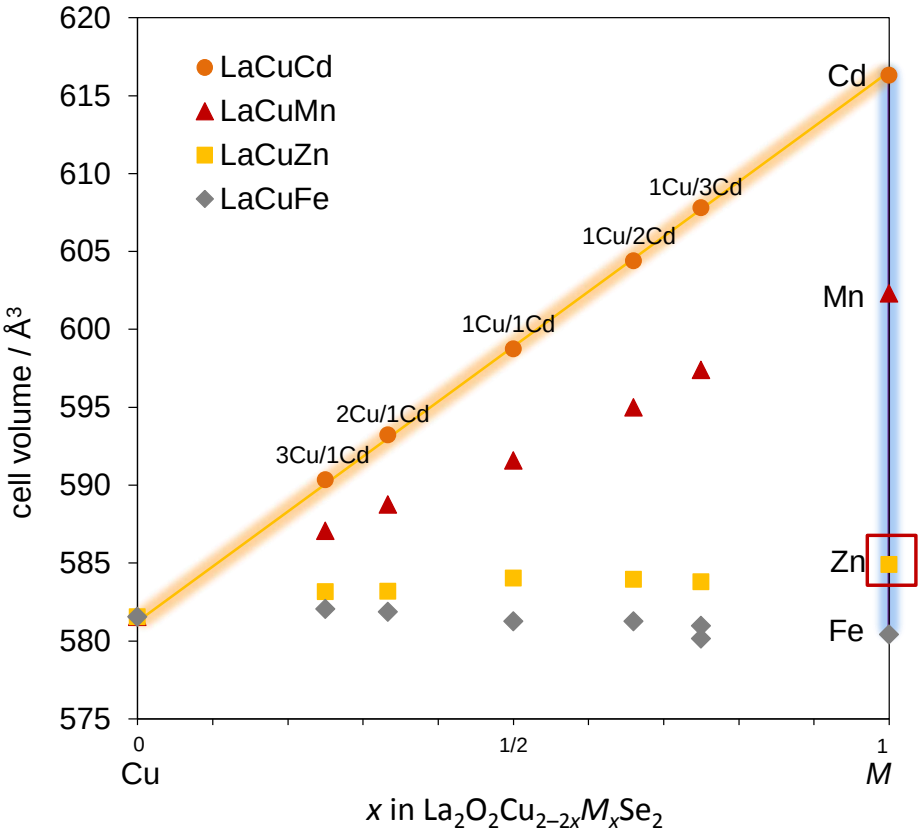

Figure 7.2. Variation in cell volume of phases formed across the $La_2O_2Cu_{2-2x}M_xSe_2$ (M = Fe, Zn, Mn, Cd) solid solutions. The blue and yellow lines represent the compositions of Chapter 4 and 5 respectively.

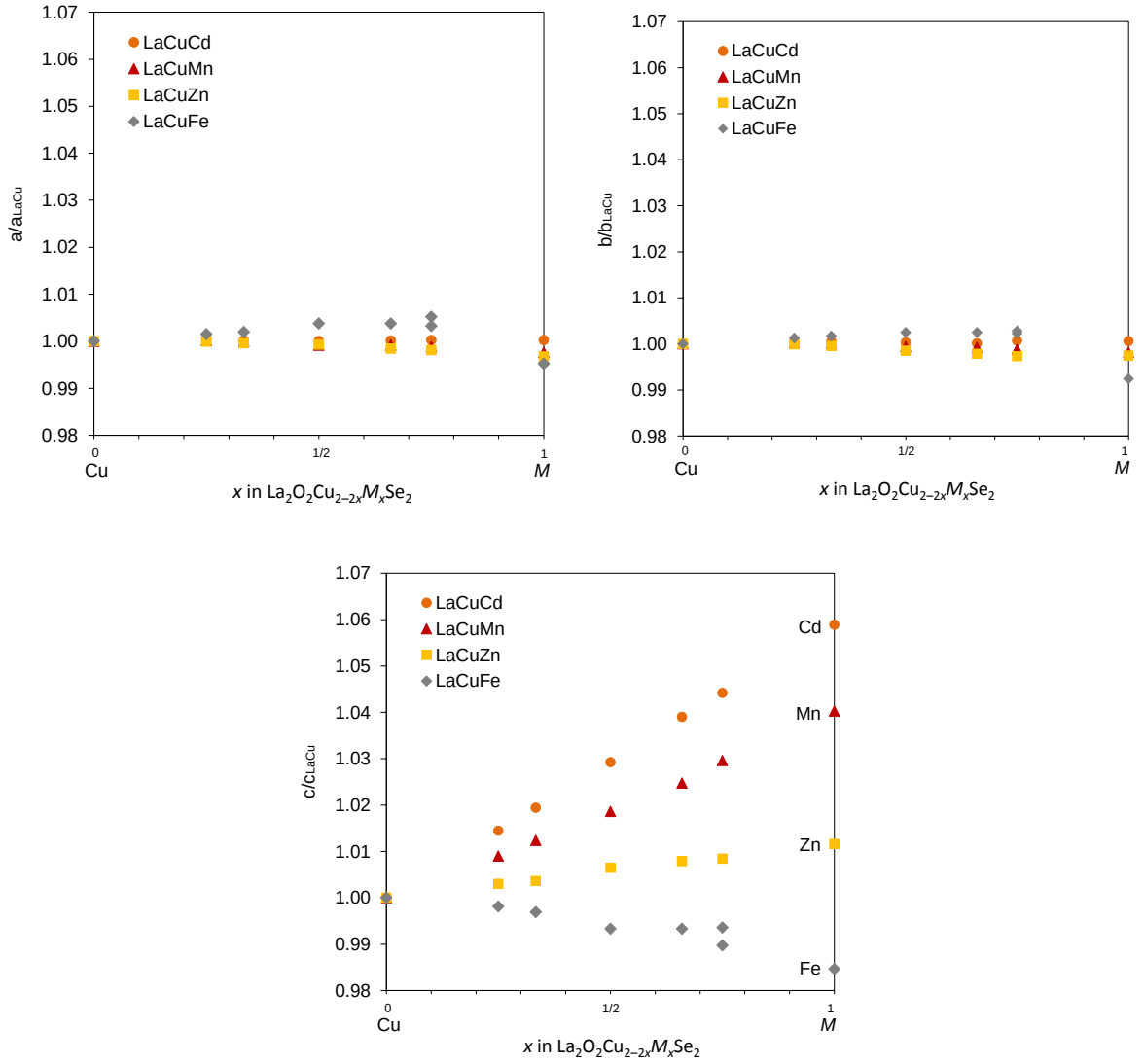

Figure 7.3. Variation in cell parameters of phases formed across the $La_2O_2Cu_{2-2x}M_xSe_2$ (M = Fe, Zn, Mn, Cd) solid solutions. Rietveld error bars are smaller than data points.

7.3.2 $La_2O_2Cu_{2-2x}Mn_xSe_2$ Solid Solution

Chapter 4 showed how all $Ln_2O_2MSe_2$-type compounds can be described as an evolving series using a modulated approach based on a $\sqrt{2}a_{subcell} \times \sqrt{2}b_{subcell} \times 2c_{subcell}$ parent cell with a modulation vector of **q** = α**a*** + 0**b*** + ½**c*** and superspace group *Cmme*(α01/2)0s0. The **q**-vectors for commensurate structures are α = 1 (0C-1E), α = 1/4 (3C-1E), α = 1/5 (4C-1E), α = 1/6 (5C-1E); for an *m*C-1E structure α = 1/(*m*+1). The **q**-vectors for incommensurate structures lie between these values. The modulation approach was used to determine α for all compounds reported in Chapter 4, by fitting the weak unindexed satellite peaks in the powder pattern of each sample by using the Pawley method to fit the subcell peaks and determine the subcell parameter, while satellite reflections were simultaneously fitted using a pseudo-Voigt peakshape at positions constrained by refining the magnitude of α.

If this modulation approach had been applied to compounds across the $La_2O_2Cu_{2-2x}Cd_xSe_2$ solid solution, it would have provided a fit to supercell reflections arising from ordering in the

ab plane (α = 0 across all samples as Cd checkerboard ordering is maintained throughout), though would have failed to fit supercell reflections present due to ordering of layers in the *c*-direction. An example is shown in Figure 7.4, for the x = 0.5 example, $La_2O_2CuCd_{0.5}Se_2$ (1Cu/1Cd).

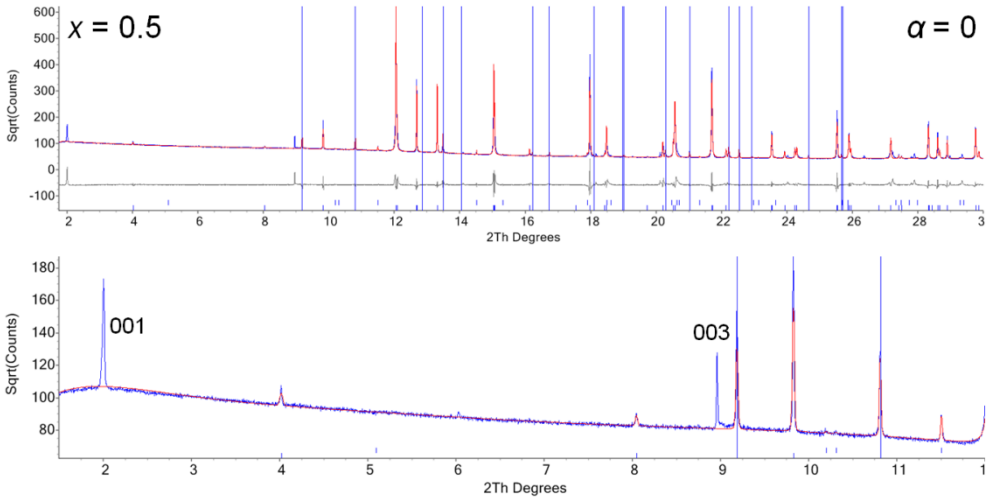

Figure 7.4. The modulation approach to fitting satellite peaks caused by transition metal ordering within layers (blue vertical lines) in $La_2O_2CuCd_{0.5}Se_2$ (1Cu/1Cd), as described in Chapter 4. Supercell reflections caused by layer ordering in the c-direction are unfitted.

This approach can therefore be very useful to learn about the ordering of transition metals in the *ab* plane, even though it cannot be used to study layer stacking in the *c*-direction. It was therefore used to study compounds across the $La_2O_2Cu_{2-2x}Mn_xSe_2$ series, shown in Figure 7.5. It should be noted that there may be potential to simultaneously determine the **q**-vector along the *a*-direction and *c*-direction, by a more complex application of the modulation approach.

At x = 0, no supercell reflections are expected due to full occupancy of transition metal sites in $La_2O_2Cu_2Se_2$. No observable supercell reflections appear until x = 0.667 where their appearance is very sudden, giving α = 0.210 suggesting in-plane ordering which is incommensurate in nature, between 4C-1E and 3C-1E. It therefore seems there must be a critical ratio of Cu to Mn when ordering begins to occur, somewhere between x = 0.5 and x = 0.667. In x = 0.75, in-plane ordering is still prevalent with α = 0.204, close to commensurate 4C-1E transition metal ordering. With such strong apparent in-plane ordering in the x = 0.667 and x = 0.75 samples, it seems likely that the samples are behaving in the same way as the analogous $La_2O_2Cu_{2-2x}Cd_xSe_2$ compounds with Cu and Mn in distinct layers, though there are no obvious unfitted supercell reflections caused by a layer stacking sequence along the *c*-direction, such as those seen in Figure 7.4. However Chapter 5 showed that even a small number of stacking faults of only a few percent along the c-axis can have a large effect on such peaks, so perhaps a greater number of faults has caused them to lose all intensity. At x = 1, the $La_2O_2MnSe_2$ layered phase reported by others adopts the perfectly commensurate 4C-1E structure, though under our experimental conditions the β-phase forms.[1,2]

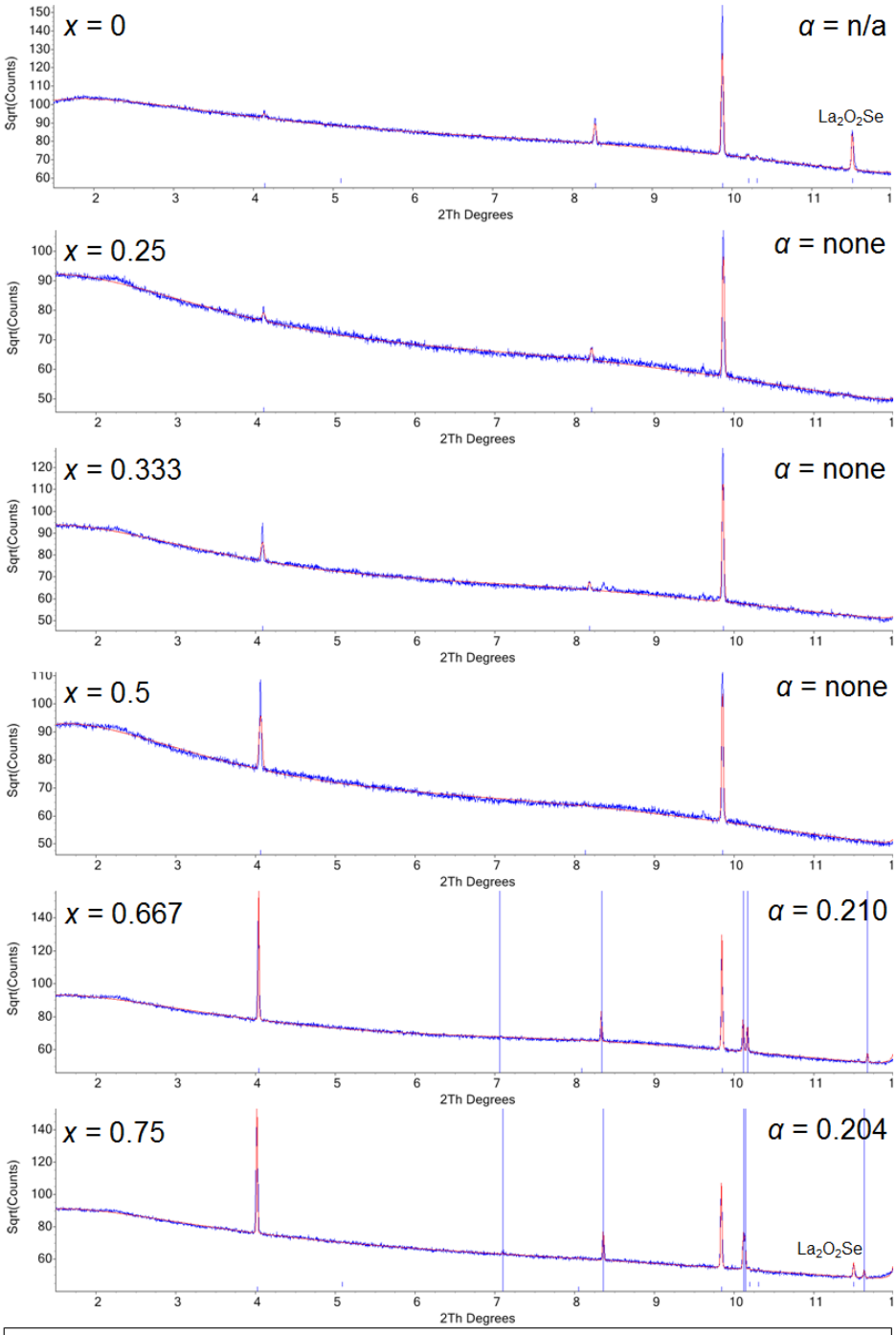

$x = 1$ $\alpha = 0.200$

2D $La_2O_2MnSe_2$ has been prepared by a single crystal synthesis by others. The β structure is adopted under our synthetic conditions.

Figure 7.5. The modulation approach to fitting satellite peaks caused by in-plane transition metal ordering (blue vertical lines) across the $La_2O_2Cu_{2-2x}Mn_xSe_2$ series from 1.5 to 12 2θ. 2D $La_2O_2MnSe_2$ is reported by others.[1] A $\sqrt{I}$ scale is used to emphasize the weaker supercell reflections.

The x = 0.667 sample was reheated for a further 12 hours and revealed an extremely interesting and important aspect of these compounds. Figure 7.6 shows the data for samples both after one 12 hour heat cycle (also shown in Figure 7.5) and two 12 hour heat cycles, fitted using the modulation approach. It can be seen that α changes from 0.210 (incommensurate in-plane ordering) to 0.200, suggesting perfectly commensurate 4C-1E in-plane ordering. An α value of 0.200 would be expected from a half occupied layer containing purely Mn, hence it seems reasonable to suggest that before reheating there could be slight mixing of the Mn and Cu within individual layers. As Cu has a smaller effective ionic radius than Mn, α would be expected to be larger if Cu is contained in the Mn layers, as per the theory described in Chapter 4; this seems to be the case. It should be noted that there is no evidence of phase separation, and an almost neglible change in the c-axis after heating (9.01533(4) Å before vs 9.01612(4) Å after). This is again consistent with our model.

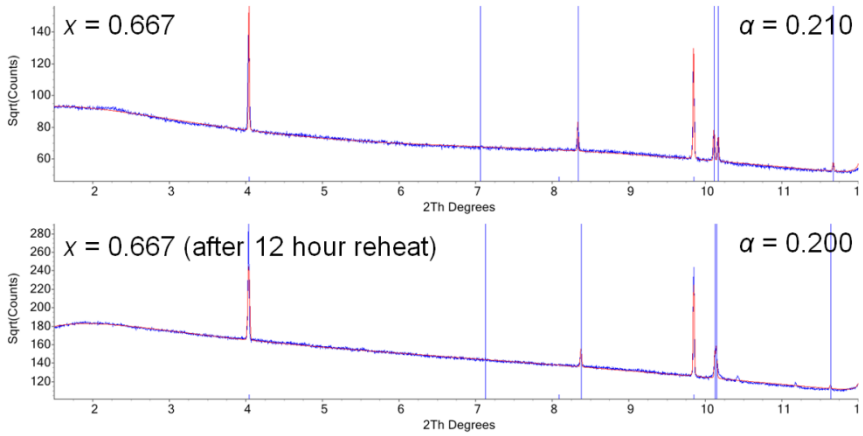

Figure 7.6. The fitting of satellite peaks caused by in-plane transition metal ordering (blue vertical lines) in x = 0.667 $La_2O_2Cu_{2-2x}Mn_xSe_2$ before and after a 12 hour reheat. A $\sqrt{I}$ scale is used to emphasize the weaker supercell reflections.

An attempt to quantify the amount of Cu within the Mn layers before reheating was done by using the α value of 0.210 and the results of Chapter 4. The sample $La_2O_2Zn_{0.3}Mn_{0.7}Se_2$ is shown to also have α = 0.210, and has an average transition metal ionic radii of 0.642 Å. To achieve the same average ionic radii using Mn^{2+} and Cu^{1+} ions there would need to be a 9:1 ratio respectively, therefore it seems reasonable to assume that before the sample is reheated there is ~10% of the Cu "stuck" in the Mn layers. Additional heating may allow time for the Cu and Mn to fully segregate into distinct layers.

Incommensurate ordering makes structure solution very difficult, and near impossible when stacking faults are also thrown into the mix. However the reheated x = 0.667 commensurate sample with α = 0.200 means this difficulty is avoided hence this sample would be a perfect candidate for full structural solution, including stacking microstructure; at present this has not been fully attempted. Figure 7.7 shows the unit cell if the same stacking rules (excluding stacking faults) are applied as in the $La_2O_2Cu_{2-2x}Cd_xSe_2$ solid solution, where Cu and Mn are in distinct layers with 4C-1E ordering within the Mn layers, and Mn atoms occupy the same sites either side of a given Cu layer; this could be termed a 1Cu/2Mn model. Figure 7.8 shows the Rietveld fit using this structural model. Clearly there are weak calculated 00*l* reflections that are not present in the experimental data, which a small proportion of stacking faults (relative to those present in the $La_2O_2Cu_{2-2x}Cd_xSe_2$ solid solution) would cause to lose

all intensity. It should be noted that allowing atomic positions and temperature factors to refine without considering stacking faults would lead to a structure that makes little chemical sense. This is shown, for example, by the data in Figure 5.17. These models have therefore not been refined at present.

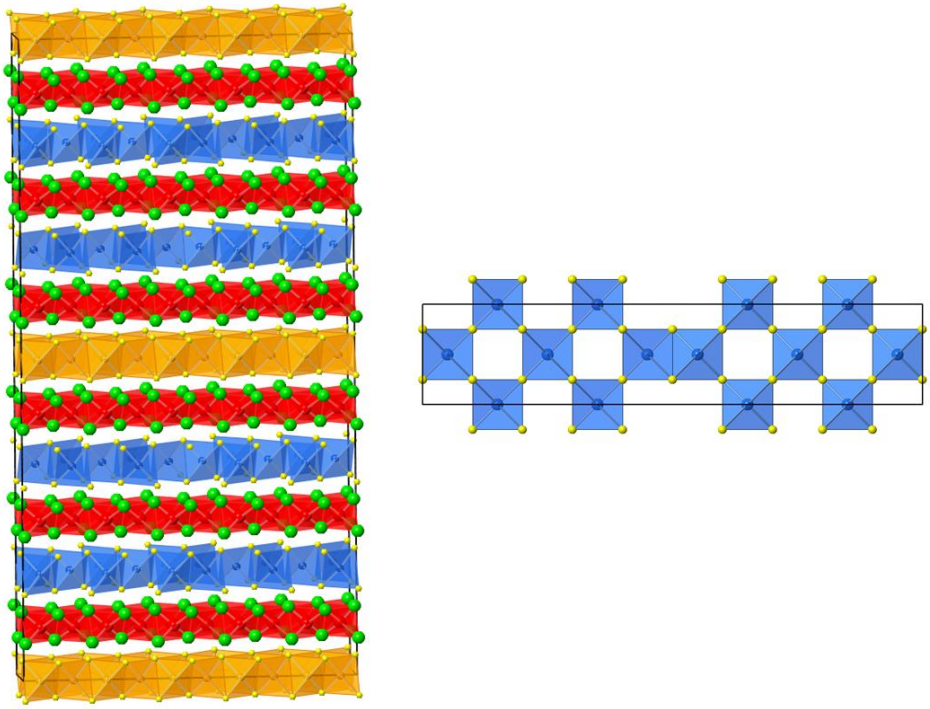

Figure 7.7. Left, fully ordered structural model for $La_2O_2Cu_{0.667}Mn_{0.667}Se_2$ (1Cu/2Mn) viewed down [100], space group Imcb. La^{3+} cations are shown in green, O^{2-} anions in red, Cu^{1+} cations in orange, Mn^{2+} cations in blue and Se^{2-} anions in yellow. Right, view down [001] showing 4C-1E ordering of Mn layers.

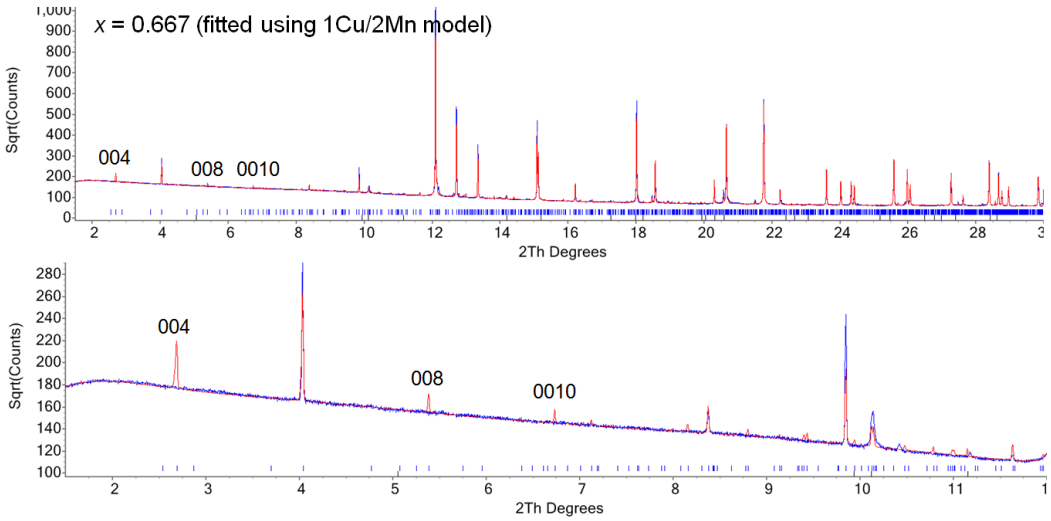

Figure 7.8. Rietveld refinement profile of synchrotron powder diffraction data for $La_2O_2Cu_{0.667}Mn_{0.667}Se_2$ using the fixed structural model proposed in Figure 7.7, without consideration of stacking faults. A $\sqrt{I}$ scale is used to emphasize the weaker supercell reflections.

One problem with performing a stacking fault analysis (such as those outlined in Chapter 5) on the reheated x = 0.667 sample, is the increased size of the unit cell relative to $La_2O_2Cu_{2-2x}Cd_xSe_2$-type compounds, which are smaller due to the simpler checkerboard-type Cd ordering across this series. This makes defining the layers more difficult, especially as there are now also subtle xy distortions within the Mn^{2+} layers. The refinements are also much more computationally demanding. However, the stacking fault method proposed in Chapter 5 has been further improved since this work was performed, in particular to speed up calculations. This refinement may now be possible, and perhaps even more complex structures can be solved in this way. Other researchers in the group will attempt this in the near future.

7.3.3 $La_2O_2Cu_{2-2x}Zn_xSe_2$ Solid Solution

Figure 7.9 shows data for the $La_2O_2Cu_{2-2x}Zn_xSe_2$ series fitted using the modulation approach discussed above. The most obvious difference is the onset of in-plane ordering in the first Zn^{2+} containing compound at x = 0.25, shown by vertical blue lines. The superstructure peaks sharpen and further grow in intensity as x increases and Zn levels increase. This is unlike the $La_2O_2Cu_{2-2x}Mn_xSe_2$ series, where in-plane ordering seemed to come about suddenly at x = 0.667. Another peculiarity is the consistent incommensurate α-value present in all samples except the x = 1 end member. Persistent heating of the x = 0.667 sample yielded no change in α from 0.242, suggesting that in-plane ordering is established quickly and is fixed. Perhaps this hints at a thermodynamic preference for slight Cu/Zn mixing, though at present this is somewhat speculative.

A full structural solution of the incommensurately ordered compound $Ce_2O_2MnSe_2$ was achieved by Dr Chun-Hai Wang, during work conducted alongside that of this thesis. In this compound α = 0.158, though an approximate structure was constructed by merging 5C-1E type ordering (α = 0.167) with 6C-1E type ordering (α = 0.143), resulting in $\alpha = \left(\frac{(0.167+0.167+0.143)}{3}\right) = 0.159$, as shown in Figure 7.10. By using such an approximation, any incommensurately modulated ordering pattern can be approximated, though unit cells can become extremely large, For example, in the $La_2O_2Cu_{2-2x}Zn_xSe_2$ solid solution a structural model for the x = 0.375 sample, α = 0.244, could be approximately achieved by nine adjacent 4C-1E-type and one 5C-1E-type orderings:

$$\alpha = \left(\frac{(0.25+0.25+0.25+0.25+0.25+0.25+0.25+0.25+0.25+0.2)}{10}\right) = 0.245.$$

A 1Cu/3Zn-type model was constructed using this Zn ordering and the stacking conditions determined in Chapter 5 for the $La_2O_2Cu_{2-2x}Cd_xSe_2$ solid solution, shown in Figure 7.11. This model was used to fit the synchrotron data, Figure 7.12, and by refining only cell parameters provides a reasonable fit. Attempts to refine any other structural information (atomic positions, temperature factors, etc) were, as expected, unsuccessful due to computational limitations. In-plane superstructure peaks are predicted at the correct 2θ value, and it would be expected that if distortions could be refined within Zn layers a better fit would be achieved to these peaks. There are also two superstructure peaks at ~3 and ~5 2θ, which are almost in the correct position for the 003 and 005 reflections; perhaps refinement of atomic positions in the c-direction (hence layer separation) would more accurately predict their 2θ position. Nonetheless, this seems to suggest that the stacking conditions determined in Chapter 5 for the $La_2O_2Cu_{2-2x}Cd_xSe_2$ solid solution may be applicable in this compound. If it were

computationally feasible, stacking faults would also need to be included into the model to lose intensity from certain reflections such as 002, labelled in Figure 7.12.

Interestingly, the same low angle peaks in x = 0.75, believed to arise from ordering along c by a 1Cu/3Zn model (at ~3 and ~5 2θ), are present in the x = 0.667 data. Therefore, a 1Cu/3Zn model provides a better fit to the data than a 1Cu/2Zn model. It is unclear at present why this is the case.

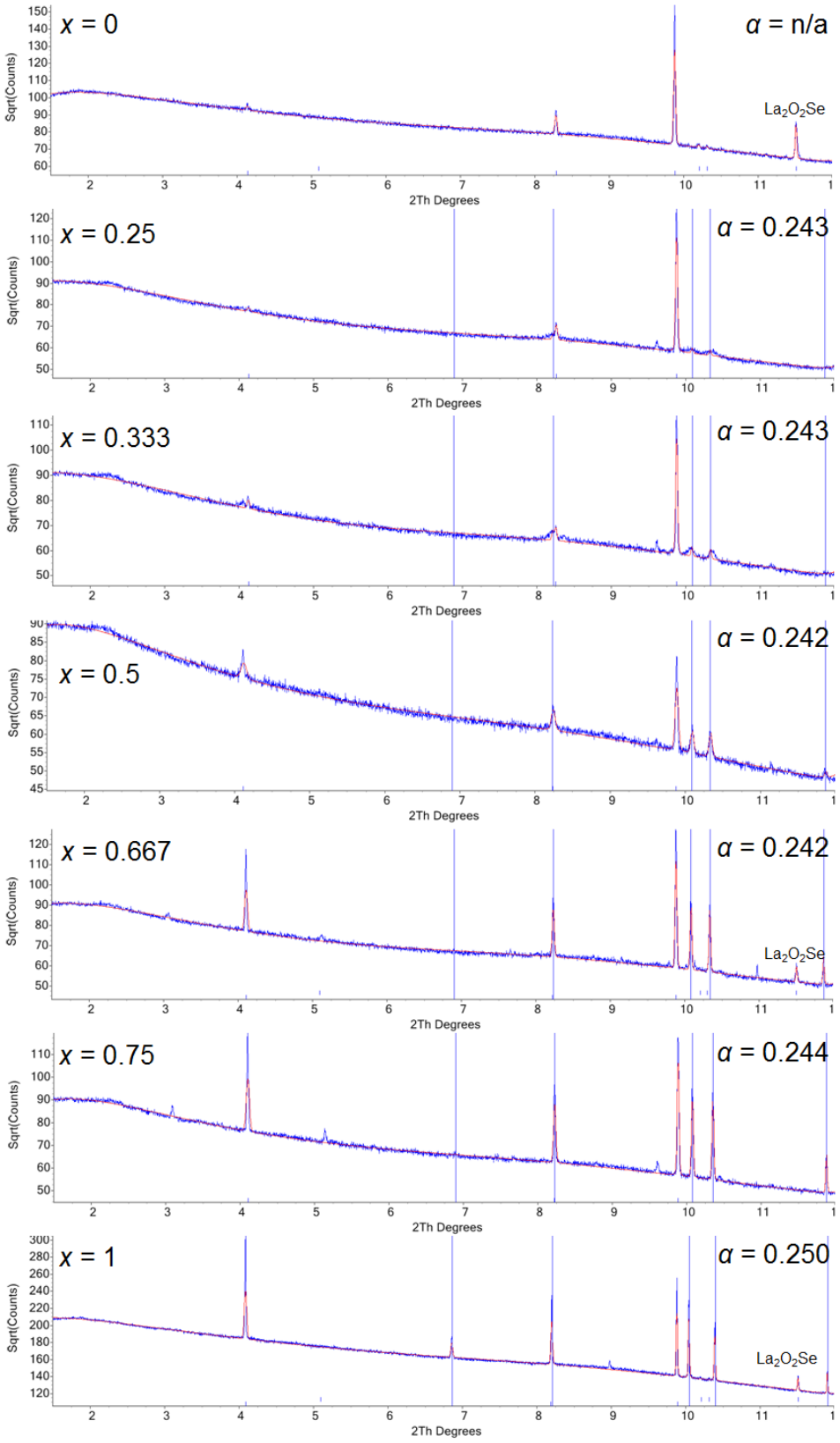

Figure 7.9. The modulation approach to fitting satellite peaks caused by in-plane transition metal ordering (blue vertical lines) across the $La_2O_2Cu_{2-2x}Zn_xSe_2$ series from 1.5 to 12 2θ. A $\sqrt{I}$ scale is used to emphasize the weaker supercell reflections.

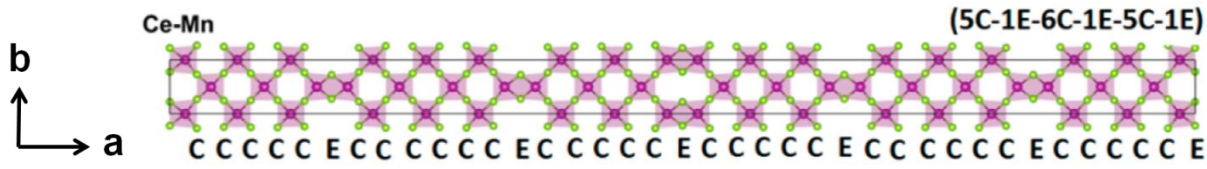

Figure 7.10. In-plane Mn ordering pattern adopted in $Ce_2O_2MnSe_2$. Figure taken from Wang et al..[3]

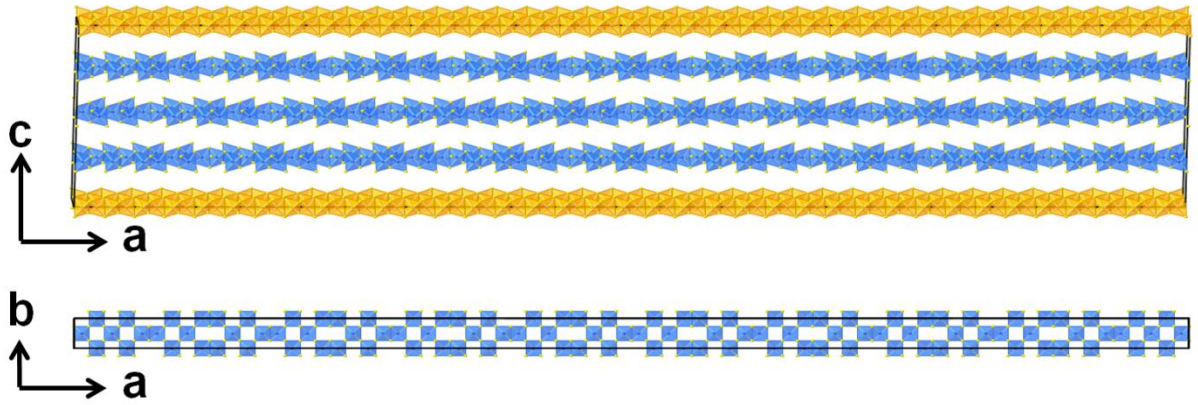

Figure 7.11. Approximated 1Cu/3Zn structural model for $La_2O_2Cu_{0.5}Zn_{0.75}Se_2$ (x = 0.75). Yellow polyhedra are $[Cu_2Se_2]^{2-}$ layers, blue polyhedra are $[ZnSe_2]^{2-}$ layers. $[La_2O_2]^{2+}$ layers are omitted for clarity.

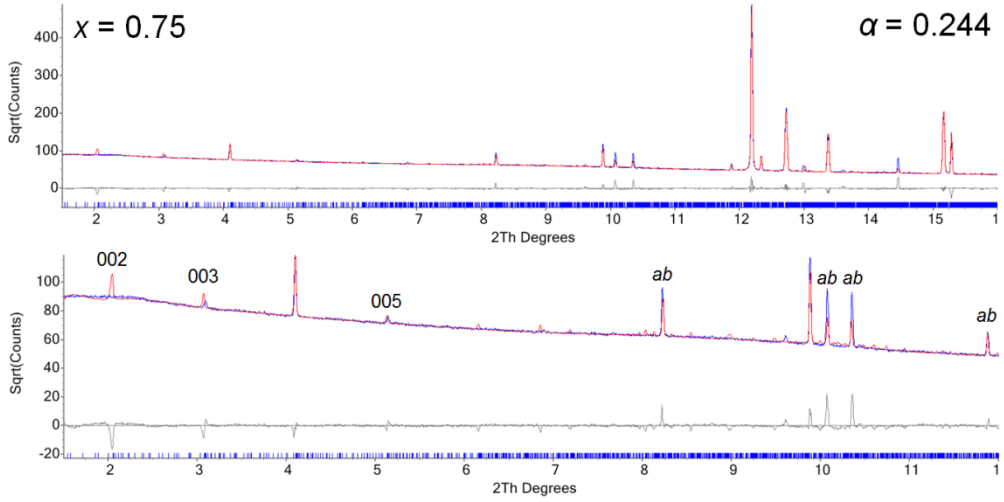

Figure 7.12. Rietveld refinement profiles of synchrotron powder diffraction data for $La_2O_2Cu_{0.5}Zn_{0.75}Se_2$ (x = 0.75) using the structural model shown in Figure 7.11. In-plane ordering peaks (shown by vertical blue lines in previous figures) are marked by ab, 00l reflections are labelled. A $\sqrt{I}$ scale is used to emphasize the weaker supercell reflections.

7.3.4 $La_2O_2Cu_{2-2x}Fe_xSe_2$ Solid Solution

Figure 7.13 shows the $La_2O_2Cu_{2-2x}Fe_xSe_2$ series fitted using the same modulation approach. There are no significant experimental supercell reflections observable until x = 0.5, where a broad peak emerges with α = 0.997 (0C-1E), shown by vertical blue lines. This peak progressively grows in intensity up to x = 1 ($La_2O_2FeSe_2$), becoming significantly sharper from x = 0.75 upwards. In x = 0.75 there are two phases; cell parameter behaviour suggests these consist of a phase similar in composition to x = 0.667, and a phase similar to x = 1 ($La_2O_2FeSe_2$). This is likely the cause of the sharpened in-plane superstructure reflections.

There is also evidence that reheating can enhance the in-plane Fe ordering, as was found in the x = 0.667 $La_2O_2Cu_{2-2x}Mn_xSe_2$ sample. Figure 7.13 shows an inset of the most intense in-plane supercell peak from PXRD data (at ~6.5 2θ in synchrotron data) for the x = 0.667 sample in the $La_2O_2Cu_{2-2x}Fe_xSe_2$ series. The blue pattern was collected after one 12 hour heat cycle, the green pattern after a further two 48 hour heat cycles. The reheats have caused the peak to become much more defined.

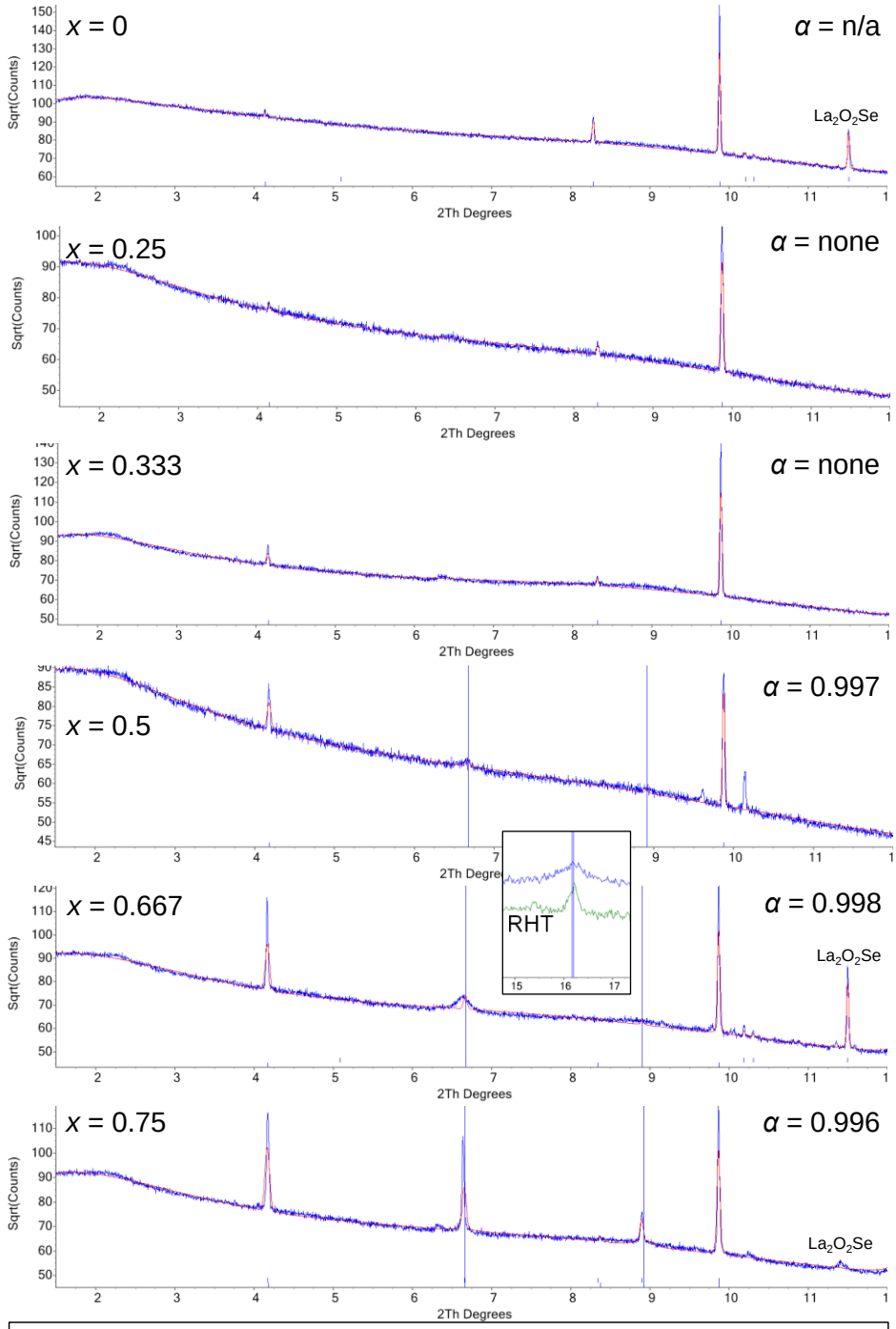

x = 1 α = 1

2D $La_2O_2FeSe_2$ has been prepared by a single crystal synthesis by others. The β structure is adopted under our synthetic conditions.

Figure 7.13. The modulation approach to fitting satellite peaks caused by in-plane transition metal ordering (blue vertical lines) across the $La_2O_2Cu_{2-2x}Fe_xSe_2$ series from 1.5 to 12 2θ. 2D $La_2O_2FeSe_2$ is reported by others.[4] A $\sqrt{I}$ scale is used to emphasize the weaker supercell reflections.

7.4 $La_2O_2Cu_{2-2x}(M_{1-y}M'_y)_xSe_2$ (*M*/*M'* = Fe/Zn, Zn/Mn, Mn/Cd) Solid Solutions

Six more series of compounds were prepared which fixed the ratio of Cu^{1+} to M^{2+}, and systematically changed the average ionic radii of the M^{2+} ion, similar in nature to the work performed in Chapter 4. They include the La containing series $La_2O_2Cu_{0.5}(Fe_{1-y}Zn_y)_{0.5}Se_2$, $La_2O_2Cu_{0.5}(Zn_{1-y}Mn_y)_{0.5}Se_2$ and $La_2O_2Cu_{0.5}(Mn_{1-y}Cd_y)_{0.5}Se_2$, which share common end-members so can be plotted continuously akin to the series plotted in Chapter 4. The same applies to the series $La_2O_2Cu_{0.667}(Fe_{1-y}Zn_y)_{0.66}Se_2$, $La_2O_2Cu_{0.66}(Zn_{1-y}Mn_y)_{0.66}Se_2$ and $La_2O_2Cu_{0.66}(Mn_{1-y}Cd_y)_{0.66}Se_2$. It is perhaps best shown how these series are related to others in this thesis by the thesis map in Figure 7.1, where they are labelled as 7d and 7e for x = 0.5 and 0.667 respectively.

Unit cell volumes, Figure 7.14, showed a smooth variation up to x = 0.2 in the $La_2O_2Cu_{0.5}(Mn_{1-y}Cd_y)_{0.5}Se_2$ and $La_2O_2Cu_{0.66}(Fe_{1-y}Zn_y)_{0.66}Se_2$ series; beyond this there is clear phase separation. At present little work has been done to fully understand these phase-separated systems, though based on cell volumes and preliminary Rietveld fits it seems they are showing a preference for forming one of the $La_2O_2Cu_{2-2x}Cd_xSe_2$-type phases reported in Chapter 5 (1Cu/1Cd, 1Cu/2Cd, etc), then a second layered phase forms from the elements still available. This seems to signify a thermodynamic stability for the $La_2O_2Cu_{2-2x}Cd_xSe_2$-type phases, and is perhaps not too surprising based on the different chemical behaviour of the $La_2O_2Cu_{2-2x}Cd_xSe_2$ solid solution (relative to analogous Fe, Zn and Mn series) which exhibit much stronger ordering along the *c* direction.

Cell parameter trends, Figure 7.15, are entirely as expected, with little change in *a* or *b* across the series. The changes in cell volume are caused entirely by changes in the *c* cell parameter, almost certainly due to the inherent rigidity of $[Ln_2O_2]^{2+}$ layers relative to $[M_xO_2]^{2-}$ layers, discussed in Chapter 4. Tabulated values for the cell volume/parameters of all samples are given in Appendix 4.

Low angle PXRD patterns fitted using the modulation approach will not be shown for the six $La_2O_2Cu_{2-2x}(M_{1-y}M_y)_xSe_2$-type series as at present they have not been considered in full detail (and also out of consideration for the reader!). However where an α value could be determined, these are given in Table 7.2. Strong in-plane ordering is observed for Zn containing compounds, which is not surprising based on the strong ordering across the $La_2O_2Cu_{2-2x}Zn_xSe_2$ series, as well as for end members.

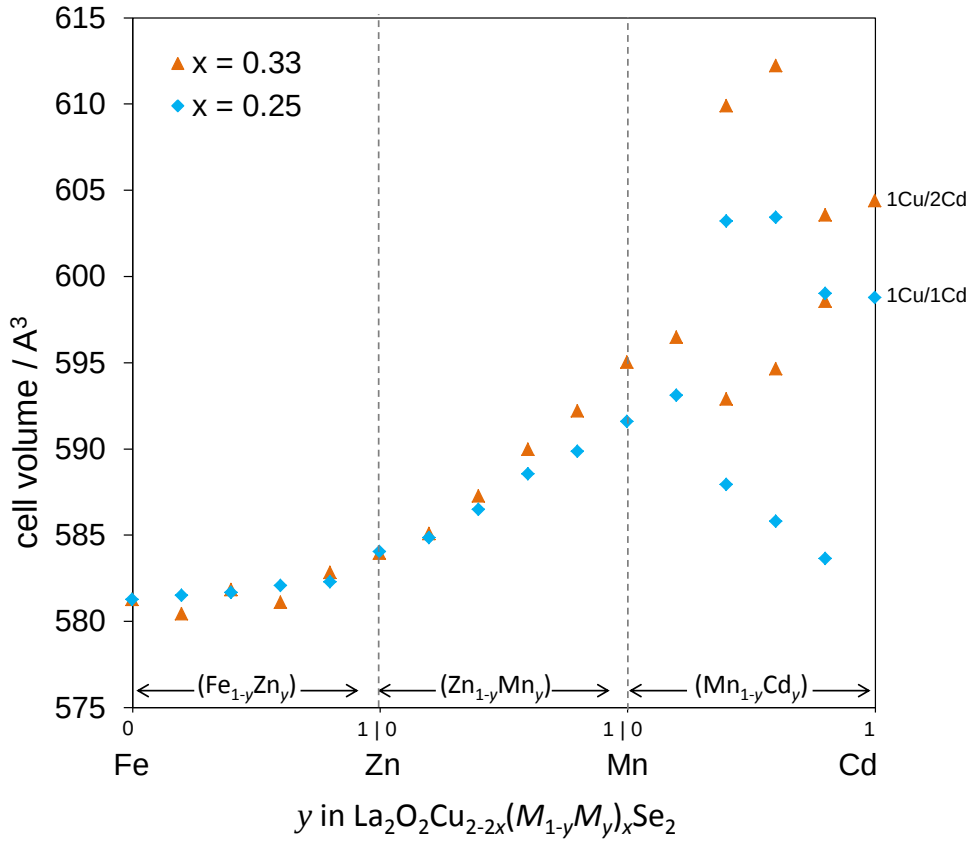

Figure 7.14. Variation in cell volume of phases formed across $La_2O_2Cu_{2-2x}(M_{1-y}M'_y)_xSe_2$ (M/M' = Fe/Zn, Zn/Mn, Mn/Cd) solid solutions. In the $La_2O_2Cu_{2-2x}(Mn_{1-y}Cd_y)_xSe_2$ series we see clear phase separation so volumes of each layered phase are reported.

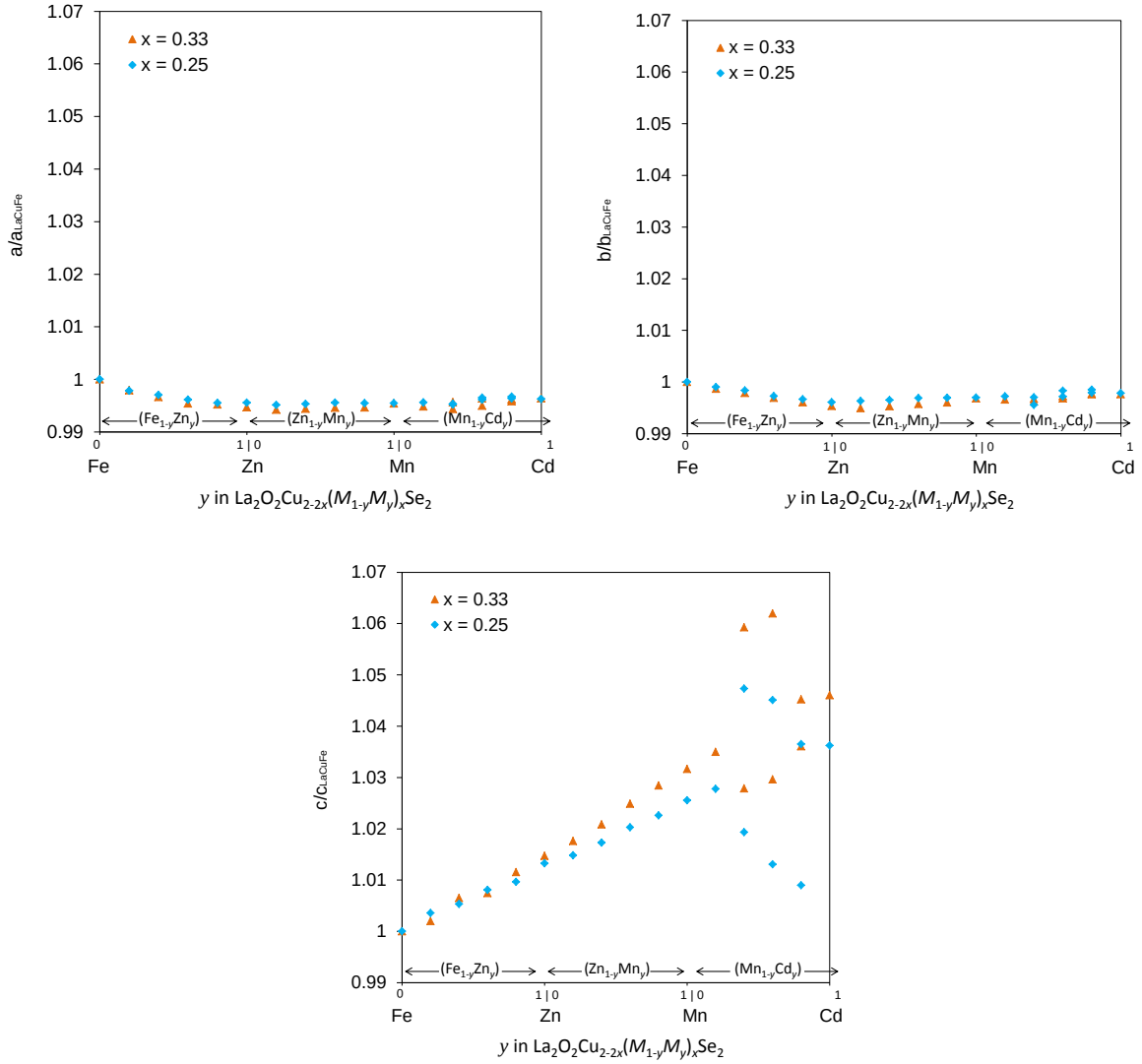

Figure 7.15. Variation in cell parameters of phases formed across $La_2O_2Cu_{2-2x}(M_{1-y}M'_y)_xSe_2$ (M/M' = Fe/Zn, Zn/Mn, Mn/Cd) solid solutions.

x = 0.5	y	*α*	*x = 0.667*	y	*α*
$La_2O_2CuFe_{0.5}Se_2$	0.0	0.997	$La_2O_2Cu_{0.667}Fe_{0.667}Se_2$	0.0	0.998
	0.2	none		0.2	none
	0.4	none		0.4	none
	0.6	none		0.6	0.239
	0.8	0.239		0.8	0.242
$La_2O_2CuZn_{0.5}Se_2$	1.0 / 0.0	0.242	$La_2O_2Cu_{0.667}Zn_{0.667}Se_2$	1.0 / 0.0	0.242
	0.2	0.235		0.2	0.238
	0.4	0.229		0.4	0.233
	0.6	0.222		0.6	0.224
	0.8	none		0.8	0.213
$La_2O_2CuMn_{0.5}Se_2$	1.0 / 0.0	none	$La_2O_2Cu_{0.667}Mn_{0.667}Se_2$	1.0 / 0.0	0.210
	0.2	none		0.2	0.180
	0.4	2 phases		0.4	2 phases
	0.6	2 phases		0.6	2 phases
	0.8	2 phases		0.8	2 phases
$La_2O_2CuCd_{0.5}Se_2$	1.0	1.000	$La_2O_2Cu_{0.667}Cd_{0.667}Se_2$	1.0	1.000

Table 7.2. Progression of α value, hence in-plane M^{2+} ordering, in $La_2O_2Cu_{2-2x}(M_{1-y}M'_y)_xSe_2$ (M/M' = Fe/Zn, Zn/Mn, Mn/Cd) solid solutions. Typical errors for α are ~0.0001, though a more realistic error is ~0.001, hence 3 decimal places are reported.

7.5 Conclusions

Samples across the $La_2O_2Cu_{2-2x}M_xSe_2$ (*M* = Fe, Zn, Mn) solid solutions were synthesised, and almost all form near single phase compounds. As they are analogous to the $La_2O_2Cu_{2-2x}Cd_xSe_2$ series, we wanted to investigate whether the layers would order along the *c*-axis in the same manner. Instead of 0C-1E ordering as in Cd^{2+} layers, we were interested in whether the structures would adopt 1C-0E, 3C-1E and 4C-1E ordering in Fe^{2+}, Zn^{2+} and Mn^{2+} layers respectively; this does not occur in all cases.

In the $La_2O_2Cu_{2-2x}Mn_xSe_2$ series, it seems a critical amount of Mn is required before in-plane ordering is established and further reheats are required to establish full in-plane order. However Cu/Mn segregated layers show little or no order along the *c*-axis. $La_2O_2Cu_{2-2x}Zn_xSe_2$ on the other hand readily orders in-plane, though ordering is surprisingly incommensurate in nature consistently forming Zn^{2+} layers with the same *α* value, which is between 3C-1E and 4C1E. It is unknown why this is the case (further heating has no experimentally observable effect). There is also some evidence of ordering along *c*, though by no means as pronounced as in the $La_2O_2Cu_{2-2x}Cd_xSe_2$ series of Chapter 5. $La_2O_2Cu_{2-2x}Fe_xSe_2$ does not establish obvious in-plane 0C-1E ordering synonymous with Fe^{2+} layers until *x* = 0.667, then it becomes clear beyond this. There is also evidence that reheats further increase in-plane ordering, as was the case with the $La_2O_2Cu_{2-2x}Mn_xSe_2$ series.

Samples across the $La_2O_2Cu_{2-2x}(M_{1-y}M'_y)_xSe_2$ (*M*/*M'* = Fe/Zn, Zn/Mn, Mn/Cd) solid solutions were also synthesised. Most form single phase compounds, though some across the $La_2O_2Cu_{2-2x}(Mn_{1-y}Cd_y)_xSe_2$ series show clear phase separation, likely driven by the stability of $La_2O_2Cu_{2-2x}Cd_xSe_2$-type compounds.

It should be stated that the compounds reported in this chapter are far from fully understood. There are certainly aspects of the in-plane ordering established in Chapter 4 present in these compounds, as well as hints of layer stacking akin to the Chapter 5 work. However there seems to be an added level of complexity in these series, and their full understanding

could likely form the basis of a PhD thesis in its own right. Consideration of ordering in the *ab* plane, stacking arrangements in the *c* direction, stacking faults, mixing of Cu/*M*, time dependence of ordering, and phase separation would all need to be considered. The implications on electronic and magnetic properties will also be fascinating.

7.6 References

(1) Peschke, S.; Nitsche, F.; Johrendt, D. *Z. Anorg. Allg. Chem.* **2015**, *641*, 529.
(2) McCabe, E. E.; Free, D. G.; Mendis, B. G.; Higgins, J. S.; Evans, J. S. O. *Chem. Mater.* **2010**, *22*, 6171.
(3) Wang, C.-H.; Ainsworth, C. M.; Gui, D.-Y.; McCabe, E. E.; Tucker, M. G.; Evans, I. R.; Evans, J. S. O. *Chem. Mater.* **2015**, *27*, 3121.
(4) Nitsche, F.; Niklaus, R.; Johrendt, D. *Z. Anorg. Allg. Chem.* **2014**, *640*, 2897.

Chapter 8: Summary

The work presented in this thesis has involved the synthesis of ~150 new phases. A careful and systematic study has led to a detailed understanding of many of their complex structures, which can now be controlled in all three dimensions. This high level of structural control will assist in the exploitation of the physical properties associated with these materials in future work, and offers the possibility of tuning in specific electronic and/or magnetic properties. The purpose of this Chapter is to briefly summarise and link Chapters 3 to 7, which will be done by discussing the whole area of the "fully explored" thesis map shown in Figure 8.1.

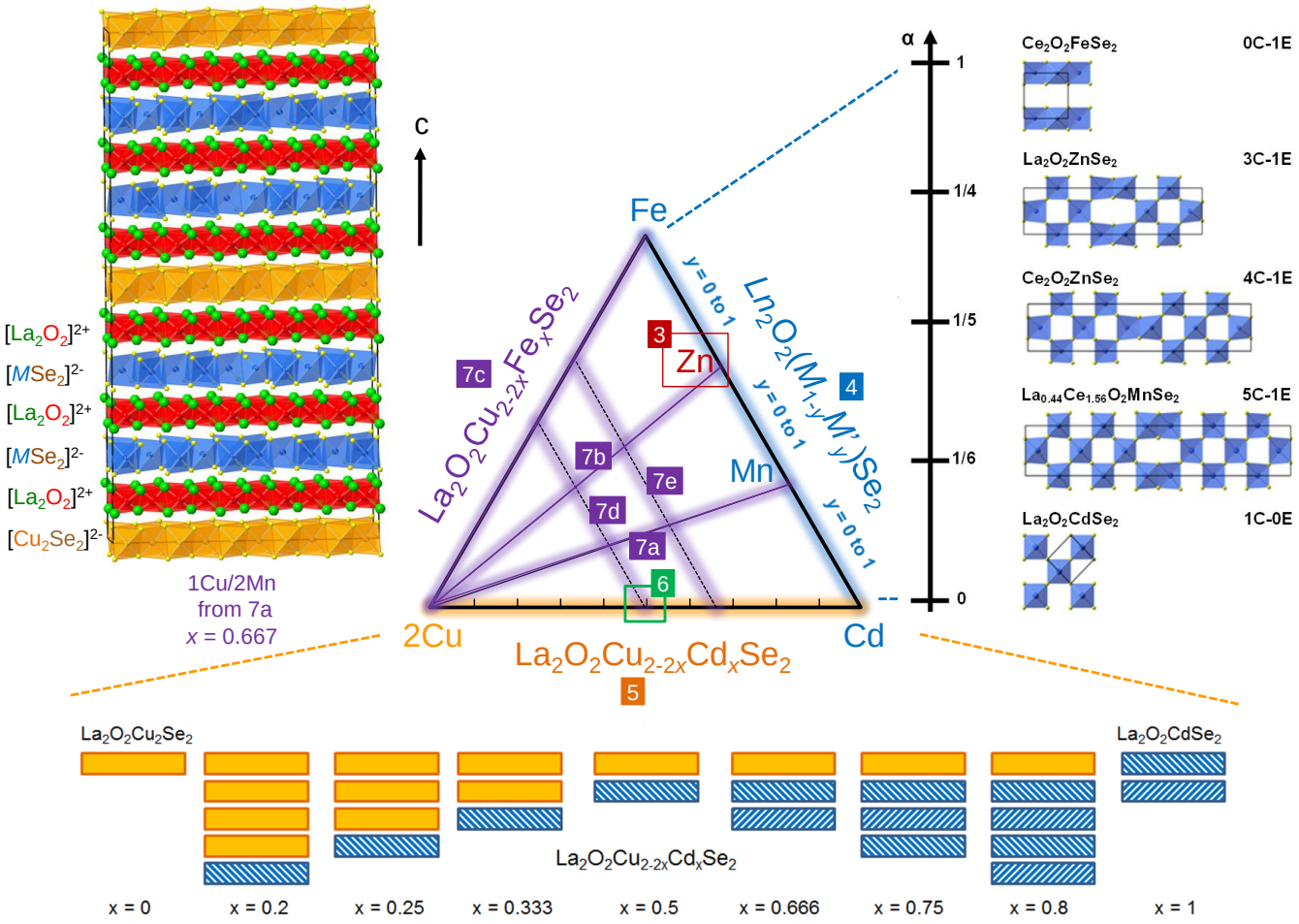

Figure 8.1. Annotated thesis map.

Chapter 3 (highlighted red on the thesis map) described the synthesis and structural characterisation of a previously unreported quaternary oxychalcogenide, $Ce_2O_2ZnSe_2$. The transition metal ordering in this material contains both corner-sharing and edge-sharing tetrahedra and is intermediate between ordering patterns observed for $Ce_2O_2FeSe_2$ (0C-1E) and $La_2O_2CdSe_2$ (1C-0E). It is similar to previously reported $La_2O_2ZnSe_2$ (3C-1E) except that $Ce_2O_2ZnSe_2$ has extended corner-shared regions (4C-1E). The structure solution of $Ce_2O_2ZnSe_2$ was crucial towards directing future work, as it hinted that the exotic transition metal ordering of $La_2O_2ZnSe_2$ (relative to the simpler pure checkerboard and pure stripe

ordering of $La_2O_2CdSe_2$ and $Ce_2O_2FeSe_2$ respectively) was not a one-off, and that there could be a series of compounds with evolving structures. It also showed that subtle changes in the synthetic conditions can be exploited to oxidise Ce^{3+} to Ce^{4+} to varying degrees. This in turn affects the size of $[Ce_2O_2]^{2+}$ layers and drives subtle changes in the transition metal ordering. It also provided the first tantalising evidence that superstructure peaks in these materials (hence the crystal structures of these materials) aren't always at commensurate positions.[1]

Chapter 4 (highlighted blue on the thesis map) was inspired by the work of Chapter 3. It aimed to investigate the degree of control possible over transition metal ordering in $Ln_2O_2MSe_2$ type oxychalcogenides. This was done by systematically tuning the properties of each layer by changing their chemistries. It transpires that transition metal ordering is determined by the relative sizes of the $[Ln_2O_2]^{2+}$ and $[MSe_2]^{2-}$ layers in the *ab* plane and can be tuned by substitution in either layer, and is determined by the relative rigidity and flexibility of $[Ln_2O_2]^{2+}$ and $[MSe_2]^{2-}$ layers respectively. We find that doping in the $[MSe_2]^{2-}$ layers leads to changes exclusively along the *c*-axis, while doping in the $[Ln_2O_2]^{2+}$ layers leads to changes in all cell parameters (roughly double within the *ab* plane relative to the *c*-axis). This is shown schematically in Figure 8.2. The two extremes of transition metal ordering contain $MSe_{4/2}$ tetrahedra that are exclusively edge-sharing (stripe-like, 0C-1E) or exclusively corner-sharing (checkerboard-like, 1C-0E), with an array of systematically evolving commensurate and incommensurate ordering patterns in between.[2] These compounds therefore form an infinitely adaptive series, where small compositional changes lead to unique structures (even if closely related to those of neighbouring compositions), and can be considered in the same light as other classic systems of this type. These include the rutile TiO_2 structure, where there is an infinitely adaptable series between compositions $TiO_{1.67}$ and TiO_2 brought about by shear planes. The resulting structures contain slabs of TiO_2 separated by regions with a portion of face-shared octahedra. Another classic example would be the $YO_{1-x}F_{1+2x}$ series, where an infinitely adaptable series exists between $YO_{0.87}F_{1.26}$ and $YO_{0.78}F_{1.44}$. This is enabled by small adjustments in the size of triangular anion nets within the structure. Traditionally systems of this sort have been described using large unit cells, but the continuous range of structures within a given system means that they are often better described using the language of incommensurate or modulated structures.[7,8,9]

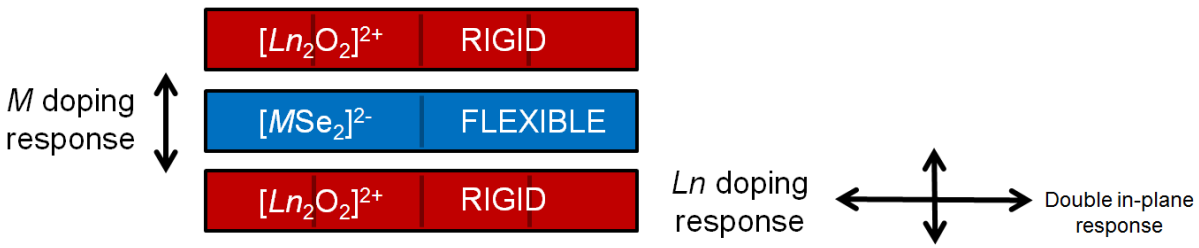

Figure 8.2. The effects on the cell parameters of M and Ln site doping, driven by the relative rigidity and flexibility of $[Ln_2O_2]^{2+}$ and $[MSe_2]^{2-}$ layers respectively. The figure represents a commensurate structure. In incommensurate structures there is a layer mismatch.

Important collaborative work which was conducted alongside the work of Chapter 4 (by Dr Chun-Hai Wang) provided a full structural solution for the incommensurate compound $Ce_2O_2MnSe_2$ using a modulation approach.[3] As this identified the important satellite reflections, Dr Wang was able to develop a Pawley-like approach to determine the

modulation vector which was applied to all the compounds of Chapter 4 (with supercell reflections in a range of 2θ positions). This approach showed conclusively that systematic changes to ordering are a direct result of tuning the layer sizes. Detailed structural information was determined for the commensurate compounds $Ce_2O_2(Fe_{3/4}Zn_{1/4})Se_2$ (3C-1E), $Ce_2O_2(Fe_{1/8}Zn_{7/8})Se_2$ (4C-1E), $Ce_2O_2(Zn_{1/6}Mn_{5/6})Se_2$ (5C-1E), $La_2O_2(Zn_{1/10}Mn_{9/10})Se_2$ (4C-1E) and $Ce_2O_2CdSe_2$ (1C-0E), confirming the model.[2]

After demonstrating a remarkable level of in-plane control, Chapter 5 (highlighted yellow on the thesis map) shows that it is also possible to control transition metal ordering along the third or stacking dimension; this is shown across the $La_2O_2Cu_{2-2x}Cd_xSe_2$ solid solution. In these compounds, Cu and Cd are formally in the +1 and +2 oxidation states respectively, and these are therefore the first M^{1+}/M^{2+} systems reported. Due to the different sizes of the two transition metals, they segregate into $[Cu_2Se_2]^{2-}$ and $[CdSe_2]^{2-}$ layers, making it possible to access each of the new structure types shown schematically at the bottom of Figure 8.1, from $x = 0$ (all Cu) to $x = 1$ (all Cd). On top of this, in order to fully understand the structure (by refining atomic coordinates) and microstructure (by analysing stacking fault probabilities) of these new materials, a new methodology was implemented for studying low and high-probability stacking faults, using a Rietveld compatible supercell approach capable of analysing systems with thousands of layers.[4]

Chapter 6 (green on the thesis map) takes a brief respite from complex structural analysis and explores the effects of Sr doping on the physical properties of $La_2O_2CuCd_{0.5}Se$ from Chapter 5 ($x = 0.5$, 1Cu/1Cd). Sr can be successfully doped onto the La site of $(La_{2-Z}Sr_Z)O_2CuCd_{0.5}Se_2$ and cell volume/parameter plots show that the doping limit is ~15%. Undoped $La_2O_2CuCd_{0.5}Se_2$ shows insulating behaviour, while all samples between 2.5% – 20% doping show semiconducting behaviour, with doping giving a resistivity decrease from 1.5×10^{4} Ω cm to ~6×10^{-1} Ω cm at 300 K such that samples approach the metallic regime. DFT calculations of undoped $La_2O_2CuCd_{0.5}Se_2$ show that the valence band maximum consists of Cu 3d and Se 4p states. Therefore charge compensation for Sr doping is likely achieved by the introduction of electronic holes into these states, hence electronic conduction is confined to the $[Cu_2Se_2]^{2-}$ layers.[5] Aside from this and speaking more generally about layered structures of this type, perhaps the soft nature of the bonding in transition metal selenide layers may also lead to desirable thermoelectric properties.

The work described in Chapter 7 (highlighted purple on the thesis map) is a first attempt to move beyond the edges of the pseudo phase diagram of the thesis map and to explore the purple areas where the type, charges and overall quantities of transition metals are simultaneously varied. Initially, $La_2O_2Cu_{2-2x}Fe_xSe_2$, $La_2O_2Cu_{2-2x}Zn_xSe_2$ and $La_2O_2Cu_{2-x}Mn_xSe_2$ are investigated, labelled as lines 7a, 7b and 7c respectively on the thesis map. These are formally equivalent to the work of Chapter 5 with Cu and Cd. It also investigates the effect of systematically varying the +2 transition metal size in the solid solutions $La_2O_2Cu(M_{0.5-y}M'_y)Se_2$ and $La_2O_2Cu_{0.667}(M_{0.667-y}M'_y)Se_2$ (*M*/*M'* = Fe/Zn, Zn/Mn & Mn/Cd), labelled as lines 7d and 7e. This is an extension of the type of study in Chapter 4 but for systems that could segregate to form either 1Cu:1*M* or 2Cu:1*M* layers. The most definitive conclusions are for $La_2O_2Cu_{2-2x}M_xSe_2$ materials. In the $La_2O_2Cu_{2-2x}Mn_xSe_2$ series, it seems a critical amount of Mn is required before in-plane Mn ordering is established and further reheats are required to establish full in-plane order. The structure to the left of Figure 8.1 is our best model for $La_2O_2Cu_{0.667}Mn_{0.667}Se_2$ (1Cu/1Mn) after two 12 hour heating cycles,

though stacking faults are almost certainly present. $La_2O_2Cu_{2-2x}Zn_xSe_2$ on the other hand readily orders in-plane, though ordering is surprisingly incommensurate in nature consistently forming Zn^{2+} layers with the same α = ~0.24 value; it is unknown why this is the case. $La_2O_2Cu_{2-2x}Fe_xSe_2$ does not establish obvious in-plane 0C-1E expected for pure Fe^{2+} layers until x = 0.667, and it becomes clear thereafter.

It should be stated that the compounds reported in Chapter 7 are far from fully understood. There are certainly aspects of the in-plane ordering work established in Chapter 4 present in these compounds, as well as strong indications of metals segregating into separate layers as found in the work of Chapter 5. However there seems to be an added level of complexity in these series, including examples with mixing of Cu^{1+} and M^{2+} ions within layers, time dependence to ordering and phase separation.

Perhaps one unified way of considering all compounds presented in the thesis that contain two or more transition metals (whether M^{2+}/M'^{2+} or M^{1+}/M^{2+}) is by the extent of two different phenomena: the level of TM segregation into separate layers and the degree of stacking faults of any segregated layers, Figure 8.3. In the $Ln_2O_2(M_{1-y}M'_y)Se_2$ solid solutions of Chapter 4 (where both TM's are in the +2 oxidation state), there seems to be complete mixing of TM's such that layer stacking faults aren't relevant. We also see no evidence for *pb* type faulting in any materials which might occur if metals segregated. In the $La_2O_2Cu_{2-2x}Cd_xSe_2$ solid solution of Chapter 5, it seems there is no mixing of the Cu^{1+} and Cd^{2+} and very low levels of this type of stacking faults in the majority of phases. In particular, $La_2O_2CuCd_{0.5}Se_2$ (1Cu/1Cd) seems fully ordered. The compounds of Chapter 7 (mainly compounds from 7a, 7b and 7c of the thesis map, as 7d and 7e have had less consideration) show more variation, with evidence of TM mixing and stacking faults across all solid solutions in varying levels depending on the TM identity, specific composition and synthetic conditions.

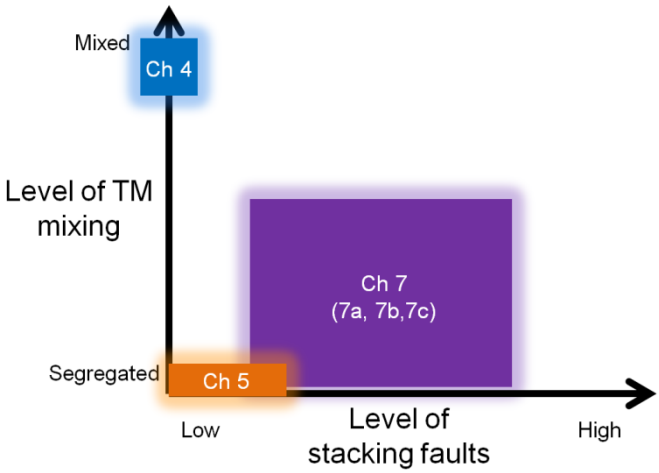

Figure 8.3. Schematic diagram broadly showing the range of TM mixing and stacking faults across the compounds presented in Chapters 4, 5 and 7.

Overall, the explorative study of $Ln_2O_2MSe_2$-type and closely related materials has proven extremely fruitful, allowed in part by the staggering and beautiful structural flexibility inherent with these systems. As a result, the work has been published in the articles (or soon to be submitted articles), listed below:

1. Ainsworth, C. M.; Wang, C.-H.; Tucker, M. G.; Evans, J. S. O., Synthesis, Structural Characterization, and Physical Properties of the New Transition Metal Oxyselenide $Ce_2O_2ZnSe_2$. *Inorg. Chem.* **2015,** 54, (4), 1563-71.

2. Ainsworth, C. M.; Wang, C.-H.; Johnston, H. E.; McCabe, E. E.; Tucker, M. G.; Brand, H. E. A.; Evans, J. S. O., Infinitely Adaptive Transition-Metal Ordering in $Ln_2O_2MSe_2$-Type Oxychalcogenides. *Inorg. Chem.* **2015,** 54, (15), 7230-7238.

3. Wang, C.-H.; Ainsworth, C. M.; Gui, D.-Y.; McCabe, E. E.; Tucker, M. G.; Evans, I. R.; Evans, J. S. O., Infinitely Adaptive Transition Metal Oxychalcogenides: The Modulated Structures of $Ce_2O_2MnSe_2$ and $(Ce_{0.78}La_{0.22})_2O_2MnSe_2$. *Chem. Mater.* **2015**, 27, (8), 3121-3134.

4. Ainsworth, C. M.; Lewis, J. W.; Wang, C.-H.; Coelho, A. A.; Johnston, H. E.; Brand, H. E. A.; Evans, J. S. O., 3D Transition Metal Ordering and Rietveld Stacking Fault Quantification in the New Oxychalcogenides $La_2O_2Cu_{2-4x}Cd_{2x}Se_2$. *Chem. Mater.* **2016,** 28, (9), 3184-3195.

5. Ainsworth, C. M.; Lazarus, V.; Evans, J. S. O., Electronic Properties of Sr Doped $(La_{2-z}Sr_z)O_2CuCd_{0.5}Se_2$, close to submission.

6. Wang, C.-H.; Ainsworth, C. M.; Stewart, G.; Brand, H. E. A.; Evans, J. S. O., Crystal Structure and Magnetic Modulation in β-$Ce_2O_2FeSe_2$, close to submission.

Reference 2 was invited to be the cover article for the August 3rd 2015 issue of *Inorg. Chem.*. A “Minecraft” theme seemed fitting as it was felt that a (rather loose) comparison could be drawn between the Minecraft world and the layered oxychalcogenide world. This is shown overleaf, followed by an alternative “Tetris” based cover which was not eventually used. Who said chemistry couldn’t be fun!

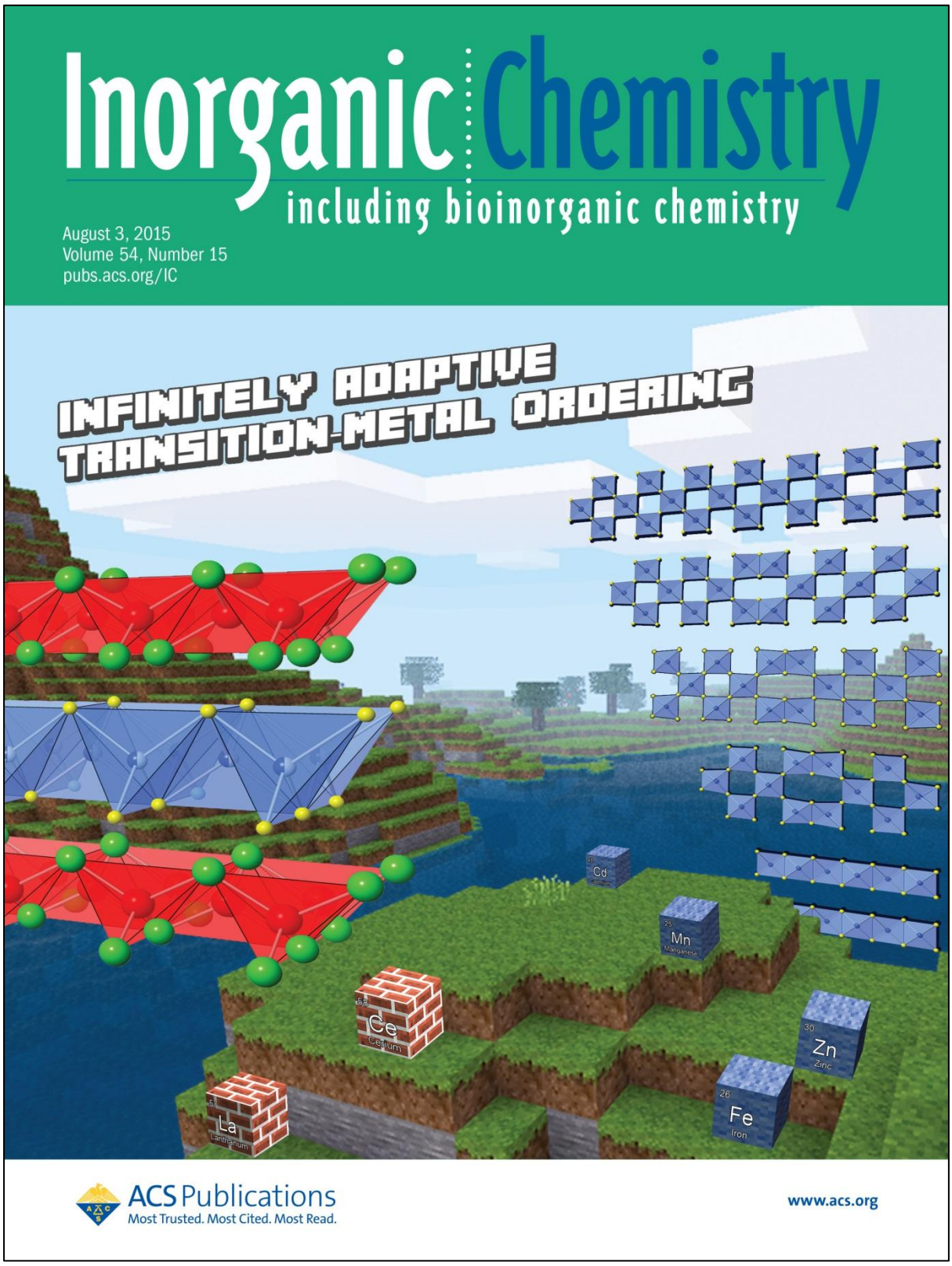
Inorganic Chemistry
including bioinorganic chemistry
August 3, 2015
Volume 54, Number 15
pubs.acs.org/IC
INFINITELY ADAPTIVE TRANSITION-METAL ORDERING
Cd
Mn
Manganese
Ce
Cerium
Zn
Zinc
Fe
Iron
La
Lanthanum
ACS Publications
Most Trusted. Most Cited. Most Read.
www.acs.org

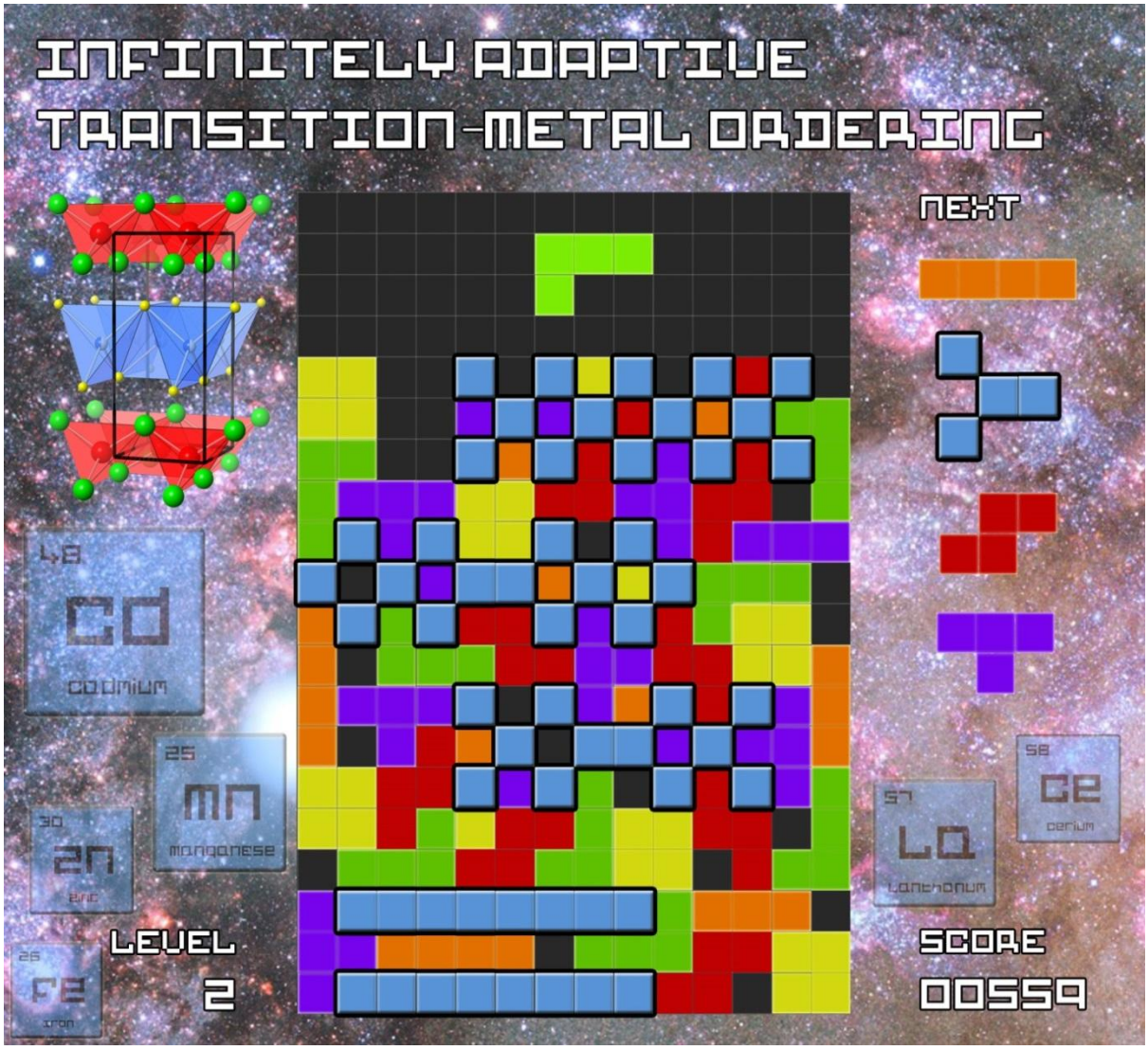
INFINITELY ADAPTIVE
TRANSITION-METAL ORDERING
NEXT
48
Cd
CADMIUM
25
Mn
MANGANESE
30
Zn
ZINC
26
Fe
IRON
58
Ce
CERIUM
57
La
LANTHANUM
LEVEL
2
SCORE
00559

Other references cited:

7. Wadsley, A. D. *Nonstoichiometric Compounds*; American Chemical Society, 1963.

8. Anderson, S. J. *J. Chem. Soc., Dalton Trans.*, **1973**, 1107-1115.

9. Smaalen, S. V. *Incommensurate Crystallography*; Oxford University Press, 2007.

Appendix 1

Mode number	Atom type	Mode label	*k* point	Order parameter direction
a1	Ce	GM1+	[0,0,0]	(a)
a2	Ce	SM1	[2/5,2/5,0]	(a,-3.078a,0,0)
a3	Ce	SM1	[2/5,2/5,0]	(a,-3.078a,0,0)
a4	Ce	SM1	[1/5,1/5,0]	(a,-0.727a,0,0)
a5	Ce	SM1	[1/5,1/5,0]	(a,-0.727a,0,0)
a6	Ce	A2	[1/2,1/2,1/2]	(a,0)
a7	Ce	S4	[1/10,1/10,1/2]	(a,-3.078a,0,0)
a8	Ce	S4	[3/10,3/10,1/2]	(a,-0.727a,0,0)
a9	Zn	SM1	[2/5,2/5,0]	(a,-3.078a,0,0)
a10	Zn	SM1	[1/5,1/5,0]	(a,-0.727a,0,0)
a11	Zn	S4	[1/10,1/10,1/2]	(a,-3.078a,0,0)
a12	Zn	S4	[3/10,3/10,1/2]	(a,-0.727a,0,0)
a13	O	SM1	[2/5,2/5,0]	(a,-3.078a,0,0)
a14	O	SM1	[1/5,1/5,0]	(a,-0.727a,0,0)
a15	O	A2	[1/2,1/2,1/2]	(a,0)
a16	O	S4	[1/10,1/10,1/2]	(a,-3.078a,0,0)
a17	O	S4	[1/10,1/10,1/2]	(a,-3.078a,0,0)
a18	O	S4	[3/10,3/10,1/2]	(a,-0.727a,0,0)
a19	O	S4	[3/10,3/10,1/2]	(a,-0.727a,0,0)
a20	Se	GM1+	[0,0,0]	(a)
a21	Se	SM1	[2/5,2/5,0]	(a,-3.078a,0,0)
a22	Se	SM1	[2/5,2/5,0]	(a,-3.078a,0,0)
a23	Se	SM1	[1/5,1/5,0]	(a,-0.727a,0,0)
a24	Se	SM1	[1/5,1/5,0]	(a,-0.727a,0,0)
a25	Se	A2	[1/2,1/2,1/2]	(a,0)
a26	Se	S4	[1/10,1/10,1/2]	(a,-3.078a,0,0)
a27	Se	S4	[3/10,3/10,1/2]	(a,-0.727a,0,0)
b1	Zn	GM1+	[0,0,0]	(a)
b2	Zn	SM1	[2/5,2/5,0]	(a,-3.078a,0,0)
b3	Zn	SM1	[1/5,1/5,0]	(a,-0.727a,0,0)
b4	Zn	A2	[1/2,1/2,1/2]	(a,0)
b5	Zn	S4	[1/10,1/10,1/2]	(a,-3.078a,0,0)
b6	Zn	S4	[3/10,3/10,1/2]	(a,-0.727a,0,0)

Occupancy mode number (a – displacive, b – ordering), atom type, mode label, k-point and order parameter direction for the Ibam (S4) distorted model of $Ce_2O_2ZnSe_2$ described in Chapter 3.

Mode number	Atom type	Mode label	*k* point	Order parameter direction
a1	Ce	GM1+	[0,0,0]	(a)
a2	Ce	SM1	[1/5,1/5,0]	(a,-0.727a,0,0)
a3	Ce	SM1	[1/5,1/5,0]	(a,-0.727a,0,0)
a4	Ce	SM1	[2/5,2/5,0]	(a,-3.078a,0,0)
a5	Ce	SM1	[2/5,2/5,0]	(a,-3.078a,0,0)
a6	Ce	S4	[1/10,1/10,1/2]	(a,-0.325a,0,0)
a7	Ce	S4	[3/10,3/10,1/2]	(a,-1.376a,0,0)
a8	Zn	SM1	[1/5,1/5,0]	(a,-0.727a,0,0)
a9	Zn	SM1	[2/5,2/5,0]	(a,-3.078a,0,0)
a10	Zn	A4	[1/2,1/2,1/2]	(0,a)
a11	Zn	S4	[1/10,1/10,1/2]	(a,-0.325a,0,0)
a12	Zn	S4	[3/10,3/10,1/2]	(a,-1.376a,0,0)
a13	O	SM1	[1/5,1/5,0]	(a,-0.727a,0,0)
a14	O	SM1	[2/5,2/5,0]	(a,-3.078a,0,0)
a15	O	A4	[1/2,1/2,1/2]	(0,a)
a16	O	S4	[1/10,1/10,1/2]	(a,-0.325a,0,0)
a17	O	S4	[1/10,1/10,1/2]	(a,-0.325a,0,0)
a18	O	S4	[3/10,3/10,1/2]	(a,-1.376a,0,0)
a19	O	S4	[3/10,3/10,1/2]	(a,-1.376a,0,0)
a20	Se	GM1+	[0,0,0]	(a)
a21	Se	SM1	[1/5,1/5,0]	(a,-0.727a,0,0)
a22	Se	SM1	[1/5,1/5,0]	(a,-0.727a,0,0)
a23	Se	SM1	[2/5,2/5,0]	(a,-3.078a,0,0)
a24	Se	SM1	[2/5,2/5,0]	(a,-3.078a,0,0)
a25	Se	S4	[1/10,1/10,1/2]	(a,-0.325a,0,0)
a26	Se	S4	[3/10,3/10,1/2]	(a,-1.376a,0,0)
b1	Zn	GM1+	[0,0,0]	(a)
b2	Zn	SM1	[1/5,1/5,0]	(a,-0.727a,0,0)
b3	Zn	SM1	[2/5,2/5,0]	(a,-3.078a,0,0)
b4	Zn	S4	[1/10,1/10,1/2]	(a,-0.325a,0,0)
b5	Zn	S4	[3/10,3/10,1/2]	(a,-1.376a,0,0)

Occupancy mode number (a – displacive, b – ordering), atom type, mode label, k-point and order parameter direction for the Ibca (S4) distorted model of $Ce_2O_2ZnSe_2$ described in Chapter 3.

Appendix 2

$La_2O_2(Fe_{1-y}Zn_y)Se_2$					$La_2O_2(Zn_{1-y}Mn_y)Se_2$					$La_2O_2(Mn_{1-y}Cd_y)Se_2$				
x	V/Å^3	a/Å	b/Å	c/Å	x	V/Å^3	a/Å	b/Å	c/Å	x	V/Å^3	a/Å	b/Å	c/Å
0	β only	β only	β only	β only	0	584.9(2)	5.732(2)	5.7330(8)	17.799(1)	0	β only	β only	β only	β only
0.125	β only	β only	β only	β only	0.1	586.58(3)	5.7332(3)	5.7332(3)	17.8502(3)	0.025	603.0(3)	5.739(3)	5.736(1)	18.3171(3)
0.25	β only	β only	β only	β only	0.2	588.55(2)	5.7328(2)	5.7349(1)	17.9015(2)	0.05	603.23(3)	5.7363(2)	5.7387(1)	18.3245(3)
0.275	β only	β only	β only	β only	0.3	590.41(3)	5.7333(2)	5.7368(2)	17.9507(3)	0.1	604.10(4)	5.7367(2)	5.7392(1)	18.3481(9)
0.325	β only	β only	β only	β only	0.4	592.6(2)	5.7348(8)	5.739(1)	18.007(2)	0.15	604.9(1)	5.738(1)	5.7400(4)	18.365(2)
0.35	584.19(1)	5.7395(1)	5.7446(1)	17.7181(1)	0.5	594.18(4)	5.7354(2)	5.7390(2)	18.0518(6)	0.2	605.85(2)	5.7402(1)	5.7397(1)	18.3886(2)
0.375	584.23(1)	5.7393(1)	5.7438(1)	17.7226(2)	0.6	595.57(4)	5.7342(3)	5.7366(2)	18.1051(2)	0.25	606.98(2)	5.7420(1)	5.7401(1)	18.4157(3)
0.5	584.54(2)	5.7398(1)	5.7413(2)	17.7380(5)	0.7	597.84(2)	5.7362(1)	5.7391(2)	18.1602(2)	0.3	607.30(1)	5.7422(1)	5.7403(1)	18.4240(3)
0.625	584.66(3)	5.7370(2)	5.7377(2)	17.7615(3)	0.8	598.44(2)	5.7330(2)	5.7364(1)	18.1971(3)	0.35	607.75(1)	5.7404(1)	5.7420(1)	18.4379(2)
0.75	584.92(3)	5.7352(1)	5.7359(2)	17.7806(3)	0.9	601.26(3)	5.7349(2)	5.7371(2)	18.2744(1)	0.4	608.28(2)	5.7399(1)	5.7414(1)	18.4580(2)
0.875	585.00(4)	5.7332(2)	5.7340(2)	17.7950(3)	0.95	601.38(2)	5.7351(1)	5.7372(1)	18.2769(2)	0.45	608.19(1)	5.7390(1)	5.7370(1)	18.4721(3)
1	584.9(2)	5.732(2)	5.7330(8)	17.799(1)	0.975	601.63(5)	5.7350(3)	5.7366(3)	18.2869(8)	0.5	608.63(3)	5.7364(2)	5.7375(2)	18.4924(1)
					0.9875	602.1(1)	5.7362(4)	5.7373(9)	18.295(2)	0.6	610.06(3)	5.7391(3)	5.7396(2)	18.5205(1)
					1	β only	β only	β only	β only	0.7	611.61(2)	5.7420(1)	5.7429(1)	18.5474(1)
										0.8	613.2(2)	5.746(2)	5.745(1)	18.576(2)
										0.9	614.91(2)	5.7482(1)	5.7496(1)	18.6055(4)
										1	616.32(2)	5.7520(2)	5.7510(2)	18.6314(1)

Cell volume/parameters across the $La_2O_2(M_{1-y}M'_y)Se_2$ solid solutions of Chapter 4.

$Ce_2O_2(Fe_{1-y}Zn_y)Se_2$					$Ce_2O_2(Zn_{1-y}Mn_y)Se_2$					$Ce_2O_2(Mn_{1-y}Cd_y)Se_2$				
x	V/Å^3	a/Å	b/Å	c/Å	x	V/Å^3	a/Å	b/Å	c/Å	x	V/Å^3	a/Å	b/Å	c/Å
0	565.53(1)	5.7038(1)	5.7230(1)	17.3245(2)	0	572.0(1)	5.6785(10)	5.6816(7)	17.729(1)	0	588.37(3)	5.6832(2)	5.6838(1)	18.2147(5)
0.03	566.00(2)	5.7031(1)	5.7183(1)	17.3554(3)	0.2	575.64(5)	5.6799(3)	5.6829(3)	17.8337(7)	0.05	589.4(2)	5.684(1)	5.6865(2)	18.2347(2)
0.0625	570.36(4)	5.6918(2)	5.6983(2)	17.5855(8)	0.4	578.78(6)	5.6817(6)	5.6827(3)	17.9259(2)	0.1	588.96(3)	5.6836(2)	5.6854(2)	18.2266(4)
0.125	570.36(3)	5.6896(2)	5.6949(2)	17.6026(7)	0.6	581.58(1)	5.6809(1)	5.6819(1)	18.0177(2)	0.125	589.48(4)	5.6853(4)	5.6855(1)	18.2367(3)
0.25	570.80(1)	5.6880(1)	5.6927(1)	17.6281(2)	0.8	585.42(2)	5.6824(1)	5.6841(2)	18.1247(3)	0.15	590.69(7)	5.6855(5)	5.6871(4)	18.268(1)
0.375	571.34(3)	5.6880(1)	5.6911(2)	17.6495(4)	0.833	586.88(7)	5.6823(7)	5.6848(1)	18.1682(8)	0.2	591.21(4)	5.6849(3)	5.6868(2)	18.2872(4)
0.5	571.63(5)	5.6856(4)	5.6862(4)	17.6813(3)	0.9	587.78(2)	5.6827(1)	5.6849(1)	18.1943(2)	0.25	591.31(3)	5.6864(3)	5.6882(1)	18.2812(3)
0.625	571.76(3)	5.6844(2)	5.6858(2)	17.6905(3)	1	588.37(3)	5.6832(2)	5.6838(1)	18.2147(5)	0.3	592.09(3)	5.6824(3)	5.6826(1)	18.3363(3)
0.75	571.91(4)	5.6817(3)	5.6827(2)	17.7131(4)						0.4	592.42(2)	5.6828(1)	5.6838(2)	18.3412(4)
0.8125	571.34(2)	5.6798(1)	5.6814(1)	17.7055(4)						0.5	594.88(2)	5.6867(1)	5.6879(1)	18.3917(3)
0.875	570.96(9)	5.6791(5)	5.6796(7)	17.7013(5)						0.6	596.54(5)	5.6897(2)	5.6915(3)	18.4213(8)
0.9375	570.31(3)	5.6757(2)	5.6764(2)	17.7020(2)						0.7	597.97(7)	5.6929(4)	5.6937(5)	18.4479(4)
0.97	569.88(2)	5.6727(2)	5.6736(2)	17.7064(2)						0.8	599.33(10)	5.6958(5)	5.6967(7)	18.4711(4)
1	572.0(1)	5.6785(10)	5.6816(7)	17.729(1)						0.9	600.49(5)	5.6984(3)	5.6996(3)	18.4890(4)
										1	602.80(4)	5.7022(3)	5.7030(3)	18.5364(3)

Cell volume/parameters across the $Ce_2O_2(M_{1-y}M'_y)Se_2$ solid solutions of Chapter 4.

$La_{2-z}Ce_zO_2FeSe_2$					$La_{2-z}Ce_zO_2ZnSe_2$				
x	V/Å^3	a/Å	b/Å	c/Å	x	V/Å^3	a/Å	b/Å	c/Å
0	β only	β only	β only	β only	0	584.90(5)	5.7328(4)	5.7324(3)	17.7983(3)
0.5	576.18(6)	5.7680(2)	5.7490(5)	17.3756(8)	0.2	583.73(3)	5.7299(2)	5.7259(2)	17.7916(3)
1	572.67(2)	5.7530(1)	5.7339(1)	17.3604(3)	0.6	581.09(3)	5.7194(2)	5.7156(2)	17.7758(5)
1.5	569.23(2)	5.7369(1)	5.7199(1)	17.3472(4)	1	578.80(4)	5.7102(3)	5.7067(2)	17.7619(4)
2	565.53(1)	5.7230(1)	5.7038(1)	17.3245(2)	1.4	576.29(8)	5.7002(4)	5.6970(7)	17.7464(5)
					1.8	573.02(3)	5.6863(2)	5.6826(2)	17.7336(3)
					2	572.0(1)	5.6816(10)	5.6785(7)	17.729(1)

$La_{2-z}Ce_zO_2MnSe_2$					$La_{2-z}Ce_zO_2CdSe_2$				
x	V/Å^3	a/Å	b/Å	c/Å	x	V/Å^3	a/Å	b/Å	c/Å
0	β only	β only	β only	β only	0	616.32(2)	5.7520(2)	5.7510(2)	18.6314(1)
0.1	β only	β only	β only	β only	0.5	613.65(2)	5.7437(1)	5.7391(1)	18.6157(4)
0.2	β only	β only	β only	β only	1	610.05(3)	5.7309(2)	5.7249(2)	18.5941(1)
0.4	β only	β only	β only	β only	1.5	606.57(2)	5.7157(1)	5.7151(1)	18.5691(2)
0.6	597.09(2)	5.7174(1)	5.7165(1)	18.2687(4)	2	602.80(4)	5.7030(3)	5.7022(3)	18.5364(3)
0.8	595.96(1)	5.7137(1)	5.7113(1)	18.2628(2)					
1	594.39(2)	5.7077(1)	5.7049(2)	18.2539(2)					
1.2	592.84(2)	5.7019(1)	5.6992(1)	18.2435(2)					
1.4	591.34(2)	5.6961(1)	5.6935(1)	18.2340(3)					
1.6	589.83(1)	5.6899(1)	5.6879(1)	18.2250(2)					
1.8	588.45(2)	5.6851(1)	5.6821(2)	18.2163(2)					
2	587.79(4)	5.6817(3)	5.6804(2)	18.2125(4)					

Cell volume/parameters across the $La_{2-z}Ce_zO_2MSe_2$ solid solutions of Chapter 4.

Appendix 3

Min of rwp	*pa*								
pb	0	0.001	0.005	0.015	0.02	0.03	0.05	0.1	Minimum
0.000	4.56077	3.87566	3.17356	2.8925	2.92745	2.95107	3.36628	4.78753	2.8925
0.001	4.24255	3.59179	3.03484	2.801	2.90356	2.99018	3.28886	5.38015	2.801
0.005	4.15886	3.59346	2.97501	2.85413	2.84286	2.96893	3.33454	4.94368	2.84286
0.015	4.15092	3.56566	3.02357	2.86411	2.78379	2.92087	3.67791	5.12557	2.78379
0.02	4.15275	3.53323	3.19296	2.82451	2.84935	3.1538	3.8391	5.3454	2.82451
0.03	4.15474	3.60489	3.24269	3.03392	3.26709	3.2552	3.97415	5.2593	3.03392
0.05	4.19513	3.88461	3.19968	3.50171	3.84177	3.90579	4.64926	6.38269	3.19968
0.1	5.10228	5.61372	5.02817	4.4694	4.92226	4.70741	5.08609	7.01791	4.4694
(blank)									
Minimum	**4.15092**	**3.53323**	**2.97501**	**2.801**	**2.78379**	**2.92087**	**3.28886**	**4.78753**	**2.78379**

Dependence of R_{wp} on *pa* and *pb* for $La_2O_2Cu_{0.667}Cd_{0.667}Se_2$ of Chapter 5.

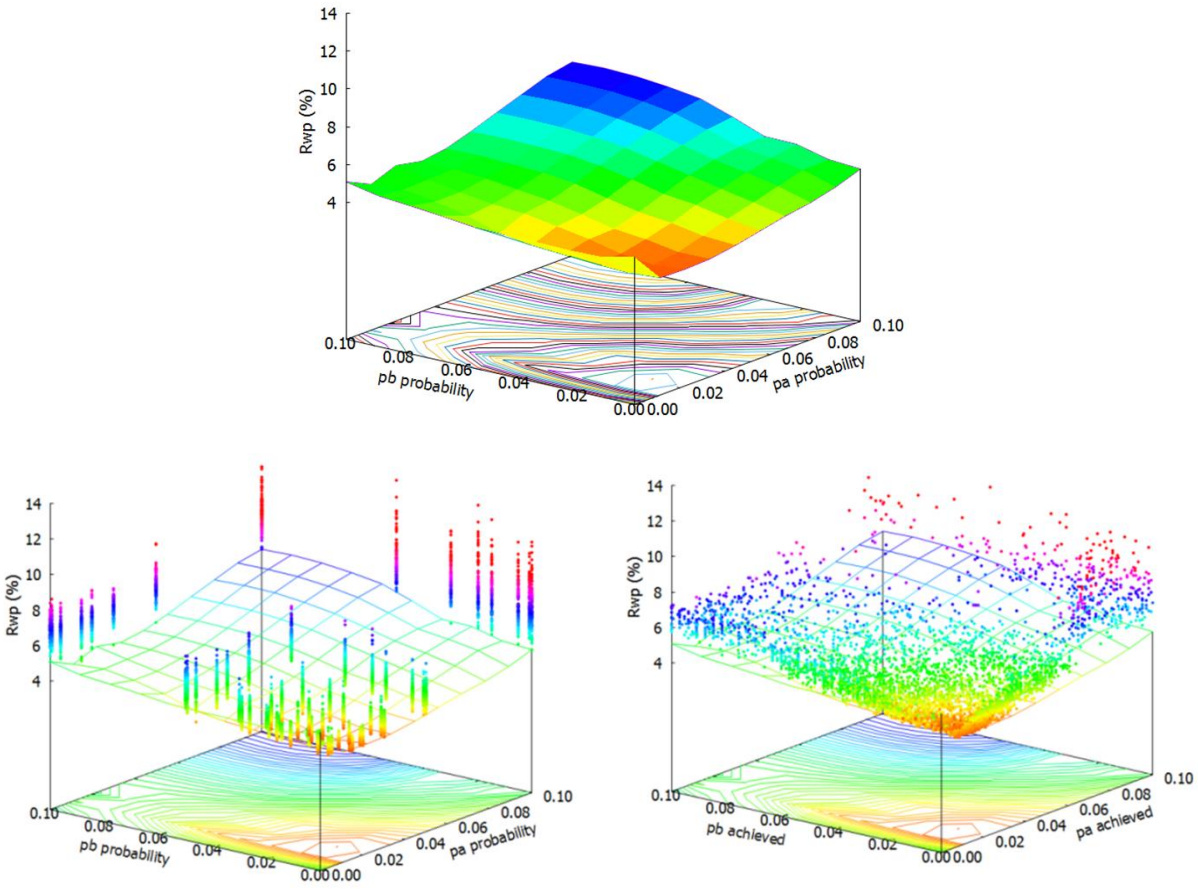

Top, minimum R_{wp} surface found from 100 stacks generated for each *pa/pb* combination for $La_2O_2Cu_{0.667}Cd_{0.667}Se_2$ of Chapter 5. Bottom left, actual R_{wp} found for each stack at each *pa/pb* combination, plotted on the minimum surface of the left hand plot. The vertical columns are 100 different R_{wp} values at each *pa/pb* combination. Bottom right, R_{wp} values plotted as a function of actual *pa/pb* value that was created in each stack. Note that points lie close to the minimum R_{wp} surface.

Min of rwp	*pa*									
pb	0	0.001	0.005	0.01	0.02	0.04	0.06	0.08	0.1	Minimum
0	7.84338	7.03098	6.52233	6.25681	6.10946	6.0658	6.21474	7.01132	7.70787	6.0658
0.001	7.28945	6.96143	6.50879	6.23288	5.98347	5.92232	6.41892	7.02065	7.24994	5.92232
0.005	7.05274	6.86754	6.38252	6.11791	5.93108	6.05867	6.45219	6.83842	7.18646	5.93108
0.1	5.97228	5.72265	5.40458	5.36698	5.33224	5.48847	6.09017	6.56915	6.89253	5.33224
0.2	5.89292	5.45246	5.27885	5.23121	5.24434	5.45838	5.98024	6.69211	6.80914	5.23121
0.3	5.87588	5.4562	5.27429	5.20814	5.2488	5.35201	5.9296	6.42553	7.33913	5.20814
0.4	5.90301	5.5807	5.28419	5.23463	5.25682	5.45186	5.9131	6.54704	7.01588	5.23463
0.5	5.96901	5.67742	5.38023	5.35175	5.37042	5.48953	5.97962	6.7136	7.40721	5.35175
0.6	6.02538	5.68381	5.53021	5.42719	5.49674	5.73168	6.14403	6.62044	6.87932	5.42719
0.7	6.20665	5.97233	5.67704	5.63658	5.6252	5.86661	6.37127	6.9838	7.28562	5.6252
0.8	6.47639	6.12997	5.87349	5.83386	5.88731	6.16777	6.48526	6.97752	7.71373	5.83386
0.9	6.85697	6.60832	6.53938	6.3951	6.3078	6.81957	7.31222	7.81646	8.72012	6.3078
0.999	9.09045	9.0644	8.71835	8.47888	8.23406	8.11066	8.15884	8.24909	8.34906	8.11066
(blank)										
Minimum	**5.87588**	**5.45246**	**5.27429**	**5.20814**	**5.24434**	**5.35201**	**5.9131**	**6.42553**	**6.80914**	**5.20814**

Dependence of R_{wp} on *pa* and *pb* for $La_2O_2Cu_{0.333}Cd_{0.333}Se_2$ of Chapter 5.

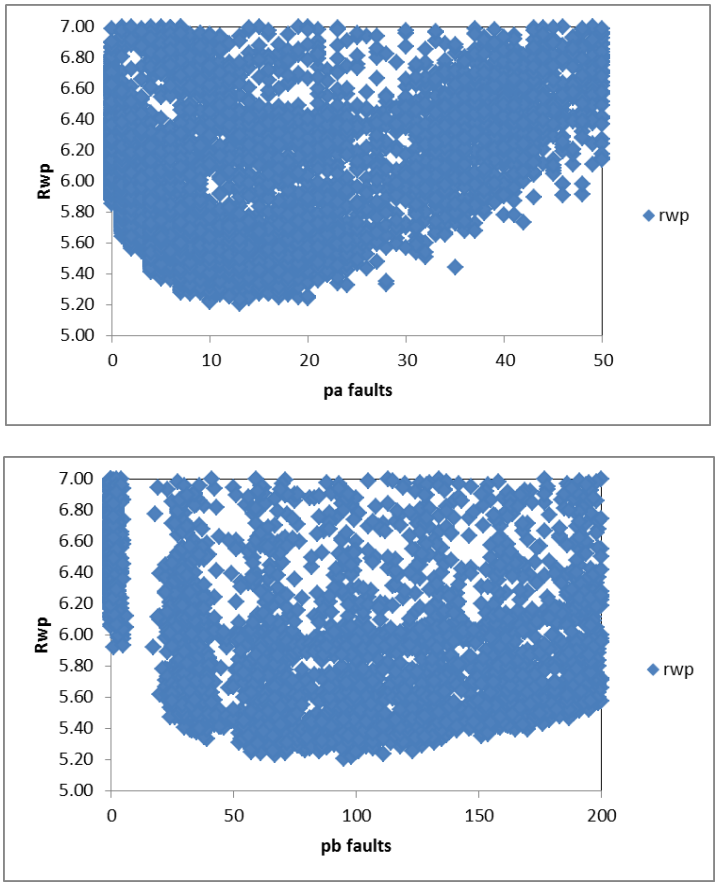

Scatter plot showing R_{wp} for stacks with different numbers of *pa*-type and *pb*-type faults for $La_2O_2Cu_{0.333}Cd_{0.333}Se_2$ of Chapter 5. 11700 different stacks were tested with different values of *pa* and *pb*. Note that a large spread in R_{wp} is observed for each count of *pa*/*pb* faults. This is due to compression of the *pa*/*pb* scatter plot onto one dimension – at each *pa* value there will be stacks with a "bad" number of pb faults. Surface plots as shown on the previous page were not generated for this sample.

Min of rwp	*pa*								
pb	**0**	**0.001**	**0.01**	**0.03**	**0.05**	**0.07**	**0.1**	**0.2**	**Minimum**
0	7.45748	7.1399	6.37877	5.92556	5.5796	5.33055	5.36178	5.61077	5.33055
0.001	7.07764	6.97411	6.38275	5.96862	5.43802	5.52509	5.41193	5.75387	5.41193
0.1	5.96387	6.03285	5.51443	5.27939	5.19794	5.14682	5.1763	5.88345	5.14682
0.2	5.77208	5.63329	5.29556	5.17236	5.07374	5.05682	5.06031	5.4985	5.05682
0.3	5.63932	5.53172	5.28287	5.04327	4.99807	5.00664	5.07766	5.56264	4.99807
0.4	5.61123	5.47434	5.16273	5.02479	4.95914	4.98038	5.03002	5.62509	4.95914
0.5	5.61027	5.4544	5.16559	5.03081	4.9858	4.99113	5.06964	5.60408	4.9858
0.6	5.62956	5.49238	5.19674	5.05366	5.02197	4.99898	5.06773	5.65513	4.99898
0.8	5.75235	5.6446	5.40302	5.18134	5.17493	5.1904	5.24503	5.84353	5.17493
0.999	7.15291	6.95906	6.46471	6.00967	5.72874	5.52462	5.45596	5.46582	5.45596
(blank)									
Minimum	**5.61027**	**5.4544**	**5.16273**	**5.02479**	**4.95914**	**4.98038**	**5.03002**	**5.46582**	**4.95914**

Dependence of R_{wp} on *pa* and *pb* for $La_2O_2Cu_{1.5}Cd_{0.25}Se_2$ of Chapter 5.

Min of rwp	*pa*									
pb	**0.001**	**0.005**	**0.01**	**0.015**	**0.02**	**0.03**	**0.05**	**0.1**	**(blank)**	**Minimum**
0.001	5.02833	3.87931	3.4602	3.46088	3.35955	3.21569	3.40741	5.72276		3.21569
0.005	4.87039	4.13404	3.71141	3.48468	3.31363	3.22576	3.49275	5.31287		3.22576
0.01	4.91691	4.36995	3.64631	3.37352	3.38965	3.40755	3.51803	5.64017		3.37352
0.015	4.90474	4.32275	3.75976	3.57632	3.35011	3.39111	3.73049	5.93397		3.35011
0.02	4.95334	4.38202	3.68949	3.42265	3.56966	3.42069	3.78243	5.97277		3.42069
0.03	4.93054	4.327	3.86944	3.69326	3.65917	3.56636	4.08857	5.60994		3.56636
0.05	5.00364	4.98133	4.26324	3.84262	4.4345	4.01389	3.75873	5.86479		3.75873
0.1	5.94673	5.4671	6.02701	5.73281	5.46829	5.31949	6.38659	7.55232		5.31949
(blank)										
Minimum	**4.87039**	**3.87931**	**3.4602**	**3.37352**	**3.31363**	**3.21569**	**3.40741**	**5.31287**		**3.21569**

Dependence of R_{wp} on *pa* and *pb* for $La_2O_2Cu_{0.5}Cd_{0.75}Se_2$ of Chapter 5.

Min of rwp	*pa*								
pb	0.001	0.01	0.03	0.05	0.07	0.1	0.2	(blank)	Minimum
0.001	4.91759	4.64635	4.46465	4.41482	4.42291	4.4201	4.87002		4.41482
0.1	4.5662	4.46587	4.36068	4.34128	4.35203	4.3834	4.70184		4.34128
0.2	4.47051	4.38063	4.32593	4.31713	4.30802	4.39112	4.7542		4.30802
0.3	4.45602	4.35588	4.30067	4.29958	4.32167	4.39893	4.64683		4.29958
0.4	4.42437	4.31346	4.28097	4.27059	4.3043	4.37818	4.85498		4.27059
0.5	4.41826	4.33979	4.28464	4.27219	4.30038	4.34274	4.90461		4.27219
0.6	4.42106	4.33168	4.29231	4.28736	4.29071	4.36015	4.78838		4.28736
0.8	4.45467	4.36577	4.32695	4.33328	4.34463	4.42729	4.69252		4.32695
0.999	4.8691	4.69799	4.50986	4.4435	4.4367	4.4399	4.75675		4.4367
(blank)									
Minimum	**4.41826**	**4.31346**	**4.28097**	**4.27059**	**4.29071**	**4.34274**	**4.64683**		**4.27059**

Dependence of R_{wp} on *pa* and *pb* for $La_2O_2Cu_{1.6}Cd_{0.2}Se_2$ of Chapter 5.

Appendix 4

$La_2O_2Cu_{2-2x}Fe_xSe_2$					$La_2O_2Cu_{2-2x}Zn_xSe_2$				
x	V/Å^3	a/Å	b/Å	c/Å	x	V/Å^3	a/Å	b/Å	c/Å
0	581.54(2)	5.7506(1)	5.7475(1)	8.7975(1)	0	581.54(2)	5.7506(1)	5.7475(1)	8.7975(1)
0.25	582.05(1)	5.7592(1)	5.7547(1)	8.7810(1)	0.25	583.17(1)	5.7501(1)	5.7469(1)	8.8237(1)
0.333	581.87(1)	5.7620(1)	5.7572(1)	8.7704(1)	0.333	583.19(1)	5.7483(1)	5.7452(1)	8.8293(1)
0.5	581.26(2)	5.7723(1)	5.7617(1)	8.7386(1)	0.5	584.04(3)	5.7466(1)	5.7390(2)	8.8544(2)
0.667	581.26(2)	5.7723(1)	5.7617(1)	8.7386(1)	0.667	583.95(1)	5.7417(1)	5.7350(1)	8.8670(1)
0.75	580.16(2)	5.7805(1)	5.7636(1)	8.7070(2)	0.75	583.78(1)	5.7398(1)	5.7322(1)	8.8717(1)
0.75	580.98(2)	5.7691(1)	5.7606(1)	8.7410(1)	1	584.90(2)	5.732(2)	5.7330(8)	8.899(1)
1	580.40(2)	5.723(2)	5.7038(8)	8.662(1)					

$La_2O_2Cu_{2-2x}Mn_xSe_2$					$La_2O_2Cu_{2-2x}Cd_xSe_2$				
x	V/Å^3	a/Å	b/Å	c/Å	x	V/Å^3	a/Å	b/Å	c/Å
0	581.54(2)	5.7506(1)	5.7475(1)	8.7975(1)	0	581.54(2)	5.7506(1)	5.7475(1)	8.7975(1)
0.25	587.07(1)	5.7517(1)	5.7491(1)	8.8769(1)	0.25	590.36(6)	5.7515(2)	5.7507(5)	8.9245(2)
0.333	588.76(1)	5.7504(1)	5.7479(1)	8.9064(1)	0.333	593.22(5)	5.7513(2)	5.7505(4)	8.9684(1)
0.5	591.57(1)	5.7460(1)	5.7443(1)	8.9615(1)	0.5	598.8(3)	5.7507(5)	5.749(2)	9.055(2)
0.667	595.01(1)	5.7457(1)	5.7433(1)	9.0153(1)	0.667	604.40(3)	5.7514(1)	5.7481(2)	9.1409(2)
0.75	597.39(1)	5.7439(1)	5.7409(1)	9.0582(1)	0.75	607.80(2)	5.7521(1)	5.7515(1)	9.1860(1)
1	602.30(1)	5.7370(1)	5.7370(1)	9.1521(1)	1	616.30(2)	5.7520(2)	5.7510(2)	9.3157(1)

Cell volume/parameters across the $La_2O_2Cu_{2-2x}M_xSe_2$ solid solutions of Chapter 7.

$La_2O_2Cu(M_{1-y}M'_y)_{0.5}Se_2$						$La_2O_2Cu_{0.667}(M_{1-y}M'_y)_{0.667}Se_2$				
	y	V/Å^3	a/Å	b/Å	c/Å	y	V/Å^3	a/Å	b/Å	c/Å
All Fe	0	581.26(2)	5.7723(1)	5.7617(1)	8.7386(1)	0	581.26(2)	5.7723(1)	5.7617(1)	8.7386(1)
	0.2	581.51(1)	5.7598(1)	5.7561(1)	8.7699(1)	0.2	580.44(1)	5.7603(1)	5.7541(1)	8.7560(1)
	0.4	581.66(1)	5.7550(1)	5.7523(1)	8.7852(1)	0.4	581.83(1)	5.7528(1)	5.7496(1)	8.7953(1)
	0.6	582.07(1)	5.7498(1)	5.7460(1)	8.8090(1)	0.6	581.09(5)	5.7456(2)	5.7439(4)	8.8037(2)
	0.8	582.29(2)	5.7464(1)	5.7425(1)	8.8229(1)	0.8	582.82(2)	5.7446(1)	5.7390(1)	8.8392(1)
All Zn	1/0	584.04(3)	5.7466(1)	5.7390(2)	8.8544(2)	1/0	583.95(1)	5.7417(1)	5.7350(1)	8.8670(1)
	0.2	584.83(1)	5.7442(1)	5.7404(1)	8.8680(1)	0.2	585.07(1)	5.7389(1)	5.7324(1)	8.8923(1)
	0.4	586.48(1)	5.7452(1)	5.7416(1)	8.8896(1)	0.4	587.26(1)	5.7400(1)	5.7346(1)	8.9205(1)
	0.6	588.54(1)	5.7465(1)	5.7437(1)	8.9157(1)	0.6	589.96(1)	5.7410(1)	5.7371(1)	8.9560(1)
	0.8	589.85(1)	5.7460(1)	5.7440(1)	8.9358(1)	0.8	592.20(1)	5.7412(1)	5.7388(1)	8.9870(1)
All Mn	1/0	591.57(1)	5.7460(1)	5.7443(1)	8.9615(1)	1/0	595.01(1)	5.7457(1)	5.7433(1)	9.0153(1)
	0.2	593.10(2)	5.7469(1)	5.7456(2)	8.9810(1)	0.2	596.45(5)	5.7426(2)	5.7421(3)	9.0442(1)
	0.4	603.19(8)	5.7452(3)	5.7361(5)	9.1518(5)	0.4	592.89(8)	5.7470(3)	5.7428(5)	8.9820(4)
	0.4	587.92(2)	5.7447(2)	5.7447(2)	8.9075(2)	0.4	609.90(5)	5.7398(2)	5.7398(2)	9.2563(4)
	0.6	603.41(6)	5.7500(2)	5.7454(4)	9.1327(3)	0.6	612.21(5)	5.7433(1)	5.7433(1)	9.2800(2)
	0.6	585.78(2)	5.7520(2)	5.7520(2)	8.8525(2)	0.6	594.64(5)	5.7512(2)	5.7458(4)	8.9972(2)
	0.8	599.01(4)	5.7511(1)	5.7497(3)	9.0574(1)	0.8	603.56(2)	5.7481(1)	5.7481(1)	9.1336(1)
	0.8	583.63(2)	5.7530(1)	5.7530(1)	8.8168(2)	0.8	598.54(4)	5.7503(1)	5.7485(2)	9.0536(2)
All Cd	1/0	598.8(3)	5.7507(5)	5.749(2)	9.055(2)	1/0	604.40(3)	5.7514(1)	5.7481(2)	9.1409(2)

Cell volume/parameters across the $La_2O_2Cu(M_{1-y}M'_y)_{0.5}Se_2$ and $La_2O_2Cu_{0.667}(M_{1-y}M'_y)_{0.667}Se_2$ solid solutions of Chapter 7.

Index to the E-appendix

Chapter	Compound	file type	Description
Chapter 3	$Ce_2O_2ZnSe_2$	input	Pawley refinement using $5\sqrt{2}a_{subcell} \times \sqrt{2}a_{subcell} \times 2c_{subcell}$ supercell (lab X-ray data)
		input	Occupancy mode ISODISTORT refinement using Ibam S4 model (lab X-ray data)
		input	Occupancy mode ISODISTORT refinement using Ibca S4 model (lab X-ray data)
		input	Occupancy and distortion mode combined ISODISTORT refinement using Ibam S4 model (lab X-ray and neutron data)
		input	Combined final refinement (lab X-ray and neutron data)
		cif	Combined refinement CIF
		data	Raw lab X-ray data (14 hours on d7)
		data	Raw neutron data (banks 1 to 6 from GEM)
		spreadsheet	Diffuse reflectance data
		spreadsheet	Squid data
Chapter 4	$La_2O_2(Zn_{0.3}Mn_{0.7})Se_2$	input	An example of the modulation approach to fitting satellite peaks (lab X-ray data)
		data	Raw lab X-ray data (1 hour on d7)
	$Ce_2O_2(Fe_{3/4}Zn_{1/4})Se_2$	input	Combined final refinement (lab X-ray and neutron data)
		cif	Combined refinement CIF
		data	Raw lab X-ray data (14 hours on d7)
		data	Raw neutron data (banks 1 to 6 from GEM)
	$Ce_2O_2(Fe_{1/8}Zn_{7/8})Se_2$	input	Combined final refinement (lab X-ray and neutron data)
		cif	Combined refinement CIF
		data	Raw lab X-ray data (14 hours on d7)
		data	Raw neutron data (banks 1 to 6 from GEM)
	$Ce_2O_2(Zn_{1/6}Mn_{5/6})Se_2$	input	Combined final refinement (lab X-ray and neutron data)
		cif	Combined refinement CIF
		data	Raw lab X-ray data (14 hours on d7)
		data	Raw neutron data (banks 1 to 6 from GEM)
	$La_2O_2(Zn_{1/10}Mn_{9/10})Se_2$	input	Combined final refinement (lab X-ray and neutron data)
		cif	Combined refinement CIF
		data	Raw lab X-ray data (14 hours on d7)
		data	Raw neutron data (banks 1 to 6 from GEM)
	$Ce_2O_2CdSe_2$	input	Final refinement (synchrotron data)
		cif	CIF
		data	Raw synchrotron data
Chapter 5	$La_2O_2CuCd_{0.5}Se_2$ 1Cu1Cd	Input	Refinement using standard 1Cu/1Cd model (synchrotron data)
		cif	CIF
		data	Raw synchrotron data
	$La_2O_2Cu_{0.667}Cd_{0.667}Se_2$ 1Cu2Cd	Input	Refinement using standard 1Cu/2Cd model (synchrotron data)
		cif	CIF
		Input	Refinement using 1Cu/2Cd model with antiphase boundary every ~7 unit cells (synchrotron data)
		Input	Refinement using 1Cu/2Cd model containing 0.16% *pa* stacking faults (synchrotron data)
		Python script	The general Python script used alongside all stacking fault input files

		data	Raw synchrotron data
	$La_2O_2Cu_{0.333}Cd_{0.333}Se_2$ 2Cu1Cd	Input	Refinement using standard 2Cu/1Cd model (synchrotron data)
		cif	CIF
		data	Raw synchrotron data
Chapter 6	$(La_{2-z}Sr_z)O_2CuCd_{0.5}Se_2$ z = 0, 0.05, 0.1, 0.15, 0.2, 0.4	spreadsheet	PPMS resistivity data from 4 to 300 K
	$La_2O_2Cu_2S_2$	CASTEP parameter files	Geometry optimisation 1 (with cell fixed), geometry optimisation 2 (with cell NOT fixed), DOS calculation
	$La_2O_2Cu_2Se_2$	CASTEP parameter files	Geometry optimisation 1 (with cell fixed), geometry optimisation 2 (with cell NOT fixed), DOS calculation
	$La_2O_2CuCd_{0.5}Se_2$	CASTEP parameter files	Geometry optimisation 1 (with cell fixed), geometry optimisation 2 (with cell NOT fixed), DOS calculation
	$La_2O_2CdSe_2$	CASTEP parameter files	Geometry optimisation 1 (with cell fixed), geometry optimisation 2 (with cell NOT fixed), DOS calculation
Chapter 7	$La_2O_2Cu_{0.667}Mn_{0.667}Se_2$ 1Cu2Mn	input	Refinement using standard 1Cu/2Mn model of Figure 7.7 (synchrotron data)
		cif	CIF
		data	Raw synchrotron data
	$La_2O_2Cu_{0.5}Mn_{0.75}Se_2$ 1Cu3Zn	input	Refinement using modulated 1Cu/2Zn model of Figure 7.11 (synchrotron data)
		cif	CIF
		data	Raw synchrotron data